University of Leicester

Galactic Cluster Dwarfs

Sarah Louise Casewell

Supervisor:

Richard F Jameson

Thesis to be submitted for the degree of

Doctor of Philosophy

at the University of Leicester.

X-ray & Observational Astronomy Group

Department of Physics and Astronomy

University of Leicester

November 20, 2007

UMI Number: U233568

UMI U233568

Declaration

I hearby declare that no part of this thesis has been previously submitted to this or any other University as part of the requirement for a higher degree. The work described here was conducted by the under signed except for contributions from colleagues as acknowledged in the text.

Sarah Louise Casewell
November 20, 2007

Galactic Cluster Dwarfs

Sarah Louise Casewell

ABSTRACT

This work describes the results of studies into galactic cluster brown and white dwarfs. Galactic cluster dwarfs have a known age increasing their use to the observer and allowing meaningful comparisons to models to be made. For brown dwarfs this is to increase knowledge of the initial mass function and star formation. For white dwarfs it is to increase understanding of the relationship between the progenitor star and its resultant white dwarf.

Introductory material is in the first three chapters and the main science results in the following four chapters. The final chapter summarises the science chapters and suggests future work.

Chapter 4 describes a deep, large area (2.5 square degrees) survey of the Pleiades using optical (I and Z) and infrared (J) data. Three possible L dwarfs and six possible T dwarf new members of the cluster remain after proper motion measurements and follow up infrared photometry.

Chapter 5 presents results of a catalogue survey of Melotte 111 which more than doubled the number of stellar members of the cluster. Also described is a deep survey of the cluster centre, with follow up photometry, proper motions and spectra. Thirteen brown dwarf candidates are discovered.

Chapter 6 describes work which measured proper motions of 143 known brown dwarfs using WFCAM and 2MASS. Five candidate wide binaries are discovered, as well as 8 fast moving L dwarfs that may belong to the thick disc. The moving group method was used to identify 25 dwarfs as possible members of the Hyades, Ursa Major and Pleiades moving groups.

Chapter 7 presents the results of a spectroscopic study of 9 Praesepe white dwarfs. One is shown to be a non member of the cluster and another a possible double degenerate. A more precise initial-final mass relation is calculated.

Acknowledgements

First and foremost I would like to thank my supervisor Richard Jameson for all his help and guidance over the last three years. He has answered all my (occasionally stupid) questions with patience and has a knack of explaining complicated things in a clear way.

I also would like to thank Paul Dobbie for being prepared to be bombarded with emails when things go wrong, but without whom I never would have got anywhere near finishing this. Thanks also to Nigel H and Simon Hodgkin for their advice and assistance. Thanks to Matt for my introduction to observing as well as for all the advice, assistance and encouragement he has provided, and hopefully it won't snow on La Palma for another 20 years or so! Thanks also to Emma for mending IRAF over and over again and to Ann-Marie and Kim for their Thesis advice. I also would like to thank the department in general for making the last three years so enjoyable.

Big thanks also go to Karen, Sue, Hayley, Pixie, Col, Ann-Marie, Mark and Liz for making me laugh and helping me to get through the tough times.

My family have always encouraged and supported me and I am incredibly grateful for that, even if they aren't quite sure what I do at work with these dwarfs! My final thanks go to Merv, who has permanently been there for me throughout these last 3 years and has have to suffer numerous occasions where I have been distraught because "I can't do it". He has always suffered these situations with good humour and has put me back on my feet, told me not to be so silly and to get on with it. And three years later I have. And I can do it (maybe). Thank you so much.

Publications

1. New stellar and substellar candidate members of the Coma Berenices open star cluster
   S. L. Casewell, R. F. Jameson and P. D. Dobbie, 2005, AN, 326, 991

2. New stellar members of the Coma Berenices open star cluster
   S. L. Casewell, R. F. Jameson and P. D. Dobbie, 2006, MNRAS, 365, 447

3. New Praesepe white dwarfs and the initial mass-final mass relation
   P. D. Dobbie, R. Napiwotzki, M. R. Burleigh, M. A. Barstow, D. D. Boyce, S.L. Casewell,
   R. F. Jameson, I. Hubeny and G. Fontaine, 2006, MNRAS, 369, 383

4. The nature of the close magnetic white dwarf + probable brown dwarf binary
   SDSSJ121209.31+013627.7
   M. R. Burleigh et al., 2006, MNRAS, 373, 1416

5. Two T dwarfs from the UKIDSS early data release
   T. R. Kendall et al., 2007, A&A, 466, 1057

6. Proper motion L and T dwarf candidate members of the Pleiades
   S. L. Casewell, P. D. Dobbie, S. T. Hodgkin, E. Moraux, R. F. Jameson, N. C. Hambly,
   J. Irwin and N. Lodieu, 2007, MNRAS, 378, 1131

7. Eight new T4.5-T7.5 dwarfs discovered in the UKIDSS Large Area Survey Data Release 1
   N. Lodieu et al., 2007, MNRAS, accepted

8. GRB 060206 and the quandary of achromatic breaks in afterglow light curves
   P. A. Curran et al., 2007, MNRAS, accepted

9. Proper motions of L and T dwarfs
   R. F. Jameson, S. L. Casewell, N. P. Bannister , N. Lodieu, K. Keresztes, P. D. Dobbie
   and S. T. Hodgkin, 2007, MNRAS, Submitted

10. The ages of L dwarfs
    R. F. Jameson, N. Lodieu, S. L. Casewell, N. P. Bannister, and P. D. Dobbie, 2007, MNRAS, In Prep.

Contents

List of Figures

XXV

List of Tables

Chapter 1

Introduction

1.1 Galactic cluster dwarfs

The title of this thesis "Galactic cluster dwarfs" concerns both brown and white dwarfs in open star clusters and moving groups within the galaxy.

The majority of the work presented here in the thesis is about brown dwarfs, and so the introductory material will concentrate on them. There is an introduction to formation and importance of white dwarfs in the relevant chapter.

1.2 Brown dwarfs

A brown dwarf is best described as a failed star. They have masses between those of stars and planets (≈ 0.015 $M_\odot$ and 0.075 $M_\odot$, Burrows et al. 2001). Brown dwarfs form like stars from the gravitational collapse of a gas cloud, but they are never massive enough to generate the internal temperatures and pressures required for hydrogen burning. The masses of brown dwarfs and planets may overlap and brown dwarfs with masses lower than 0.015 $M_\odot$ have

been discovered. However, the fundamental difference between brown dwarfs and planets is their formation mechanism which will be discussed in more detail in the next chapter.

1.3 Why are brown dwarfs important?

Why do we study brown dwarfs? The first brown dwarfs were discovered over a decade ago (Gl 229B, Nakajima et al. 1995 and Teide 1, Rebolo et al. 1995) and the advent of deep wide field surveys have led to the discovery of more than 100 T dwarfs and 500 L dwarfs. These dwarfs are studied in detail, mainly to improve understanding of the initial mass function. The initial mass function describes the mass distribution of star formation. Young open star clusters are assumed to be representative of the initial mass function as a whole. Clusters such as the Pleiades, Blanco 1, σ Orionis, IC2391, Upper Sco and many more are searched for low mass members to determine the lowest mass that is able to form a brown dwarf, and how many low mass objects are present in clusters. The minimum mass of an object that can form in a cluster is still unknown, but low mass brown dwarfs (<13 M_{Jup}) are being discovered. Thanks to the invention of adaptive optics, more and more brown dwarfs are now being found from searches for binaries.

1.4 Project aims

Both brown dwarfs and white dwarfs are degenerate objects and in order to study them in a meaningful way their age must be known. Studying them in galactic clusters is the best way to accomplish this.

This thesis concerns mainly brown dwarfs, although Chapter 7 concentrates on white dwarfs in the Praesepe open star cluster. The work presented here aims to increase our knowledge of brown dwarfs by searching for them with increasingly fainter magnitudes to constrain the lower end of the initial mass function in the studied clusters. For the two open star clusters and

2

three moving groups studied here, this has been done by the use of photometric surveys (both optical and infrared) and proper motion measurements of candidate members of the cluster. The work on white dwarfs has been undertaken to constrain the fundamental relationship between the initial mass and final mass of a white dwarf. Open star clusters are the best places to do this, as the age of the white dwarfs are known, making calculations of the pre and post white dwarfs stages easier. As the mass loss involved when a white dwarf is formed is not entirely understood and cannot as yet be modelled, observational data must be used to constrain this relationship.

1.5 Thesis structure

Chapter 2 provides an overview of the work that has been done concerning brown dwarfs. The theory of brown dwarfs is discussed including their formation, structure and evolution as well as the models that are used to describe them. The observational part of the chapter describes recent work and searches for brown dwarfs in the field, in binaries and in open star clusters.

Chapter 3 describes the methods and instruments used throughout this work. An introduction to photometry, astrometry and detectors is provided, followed by a description of the instruments used and data reduction techniques used in the thesis. At the end of the chapter there are descriptions of the wide field surveys that have also been used to obtain data.

Chapter 4 presents the results of a 2.5 square degree multi wavelength survey of the Pleiades open star cluster. The subsequent proper motion analysis is discussed as well as the follow up photometry. The probability of cluster membership of the new candidates, and the resultant mass function are calculated.

Chapter 5 describes a study of Melotte 111 (the Coma Berenices open star cluster) that has made use of the 2 Micron All Sky survey and the United States Naval Observatory catalogue B1.0 to find stellar members of the cluster. Also described is a 15 square degree deep i and Z band survey conducted with the Wide Field Camera on the Isaac Newton Telescope and

the subsequent J and K band follow up photometry, proper motion analysis and infrared spectroscopy of low mass candidate cluster members.

Chapter 6 details a study of 143 known field brown dwarfs for which proper motions were measured. From these 8 high velocity L dwarfs are found and 5 possible wide binary objects. Finally, using the moving group method, new members of the Hyades, Ursa Major and Pleiades moving groups are found and discussed.

Chapter 7 presents high resolution spectra of 9 white dwarfs in the Praesepe open star cluster. Effective temperatures, gravities and radial velocities were measured for these objects and their cluster membership is discussed. The new initial mass-final mass relation is presented using these new measurements.

Chapter 8 summarises the conclusions from the previous 4 science chapters (Chapters 4, 5, 6 and 7) and suggests ways in which the work presented here may be followed up in the future.

Chapter 2

Review of brown dwarfs

2.1 Introduction

This chapter contains an overview of the observational and theoretical work that has been carried out to date in the field of brown dwarfs. The observational summary concentrates on the searches for brown dwarfs that have been carried out over the last decade. The theoretical summary will discuss the models and physics involved in the structure of brown dwarfs.

2.2 Brown dwarf theory

Brown dwarfs are composed of mainly metallic hydrogen and helium, and are supported in hydrostatic equilibrium by electron degeneracy pressure. As brown dwarfs contract along the Hayashi track during their formation, their cores are completely convective.

As the physics involved in modelling stars and brown dwarfs is quite complex, it can be simplified by using stellar models called polytropes. All objects with completely convective interiors (very low mass stars and brown dwarfs) can be described by a $n = 3/2$ polytrope. The

5

non-relativistic nature of the pressure support sets $n = 3/2$. Equations 2.1 and 2.2 describe the relationships between density ρ, pressure P, and the specific heats at constant pressure C_p and constant volume C_v for these polytropes.

$$P \propto \rho^{\frac{n+1}{n}},$$ (2.1)

$$\frac{n+1}{n} = \gamma = \frac{C_p}{C_v}.$$ (2.2)

In equation 2.2 $(n+1)/n = 5/3$ for $n = 3/2$, which is γ for an adiabatic monatomic gas. 5/3 is also the index for a non relativistic degenerate gas. This polytropic model can be used to show that there is a limiting mass of $\approx$ 0.07-0.09 $M_\odot$, below which a contracting star cannot reach the main sequence stage. Instead, due to the lack of thermonuclear processes, it becomes a degenerate object. This electron degeneracy pressure provides the pressure needed to counteract the gravitational collapse of the object. This theory was first postulated independently by Kumar (1963) and Hayashi & Nakano (1963). These objects have radii of $\approx$0.1 $R_\odot$.

It can been seen from the above theory that the idea of brown dwarfs has been around for a long time, however, it was soon realised that if they were to be detected, then their physics could be used to create evolutionary models which could be compared to the colour magnitude diagrams used by astronomers. This physics is complex and involves an understanding of the standard equations of stellar structure, an appropriate equation of state, an understanding of the convection that occurs inside a brown dwarf, and an understanding of the boundary conditions present at the surface of the star, which includes the cool molecules present in the atmospheres, and at cooler temperatures, grains.

It is shown in Burrows & Liebert (1993) that the surface boundary condition governs the evolution of the brown dwarf. This has helped progress within the field of modelling brown dwarfs. The ability of the models to deal with dust in the atmospheres of brown dwarfs has improved matters, and the uncertainties in the surface opacities have been reduced, although

some uncertainties still remain.

2.2.1 Formation

Since the first brown dwarfs were discovered in 1995, (Rebolo et al., 1995; Nakajima et al., 1995; Oppenheimer et al., 1995) questions began to be asked about their formation. These questions are:

1. Is there a distinct difference between the mechanisms that form brown dwarfs and those that form planets?

2. Do brown dwarfs form the same way as stars?

The answer to the first question is complex. It has been shown by theory (Whitworth et al., 2007) and observations (Zapatero Osorio et al., 2002; Lodieu et al., 2006; Casewell et al., 2007) that the star formation process can produce objects with masses within the "planetary regime" i.e. below the deuterium burning limit at 13 M_{Jup}. However, planets are generally defined to be objects that form from the remnants of a stellar T tau type accretion disc, and involve the accumulation of a rocky core, and possibly the subsequent acquisition of a gassy envelope (Burrows et al., 2001).

As far as the second question is concerned, it is generally argued that stars and brown dwarfs do form in a common manner, because the statistical properties of brown dwarfs (mass function, clusters, kinematics, binary statistics, etc) appear to form a smooth continuum with those of low mass stars. There are currently 5 main mechanisms thought to form brown dwarfs, however, it is not yet known what proportion of brown dwarfs are formed by which method. See Whitworth et al. (2007) for a review.

Turbulent fragmentation of molecular clouds

This mechanism of brown dwarf formation was theorised about after a similarity was noticed between the protostellar core mass function and the stellar initial mass function. The mechanism involves a collapsing gas cloud, out of which fragments will condense if they have mass greater than the Jeans mass of the cloud, or if the density is greater than the Jeans density of the cloud. The process is thought to be hierarchical in that once the cloud has contracted and hence its density has increased, it will fragment into a number of smaller clouds which will also contract and fragment etc. The process stops when the smallest clouds are collapsing so rapidly, or are so optically thick that the work (PdV) being done on them cannot be radiated away fast enough, and so the cloud begins to heat up. The minimum mass for star formation can be calculated this way (Rees, 1976; Low & Lynden-Bell, 1976), which is $\approx 0.004 \ M_\odot$ as calculated by Whitworth et al. (2007). The problem with this mechanism is that the density needs to be very high for a brown dwarf mass fragment to gravitationally collapse. It is likely that cores of this density are not common, and exceptional circumstances must form them. Whitworth et al. (2007) calculates that the number of brown dwarfs with $M \sim 0.01 \ M_\odot$ is approximately equal to the number of stars with $M \sim 100 \ M_\odot$, which was predicted theoretically by Zinnecker (1984). There is, however, no evidence that this hierarchical fragmentation occurs in nature, and it is likely that any small fragments formed condense out more slowly than the larger structure to which they belong. This means the fragments are likely to merge with each other, creating higher mass objects.

Collapse and fragmentation of large prestellar cores

Large prestellar cores collapse to form clusters of stars and brown dwarfs. There are many mechanisms involved which affect the final stellar masses produced. There is a high likelihood of these high mass cores fragmenting during collapse, due to their having a Jeans mass of $\approx 0.8 \ M_\odot$. These fragments are not generally spherical (Goodwin et al., 2002). Gravity then works to enhance the non-spherical nature of the fragments (Lin et al., 1965), where the collapse occurs fastest along the shortest axis which forms sheets and filaments, which then fragment.

This situation is very hard to model using numerical simulations due to the lack of knowledge about the initial conditions (Hennebelle et al., 2004). However, various attempts have been made (Boss et al., 2000; Whitehouse & Bate, 2006).

Disc fragmentation

The study of brown dwarfs formed by the fragmentation of a disc is split into three sections, depending on whether the disc is isolated and relaxed, unrelaxed or interacting with a star. All of these conditions affect the fragmentation process. The disc becomes unstable against fragmentation depending on the conditions and the disc. These fragments may then cool and condense out to form brown dwarfs.

Premature ejection of protostellar embryos

This mechanism involves a large number of protostellar embryos which have already formed, but are still embedded in their parental core or disc. The individual embryos then begin to evolve by accreting gas, and by interacting with each other. This method can form brown dwarfs of a range of masses - those which move through, and thus accrete from, the densest regions near the centre of the core can grow to be massive. Those embryos that remain on the outskirts of the core, where the gas is much less dense, do not grow much. Many numerical simulations of this method have been performed (see Bate et al. 2003; Goodwin et al. 2004a,b), and it has been shown by Bonnell et al. (1997, 2001) that this method of brown dwarf formation can reproduce the general form of the initial mass function.

Photo-erosion of pre-existing cores

This method begins with a pre-existing core of less than 1 $M_\odot$, which is then overrun by an HII region (Hester et al., 1996). As a result of this, an ionisation front begins to "eat away" at the core, photo-eroding it. This ionisation front is preceded by a compression wave, which when it

reaches the centre of the core, creates a protostar. This protostar then begins to accrete gas. The accretion is aided by an expansion wave propagating outwards creating an inflow, which feeds the protostar. The expansion wave and ionisation front eventually meet, causing the ionisation front to ionise gas which remains bound to the protostar. All the material inside the ionisation front at this point remains within the protostar. There is evidence that some protostars formed by this method exist (Hester et al., 1996; McCaughrean & Andersen, 2002), however, it is a very inefficient method for creating protostars as massive pre-existing prestellar cores are needed to begin the process. The mechanism also only occurs within the vicinity of an OB star, making it an unlikely method for the formation of the majority of brown dwarfs, however, brown dwarf-brown dwarf binaries can be created via this mechanism.

2.2.2 Evolution

Evolutionary models allow many properties of brown dwarfs such as luminosity, radius and temperature to be determined as a function of age. These models cover the main stages in the evolution of brown dwarfs.

At very young ages ($<10^6$ years) brown dwarfs steadily evolve with a constant effective temperature. The luminosity and radius decrease as the object contracts under the influence of gravity, along the "Hayashi track".

After this contracting stage, between the ages of 10^6 and 3×10^6 years, the objects burn their small supply of deuterium (if massive enough) and hence maintain some balance against gravity. During this phase they have a constant radius, effective temperature and luminosity.

After all of the deuterium has been burnt, the hydrostatic equilibrium cannot be maintained, gravity takes hold, and the objects contract once more.

As the core of a brown dwarf never reaches the temperature or pressure required to ignite hydrogen, this contraction is stopped by the onset of electron degeneracy, which limits the radius of the object, while supporting it against gravity. The brown dwarf then simply cools

and fades.

The models of Burrows et al. (2001) are some of the most recent theoretical models of brown dwarfs, and provide predictions of effective temperature, core temperature, luminosity and radius for various ages ranges. These predictions are shown in figures 2.1 to 2.4.

2.2.3 Lithium indicators

Substellar objects are characterised by the fact that they do not use pressure generated by thermonuclear power to support themselves against gravity. However, they may still have some form of thermonuclear burning occur in their cores. Objects more massive than 13 M_{Jup} will burn deuterium, and objects more massive than $\approx$ 0.06 $M_{\odot}$ will burn lithium (T $\approx$ 2.4$\times$ 10^6 K) using the following reactions;

$$Li^6 + H^1 \rightarrow He^3 + He^4, \qquad (2.3)$$

$$Li^7 + H^1 \rightarrow 2He^4. \qquad (2.4)$$

This leads to the lithium test (Rebolo et al., 1986). In main sequence stars, the lithium is consumed long before the star reaches the main sequence. Therefore if the Li I doublet at 6708 Å is found in the spectrum of a candidate brown dwarf, it is known that it has a core temperature of less than 2.4$\times 10^6$ K, as the lithium never ignited. However, there is one drawback to this test, this being that the highest mass brown dwarfs will burn lithium eventually. As well as being a useful test of whether an object is substellar, the lithium abundances in the spectra of objects may also be used to determine the age of the object. This method has been used to find the age of a number of open star clusters including the Pleiades (Basri et al., 1996). Figure 2.5 shows how a cluster's age is found using lithium. The objects PPL15 and HHJ3 are indicated on the diagram, which also shows mass isochrones and lithium depletion boundaries calculated from the models of Nelson et al. (1993). A review of the work done on using lithium ages for open star clusters is presented in Jeffries (2000).

11
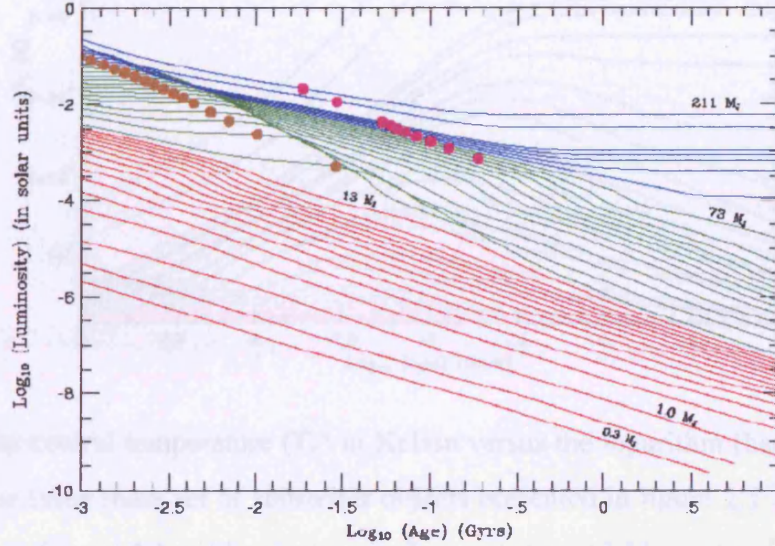
Figure 2.1: Evolution of the luminosity (in $L_\odot$) of isolated solar-metallicity red dwarf stars and substellar-mass objects versus age (in years). The stars are shown in blue, those brown dwarfs above 13 M_{Jup} are shown in green, and brown dwarfs/giant planets equal to or below 13 M_{Jup} are shown in red. Though the colour categories are based on deuterium or light hydrogen burning, they should be considered arbitrary vis à vis whether the object in question is a brown dwarf or a planet, sensibly distinguished on the basis of origin. The masses of the substellar objects/stars portrayed are 0.3, 0.5, 1.0, 2.0, 3.0, 4.0, 5.0, 6.0, 7.0, 8.0, 9.0, 10.0 11.0, 12.0, 13.0, and 15.0 M_{Jup} and 0.02, 0.025, 0.03, 0.035, 0.04, 0.045, 0.05, 0.055, 0.06, 0.065, 0.07, 0.075, 0.08, 0.085, 0.09, 0.095, 0.1, 0.15, and 0.2 $M_\odot$ ($\equiv$ 211 M_{Jup}). For a given object, the gold dots mark when 50% of the deuterium has burned and the magenta dots mark when 50% of the lithium has burned. Note that the lithium sequence penetrates into the brown dwarf regime near 0.065 $M_\odot$, below the hydrogen burning main sequence edge mass. Caption and figure from Burrows et al. (2001).

12
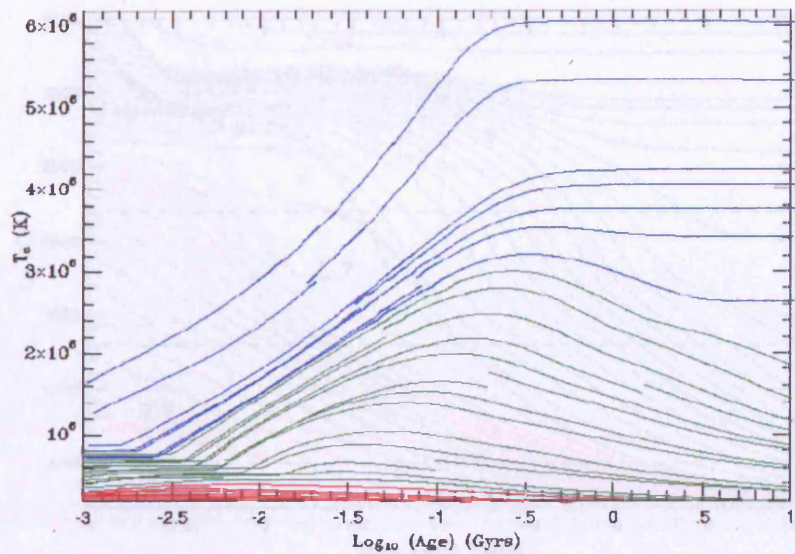
Figure 2.2: The central temperature (T_c) in Kelvin versus the logarithm (base ten) of the age (in Gyr) for the same mass set of substellar objects presented in figure 2.1. As in figure 2.1, the red lines are for models with masses equal to or below 13 M_{Jup}, the green lines are for objects above 13 M_{Jup} and below the edge of the main sequence, and the blue are for stars (red dwarfs) up to 0.2 $M_\odot$. Caption and figure from Burrows et al. (2001).

2.2.4 Atmospheres

The main obstruction to creating models of brown dwarfs is their cool atmospheres (T<3500 K) which are notoriously difficult to model because of the complex molecules (TiO, H_2O, CH_4, etc) present. These molecules lead to uncertainties in predicting opacities in the atmospheres, and in the coolest brown dwarfs the molecules begin to condense out into grains causing more problems. Black and grey atmosphere models (non wavelength dependant) cannot be used as the molecular absorption coefficients are strongly wavelength dependent. In 1997 Chabrier & Baraffe used the non-grey dust free atmospheres of Allard et al. (1997) to develop models of the structure and evolution of low mass, dense objects. These models developed into the NEXTGEN models (Baraffe et al., 1998). These NEXTGEN models cover the range of masses between 1 $M_\odot$ and 0.01 $M_\odot$, describing objects with T_C >2200 K. There are known errors within these models, particularly below temperatures of 3700 K where the optical colours

13
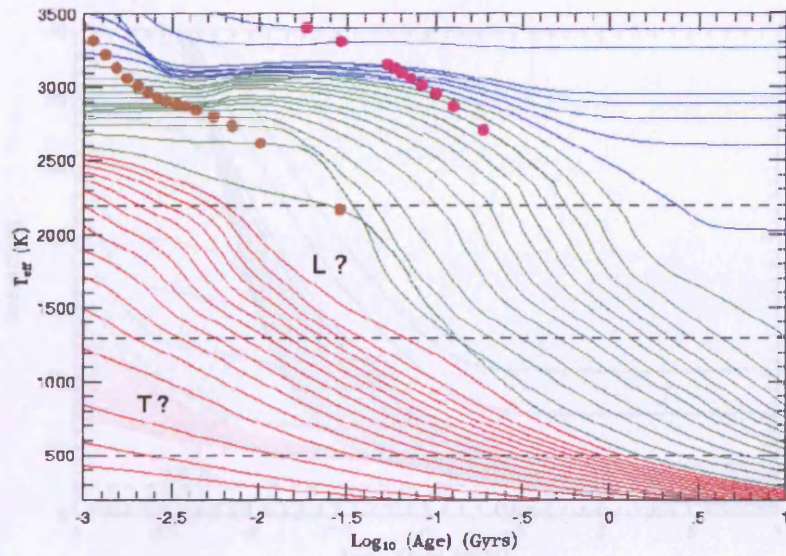
Figure 2.3: This figure depicts the evolution of T_{eff} (in K) with age for the mass set used in figure 2.1 and with the same colour scheme. Superposed are dots which mark the ages for a given mass at which 50% of the deuterium (gold) and lithium (magenta) are burned. Though the L and T dwarf regions are as yet poorly determined and are no doubt functions not only of T_{eff}, but of gravity and composition, approximate realms for the L and T dwarfs are indicated with the dashed horizontal lines. The spectral type M borders spectral type L on the high-temperature side. Note that the edge of the hydrogen-burning main sequence is an L dwarf and that almost all brown dwarfs evolve from M to L to T spectral types. Caption and figure from Burrows et al. (2001).

predicted by the models are too blue by ≈ 0.5 mags. This colour difference is due to a missing opacity source at the onset of grain formation within the object's atmosphere. For cooler objects the NEXTGEN models are replaced by the DUSTY models (Chabrier et al., 2000). These models take into account the formation of dust in the atmosphere of the brown dwarf and the scattering and absorption that result from it. The DUSTY models cover the effective temperature range between 2800 K and 900 K, covering a mass range of 0.1 to 0.01 $M_{\odot}$ for objects with ages between 10^8 and 10^{10} yr. Although these models extend as low as 900 K, it is unrealistic to use them below a temperature of ≈ 1300 K. This corresponds to a spectral type of late L. Below this point, the dust clouds become less important, either because of

14
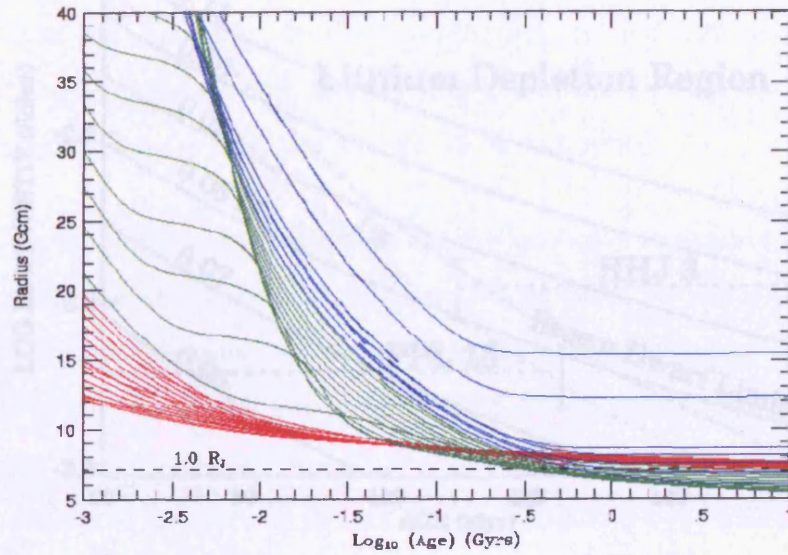
Figure 2.4: The radius (in units of 10^9 centimetres) of substellar objects with the masses given in figure 2.1 versus the $\log_{10}$ of the age (in Gyr). The same colour scheme that was used in figure 2.1 is used here. Red is for the low-mass substellar mass objects, green is for the intermediate-mass substellar mass objects, and blue is for the stars. Also shown is the radius of Jupiter. Note that the radii are not monotonic with mass and that they cluster near the radius of Jupiter at late times, despite the wide range of masses from $0.3\,M_{Jup}$ to $0.2\,M_\odot$ represented. Caption and figure from Burrows et al. (2001).

increasing cloud gaps or the clouds sinking below the photosphere. This point is known as the L to T transition and has been recently modelled by Burrows et al. (2006). Eventually methane begins to become evident in the spectra of the brown dwarfs, which marks the beginning of the T dwarfs. The T dwarfs are modelled by the COND models (Baraffe et al., 2003). In these models the dust clouds are below the photosphere. Heavy elements such as Fe, Ti and V, which form part of the dust are removed from the atmosphere. The COND models are known to be inaccurate for optical wavelengths (e.g. I, Z). The COND models should also be used with caution for objects younger than a few Myr, due to oversimplified initial conditions used to create the models. All of the above mentioned models are sensitive to the initial conditions. After a few Myr the models converge onto a single track, thus making them more reliable for
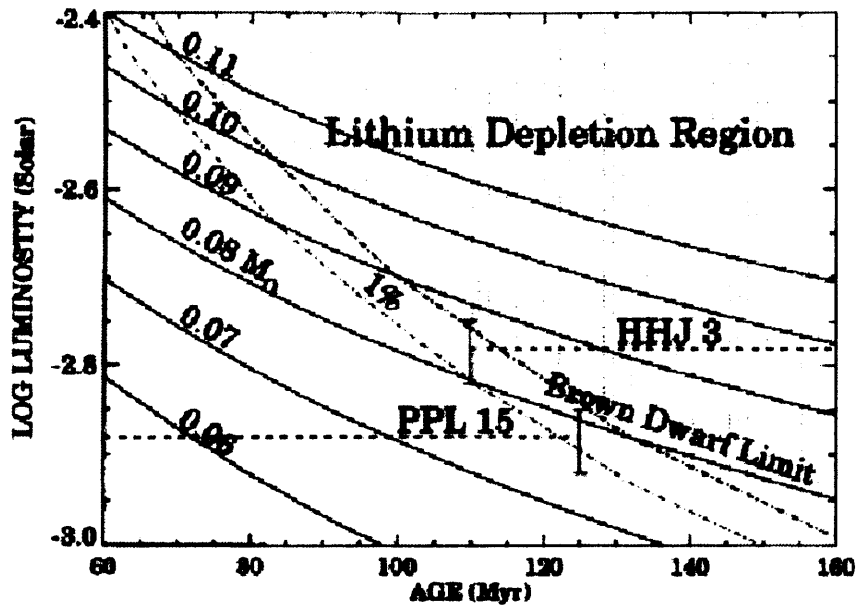
Figure 2.5: The diagram used to determine the age of the Pleiades from measurements of lithium abundance of two objects, HHJ3 and PPL15. HHJ3 shows partial depletion of lithium, whereas PPL15 shows no evidence of lithium at all. Using the models of Nelson et al. (1993) to plot the mass isochrones, and also using the observed lithium abundances (the depletion boundary and the 1% limit are plotted) and object luminosity, the age of the cluster can be determined. The figure is taken from (Basri et al., 1996). Since this work in 1996 it has been determined that PPL15 is in fact a binary, which changes its position on the above diagram, but does not affect the method used.

the older objects (Baraffe et al., 2002).

2.2.5 Transformations from models to the observations

The models presented by Baraffe et al. (1998, 2003) and Chabrier et al. (2000) are presented in terms of absolute magnitudes and in the common wavebands used by astronomers. Alternative filters require transforms (usually colour based) between the photometric systems being used, particularly in the I band. Isabelle Baraffe has made the models (NEXTGEN, DUSTY and COND) available in other wavebands on request if the filter profile is provided, such as the

CFH12k and Sloan systems used in this thesis. These models covering a variety of ages eliminate much of the uncertainty involved in selecting brown dwarf candidates, especially when combined with empirical tracks (e.g. Leggett et al. 2002; Hawley et al. 2002; Chiu et al. 2006) for the areas where the models are known to be inaccurate.

Once the first brown dwarf was discovered, it became necessary to define a spectral classification scheme to describe brown dwarfs, similar to that for stars. As with stars, the scheme involves the strength and appearance or disappearance of spectral features. Two spectral classes were invented, L and T. L dwarfs are cooler than M dwarfs and can be both low mass stars or brown dwarfs. They cover the temperature range of $\sim$2000 K (L0) to $\sim$1200 K (L9). The most obvious difference between the spectra of M and L dwarfs is the reduction in strength of the TiO and VO bands. TiO weakens and disappears apart from the band at 8432 Å at $\sim$L2, and VO has disappeared by L5. The most prominent molecular bands are metal hydrides, CaH, FeH, CrH, MgH and H_2O vapour, and strong atomic lines of Cs, Rb, Na and K are also present. These atomic lines grow with strength towards the later spectral types. These changes are caused by the dust forming within the brown dwarf atmosphere.

The T dwarfs, of which Gl 229B is one, are characterised by methane and water absorption bands in their spectra. The T dwarf regime spans the temperature range between $\sim$1200 K to 700 K. T dwarfs may have masses that are less than the deuterium burning limit at 13 M_{Jup}. The search for T dwarfs is hindered by the fact that the near infrared colours using the J, H and K magnitudes begin to be blue due to the onset of methane in these objects, instead of getting redder as for L dwarfs. This causes many more contaminants to be accidentally selected while searching for T dwarfs. See Reid (1999); Burgasser et al. (2006a) and Lodders & Fegley (2006) for a review. Table 1 of Lodders & Fegley (2006) describes the spectral features required for each spectral type from M8 to T8. The spectra of brown dwarfs from L1 to T8 can be seen in figure 2.6.
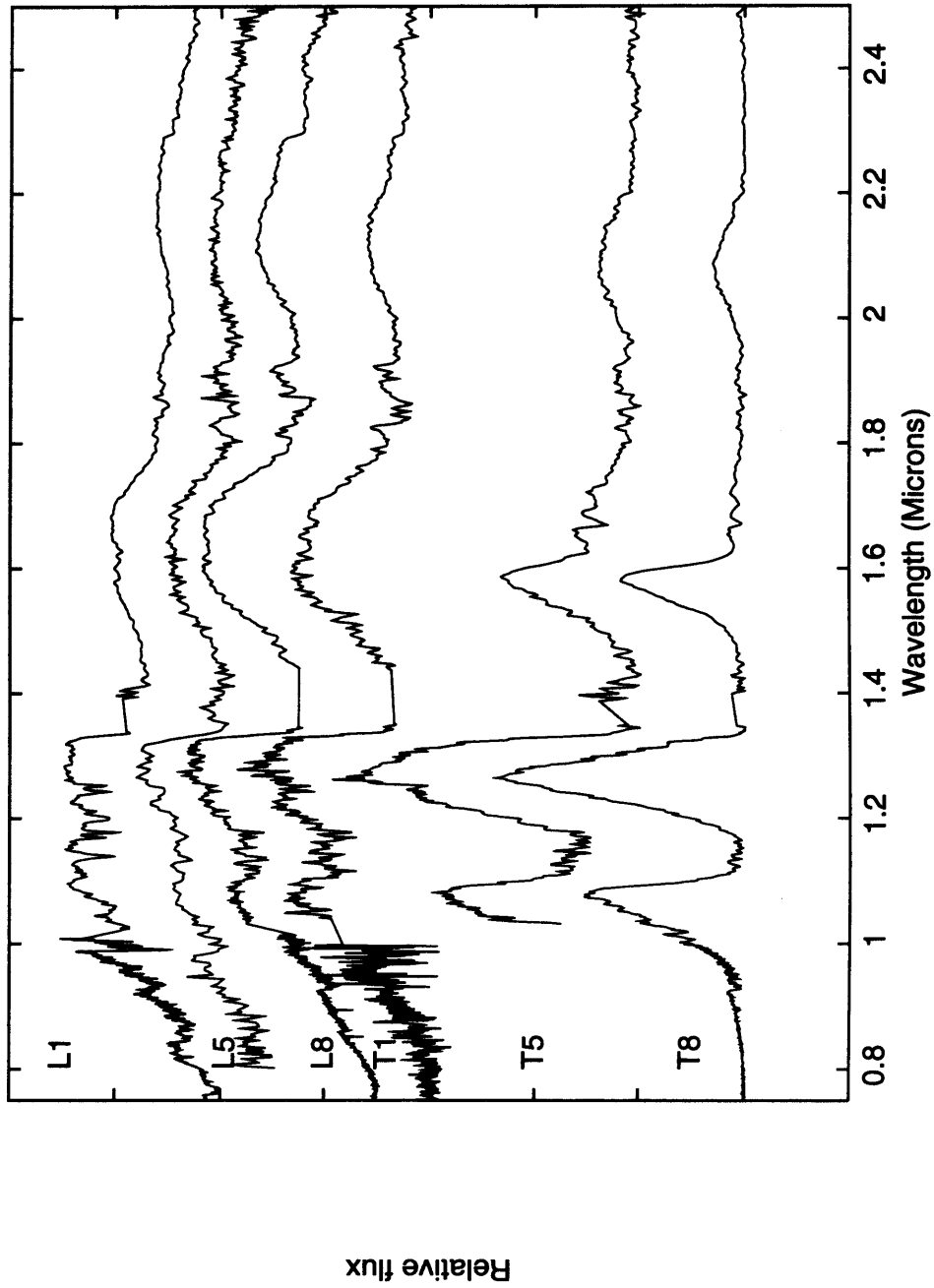
Figure 2.6: Spectra of brown dwarfs from L1 to T8. Spectra are: L1 2MASS J14392836+1929149 (Leggett et al., 2002), L5 SDSS J164916.89+464340.0 (Chiu et al., 2006), L8 2MASS J15232263+3014562 (Leggett et al., 2002), T1 SDSS J083717.21-000018.0 (Leggett et al., 2000), T5 2MASS J23391025+1352284 (Knapp et al., 2004), T8 2MASS J04151954-0935066 (Knapp et al., 2004).

2.3 Searching for brown dwarfs

Over the last decade many brown dwarfs have been discovered, with hundreds of L dwarfs and ≈ 100 T dwarfs currently known. There are three main ways to search for brown dwarfs.

- As companions to other stars.

- As members of open star clusters.

- As free floating objects.

2.3.1 Binary surveys

Searching for brown dwarfs in binary systems is preferable to searching for isolated brown dwarfs in the field. The main reasons for this are that the searches can be carried out by using high resolution imaging techniques using infrared photometry or spectroscopy. If both objects are observed, then it can be proved that they share a common proper motion (if high enough to be resolved) and there is a possibility that the dynamical mass of the system can be calculated as for GJ 569 Bab (Zapatero Osorio et al., 2004), 2MASSJ05352184-0546085 (Stassun et al., 2006), and the AB Dor system (Close et al., 2005). The dynamical mass can then be used with an age estimate to calculate the mass of the brown dwarf or brown dwarfs. Recent surveys of solar-type stars, both in the field and in clusters and associations have concentrated on searching for very low mass companions. Radial velocity surveys (Marcy & Butler, 2000; Udry et al., 2003) have shown that less than 0.5% of solar type stars have brown dwarf compantions within ≈ 5 AU. This statistic is ≈ 3 times less than the binary fraction for hydrogen-burning stars with companions of the same separation. There are more brown dwarf companions to solar-type stars known at larger separations (separation >1000 AU), in fact solar type stars have comparable numbers of brown dwarf and M dwarf companions (Gizis et al., 2001). It is still unknown why this brown dwarf desert exists at low separations. Maxted & Jeffries (2005) used Monte Carlo simulations to predict the binary fraction of brown dwarf/brown dwarf binaries and calculate it to be 32-45% overall, and 17-30% for close binaries.

Most of the recent searches for binaries have involved direct detection techniques, such as those used by Nakajima et al. (1995) which resulted in the discovery of Gl 229B, the first T dwarf to be identified. Gl 229 was the 100th object to be surveyed in this study, thus illustrating the rarity of brown dwarf companions. The first brown dwarf companion to a white dwarf was reported by Becklin & Zuckerman (1988), although at the time the nature of the infrared companion was unknown. The most comprehensive search for white dwarf-brown dwarf binaries to date was conduced by Farihi et al. (2005) who surveyed several hundred white dwarfs and determined that less than 0.5% have a brown dwarf companion. These direct imaging techniques have now evolved to use laser guide star adaptive optics and space based facilities such as *Spitzer*. Radial velocity methods have led to mass measurements being made for 5 systems to date, including the eclipsing system, 2MASSJ05352184-0546085, discovered by Stassun et al. (2006). There are now known to be many brown dwarfs existing in multiple star systems, with a primary object that may be a star such as Gl 229, (Nakajima et al., 1995), a white dwarf WD0137-349, (Maxted et al., 2006) or even another brown dwarf 2MASSJ05352184-0546085, (Stassun et al., 2006). See Burgasser et al. (2007a) for a review.

2.3.2 Open clusters

Open star clusters are ideal places to search for brown dwarfs, as any that are found to be members of the cluster, therefore have a known age, distance and metallicity. In the case of clusters with well defined proper motions, this can also be used as an additional tool with which to distinguish members from the background or foreground contaminants. Brown dwarfs in young star clusters also have relatively high temperatures which makes them easy to detect in optical and near infrared wavelengths. Because the distance to the cluster and its age are known, evolutionary models such as the NEXTGEN and DUSTY can be used to predict the main sequence of the stars and then brown dwarfs, as well as being used to estimate masses of any objects found. Below are included reviews of the main studies that have been performed on the Pleiades, Hyades and Taurus star clusters as well as discussing the ρ Ophiuchi, Trapezium and σ Orionis star forming regions and the Upper Scorpius association. There is a huge

amount of literature associated with these clusters, and so I shall only include the most recent work on the clusters in the following descriptions.

The Pleiades

The Pleiades cluster is considered an ideal place to search for brown dwarfs. This is because the cluster has a well known lithium age of 125 Myr (Stauffer et al., 1998), and is nearby at 130 pc (Stauffer et al., 1998), making brown dwarf members relatively bright and easy to observe.

The first CCD survey of the cluster was conducted in 1989 by Jameson & Skillen (1989) and covered an area of 125 square arcminutes in the R and I bands. Many brown dwarf candidates were observed, however, all turned out to be field objects. Stauffer et al. (1989) undertook a similar survey, but in the V and I bands, covering over 900 square arcminutes, with follow up photometry obtained at J, H and K. Stauffer et al. (1994) extended this survey to cover a 0.4 square degrees, identifying 6 brown dwarf candidates including PPL15, which later was shown to be a binary. Some three years later Hambly et al. (1991) studied Schmidt plates in the R and I bands covering the cluster, unearthing 30 brown dwarf candidates, and concluding that the mass function of the cluster was flat at the lower masses. In a later work Hambly et al. (1993) calculated proper motions for objects believed to be in the mass range of 0.08 to 0.5 $M_\odot$, of which 48 were followed up with infrared photometry (Steele et al., 1993). 22 of these objects were believed to have masses of below 0.08 $M_\odot$, although none showed evidence of lithium (Steele et al., 1995).

In 1995 the first brown dwarf was discovered in the cluster, Teide 1 (Rebolo et al., 1995). Teide 1 shows no evidence of lithium depletion in its spectrum, but does have a proper motion and radial velocity consistent with that of the cluster, and optical spectra showed TiO and VO bands. Since 1995, many surveys have been carried out on the Pleiades, finding many brown dwarf candidates. Most of the surveys involved using the I and Z bands to survey the cluster and select candidates, followed by infrared photometry to confirm brown dwarf status. In

21

Cossburn et al. (1997) the first I, Z survey of the cluster is described. 900 square arcminutes were covered, and one brown dwarf was discovered with an effective temperature of 2800 K and a mass of 0.08 $M_\odot$. Further studies of Festin (1997, 1998); Martín et al. (1998) and Hambly et al. (1999) uncovered further brown dwarf candidates, and in 2000 the largest study up until that point was conducted by Pinfield et al. (2000) who covered 6 square degrees of the cluster and uncovered 339 candidate cluster members, 30 of which are believed to be brown dwarfs.

After this point the surveys unearthed more and more brown dwarf candidates, but also focused on determining the form of the cluster mass function across the stellar/substellar boundary. These surveys of the Pleiades indicate that the present day cluster mass function, across the stellar/substellar boundary and down to M~0.02 $M_\odot$ (based on the evolutionary models of the Lyon Group), can be represented by a slowly rising power law model, $dN/dM \propto M^{-\alpha}$. For example, from the Canada-France-Hawaii Telescope (CFHT) survey conducted at R and I and covering 2.5 sq. degrees, Bouvier et al. (1998) identified 17 candidate brown dwarfs ($I_C \geq 17.8$) and derived a power law index of $\alpha=0.6$. From the 1.1 sq degrees Isaac Newton Telescope (INT) survey conducted at I and Z, with follow-up work undertaken at K, Dobbie et al. (2002a) unearthed 16 candidate substellar members and found a power law of index $\alpha=0.8$ to be compatible with their data. Jameson et al. (2002) showed that a powerlaw of index $\alpha=0.41\pm0.08$ was consistent with the observed mass function over the range $0.3 \geq M \geq 0.035$ $M_\odot$. This study used a sample of 49 probable brown dwarf members assembled from the four most extensive CCD surveys of the cluster available at the time, the International Time Project survey (Zapatero Osorio et al., 1998), the CFHT survey (Bouvier et al., 1998; Moraux et al., 2001), the Burrell Schmidt survey (Pinfield et al., 2000) and the INT survey Dobbie et al. (2002a). The CFHT survey was subsequently extended to an area of 6.4 sq. degrees (at I and Z) and unearthed a total of 40 candidate brown dwarfs. Moraux et al. (2003) applied statistical arguments to account for non-members in their sample and derived a power law index of $\alpha=0.6$. More recently, Bihain et al. (2006) have used deep R, I, J and K band photometry and proper motion measurements to unearth 6 robust L type Pleiades members in an area of 1.8 sq. degrees with masses in the range 0.04-0.02 $M_\odot$ and derived a power law index of $\alpha=0.5\pm0.2$.

The deepest survey to date was undertaken in 2005 using the Wide Field CAMera (WFCAM) on the United Kingdom InfraRed Telescope (UKIRT) (Casewell et al., 2007), which unearthed 7 new brown dwarf candidates, of which 5 are believed to be T dwarfs, the first in any cluster. This study is presented in this thesis. The largest study to date was performed using the galactic cluster survey from the UKIRT Infrared Deep Sky Survey (UKIDSS, Warren et al. 2007) by Lodieu et al. (2007) who discovered 73 candidate members, of which 14 are believed likely to by cluster members. They also determined a cluster binary fraction of 29%, which is lower than the 50% presented in Pinfield et al. (2003) for the cluster, but is in agreement with the binary fraction determined by Maxted & Jeffries (2005). Their mass function, calculated by fitting a lognormal function, was found to peak at 0.24 $M_\odot$ which is in agreement with other studies of the cluster.

The Hyades

The Hyades is the closest rich star cluster to the sun at a distance of 44 to 48 pc (Gatewood et al., 1992; van Altena et al., 1997; Perryman et al., 1998). The cluster has been found to have a tidal radius of 10-10.5 pc (Reid, 1993; Perryman et al., 1998) and estimates for the total cluster mass range from 300 to 460 $M_\odot$ (Oort, 1979; Reid, 1992).The age of the Hyades is estimated to be between 500 and 900 Myr (Barry et al., 1981; Kroupa, 1995). Perryman et al. (1998) fitted theoretical isochrones that include the effects of convective overshoot to the Hipparcos based cluster Hertzsprung-Russell diagram and derived an age of 625±50 Myr, the value that is generally used. The Hyades has a well known proper motion, although due to its proximity radial velocities and the moving cluster method are often used to distinguish cluster members from contaminants (Reid, 1993; Reid & Hawley, 1999). Because the Hyades covers over 200 square degrees of sky, photographic plates, and large area surveys are ideal tools with which low mass members can be discovered. Reid (1992) surveyed 110 square degrees of the cluster, down to masses of 0.1 $M_\odot$ using Palomar and UK Schmidt plates. Previous photometry and VRI CCD photometry then allowed Reid (1993) to refine the previous list of 393 proper motion members to 210. The spatial distribution of the low mass members of the Hyades reveals that the cluster is influenced by the dynamical process of mass segregation,

meaning that it is likely that the lower mass members have been ejected from the cluster (Reid, 1993). More recently there has been a survey performed by Gizis et al. (1999) who searched 28 square degrees of the Hyades centre to a depth of $K_S \approx 14.8$ ($\approx 0.06 \, M_\odot$), and no substellar members were discovered. A few dwarfs with spectral types of later than M7 were found, although none were later than M9.

Dobbie et al. (2002b) searched 10.5 square degrees of the cluster complete to $I_C \approx 20$ to search for low mass stellar and substellar cluster members. They found twenty candidates, of which only one, previously discovered object RHy279 (Reid, 1992, 1993) was shown to be a member after follow up infrared photometry, optical spectroscopy and a proper motion analysis had been performed. These findings also support the claim that there has been dynamical evaporation of low mass members in the cluster. There are only about 10 members of the cluster with masses less than $0.12 \, M_\odot$. There are, however, two candidate brown dwarfs which are in multiple star systems, which as it is estimated that 23 to 20 % of Hyads are in multiple systems, is not surprising. Both of these candidates are estimated to have masses of below $0.075 \, M_\odot$ (Reid & Mahoney, 2000; Guinan & Ribas, 2001), but neither of these brown dwarfs have been imaged as yet. Bannister & Jameson (2007) have identified 5 L dwarf and 2 T dwarfs that have apparently escaped from the Hyades and belong to its moving group. This strengthens the case that the cluster is losing its low mass members.

Taurus

The Taurus star forming region has always been an important target for brown dwarf searches, because of its low gas and stellar density relative to other star forming regions. At a distance of 140 pc it is relatively near, and because of its youth (≈ 1 Myr), brown dwarf members are among the brightest in the sky. In the late 1990s members of Taurus were discovered down to the hydrogen mass burning limit by deep imaging at X-ray, optical and near-infrared wavelengths (Strom & Strom, 1994; Luhman & Rieke, 1998). Wide field imaging with optical wavebands has uncovered many objects with substellar masses across the whole region (Briceño et al., 1998; Martín et al., 2001). This optical imaging has also been combined with

2MASS near-infrared photometry which has been successful in finding more substellar members to the region (Luhman, 2000a; Briceño et al., 2002; Luhman et al., 2003a). In 2004 Luhman (2004) published 15 new members of Taurus, all of which have spectral types of less than M6, making them substellar. The initial mass function (IMF) of Taurus has long been a subjects for discussion. Luhman (2000a) calculated an IMF for 0.7 square degrees, which was characterised by a peak at masses of $\approx$ 0.8 $M_{\odot}$. This mass function highlighted a deficit of brown dwarfs in Taurus in relation to the Trapezium cluster in Orion (Luhman, 2000a; Hillenbrand & Carpenter, 2000; Muench et al., 2002). Larger areas of Taurus were subsequently studied, 7.7 square degrees by Briceño et al. (2002) and Luhman et al. (2003a), thus taking the whole area studied up to 8.4 square degrees. The IMF was again calculated, and the ratio of brown dwarfs to stars was found to be lower than that for the Trapezium by a factor of 2. It was determined by Luhman et al. (2003b) that this brown dwarf fraction did agree with that for the similarly aged IC348, although the peak mass of the distribution was different. It was believed that IC348 and Taurus had a distinctly different IMF to that for other clusters, particularly as the stellar mass function peaked at M5 for IC348 and K7 for Taurus, making them unusual.

ρ Ophiuchi, σ Orionis and the Trapezium

The ρ Ophiuchi cloud is another near site of star formation, and so continues to be a popular choice for studying star formation. The cloud is situated on the edge of the Upper Scorpius association, and consists of many filamentary dark clouds that extend away from dense cores of molecular gas (de Geus, 1992). The central region contains an embedded cluster with ≈ 100 members (Casanova et al., 1995). The distance to the cluster is uncertain, although ≈ 160 pc (Chini, 1981) is usually adopted. The central embedded region has an estimated age of $\approx$ 0.3 to 1 Myr (Luhman & Rieke, 1999). The studies of this region currently tend to be in the X-ray regime, looking for activity that would indicate star forming, or flares from brown dwarfs (Ozawa et al., 2005). Other recent studies of the cluster have concentrated on searching for discs or accretion from brown dwarfs that will indicate how and where they form within the cloud (Gatti et al., 2006). The cluster has also been studied in the infrared (Greene &

Young, 1992; Comeron et al., 1993; Strom et al., 1995; Barsony et al., 1997), although the high internal extinction (A_v >50) makes this very difficult. Luhman & Rieke (1999) do detect objects as low in mass as 0.02 $M_\odot$, and have determined that the mass function is flat between 0.05 and 1 $M_\odot$. Bontemps et al. (2001) also obtain a similar result, which is that there is no turn down in the mass function down to 0.06 $M_\odot$. It was suggested by de Geus (1992) that the star formation in the core of ρ Ophiuchi is the latest in a series of star formation events that began in Upper Centaurus-Lupus and Lower Centaurus-Crux which then triggered the star formation of the OB stars in the Scorpius-Centaurus OB association.

The σ Orionis cluster is a young, $\approx$2-4 Myr old cluster (Zapatero Osorio et al., 2002; Oliveira et al., 2002; Sherry et al., 2004; Franciosini et al., 2006) and forms part of the Orion OB1b sub-association, which has an age of 1.7-7 Myr (Warren & Hesser, 1978; Brown et al., 1994, 1998; Briceño et al., 2005), and the same distance as the sub-association, 439±33 pc (Brown et al., 1998). As a young cluster, it has often been searched for low mass members using optical and infrared spectroscopy, X-rays and *Spitzer* (Zapatero Osorio et al., 2002; Oliveira et al., 2002; Sherry et al., 2004; Hernández et al., 2007). In 1997 Walter et al. (1997) used spectra to identify over 100 low mass, pre main sequence members, and 80 X-ray sources. Since 1997, many surveys of the cluster have been made, and many brown dwarfs have been discovered. Recent work by Béjar et al. (2001) combined surveys in the I and Z bands and the J band (Zapatero Osorio et al., 2000; Béjar et al., 1999), which covered in total 847 square arcminutes. A large number of brown dwarf candidates were discovered, and a mass function derived for the cluster, that is believed to be rising into the substellar regime. From this survey, an object, σ Orionis 70 was discovered, and is believed to be a T dwarf owing to its low mass ($\approx$3 M_{Jup}) and spectral features (Zapatero Osorio et al., 2000, 2002). Subsequent spectra of this object have been obtained (Martín & Osorio, 2003) and the gravity sensitive features examined, and it was calculated to have a lower gravity than the surrounding field dwarfs, hence making it a cluster member. However, Burgasser et al. (2004) believe that it is in fact a foreground field object. Their reasoning is that the object used as a template spectrum for the gravity measurement was a nearby background star, and not a T dwarf, thus making the comparison invalid.

The Trapezium region of the Orion nebula contains hundreds of stars within a region of a few arcminutes with the age of most being less than 1 Myr (Prosser et al., 1994; Hillenbrand, 1997). The Trapezium has been well studied due to its richness (Hillenbrand & Carpenter, 2000; Lucas & Roche, 2000; Luhman et al., 2000b; Muench et al., 2002; Lada et al., 2004). In 2000 Lucas & Roche (2000) reported the discovery of a large number of brown dwarfs, 13 of which had planetary masses. This number of planetary objects was then extended to 33 (Lucas et al., 2005) following a JHK survey. Follow up spectroscopy of 11 of these objects found four and a possible fifth to be cluster members, three to be field objects and three objects have uncertain status (Lucas et al., 2006). It is estimated that over 5% of the population in the trapezium may have masses of less than 20 M_{Jup}.(Lucas et al., 2006). Meeus & McCaughrean (2005) also has used near-infrared spectroscopy of 16 brown dwarf candidates, and looked for a low gravity for them, indicating cluster membership.

The Upper Scoripus association

Upper Scorpius (Upper Sco) is one of the three subgroups that the Scorpius Centaurus OB association is composed of, the other two being Upper Centaurus Lupus and Lower Centaurus Crux (Blaauw, 1964; de Zeeuw et al., 1999). Upper Sco has an age of 5 Myr (Preibisch & Zinnecker, 2002) and lies at a distance of 145±2 pc from the Sun (de Bruijne et al., 1997). The first survey of Upper Sco was performed in 1994 using the *Einstein* X-ray satellite (Walter et al., 1994) which discovered 28 low mass pre-main sequence stars in 7 square degrees. Five years later de Bruijne et al. (1997) discovered 115 members using kinematic information and trigonometric parallaxes for 1215 Hipparcos stars. Later on Preibisch et al. (1998) carried out another X-ray survey which revealed hundreds of X-ray sources which were later confirmed spectroscopically as being pre-main sequence members of the Scorpius Centaurus association. More recently deep optical and infrared photometric surveys have allowed many members to be identified below the hydrogen burning limit, with spectral types of later than M6 (Ardila et al., 2000; Martín et al., 2004; Slesnick et al., 2006). Before 2007, there were 46 M6, 10 M7, 6 M8 and 2 M9 dwarfs belonging to the association, all of which had been spectroscopically confirmed using chromospheric activity and weak gravity features (Martín

et al., 2004; Slesnick et al., 2006). In late 2006-2007, a 6.5 square degree survey of Upper Sco was undertaken by Lodieu et al. (2007) using the science verification data from the UKIDSS galactic cluster survey. These data were 3 magnitudes deeper than any previous surveys of the cluster and was complete to Z=20.1 mag (0.01 $M_\odot$). This survey unearthed 129 candidate members with masses between 0.3 and 0.007 $M_\odot$. 116 of these objects appear to have proper motions consistent with being members of the association and 12 appear to be brown dwarfs with masses of less than 0.02 $M_\odot$. Further to this survey Lodieu et al. (2006) used the Early Data Release from the UKIDSS galactic cluster survey to further their study of the association. They studied 9.3 square degrees of the association and selected 112 additional candidate members of the cluster. Of these 112, 80 were rejected due to their colours being affected by reddening (A_v <2, Walter et al. 1994). Of the remaining objects, 13 were then rejected owing to having incorrect proper motions for membership. Three objects were then further rejected as having optical spectroscopy inconsistent with membership. This left 15 of the 112 possible members confirmed by optical spectroscopy, proper motion and photometry, 4 of which are brown dwarfs (spectral types less than M6). The initial 12 brown dwarfs identified by Lodieu et al. (2007) have not been observed spectroscopically to date.

Many brown dwarfs have also been discovered in other clusters and associations such as Blanco 1 (Moraux et al., 2007), IC2391 (Barrado y Navascués et al., 2001), Chamaeleon (Luhman et al., 2006) and many others.

2.3.3 Field surveys

There are many difficulties associated with searching for brown dwarfs in the field. The main one is the lack of provenance of the brown dwarf, its age, metallicity and distance are not known, making it difficult to compare the discovered object with known statistics. The age of the object can be inferred from its motion, rotation and surface activity. A mass can be estimated using measurements of gravity sensitive features in the spectrum, and for nearby objects, parallax measurements can be used to calculate distances and hence luminosities.

The lithium test can also be applied to determine whether an object is a brown dwarf. Some of the first work done on brown dwarfs in the field, was done by accident such as Jones et al. (1994), who discovered a brown dwarf candidate among data from an infrared survey searching for faint galaxies. More recently Ruiz et al. (1997) discovered a nearby (10 pc) free floating brown dwarf, Kelu-1, that shows the presence of lithium in its optical spectrum. Kelu-1 is estimated to have a temperature of $\approx$ 1990 K and a mass of less than 0.075 $M_{\odot}$. Since the major sky survey data from the DEep Near Infrared Survey (DENIS), 2 Micron All Sky Survey (2MASS), Sloan Digital Sky Survey (SDSS) and most recently UKIRT Deep Sky Survey (UKIDSS) has been available, many field brown dwarfs have been identified by searching huge areas of sky and selecting objects that appear to have the correct colours. There is a huge literature available on field brown dwarfs discovered through sky surveys, see Leggett et al. (2002), Cruz et al. (2003) (2MASS), Delfosse et al. (1999) (DENIS), Hawley et al. (2002), Chiu et al. (2006) (SDSS), Kendall (2007) (UKIDSS) for examples.

2.4 Conclusions

This chapter has provided an introduction to the basic physics, formation and evolution of low mass stars and brown dwarfs. Brown dwarfs are being found currently in binary systems, in open star clusters and in the field, and all three of these have been discussed. DENIS, 2MASS and the SDSS have greatly increased our knowledge of brown dwarfs as well as the number known, and UKIDSS and the soon to become operational Visible and Infrared Survey Telescope for Astronomy (VISTA) will increase the number of brown dwarfs known. UKIDSS in fact already has, and has found possibly the coolest brown dwarf to date (T_{eff} <700 K Warren et al. 2007). Our knowledge can only increase with these deep, wide field surveys, and with the increasing ability to follow up fainter objects through laser guide star adaptive optics.

Chapter 3

Introduction to observing techniques

3.1 Introduction

This chapter aims to describe the instruments used to obtain the data presented in this thesis, as well as to provide a description of the survey catalogues that have been used. Additionally, the data reduction processes for photometry and spectroscopy in both the optical and infrared will be described.

3.2 Photometry

Photometry is an essential tool for any astronomer. The photometry of a star is a measurement of how much light, and hence energy it is emitting. An observer can determine the distribution of this energy by using a filter to separate out the flux only in the required wavelength range. The combination of filters can be used to understand more about the star - e.g. by calculating its temperature. These filters tend to be of a standard system and allow direct comparisons between theory and observations (by the use of evolutionary models etc).

30

3.2.1 The photometric scale

Since humans began to look at the stars it has been apparent that stars have a range of brightness, although it was not until Hipparchus in the second century B.C. that anyone attempted to categorise these variations. Hipparchus split the stars that could be seen with the naked eye into six groups depending on their brightness or magnitude. The brightest group were assigned a magnitude of one, and the faintest group a magnitude of six. It became clear however that this was not a practical scale, and with the invention of telescopes, not all stars could be fitted into one of the six groups. The magnitude system used today is based on the work of Pogson in 1856. Pogson found that a first magnitude star produces about 100 times the light flux than that of a sixth magnitude star. He then redefined the magnitude scale so that a difference of five magnitudes was equal to a factor of 100 in light flux. This magnitude system was first published in a paper describing the magnitudes of the minor planets (Pogson, 1856). The Pogson scale is shown in equation 3.1,

$$m_1 - m_2 = -2.5 \log \frac{I_1}{I_2},$$
(3.1)

where m_1 and m_2 are the magnitudes of stars 1 and 2 and I_1 and I_2 are the measured intensities from each star. The scale is logarithmic ($\log_{10}$) because it is based on the intensity as detected from the human eye, which is itself logarithmic. The factor of 2.5 arises from Pogson's definition of the magnitudes and their intervals. The scale today still maintains this original premise that brighter stars have smaller magnitudes than fainter ones.

3.2.2 Magnitudes

The magnitudes that have been discussed so far are apparent magnitudes - the closer an object is then the brighter it appears, and the lower its magnitude. This is not a practical scale for general use, as there is no distinction between near stars and distant bright stars. We therefore need a way of calibrating the magnitude scale. This calibration is usually done by defining certain stars such as α Lyr (Vega) as having a magnitude of zero. The result is known as the Vega magnitude system. If we wish to measure the luminosity of a star, we need to know its

absolute magnitude - the magnitude the star would be observed if the star was at a distance of 10 pc from the observer. The relationship between absolute and apparent magnitude is shown in equation 3.2,

$$m - M = 5 \log d - 5 + A, \tag{3.2}$$

where M is the absolute magnitude, m is the apparent magnitude, d is the distance to the object in question in parsecs and A is the interstellar extinction to the star. M, m and A must all be measured at the same wavelength. Another magnitude system that is used is the AB magnitude system which is defined in equation 3.3 as,

$$AB_\mu = -2.5 \log(f_\mu) - 48.60, \tag{3.3}$$

where AB_μ is the magnitude and f_μ is the flux at a certain frequency, measured in ergs cm^{-2} sec^{-1} Hz^{-1} (Oke, 1974). On this magnitude system an object with constant flux per unit frequency has zero colour.

3.2.3 Colour index

The colour of a star is defined as the difference between the magnitudes at two different wavelengths as shown by equation 3.4,

$$CI = m(\lambda_1) - m(\lambda_2), \tag{3.4}$$

where CI is referred to as the colour index. The colour index is normally calculated by subtracting the magnitude at the longer wavelength from the magnitude at the shorter wavelength. This colour index does not depend on distance. As stars have different temperatures, they are bright in different wavelengths. Brown dwarfs are cooler than stars, and tend to have red colours (apart from T dwarfs), whereas the majority of background stars are blue and white dwarfs are bluer still (CI <0). If observations are being executed in areas that contain a large amount of interstellar dust, then the colour index must also be adjusted to compensate for this. The difference between the observed and intrinsic colour indices is called the colour excess.

3.2.4 Zero points

Once data has been collected from an instrument a frame of reference must be established so that the observer can be confident that the magnitudes, as measured by the instrument, are correctly transformed into apparent magnitudes. This is done by using stars with known magnitudes (such as the UKIRT Faint Standards, (Casali & Hawarden, 1992), or a catalogue such as 2MASS) to determine the zero point of the data. In general the known magnitudes for the standard stars in the field are compared to the measured magnitudes of the same stars. When a graph of the two are plotted (which should be a straight line), and the gradient fixed to be 1, the intercept at the y axis is the zero point. In general lots of stars are used to calculate the zero point, which is independent of the stars and is a function of the instrument sensitivity, the filter and the atmospheric transmission. In particular for wide field instruments, a zero point must be calculated for each chip or array used. If the zero points can be described as stable then the conditions are said to be photometric. Figure 3.1 is a graph used to determine the zero point of a CCD chip.

3.2.5 Atmospheric corrections

Photons are scattered and absorbed as they pass through the Earth's atmosphere, thus decreasing the intensity of radiation. The amount of radiation that is lost is proportional to the wavelength of the radiation and the amount of atmosphere passed through. The amount of atmosphere is particularly important while observing the star, and is largest near the horizon and lowest when the object is overhead, at the zenith. The actual relationship is shown in equation 3.5,

$$Airmass = \sec z, \tag{3.5}$$

where z is the angular distance between the star and the zenith. Due to the curvature of the Earth, equation 3.5 is not valid for large z. Observing standard stars throughout the night (or
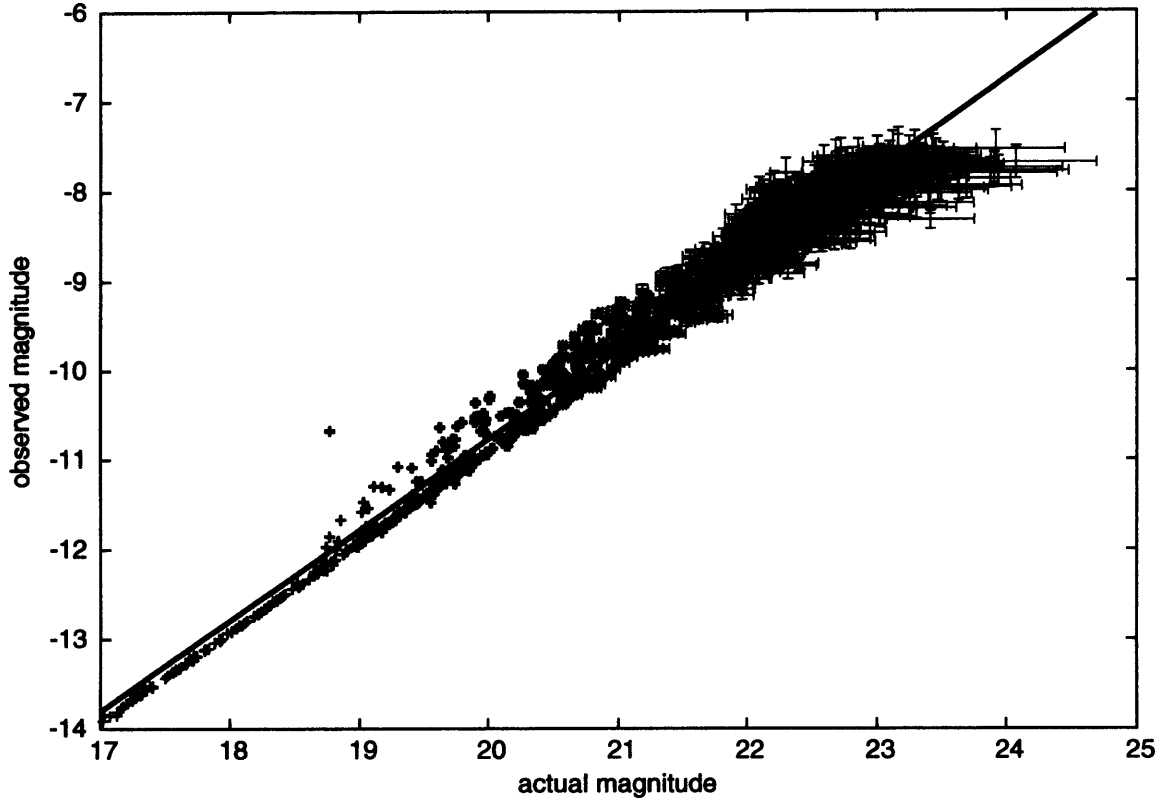
Figure 3.1: An example of a typical graph used to determine the zero point of an image. The black line is the best fit determined by linear regression. The zero point of this image was -30.72. For the linear regression to be accurate, it must be assumed that the data points follow a normal distribution. As this is not the case here, a better method would be to use robust estimation, using an iterative procedure to remove suspect data points.

at each pointing), allows a curve of airmass against zero point (ZP) to be plotted. Equation 3.6,

$$ZP_{\mathrm{star}} = -k \sec z + ZP_{zeroairmass},$$ (3.6)

can then be used to calculate the airmass coefficient (k) - which is the value at which the zero point is most accurate for the science frame in question. This procedure must be completed for each science frame, and for each filter set used.

The UFTI photometry used in Chapter 5 was calibrated in this manner (figure 3.2). The WFCAM, Isaac Newton Telescope (INT) Wide Field Camera (WFC) and CFH12k data, were airmass corrected during their pipeline processing stage.

34
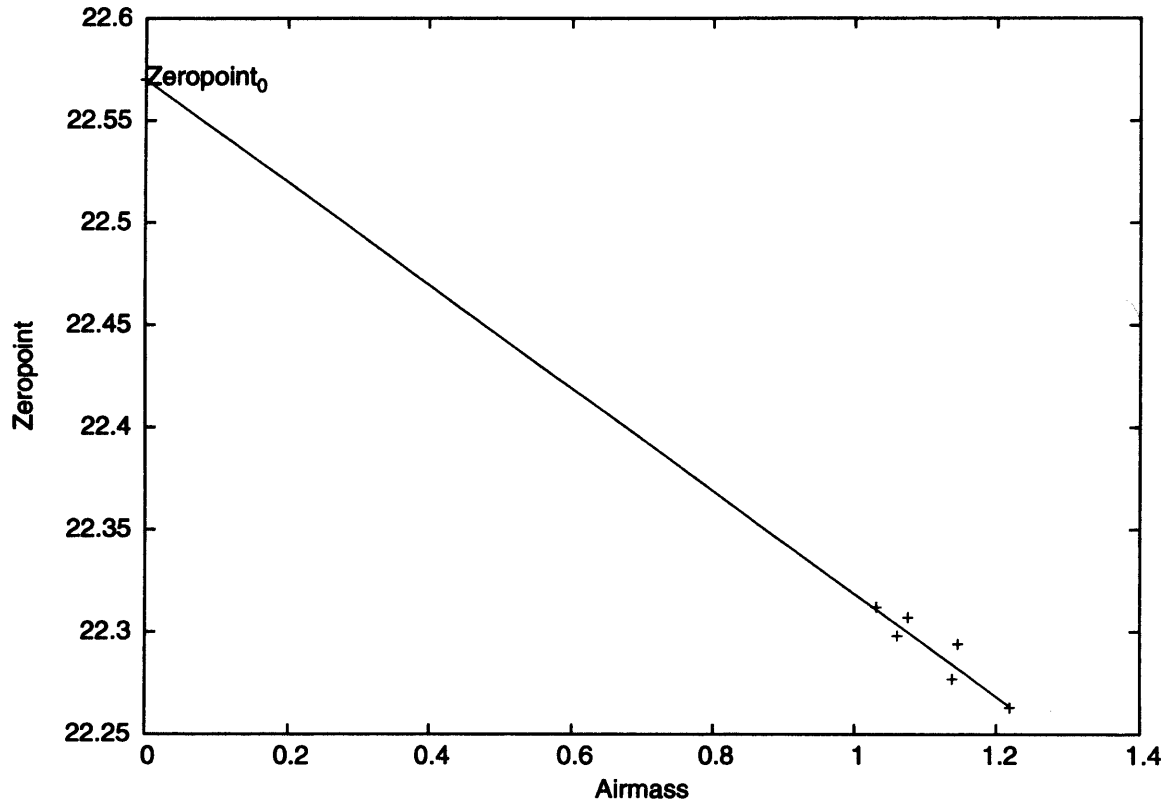
Figure 3.2: An example of a typical airmass curve taken in photometric conditions using UFTI on UKIRT in 2003 with the K98 filter. The black line is the best fit determined by linear regression. The zero point at zero airmass is marked. These data are presented in Chapter 5.

3.3 Detectors

This section will discuss the evolution and workings of the most commonly used detectors for astronomy - CCDs for optical data and IR arrays. There will also be a brief explanation on the workings of spectrographs.

3.3.1 Charged Couple Devices (CCDs)

Imaging CCDs were first created in 1970 by researchers at the Bell laboratories in the USA, and began to be used in astronomy in the 1980s. A CCD is a semiconductor device, which works via the photoelectric effect. They usually consist of a thin silicon wafer containing a

large number of electrodes which is insulated from the semiconductor by a thin oxide layer. These electrodes are arranged in an array on the surface of the wafer. Three electrodes are used for each imaging arrangement or "pixel". Each pixel stores charge independently as electrons are excited from the valence band into the conduction band by incident photons on the CCD. An electron charge is built up over time, and has a magnitude proportional to the incident radiation. A spatially digitised electric analogue of the original optical image is formed across the CCD array. Once the exposure is ended, the CCD is read out. This process involves moving the stored charge along the array to a read out point. This read out point contains an analogue to digital converter (ADC) which sequentially changes the voltages on the electrodes (see Kitchin 1997 for a more in depth discussion of this process). The number of electrons represented by one analogue to digital count, (ADU) is called the gain of the detector and depends on the electronics used in the detector. Because of their sensitivity to incoming radiation, CCDs must be cooled to $\approx$ 150 K to reduce the thermal excitations of electrons and to limit noise. This dark current is kept to a minimum at all times via cooling. It is generally negligible in optical CCDs, however, it presents more of a problem for infrared devices. CCDs are now the detector of choice for all optical detectors, this is because they have many benefits over the alternative devices such as intensifier tubes and photographic plates.

The main advantage of CCDs over their alternatives is that they have much superior imaging capabilities. To date CCDs may contain arrays of approximately 2000 $\times$ 4000 pixels, of sizes 15 μm, many of which may be tiled together to create a large instrumental field of view. A large field of view is essential for large field surveys, and aids in computing relative astrometry and photometry for data taken in non photometric conditions. The nature of CCD arrays consisting of discrete pixels are also ideal for computer data reduction processes.

CCDs have a large quantum efficiency, meaning that between $\approx$ 60 and 90% of optical photons incident on the CCD surface excite electrons in the semiconductor. This high quantum efficiency makes CCDs ideal for detecting faint sources. Detections can be made over long exposure times, and a large amount of short exposures can be stacked to create deeper images of sources. Individual pixels can hold up to about 10^5 electrons. This number is referred to as the "well depth". If more electrons than this are generated the image will be saturated. Because
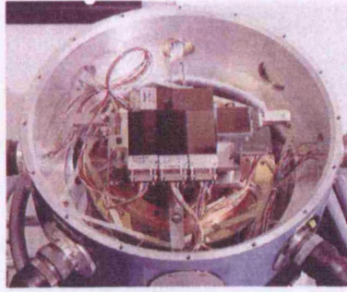
Figure 3.3: An image of the WFC on the INT. The CCD chips are named 3, 4, 1 from left to right. Chip number 2 is at right angles to the other three. The smaller chip to the right of the image is the autoguider chip.

each pixel is independent, objects of many different brightnesses may be imaged on the same chip. CCDs also remain linear over this large dynamic range allowing accurate photometry to be computed.

In the work presented in the following chapters optical CCDs have been used, most notably those on the WFC mounted on the INT in La Palma, and CFH12k, on the Canada France Hawaii Telescope (CFHT) on Hawaii.

WFC

The WFC is mounted at the prime focus of the 2.5 m INT. It consists of four thinned EEV 2k×4k CCDs with pixels sizes of 13.5 μm, which corresponds to 0.33 arcseconds/pixel. Overall the four CCDs give a field of view of 34.2 arcminutes. The CCD chip layout is shown in figures 3.3 and 3.4.

CFH12k

CFH12k is a wide field optical imager that consists of 12 2048 × 4096 pixel CCDs arranged in two rows of 6. This can be seen in figure 3.5. CFH12k was available on the prime focus
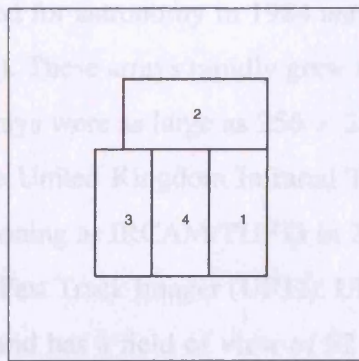
Figure 3.4: The layout of the WFC on the INT. The CCD chips are named 3, 4, 1 from left to right. Chip number 2 is at right angles to the other three.
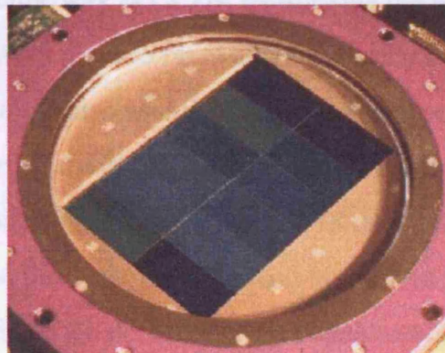
Figure 3.5: The layout of CFH12k.

of the 3.6 m CFHT from 1999 until 2003 when it was replaced by the larger MegaCam. The large mosaic of CCDs allowed CFH12k a field of view of 42 by 28 arcminutes, with a pixel scale of 0.206 arcseconds/pixel.

3.3.2   Infrared arrays

Infrared arrays are semiconductor devices, like CCDs. IR photons have longer wavelengths and hence lower energy than optical photons, and so IR arrays must be made from different materials. As with CCDs, these arrays have grown in size over time.

IR arrays began to be used for astronomy in 1984 and the first was a 32 × 32 pixel array of Indium antimonide (InSb). These arrays rapidly grew to as large as 52 × 68 pixels by the late 80s. By the 1990s the arrays were as large as 256 × 256 pixels, and were still made of InSb. IRCAM3 mounted on the United Kingdom Infrared Telescope UKIRT was one such instrument, and was still functioning as IRCAM/TUFTI in 2000. These arrays were superseded by those used in the UKIRT Fast Track Imager (UFTI). UFTI contains and array of 1024 × 1024 pixels made of HgCdTe and has a field of view of 92 arcseconds. The Wide Field CAMera (WFCAM) currently mounted on the UKIRT and WIRCam on CFHT are currently the largest IR arrays with them both containing 4 arrays of 2048 × 2048 pixels.

IR arrays work in much the same way as CCDs, by utilising the photoelectric effect. However, they cannot transfer charge from pixel to pixel and are usually bonded to a "read device" like a CCD below the array. IR arrays also usually employ a non destructive read out mode, which means that to read out the array, the charge difference is measured between the start and end of the exposure. This negates the need for a shutter on IR detectors, although it does mean that for imaging of bright objects, the array must be read out first to remove any residual photons from the previous image as these would leave ghost objects on the image.

Another fundamental difference between CCDs and IR arrays, is their smaller bandgap and therefore larger dark current, meaning the arrays must be kept much cooler than their optical counterparts ($\approx$35 K), but even then the dark current must still be removed during the data processing (it is negligible for CCD arrays). Images taken using IR arrays must also be dithered. This is because of the relative brightness of the sky in this wavelength due to mainly water and OH ions in the atmosphere. Dithering or nodding, allows this background to be removed, by moving the image around on the sky, which when median filtered creates a background image which then can be subtracted from the science frames. This process is very effective and allows long exposure times to be built up from many sets of images with small exposure times, as the arrays tend to saturate quite quickly - mainly due to the brightness of the sky. Optical images may also be dithered to remove bad pixels or columns. The IR instruments used in the course of this work are WFCAM on UKIRT, UFTI, which was discussed earlier, and the Long-slit Intermediate Resolution Infrared Spectrograph (LIRIS) mounted on the cassegrain
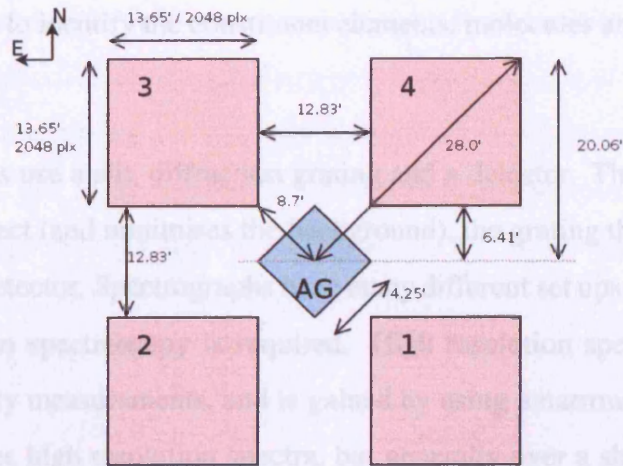
Figure 3.6: The layout of the WFCAM focal plane. The four IR arrays are labelled 1 to 4. The AG chip is the autoguider. By moving the array to one side, and up or down, a tile consisting of 4 pointings (16 arrays) can be created.

focus of the 4.2m William Herschel Telescope (WHT) on La Palma. LIRIS is both an imager and spectrograph and discussed in the section on spectrographs.

WFCAM

WFCAM (Casali et al., 2007) is mounted on the 3.8 m UKIRT on Hawaii. WFCAM operates in the wavelengths between 1 and 2.5 microns, and uses 5 filters, J, H, K, Y, and narrowband Z. WFCAM is a unique instrument in that it is designed to tile its 4 arrays together. The 4 detectors are arranged so that they are spaced by 94% of their area. This means that 4 exposures are required to create a tile of 0.75 square degrees. See figure 3.6 for the focal plane layout of WFCAM. WFCAM is the survey instrument being used to create UKIDSS.

3.3.3 Spectrographs

Spectroscopy is an invaluable tool that enable us to take a detailed look at a star's emitted flux. The spectrum allows us to examine the way that the emission intensity varies with wavelength.

This in turn allows us to identify the constituent elements, molecules and ions that are present within the star.

Modern spectrographs use a slit, diffraction grating and a detector. The slit isolates the light from the required object (and minimises the background), the grating then disperses the light, which falls onto the detector. Spectrographs have many different set ups depending on whether high or low resolution spectroscopy is required. High resolution spectroscopy tends to be used for radial velocity measurements, and is gained by using a narrow slit, or a high density grating. This produces high resolution spectra, but generally over a short wavelength range. Low resolution spectra are used when a higher signal to noise ratio is required, such as for faint objects. Wider wavelength ranges can be viewed using lower resolution set ups. Two spectrographs have been used in the course of this work, the Ultraviolet and Visual Echelle Spectrograph (UVES) and LIRIS. UVES is an echelle spectrograph, which produces a cross dispersed spectrum.

An echelle spectrograph uses two diffraction gratings, rotated 90 degrees with respect to each other and placed close to each other. A 2 dimensional CCD chip records the spectrum. Both gratings have a wide spacing and one is blazed so that only the first order is visible and the other is blazed that higher orders are seen. One spectrum is produced on the CCD. In the data reduction process these orders are generally separated for processing.

UVES

UVES is the high-resolution echelle optical spectrograph of the Very Large Telescope located at the Nasmyth B focus of the 8.2 m Unit Telescope 2 (Kueyen). It is a cross-dispersed echelle spectrograph designed to operate with high efficiency from the atmospheric cut-off at 300 nm to the long wavelength limit of the CCD detectors (about 1100 nm). The light beam from the telescope is split in two arms (UV to Blue, and Visual to Red) within the instrument. The two arms can be operated separately, or in parallel via a dichroic beam splitter. The resolving power ($\lambda/\delta\lambda$) is about 40,000 when a 1-arcsec slit is used. The maximum (two-pixel) reso-

lution is 80,000 or 110,000 in the Blue and the Red Arm, respectively. Three image slicers are also available to obtain high resolving power without excessive slit loss. The instrument is built for maximum mechanical stability and allows for accurate wavelength calibration. An iodine cell can be inserted in the light beam for observations requiring extremely high accuracy for radial velocity measurements (Dekker et al., 2000). A Th-Ar lamp is used to create the arc lamp frames.

LIRIS

LIRIS is a near infrared (0.9-2.5 mm) intermediate-resolution spectrograph using various grisms and designed to operate over the spectral resolution range between 1000 and 5000. It also capable of making images, coronographic images, multiobject spectroscopy and polarimetric observations. It has been used in both single slit spectroscopy and imaging modes for this work. The instrument allows the combination of an adequate spatial resolution (0.25 arcsec/pixel) with a large useful field of view (4.2 arcmin). It contains the same type of IR arrays as UFTI.

3.4 Image data reduction

This section will describe the processes involved in reducing imaging data in both the optical and infrared wavebands.

3.4.1 Bias level removal

The first step in reducing an image is to remove the bias level. The bias level of a CCD frame is an artificially induced electronic offset which ensures that the Analogue-to-Digital Converter (ADC) always receives a positive signal. Without this, noise on a low level background can cause a negative signal to be passed, which the ADC is unable to deal with. The frame is

created by taking a zero second exposure of the CCDs, and as it is relatively constant and independent of temperature and exposure time, these frames are usually taken in the day at the telescope. The bias frame is subtracted from all other frames (i.e flat fields, science frames, standard stars, arc lamps). This is to ensure that this offset is removed and that the image is then representative of the actual counts recorded per pixel. This step may be neglected if infrared data is being reduced, as the larger dark current is dominant in this case, meaning the bias correction is negligible.

3.4.2 Dark current correction

The dark current is important for the reduction of IR images, more so than for optical images. This is because IR arrays detect photons of lower energies than optical CCDs, making random thermal noise non negligible. This is a time dependent frame, as the thermal noise builds up over time, and is also dependant on the temperature of the detector. This means that the frame must have the same exposure time as the science frame, but is taken with the shutter closed, to image the thermal noise. This frame is subtracted from the image data. The ORAC-DR routine REDUCE_DARK was used for the UFTI data.

3.4.3 Flat fielding

A flat field frame is an image that is created with the aim of removing the pixel to pixel variation across the detector. These variations are filter dependent, and so one must be taken for each filter that the observations are made in. There are three ways of doing this. The first is by imaging a bright screen or the inside of the telescope dome, that is uniformly lit. This "dome flat" may then be normalised to a flux of 1.0 so that the pixel to pixel variation may be removed from the data. The second method of creating a flat field is by taking "sky or twilight flats". These images are taken as their name suggests on the sky, at twilight, either in the late evening, or early morning. This method is slightly difficult to achieve as care must be taken not to saturate the detector. This means that only a small amount of time is available to

43

complete the observations of these frames. The final method involves a "self flat" approach, which is commonly used in IR observations. The observations themselves are "dithered" i.e. moved around a set pattern on the sky, with the desired observation within each frame. These frames are then median filtered and the flux is normalised to 1.0 to create a sky frame. This method will also remove cosmic rays incident on the detector during the observations. It is commonly used for infrared observations as it also removes the background level, which is high in the IR. The science frames are divided by the flat field frames. This ensures that the same flux is represented by each ADU registered in any pixel. The ORAC-DR routine JITTER_SELF_FLAT using the "self flat" method was used for the UFTI images. The IRAF routine imcombine was used to create the sky flat for the LIRIS images. Twilight flats are used for the reduction of WFCAM data.

3.4.4 Source detection

The majority of source detections mentioned in this thesis were undertaken using SExtractor either from within the STARLINK GAIA program, or from the command line. An object is counted as a detection, when it meets user specified requirements. Normally, a number of connected pixels, with flux above a specified background level are required for a detection. The WFCAM object detection software for instance requires that a detection must have 4 connected pixels with flux of more than 1.5σ above the mean background level, where sigma is a measure of the background fluctuation. This method is also used by SExtractor. These parameters must be chosen carefully to ensure that the maximum amount of faint objects are selected, while minimising the amount of false detections due to cosmic rays, galaxies, diffraction spikes etc.

3.4.5 Aperture photometry

Once sources in a field have been detected, the amount of flux in each source must be determined. This flux is then used to calculate the magnitude of each source. This is done by

placing an aperture of a specified radius around the source and counting the flux within the aperture. This flux is from both the star and the background surrounding it. An annulus is then placed around the source, with an inner radius of that of the aperture, and an outer radius typically twice that. This is to ensure that all the flux counted is received from the background only, and not from the source. This background measurement is then subtracted from the total measurement (from the aperture) to calculate how much flux comes from the source alone. The magnitude is then calculated from the flux using equation 3.7,

$$M = ZP - 2.5 \log_{10} \frac{f}{t} - A, \qquad (3.7)$$

where M is the final magnitude, ZP is the zero point of the observation, f is the calculated flux, t is the exposure time of the observation and A is the aperture correction. The aperture correction is needed as no aperture size will be perfect for an image - a small aperture will contain all the flux from a faint object and will keep the background to a minimum, but will be too small to ensure all the flux from a bright object is collected. This fraction of missed flux for bright objects is accounted for by the aperture correction. The aperture corrections used in this thesis have been calculated by the WFCAM and Cambridge Astronomical Survey Unit (CASU) pipelines.

The photometry that was produced by the WFCAM pipeline used an annulus of radius 5 pixels (1" seeing) for the J band images (including microstepping) and a radius of 2.5 pixels for the H band images (no microstepping). The CFH12k images used an aperture of 4 pixels. The photometry measured for the UFTI images of Melotte 111 uses the ORAC_DR photometry recipe DITHER_SELF_FLAT_APHOT. The photometry from the UFTI and LIRIS images of the Pleiades was measured using SExtractor and calibrated using standard stars and 2MASS.

3.5 Spectroscopic data reduction

Both optical and infrared spectra are presented in this thesis, and like optical and infrared images, must be reduced following different methods.

3.5.1 Optical spectroscopic data reduction

The optical spectra presented in this thesis were reduced using the UVES pipeline written specifically for MIDAS (Grosbol, 1989). Although UVES is an echelle spectrograph, and the pipeline requires some instrument specific data, the reduction of the spectra is essentially standard. In addition to the bias and flat field frames (lamp flat fields, normally taken within the instrument) as described above, two additional frames are required.

The first is the arc lamp frame, which is a standard spectrum provided by a short exposure of a lamp with a known spectrum such as Th-Ar or Cu-Ar. Comparing these observed lines with the standard set of emission lines for the lamp allows wavelength calibration of the spectra. The other frame is a spectrum of a standard star with a known spectrum. This spectrum is reduced and wavelength calibrated as for the science spectrum, and is then used to flux calibrate the science spectra.

The reduction procedure is as follows. The science, standard star and arc lamp frames are first reduced as for image reduction - the bias level is subtracted and each frame is flat fielded. The spectrum must then be located on the image - in theory the axis of the spectrum should be at right angles to the slit. In reality this never happens due to the instrument set up. Once the spectrum has been located a window of about 10 pixels either side is selected to provide an estimate of the background, and to remove any sky lines. This background is then subtracted from the spectra. The arc lamp frame is used to provide the wavelength calibration (Th-Ar was used for the UVES data). The lines in this frame are compared to a standard line list of emission lines and a dispersion curve is generated which maps the pixel positions to wavelength. This curve is then used to wavelength calibrate the spectra. For spectra requiring

an accurate flux calibration a standard star is used (UVES observations do not use standards - there is a flux calibration frame specific to the instrument). The standard star spectrum is also extracted and wavelength calibrated as above. The standard is then used to create a sensitivity function. Some data reduction programs also require an extinction map for the observatory at this point. This sensitivity function is then applied to the science spectra. Usually I would use IRAF to reduce optical spectra, however, for the UVES data the instrument specific pipeline and MIDAS were used.

3.5.2 Infrared spectroscopic data reduction

Infrared spectral data reduction requires all the same frames as the optical data reduction, they are just reduced in a slightly different way. As with infrared images, infrared spectra suffer from high background, and in particular OH sky lines which pass through the spectra. To remove this problem, the spectra are nodded along the slit, usually in a set pattern such as AB BA where A is the upper position and B the lower. These A and B frames can be subtracted to remove the background. The infrared spectra presented in this thesis were reduced using the STARLINK Figaro and Kappa packages. In general infrared spectra are more complicated to reduce than optical spectra.

Firstly bad pixels are selected from the flat field to create a bad pixel mask. This bad pixel mask is then added to the science frames as well as to the arcs and flat fields and a normalised flat field is then created by collapsing the observed flat field along the spatial direction, and fitting a function to it. This model is then expanded along the spatial direction to form a 2d model flat field and the observed flat field is divided by this model flat field to create a normalised flat field. The remaining science frames - arcs, standards and objects are then divided by this normalised flat field. The spectra are subtracted from each other (A-B), removing the majority of the sky lines and stacked. The spectra can be stacked in groups of A and B then subtracted, or subtracted in A-B pairs and each pair stacked. I generally use the second of these methods. Any remaining skylines are then removed. The standard star exposures are similarly subtracted (A-B). The spectra are finally extracted from the stacked frames along

the dispersion direction and then the positive and negative traces (left by the A-B process) are then subtracted from each other.

The calibrations are done using the Figaro package. The arcs are also extracted and the emission lines from the arc lamp (Xenon) are identified and this wavelength calibration is applied to the arc spectrum. The wavelength calibrated arc spectrum is then applied to all of the science and standard spectra. The standard star spectra must be edited to remove spectral features specific to the star (i.e. the hydrogen absorption lines and not the telluric features) and this spectrum is then used with the temperature and a magnitude (the K band was used) of the standard to flux calibrate and remove telluric features from the science spectra. In general this flux calibration is less accurate than the flux calibration of optical spectra as a black body spectrum of the temperature of the standard is assumed and then adjusted to the magnitude of the standard. The science spectra are then corrected for differences in exposure times between the standard and science frames, and smoothed. This part of the data reduction is done by following the instructions on the UKIRT CGS4 website (http://www.jach.hawaii.edu/UKIRT/instruments/cgs4-old/software/cgs4_figred.html).

3.6 Filter systems

There are a wide range of different filters and systems, but in general they may be categorised into three groups.

- Broad band filters with widths of about 1000 Å.

- Intermediate band filters with widths between 100 and 500 Å.

- Narrow band filters with widths between 5 and 100 Å.

Narrow band filters only transmit a small amount of light from the star, but tend to be centred on wavelengths where specific spectral information is concentrated - i.e. on Hα lines. As a result these filters are most useful on large telescopes otherwise only very bright objects can be observed. Broad band filters, as their name implies have a wide filter width and are not limited by the restrictions of narrow band filters.

The first filter systems were based on the wavelengths of light that the human eye is sensitive to (5100 Å, with a bandwidth of $\sim$ 200 Å). Once photographic plates became a common tool for astronomers, it became apparent that most objects varied in magnitude when imaged in different spectral regions. These magnitudes were known as m_v and m_p for visual and photographic magnitudes. Nowadays the visual magnitude is defined by using images taken with an orthochromatic plate and a yellow filter which mimics the waveband of the human eye. This magnitude is known as a photo-visual magnitude (m_{mp}).

There are many filter systems in use today. The most common of these is the UBV filter system of Johnson & Morgan (1953). This is a broad band filter system and is defined so that the B ($\sim$ 4400 $\pm$ 600 Å) and V ($\sim$ 5500 $\pm$ 500 Å) wavebands follow the responses of the visual and photographic magnitudes. The U band ($\sim$ 3600 $\pm$ 500 Å) covers the violet and ultraviolet wavelengths. Brown dwarfs emit the majority of their light at the red end of the optical and in the infrared filter set.

3.6.1   Far optical filters

The far optical filter sets used in this data have been RGO Z, Z prime, Sloan i and I Mould (Sloan g, a blue optical filter was also used for the work on Praesepe). The far optical filters are the reddest optical filters used with a CCD. Usually the Kron-Cousins system is taken as standard for red (R) and infrared (I) wavelengths. The Sloan i (Melotte 111 and Praesepe white dwarfs) and Mould I (Pleiades) filters have been used in the course of this work. The other filter that has been used for the data presented here is the Z band. This filter is open ended at the infrared end, and begins transmission at about 0.8 microns. Two Z filters were

49
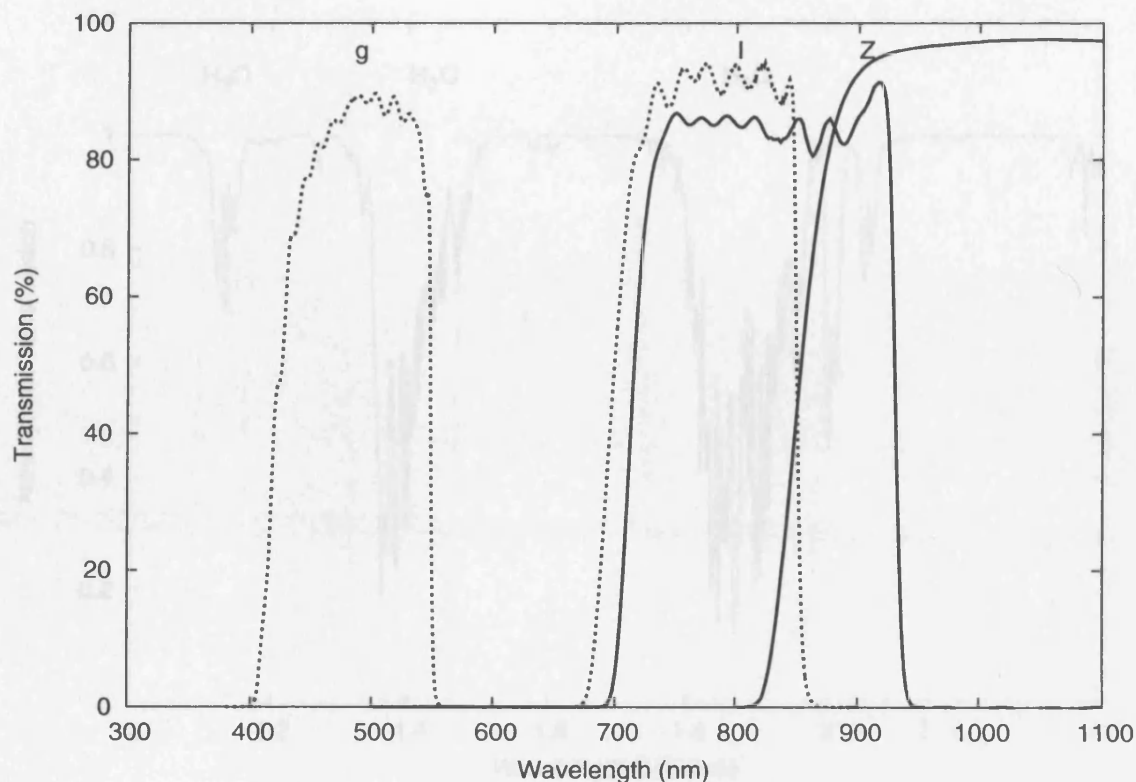
Figure 3.7: Filter profiles for the optical filters used in this thesis; Sloan g and i (dotted line), CFHT filters Z prime and I Mould (solid line). The RGO Z used by the WFC on the INT is nearly the same as Z prime.

used for this work, RGO Z (Melotte 111) and Z prime (Pleiades). The profiles for these filters may be seen in figure 3.7.

3.6.2 Infrared filters

The Earth's atmosphere is not completely transparent at wavelengths longer than 1 micron and a series of water vapour bands are present within the infrared wavelengths (1-2.5 microns, figure 3.8). The infrared filters have therefore been chosen to avoid these water bands and take advantage of the atmosphere between them where the transmission is nearly 100%. These filters are known as J ($\sim$1.2 μm), H ($\sim$1.6 μm) and K ($\sim$2.2 μm). Most infrared instruments use a common set of these filters developed at the Mauna Kea Observatory (MKO), (see the
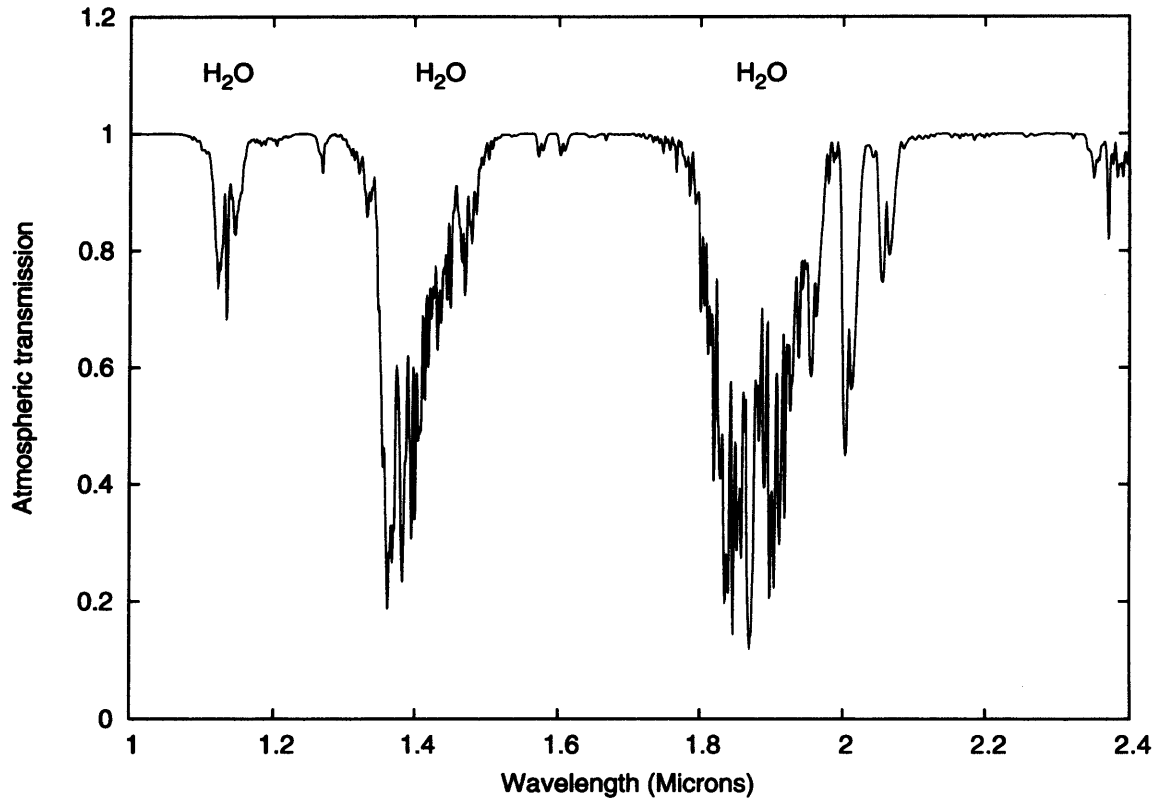
Figure 3.8: The transmission of the Earth's atmosphere as a function of wavelength within the infrared wavelengths. These data, produced using the program IRTRANS4, were obtained from the UKIRT worldwide web pages.

UKIRT webpages for details). The photometry from UKIRT (UFTI and WFCAM) in this thesis are on this system and use the J98, H98 and K98 filters. The 2MASS photometry is on a slightly different filter system involving the use of a K_S (K short) filter as well as different J and H filters. These filter profiles are plotted in figure 3.9.

3.7 Astrometry

Once the data has been reduced, a coordinate system should be attached. This system must take into account the fact that while the pixel scale is linear, the coordinates will not be, and especially for large fields of view the radial distortion must be considered. There is usually a
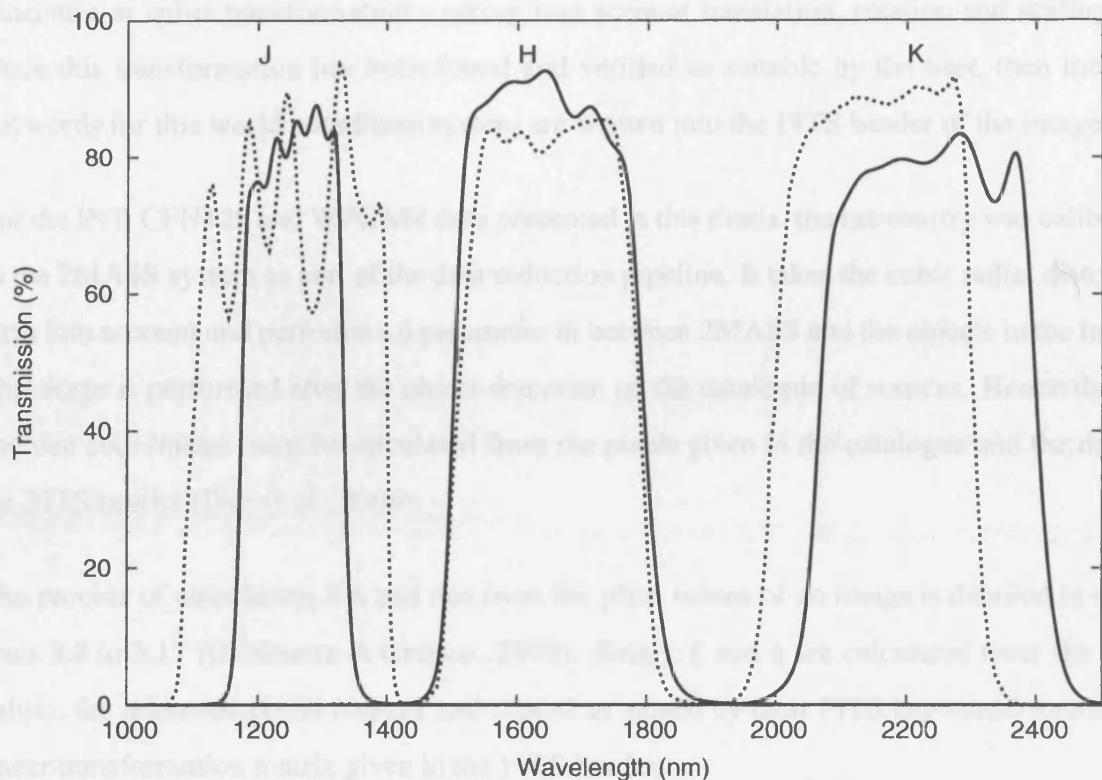
Figure 3.9: Filter profiles for the IR filters used in this thesis; MKO J, H, and K filters used by UFTI and WFCAM (solid line), filters used by the 2 micron all sky survey (2MASS) J, H and K_S (dotted line).

basic coordinate system attached to every image. The RA and dec of the centre of the pointing are written to the FITS header during the observation. The astrometry is calculated using the pixel values and coordinate matrices which are written to the FITS or NDF header during the data reduction process. Refining the astrometric solution can be a difficult process. The method that has been used in the data reduction in this thesis for the UFTI data was performed by the STARLINK software ASTROM which runs through GAIA. ASTROM calculates a co-ordinate system for each image by comparing star positions to those of known objects usually by using a catalogue (all the work in this thesis has been calibrated using 2MASS). More specifically ASTROM reads in the world coordinate system written in the FITS header (including the parameters that describe the radial distortion) and uses this to query the online catalogue - 2MASS. The two sets of coordinates (one set from the image and one set from the catalogue) are then matched by using a match algorithm that calculates either a linear,

quadratic or cubic transformation - taking into account translation, rotation and scaling etc. Once this transformation has been found and verified as suitable by the user, then the new keywords for this world coordinate system are written into the FITS header of the image.

For the INT, CFH12k and WFCAM data presented in this thesis, the astrometry was calibrated to the 2MASS system as part of the data reduction pipeline. It takes the cubic radial distortion term into account and performs a 6 parameter fit between 2MASS and the objects in the image. This stage is performed after the object detection on the catalogue of sources. Hence the RA and dec coordinates must be calculated from the pixels given in the catalogue and the data in the FITS header (Dye et al., 2006).

The process of calculating RA and dec from the pixel values of an image is detailed in equations 3.8 to 3.17 (Calabretta & Greisen, 2000). Firstly, ξ and η are calculated from the pixel values, the reference pixels ($crpix1$ and $crpix2$ as named by their FITS keywords) and the cd linear transformation matrix given in the FITS header,

$$\xi = cd1\_1(x - crpix1) + cd1\_2(y - crpix2), \tag{3.8}$$

$$\eta = cd2\_1(x - crpix1) + cd2\_2(y - crpix2). \tag{3.9}$$

These values, ξ and η are the first order standard coordinates, in the tangent plane, and are created from the linear part of the solution - i.e. no radial distortion has so far been taken into account.

r is used to represent the square root of the sum of the squares of ξ and η,

$$r = \sqrt{\xi^2 + \eta^2}. \tag{3.10}$$

The parameter $rfac$ uses r and the projection parameters in the first and third orders $projp1$ and $projp3$ to take into account radial distortion. These projection keywords are written into the FITS header when the astrometric calibration takes place,

53

$$rfac = projp1 + projp3 \times r^2, \tag{3.11}$$

$$r_2 = r/rfac, \tag{3.12}$$

$$rfac_2 = projp1 + projp3 \times r_2^2. \tag{3.13}$$

ξ and η are then divided by the $rfac_2$ parameter,

$$\xi_2 = \xi/rfac_2, \tag{3.14}$$

$$\eta_2 = \eta/rfac_2. \tag{3.15}$$

Finally the right ascension and declination are calculated using the transform matrix and the reference coordinates $Crval$ and $crpix$. The $Crval$ coordinates in RA (α) and dec (δ), are commonly referred to as the tangent point of the solution.,

$$\alpha = \tan^{-1} \frac{\xi \sec Crval2}{(1.0 - \eta \tan Crval2) + Crval1}, \tag{3.16}$$

$$\delta = \tan^{-1} \frac{\eta + \tan Crval2}{1.0 - \eta \tan Crval2}. \tag{3.17}$$

3.7.1 Proper motion

Every object in the celestial sphere has a particular motion across the sky relative to us. This is called the object's proper motion and is commonly measured in milliarcseconds per year

(mas yr^{-1}). This motion can be calculated for every object common between two sets of observations taken at two different times. This time difference is usually of the order a few years, although it depends on the size of the proper motion one is trying to measure. For a cluster with a large proper motion such as the Pleiades (+20, -40 mas yr^{-1}) an epoch of 5 years is adequate. For a cluster with a smaller proper motion such as Melotte 111, a much longer epoch difference is desirable.

The proper motions calculated in this thesis have been done by using a program which calls the STARLINK SLALIB software libraries sla_fitxy, sla_pxy, sla_dcmpf and sla_xy2xy to calculate the proper motions from the x, y pixel positions of the object in question.

Six coefficient transforms between the epoch 1 images and the epoch 2 band images are calculated using routines drawn from the STARLINK SLALIB package. The iterative fitting rejects objects having residuals greater than 3σ, where σ is robustly calculated as the median of absolute deviation of the reference star residuals, scaled by the appropriate factor (1.48) to yield an equivalent RMS. The program requires a list of non moving reference stars, which it uses to create a transform between the 2 epochs (being from different telescopes and instruments, the pixel scales etc are different).

More specifically, the list of input x and y values, one set for each epoch are read into the program, and the mean value for each set is subtracted from each point (ie the mean value of all the epoch 1 x pixel values is subtracted from each epoch 1 x pixel value), this makes the rms fit to the data more robust. Sla_fitxy then calculates a linear model to the mean subtracted two sets of x y coordinates. This model contains six independent coefficients, the zero points of the model, and coefficients for each second epoch pair of x and y compared to their first epoch values. These coefficients describe the squash and shear as well as origin, scale, and orientation. A minimum of 3 points is required, but the larger the sample the better. Sla_pxy then takes these zero points and coefficients and calculates a predicted list of coordinates using the transform calculated by sla_fitxy and the x and y coordinates of the two epochs of data. The second epoch values values are used to calculate predicted x and y pixel values, and the predicted and first epoch values are used to calculate the residuals to the fit. The root mean

squared value (rms) to the fit is then calculated by taking the difference between the mean subtracted first epoch values and the predicted values as calculated by sla_pxy. The rms values for x and y are then calculated by taking the median value of the rms values for the epoch and multiplying it by 1.48, which is a a standard scaling between the robust estimator median-absolute-deviation and a root-mean-square.

This is the initial rms value. This initial rms fit to the list of input coordinates, is then iterated over, recalculating the rms value and removing any objects from the input list that are moving faster than the tolerance boundaries which are set at 3 times the initial rms. This is to remove any fast moving objects, cosmic ray hits or other artifacts which may cause a bad fit to the data. The whole process is repeated again, this time using the refined list (without the fast moving objects) as an input to sla_fitxy. The final coefficients of the fit are then written out to a file using sla_dcmpf. After this process has improved the linear fit, the candidate cluster member's x and y pixel coordinates are read in for each epoch. The second epoch values are transformed into x and y pixels on the epoch 1 coordinate system - using the previously calculated transform coefficients from the sla_dcmpf output and the sla_xy2xy routine. These values are then used to calculate the motion between the 2 epochs by subtracting the transformed second epoch values from the first epoch values.

The motion in pixels is then converted it into motion in milliarcseconds per year, using the equations 3.18, 3.19 and 3.20,

$$\mu_\alpha = cd1\_1x + cd1\_2y, \tag{3.18}$$

$$\mu_\delta = cd2\_1x + cd2\_2y, \tag{3.19}$$

$$Motion = \frac{\mu_\alpha \times 3600 \times 1000}{epoch\_difference}, \tag{3.20}$$

where the cd values are the coordinate transform matrix for the first epoch from the FITS

header, x and y are the pixel motions in those directions, μ_α and μ_δ are the motion of the star in RA and dec, measured in degrees. The 3600×1000 refers to the conversion into milliarcseconds, and the *epoch_difference* is the time difference between the two observations, calculated from the difference in modified Julian dates, divided by 365.25. It is necessary to also multiply the motion in RA by $\cos\delta$ to take into account the spherical nature of the coordinates to get accurate motion.

The errors are calculated by,

$$error_x = \sqrt{rms_x^2 + xerr_{\text{epoch1}}^2 + xerr_{\text{epoch2}}^2}, \qquad (3.21)$$

where the $error_x$ is the error in the measured displacement in the x direction, rms_x is the rms fit to the linear transform between the two epochs, and $xerr$ is the error in the pixel coordinates for each epoch. Similarly for the y direction. These errors are then converted into milliarseconds per year as with the proper motion, as detailed in equations 3.18, 3.19 and 3.20, using data from the epoch 1 and epoch 2 images. The rms errors are calculated using the epoch 1 pixel scale. These errors are added quadratically to produce the error in the x pixel motion and likewise for the y pixel motion. It should be noted that as the number of reference stars used to create the fit increases, the rms will tend to zero. This means that the errors may be overestimated. To account for this the rms_x^2 term could be divided by N, where N is the number of reference stars used.

3.8 Surveys

Data from many wide field surveys have been used to complete the work presented in this thesis. Wide field surveys are extremely useful, not only for the accessibility of the data, but because acquiring photometry for the entirety of a cluster such as the 900 square degree Hyades is no longer a problem. In the past using a telescope to survey the region would have taken years. Another benefit is that cross correlating the catalogues can allow proper motion measurements to be calculated and a full range of photometry from the optical to the infrared

57

wavebands to be acquired for a single object. Data from these surveys are also used to calibrate images, both photometrically and astrometrically.

3.8.1 USNOB1.0

The United States Naval Observatory B1.0 (USNO B1.0) Catalogue was created by the digitisation of 7435 photographic survey plates. This was accomplished using the Precision Measuring Machine, located at the United States Naval Observatory Flagstaff Station (Monet et al., 2003). This is in fact the latest USNO catalogue, and supersedes the USNO A1.0 and A2.0 catalogues. 2 Epochs of POSS plates were scanned resulting in a 3 colour, 2 epoch catalogue with an epoch difference of as much as 50 years. The astrometry is calculated using standard stars from the YS4.0 catalogue. This catalogue was used to ensure that the standard stars were not saturated on the survey plates. The photometry was calibrated using stars from the Guide star photometric catalogue 2. The photometry itself consists of 2 epochs of B and R magnitudes and one epoch POSS II, I magnitude. These magnitudes typically have errors of 0.3 mags. Proper motion measurements for the objects in the catalogue were calculated by fitting a linear motion fit to them. Each object may have been present on as many as 5 separate plates and as few as 2. It stands to reason that objects detected on more plates have more accurate measurements. These proper motions are relative not absolute and typically have errors of 2 mas yr^{-1}. It should be noted that the USNOB.0 catalogue returns errors of zero if the proper motion errors are below 1 mas yr$^-$1 as the errors are quantised into integer values. The proper motion measurements themselves are quantised in units of 2 mas yr^{-1}. The reason for this is that the motions were measured for each objects and if the RA or dec motion was larger than 2.5 times the formal error, then it was entered in the catalogue, if not the motion was recorded as 0 mas yr^{-1} (Monet, 2005).

Recently Levine (2005) performed a study of high proper motion objects represented in the catalogue and came to the conclusion that for objects moving as much as 1" yr^{-1}, the catalogue may be as much as 30% incomplete, a result that agrees with Gould (2003). He suggests that in searching the catalogue it is advisable to only use sources with low proper motion and

position errors. The catalogue proper motions were used for the study on Melotte 111, but as the proper motion of this cluster is low, these error measurements are not likely to affect the results.

3.8.2 UCAC2

The second USNO CCD Astrograph Catalogue (UCAC2) utilises the 8 inch Twin Astrograph to survey the sky. It has been doing so since 1998 and stopped in 2004 (Zacharias et al., 2004). The mean formal position error is 30 mas per coordinate and is a function of magnitude. The catalogue also utilises the USNO A2.0 catalogue to calculate proper motion measurements, which have a standard error of 0.5-1.0 mas yr^{-1} .This is much more accurate than the USNO B1.0 catalogue, and in some circumstances more useful as the measurements are not quantised. The drawback to this catalogue is that it only covers stars in the magnitude range R=9-16 mags, making it too shallow for serious brown dwarf searches.

3.8.3 2MASS

2MASS is the successor to the Two Micron Sky Survey (TMSS), conducted in 1969. TMSS covered 70% of the sky and was the first large area sky survey to be conducted in the near infrared. 2MASS began in 1997 and finished surveying the northern sky in 2000. It covers the J (1.24 μm), H (1.66 μm) and Ks (2.16 μm) near-infrared bands with a pixel size of 2.0 arcseconds. The survey is complete to J=15.8, H=15.1, K_S=14.3 (10σ, Skrutskie et al. 2006)

3.8.4 SuperCOSMOS Sky Survey

SuperCOSMOS was an advanced photographic plate digitising machine which is being used to systematically digitise sky survey plates taken with the UK Schmidt telescope (UKST), the ESO Schmidt, and the Palomar Schmidt, and to make the data publicly available. The survey

is calculating proper motions more accurately than its predecessor, USNO B1.0, as the pixel size is 10 micron (0.7 arcsec). This is much smaller than the old DSS-I (25 micron) and the new DSS-II (15 micron). The northern sky survey (POSS II), provides all the information that the USNO B1.0 does, however, the colours and proper motion measurements are more accurate. Currently the whole of the northern and southern sky have been scanned, and the database is being constructed. There are three papers describing the survey, Hambly et al. (2001a) describe the survey as a whole, Hambly et al. (2001b) concentrates on the image detection, classification and photometry and Hambly et al. (2001c) describes the astrometry.

3.8.5   Sloan Digital Sky Survey (SDSS, Sloan)

The SDSS uses a dedicated 2.5m telescope on Apache Point, New Mexico, USA to image more than a quarter of the sky. In addition to this spectra of galaxies and quasars are observed. The first data release was in 2005, and to date 6 data releases have been made. The survey is now complete, and SDSS-II is now under way, which consists of the Sloan Legacy Survey, SEGUE and the Sloan Supernova Survey. Sloan magnitudes are on the AB magnitude system and the survey was completed in 5 filters, u, g, r, i, z with 5σ detection in 1" seeing at magnitudes of 22.3, 23.3, 23.1, 22.3 and 20.8 respectively (York et al., 2000).

3.8.6   UKIRT Infrared Deep Sky Survey

UKIDSS is one of the next generation near-infrared sky surveys, the successor to 2MASS in the northern hemisphere (VISTA will survey the southern hemisphere). UKIDSS began in May 2005 and will survey 7500 square degrees of the northern sky, extending over both high and low Galactic latitudes, in JHK to K=18.3 (5σ), 3.25 magnitudes deeper than 2MASS. UKIDSS will be used as a near-infrared counterpart to the SDSS, and is actually made up of five surveys, the large area survey, the galactic plane survey, the galactic clusters survey, the deep extragalactic survey and the ultra deep survey. Each survey covers a different area of the sky to a different depth. There are many science aims to the survey including searching for

the coolest and nearest brown dwarfs, high-redshift dusty starburst galaxies, elliptical galaxies and galaxy clusters at redshifts $1<z<2$, and the highest-redshift quasars, at $z=7$. Data in this thesis is from the galactic clusters survey which has a depth of J=20.0, H=19.2, K=18.4 over ≈ 1000 square degrees. A second epoch in the K band is planned for this survey to measure proper motions for the surveyed clusters and associations (Coma Berenices, Pleiades, Hyades, Taurus Auriga, Alpha Per, Praesepe, IC4665, Orion, Scorpius, Perseus OB2) (Lawrence et al., 2007).

3.9 Conclusions

In this chapter I have described the basic requirements for photometry and spectroscopy. It has also reviewed the instruments used to acquire the data presented in this thesis as well as describing the filter systems used with them, and how the filters can be used to selected brown dwarfs from field objects. I have also included discussions of astrometry and the method by which the proper motions were calculated in this thesis, as well as methods for the reduction of images and spectroscopy. There is also a description of the surveys which have been used in this thesis and their limitations.

Chapter 4

Pleiades open star cluster

4.1 Introduction

This chapter describes the results of an optical/infrared survey of 2.5 sq. degrees of the Pleiades, the aim of which was to extend empirical constraints on the cluster mass function down to the planetary mass regime ($M \sim 0.01$ $M_\odot$). The chapter describes the observations acquired/used as part for this study, their reduction, their calibration and their photometric completeness. It is then described how candidate brown dwarf members have been identified on the basis of colours and proper motions. It is concluded by briefly discussing the findings in the context of star formation models.

4.2 The initial mass function of young clusters

Recent work on very young clusters ($\tau < 10$ Myr) and star formation regions e.g. σ-Orionis, the Trapezium, IC348 and Upper Sco (Béjar et al., 2001; Muench et al., 2002, 2003; Lodieu et al., 2007) suggests that the initial mass function continues slowly rising down to masses of the order $M \sim 0.01$ $M_\odot$, at least in these environments. Indeed, it has been claimed that an ob-

ject with a mass as low as 2-3 M_{Jup} has been unearthed in σ-Ori (Zapatero Osorio et al., 2002). However, the cluster membership of σ-Ori 70 is disputed by Burgasser et al. (2004). Furthermore, mass estimates for such young substellar objects derived by comparing their observed properties to the predictions of theoretical evolutionary tracks remain somewhat controversial. Baraffe et al. (2002) have shown that to robustly model the effective temperature and luminosity of a low mass object with an age less than ~ 1 Myr, the evolutionary calculations need to be coupled to detailed simulations of the collapse and accretion phase of star formation. As the current generation of evolutionary models start from arbitrary initial conditions, theoretical predictions for ages less than a few Myr must be treated with a fair degree of caution. The few available dynamical mass measurements of pre-main sequence objects indicate that models tend to underestimate mass by a few tens of percent in the range $0.3 < M < 1.0$ $M_\odot$ (see Hillenbrand & White 2004 for review). A recent dynamical mass measurement of the 50-125 Myr old object AB Dor C (spectral type $\sim$M8), the first for a pre-main sequence object with $M < 0.3$ $M_\odot$, suggests that the discrepancy between model predictions and reality might be even larger at lower masses, with the former underestimating mass by a factor 2-3 at $M \sim 0.1$ $M_\odot$ (Close et al., 2005). However, this conclusion is dependent on the assumed age of AB Dor, which is currently a matter of great contention (Luhman et al., 2005; Janson et al., 2007). On the positive side, Zapatero Osorio et al. (2004) have determined the masses of the brown dwarf binary components of GJ 569 Bab and their luminosities and effective temperatures are in agreement with theoretical predictions, for an age of 300 Myr. Stassun et al. (2006) discuss an eclipsing brown dwarf binary in the Orion nebula star forming region and find the large radii predicted by theory for a very young dwarf. Surprisingly, they find that the secondary is hotter than the more massive primary. Clearly further work is still needed to support the predictions of theoretical models.

Despite all of the work on clusters one key question which remains unanswered is "what is the lowest possible mass of object that can be manufactured by the star formation process?". From a theoretical stance, traditional models predict that if substellar objects form like stars, via the fragmentation and collapse of molecular clouds, then there is a strict lower mass limit to their manufacture of 0.007-0.010 $M_\odot$ (Padoan & Nordlund, 2002). This is set by the rate at which

the gas can radiate away the heat released by the compression (e.g. Low & Lynden-Bell 1976). However, in more elaborate theories, magnetic fields could cause rebounds in collapsing cloud cores which might lead to the decompressional cooling of the primordial gas, a lowering of the Jeans mass and hence the production of gravitationally bound fragments with masses of only ~ 0.001 $M_{\odot}$ (Boss, 2001). In contrast, if feedback from winds and outflows which are driven by the onset of deuterium burning play a role, then the smallest objects which form via the star formation process may be restricted to masses equal to or greater than the deuterium burning limit (~ 0.013 $M_{\odot}$, Adams & Fatuzzo 1996). If very low mass brown dwarfs could be found in a mature cluster such as the Pleiades, this would provide more reliable evidence for the existence of such objects.

4.3 The Pleiades

The Pleiades open star cluster ($3^h46^m.6\pm0.2$, $24°04'\pm3$ Pinfield et al. 1998) is arguably the best studied cluster in the sky. All of its members share a common proper motion ($\mu \approx 50$ mas yr^{-1}, Jones 1981), making it easy to distinguish cluster members from the background star population. Spectroscopy of these cluster members has determined that the metallicity of the Pleiades is near solar (Fe/H=0.017 ± 0.055, Boesgaard 1989), and that it has a lithium age of 125 ± 8 Myr (Stauffer et al., 1998). This is the age used throughout this work. There are in fact a range of age estimates for the Pleiades, ranging from 70 to 150 Myr. This range is caused by using theoretical models to determine the cluster's age, and these models are very sensitive to the conditions used, particularly those relating to the convection within the stellar core. If the models used include convective core overshoot, then the age estimate of the cluster increases, as the convective core overshoot enlarges the convective core of the model stars, thus increasing their time on the main hydrogen burning sequence. The models of Mazzei & Pigatto (1989) which utilise convective core overshooting predict an age of ≈ 150 Myr as the age of the Pleiades, whereas Mermilliod (1981) neglect this effect and calculate an age of 70 Myr. It is likely that the real age resides somewhere between these two estimates, closer to the lithium age.

The distance to the Pleiades has also been a subject of some discussion, mainly because the majority of methods of deriving the distance using surveys, main sequence fitting, parallax, etc, disagreed with the distance as measured by the Hipparcos satellite ($\approx 118 \pm 4$ pc, van Leeuwen 1999). It is now accepted that the Hipparcos measurement is incorrect, due to complications involving the parallax method of using cluster members to determine the distance. This was discussed in Pinsonneault et al. (1998) and in Soderblom et al. (2005), who both independently calculate a distance of ~ 134 pc using main sequence fitting and parallax measurements respectively. A comprehensive astrometric analysis of the binary Atlas, resulted in estimates of 133 to 137 pc (Pan et al., 2004). One of the most recent distance estimates, and the one used throughout this work, is 133.8 ± 3 pc derived by Percival et al. (2005) using main sequence fitting using near infrared photometry of main sequence cluster members. In addition to the close proximity of the cluster, the reddening along the line of sight towards the Pleiades is low, E(B-V)=0.03 (Crawford & Perry, 1976). Because of the above reasons the Pleiades has been thoroughly studied, particularly involving searches for brown dwarfs, as its age, proximity and low level of reddening make it an ideal place to search for substellar objects. These surveys which notably include those of Hambly et al. (1991), Stauffer et al. (1994), Zapatero Osorio et al. (1998), Bouvier et al. (1998), Dobbie et al. (2002a), Moraux et al. (2001),Moraux et al. (2003) and Bihain et al. (2006) have unearthed numerous low mass stars and brown dwarfs down to ≈ 26 M_{Jup}, which have all been found to have spectral types of $\approx$ L1 - L3. These searches have determined a range of α for the mass spectrum of the cluster, and current estimates put it at $\approx$ 0.5-0.6.

4.4 Observations, data reduction and survey completeness

4.4.1 The J band imaging and data reduction

Approximately 3.0 square degrees of the Pleiades cluster were observed in the J band using WFCAM on UKIRT between the dates of 29/09/2005 and 08/01/2006. WFCAM is a near infrared imager consisting of 4 Rockwell Hawaii-II (HgCdTe 2048×2048) arrays with 0.4"

pixels, arranged such that 4 separate pointings (pawprints) can be tiled together to cover a 0.75 sq. degree region of sky (see http://www.ukidss.org/technical/technical.html for diagram). A total of four tiles were observed in a mixture of photometric and non-photometric conditions but in seeing of typically $\approx$ 1.0 arcsecond or better. The observations were taken of four separate fields in queue scheduled mode using a 9 point diamond dither pattern. Overall 4 tiles were observed, using five 1 hour exposures per tile. A 2×2 microstepping mode was also used to improve the spatial sampling. The location of these tiles on the sky can be seen in figure 4.1 and the coordinates of each pointing are given in table 4.1. The locations on the sky of these tiles were chosen to provide maximum overlap with the optical fields surveyed in 2000 by CFHT and CFH12k camera, but also to avoid bright stars and areas of significant interstellar extinction.

The images were reduced at CASU using procedures which have been custom written for the treatment of WFCAM data. In brief, each frame was debiased, dark corrected and then flat fielded. The individual dithered images were stacked before having an object detection routine run on them. The detection procedure employs a core radius of 5 pixels, and identifies objects as islands of more than 4 interconnected pixels with flux $>1.5\sigma$ above the background level. The frames were then astrometrically calibrated using sources in the 2MASS catalogue. This astrometric calibration involves using a cubic radial distortion term, before fitting the objects in the field to the 2MASS point source catalogue. These solutions in general had a scatter of less that 0.1 arcseconds. The photometric calibration employed by the CASU pipeline also relies on 2MASS data (there are typically hundreds of 2MASS calibrators per detector) and is found to be accurate to $\approx2\%$ in good conditions (see Warren et al. 2007b; Hodgkin et al. 2007 for details).

In measuring the photometry an aperture of 2" was used, which is approximately twice the core radius of the point sources. This 2" diameter of the aperture is also twice the seeing full width half maximum (FWHM). The reduction pipeline also attempts to classify each source depending on its morphology (e.g. galaxy, star, noise). However, at the limit of the data this classification becomes less reliable. Therefore, in the subsequent analysis stellar objects are defined as all objects which lie within 3 sigma of the stellar locus, where sigma is defined
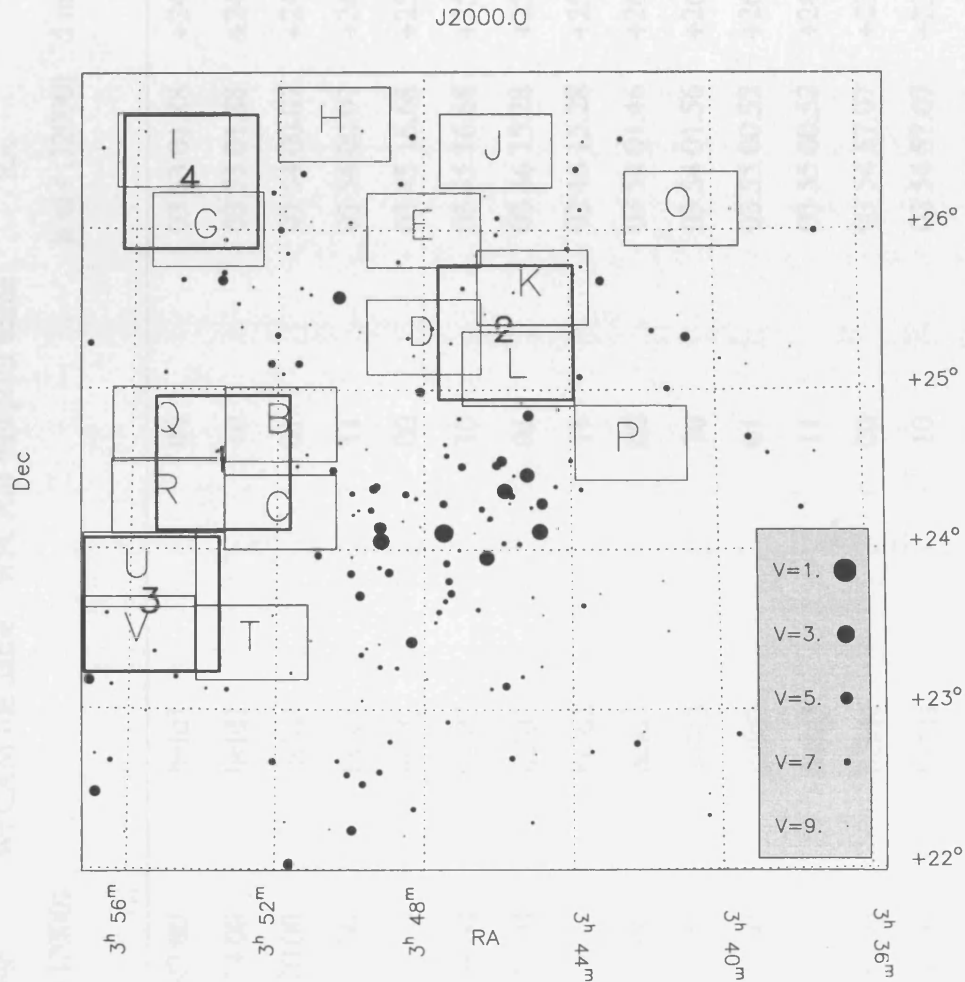
Figure 4.1: The regions imaged at I, Z and J with the CFHT and UKIRT. The CFH12k point-ings (light rectangular outlines) are labelled alphabetically as in Moraux et al. (2003), while the WFCAM tiles (bold square outlines) are labelled numerically, ranging from 1 to 4. Note that the observations avoid the region of high reddening to the south of the bright star Merope ($03^h46^m19^s.57, +23°56'54".1$) and the other bright stars in vicinity of the cluster centre.

67

Table 4.1: The centres of the CFHT and WFCAM fields as used in this work.

Field name	RA h m s (J2000)	Dec d m s (J2000)	WFCAM tile name	WFCAM pawprint name	RA h m s (J2000)	Dec d m s (J2000)
B	03 51 55	+24 47 00	field1	00	03 53 01.88	+24 26 00.28
C	03 51 55	+24 14 00	field1	10	03 53 01.88	+24 39 12.97
R	03 55 00	+24 20 00	field1	01	03 54 00.07	+24 26 00.28
Q	03 55 00	+24 47 00	field1	11	03 54 00.07	+24 39 12.97
K	03 45 00	+25 38 30	field2	00	03 45 16.68	+25 15 13.28
L	03 45 25	+25 08 00	field2	10	03 45 16.68	+25 28 25.97
D	03 48 00	+25 20 00	field2	01	03 46 15.28	+25 15 13.28
			field2	11	03 46 15.28	+25 28 25.97
U	03 55 45	+23 52 00	field3	00	03 54 01.46	+26 11 37.28
V	03 55 45	+23 28 00	field3	10	03 54 01.56	+26 24 49.97
T	03 52 40	+23 25 00	field3	01	03 55 00.52	+26 11 37.28
			field3	11	03 55 00.52	+26 24 49.97
I	03 55 00	+26 30 00	field4	00	03 54 57.07	+23 32 37.28
G	03 54 00	+26 00 00	field4	10	03 54 57.07	+23 45 29.97
			field4	01	03 55 54.87	+23 32 37.28
			field4	11	03 55 54.87	+23 45 49.97

according to Irwin et al. (2007).

4.4.2 The far-red optical imaging and a new reduction

As part of this work a subset (2.54 square degrees) of the far-red optical data obtained in the course of the IZ survey of the Pleiades conducted in 2000 by Moraux et al. (2003) has been used. The relevant CFH12k data were extracted from the Canadian Astrophysical Data Center archive and were reprocessed at Cambridge University by Simon Hodgkin using the CASU optical imaging pipeline (Irwin & Lewis, 2001). In brief, these data were bias subtracted and corrected for non-linearity prior to flat fielding. Fringe maps, which were constructed for each photometric band from images obtained during the observing run, were used to remove the effects of interference between night sky lines in the CCD substrate. Subsequently, sources at a level of significant of 3σ or greater were morphologically classified and aperture photometry obtained for each. A World Coordinate System was determined for each frame by cross-correlating these sources with the Automated Plate Measuring (APM) machine catalogue (Irwin, 1985). The approximately 100 common objects per CCD chip lead to an internal accuracy of typically better than 0.3 ".The photometry was calibrated onto a CFH12k I and Z natural system using stars with near zero colour (B-V-R-I$\approx$0) in Landolt standard field SA98 (Landolt, 1992) which was observed the same nights as the science data. The systematic errors in the photometry were calculated by comparing the photometry of overlapping fields as in Moraux et al. (2003). The photometry was found to be accurate to $\approx 3\%$.

4.4.3 The completeness of datasets

To estimate the completeness of the IR images, a random seed was used to create and inject fake stars with magnitudes in the range $12 \leq J \leq 22$ into each of the 16 chips of every WFCAM frame. The object detection software was then rerun on these new images with the same parameters that were used to detect the real sources. The objects were inserted 10 times per chip at different positions. The skylevels, gain, seeing, exposure times and zero points of the

images were all taken into account when creating the fake stars. These were created using the IRAF routine mkobjects. It was also requested that the created objects have a Moffat profile. This is an elliptical profile with a major axis half-intensity radius given by the input parameters seeing/radius scale in pixels, model parameter, axial ratio and position angle. The latter two of these parameters were set to 1 and zero, meaning the fake star was circular. The radius was set to have a value of half the seeing. The model parameter (β) was set to be equal to 2. The image profile is defined by Equation 4.1

$$I = \left(1 + \left(2^{\frac{1}{\beta}-1}\right)\left(\frac{R}{r}\right)^2\right)^{-\beta},$$ (4.1)

where I is the image profile created, r is the seeing/radius scale in pixels, and R is the circularly symmetric radius of the object and is defined in Equation 4.2,

$$R = \sqrt{dX^2 + dY^2}.$$ (4.2)

R is dependant on dX and dY the object's coordinates in transformed circular coordinates, calculated from the pixel coordinates of the object by Equations 4.3 and 4.4,

$$dX = dx \cos p + dy \sin p,$$ (4.3)

$$dY = \frac{-dx \sin p + dy \cos p}{a},$$ (4.4)

where dx and dy are the coordinates of the fake star relative to its centre, p is its position angle, and a is its axial ratio. This profile provides a suitable point spread function for the fake stars, meaning that the detection software believes that they are real stars, and not galaxies etc. I chose to insert 200 fake stars per chip, ten times so as to have enough of these objects to provide meaningful results but also to avoid significantly increasing the density of all sources in the data and biasing the results. Subsequently, I calculated the percentage completeness at a given magnitude by taking the ratio of the number of fake stars recovered to the number of fake stars injected into a given magnitude bin (and multiplying by 100). It should be noted

70

that a 100% recovery rate was never achieved at any magnitude since a small proportion of the fake stars always fell sufficiently close to other sources to be overlooked by the object detection algorithm.

The same method was then applied to determine the completeness of the I and Z band CFH12k data. However, the magnitude range of the fake stars was adjusted to be consistent with the different saturation and faint end magnitude limits of these data. The results of this procedure for all 3 photometric bands are shown in table 4.2.

A glance at this table indicates that the IR data are in general 90% complete to $J\approx19.7$, although Field 3 is less deep, due to moonlight and poor seeing. In this case the proximity of the moon led to higher background counts. The I data are typically 90% and 50% complete to I=23.5 and 22.5 respectively. The corresponding completeness limits for the Z band data are Z=22.5 and 21.5 respectively.

4.4.4 Photometric selection of candidate cluster members

An initial photometrically culled sample of candidate brown dwarfs has been obtained from the I, I-Z colour-magnitude diagram (figure 4.2) where the 120 Myr NEXTGEN (Baraffe et al., 1998) and DUSTY (Chabrier et al., 2000) model isochrones (modified to take into account the Pleiades distance of 134 pc (e.g. Percival et al. 2005) served as a guide to the location of the Pleiades sequence. With the uncertainties in both the photometry and the age of the cluster in mind, I first removed all saturated objects before selecting all objects with a morphology statistic $-3.0 < x < 3.0$ in both I and Z (classed as stellar, as with the J band), which in the magnitude range $16.5 < I < 22.5$ lay no more than 0.25 magnitudes below the DUSTY isochrone or for magnitudes $I \geq 22.5$ that had $I > 1.143(I-Z)+16.0$.

All the candidate Pleiads found by Moraux et al. (2003) and Bihain et al. (2006) lay within ±0.25 magnitudes of the DUSTY model. Thus the selection criterion is 0.25 magnitudes to the left of the DUSTY model. Below I=22.5, the DUSTY model is not red enough to

Table 4.2: 50 and 90% completeness figures for the optical and infrared fields. The positioning of these fields is shown in figure 4.1. Note that while WFCAM field 1 corresponds to CFHT fields B, C, R and Q, the individual pawprints, do not correspond on a one to one basis - i.e. field1_00 does not correspond to field B.

Field name	I 50%	I 90%	Z 50%	Z 90%	WFCAM tile	WFCAM pawprint	J 50%	J 90%
B	23.2	22.5	22.3	21.5	field1	00	20.9	19.9
C	23.7	22.6	22.6	21.6	field1	01	20.9	20.1
R	24.0	23.0	22.9	21.6	field1	10	20.9	19.8
Q	23.7	22.5	22.7	21.6	field1	11	20.9	19.7
K	23.6	22.5	23.0	21.9	field2	00	20.9	19.7
L	24.0	22.7	23.0	21.8	field2	01	20.9	19.9
D	23.7	22.4	23.0	21.7	field2	10	21.0	19.9
					field2	11	20.9	19.7
U	23.5	22.5	22.9	21.7	field3	00	19.5	18.8
V	23.8	22.5	22.7	21.7	field3	01	19.0	17.7
T	23.6	22.5	22.6	21.5	field3	10	19.6	18.6
					field3	11	18.9	17.7
I	23.9	22.3	23.1	22.0	field4	00	20.8	19.7
G	23.7	22.7	23.4	22.3	field4	01	20.8	19.7
					field4	10	20.8	19.7
					field4	11	20.8	19.7

account for known field stars, and so is inappropriate in this effective temperature regime. An approximate field star sequence from Tinney et al. (2003) and Hawley et al. (2002) was calculated and then lowered by 2 magnitudes. This results in the line I-Z= (I-19.0)/3.5. This selection is conservative, and is particularly aimed at removing the bulk of the red tail of the background stars.

Subsequently, the initial list of candidates was cross-correlated with the J band photometric catalogue (using a matching radius of 2 arcseconds) and the photometrically culled sample was refined using the resultant Z, Z-J colour-magnitude diagram (figure 4.3). These objects are also shown on the J, I-J colour-magnitude diagram, figure 4.4. As before, the 120 Myr model isochrones were used as a guide to the location of the cluster sequence. With the photometric uncertainties in mind, all candidates with $Z \leq 20$ were retained. All candidates with $20 < Z < 21$ and $Z\text{-}J \geq 1.6$ were also retained. Finally, all candidates with $Z > 21$ and $Z\text{-}J \geq 1.9$ were retained. These constraints are conservative and are based on the field L and T dwarfs sequence ($Z\text{-}J \geq 3$, Chiu et al. 2006) since the DUSTY models are known to be inappropriate in this effective temperature regime. Since the survey is limited by the depth of the I band data, all candidates with $Z > 20$ and no I band counterpart were also kept.

4.4.5 Refining the sample using astrometric measurements

To remove any non-members I measured the proper motion of each candidate brown dwarf, using the Z and J band data where the epoch difference was 5 years. In this process, only objects lying within 2 arcminutes of each candidate were chosen as potential astrometric reference stars. This compromise provided a sufficiently large number of sources but at the same time minimised the effects of non-linear distortions in the images. Furthermore, objects with large ellipticity (>0.2), classed by the photometric pipeline as non-stellar in the Z band data and with $Z < 16$ or $Z > 20$ were rejected. This ensured that, in the main, the astrometric reference sources were not of very low signal to noise (S/N) in the J band or saturated in the optical data. These criteria generally provided at least 20 suitable stars per candidate brown dwarf.
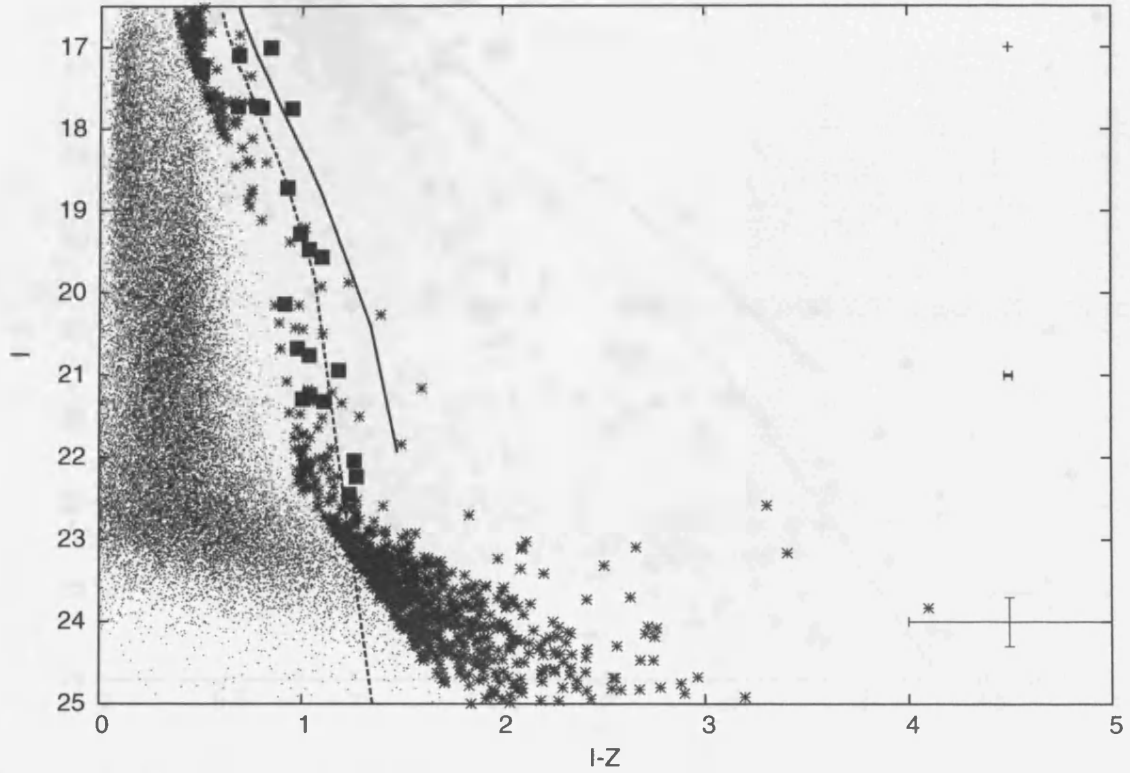
Figure 4.2: The I, I-Z colour-magnitude diagram for the whole of field 1. The solid line is the NEXTGEN model, and the dotted line the DUSTY model. The small points are all objects that were classed as stellar in both I and Z data. The stars are all objects that met the following selection criteria: classed as stellar in both I and Z data, for $16.5 < I < 22.5$, they must lie no more than 0.25 magnitudes to the left of the DUSTY isochrone, for $I \geq 22.5$, they must lie to the right of the line, I-Z= $(I-19.0)/3.5$. The filled squares are the previously identified cluster members from Bihain et al. (2006), Moraux et al. (2003) and Bouvier et al. (1998), plotted to highlight the cluster sequence.
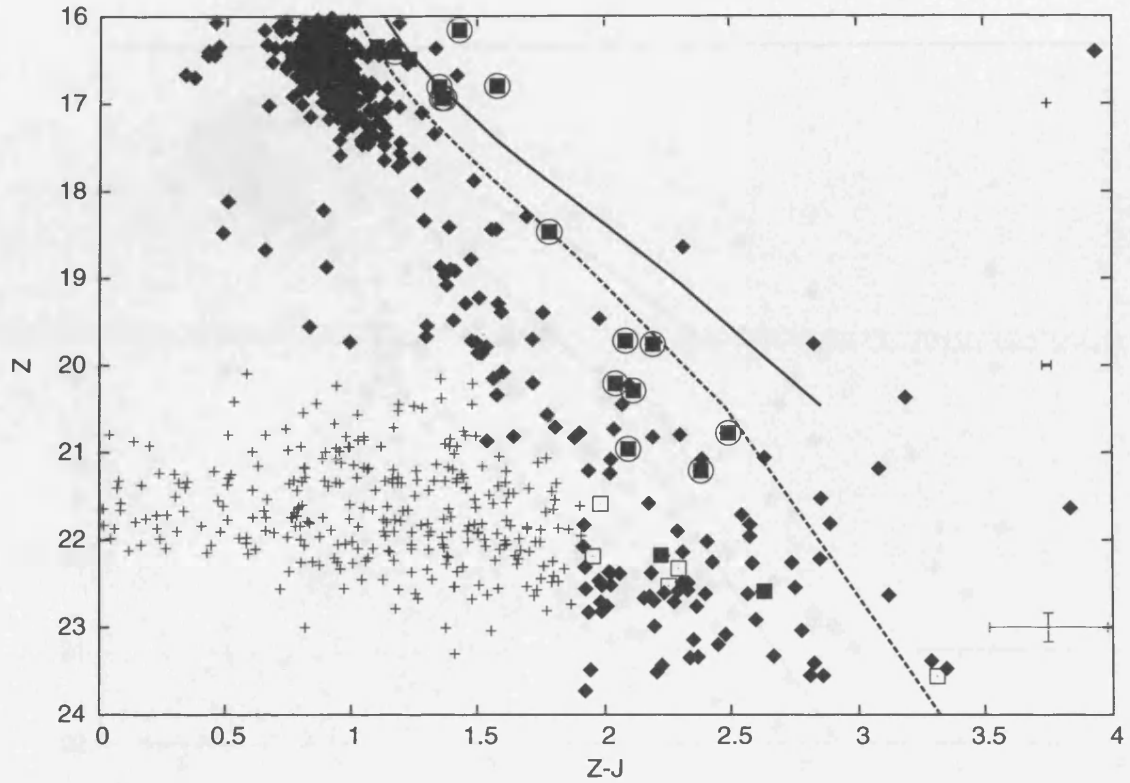
Figure 4.3: The Z, Z-J colour-magnitude diagram for the whole of the survey. The solid line is the NEXTGEN model, and the dotted line the DUSTY model. The crosses are all the objects selected from the I, I-Z (stars on figure 4.2). The filled diamonds are all objects that met the selection criteria from the I, I-Z, and Z, Z-J colour-magnitude diagrams. These were selected for proper motion analysis, and were found to be non members. The filled squares are the candidate cluster members (objects that remained after proper motion analysis). The open squares are the ZJ only candidates for all four fields that remained after proper motion analysis. The previously identified members from Bihain et al. (2006), Moraux et al. (2003) and Bouvier et al. (1998) are identified by open circles around the plotted symbols.
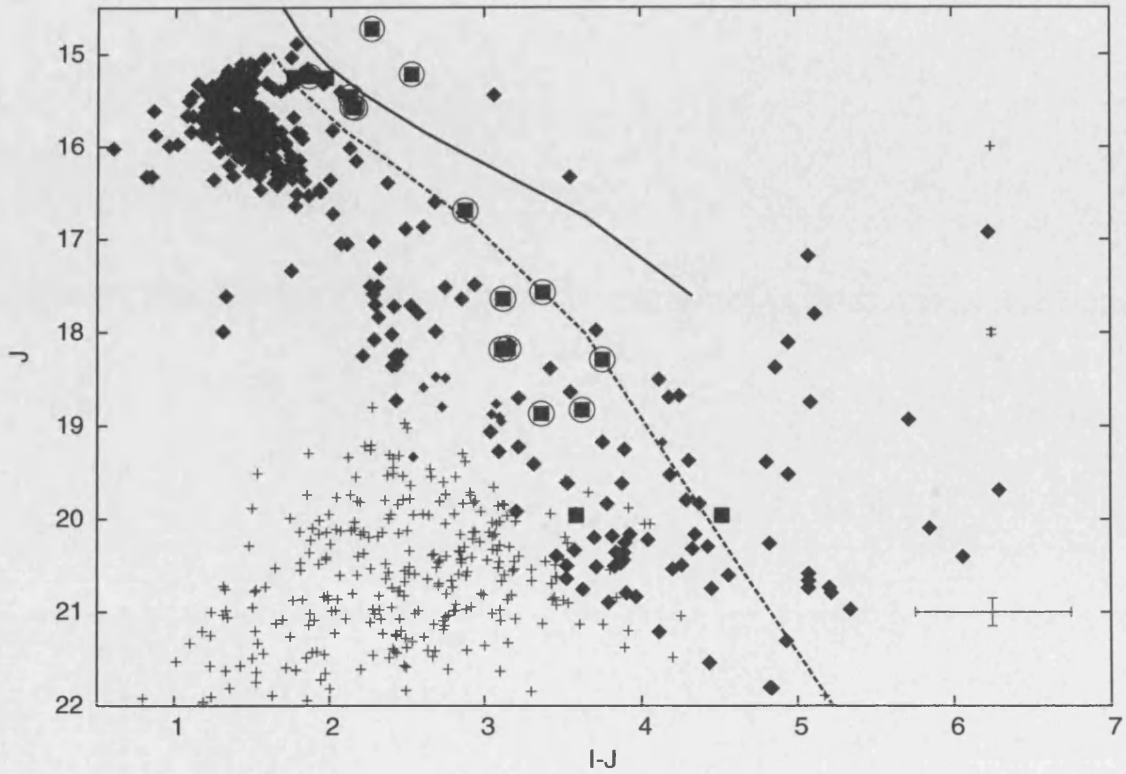
Figure 4.4: The J, I-J colour-magnitude diagram for the whole of the survey. The solid line is the NEXTGEN model, and the dotted line the DUSTY model. The crosses are all the objects selected from the I, I-Z (stars on figure 4.2). The filled diamonds are all objects that met the selection criteria from the I, I-Z,and Z, Z-J colour-magnitude diagrams. These were selected for proper motion analysis, and were found to be non members. The filled squares are the candidate cluster members (objects that remained after proper motion analysis). The previously identified members from Bihain et al. (2006), Moraux et al. (2003) and Bouvier et al. (1998) are identified by open circles around the plotted symbols.

The instruments have different pixel scales of 0.4 arcsec/pixel for WFCAM and 0.206 arcsec/pixel for CFH12k, thus requiring a coordinate transform to be calculated between the two sets of data. Six coefficient transforms between the epoch 1 Z band images and the epoch 2 J band images were calculated using routines drawn from the STARLINK SLALIB package. This process was described in more detail in Chapter 3. Once the routines had converged, the relative proper motions in pixels were calculated by dividing the fitting residuals of each candidate by the epoch difference. For these data the epoch difference is approximately 5 years. Subsequently, the astrometric motion in milliarcseconds per year in RA and dec was derived by folding these values through the world coordinate system transform matrix of the relevant WFCAM image.

The centroiding error on each of the candidate brown dwarfs was estimated using a method similar to the one used to estimate the completeness. This involved inserting fake stars into the images in the same way as for the completeness calculation, but this time, after the objects were recovered by the object detection software, the difference in pixels was measured between the inserted position and the recovered co-ordinates. 2D Gaussians were then fitted to these differences in bins of width two magnitudes, as the uncertainty in measurement increases as the object to be measured gets fainter. I found that in the Z band data, for objects with magnitudes $Z \leq 21$, the centroiding uncertainty is equivalent to 3 mas yr^{-1} in each axis, while for objects with $23 \geq Z > 21$ this number increases to 8 mas yr^{-1}. For the faintest Z band objects, $24 \geq Z > 23$, the centroiding uncertainty is equivalent to 12 mas yr^{-1} in each axis. In the J band data, for objects with magnitudes $21 \geq J > 17$, the centroiding uncertainty is equivalent to 5 mas yr^{-1} in each axis. Thus for the brightest candidates ($Z < 21$, $J < 19$), the quadratic sum of the Z and J band centroiding errors is less than or comparable to the RMS of the residuals of the linear transform fit, which is typically 5-10 mas yr^{-1} in each axis. This latter quantity has been adopted as the proper motion uncertainty in both the RA and dec directions for these objects. These errors may appear large, however, they are representative of the limitations within these measurements.

I fitted the proper motions of all of the photometric candidates (excluding the ZJ only candidates, as there were not enough objects to make the fitting reliable) with a Gaussian, which

was found to be centred on 1.44, -5.968 mas yr^{-1}. This Gaussian had a σ of 14.0. The equation of this Gaussian is detailed in equation 4.5.

$$f(\mu_\alpha cos\delta, \mu_\delta) = 1.165\exp\left\{-\frac{1}{2}\left[\left(\frac{\mu_\alpha cos\delta - 1.44}{14.572}\right)^2 + \left(\frac{\mu_\delta + 5.968}{13.460}\right)^2\right]\right\}. \qquad (4.5)$$

I was not able to fit two Gaussians, one to the background stars and one to the Pleiades dwarfs, as described in Moraux et al. (2003), since only $\approx$ 30 objects have the correct proper motion for cluster membership. This meant that while the cluster Gaussian could be seen in the tail of the background Gaussian, it was no larger than the noise level. Consequently, objects were only selected to be proper motion members if they had proper motions that fell within 1σ of the proper motion of the cluster at +20, -40 mas yr^{-1} (Jones, 1981; Hambly et al., 1991; Moraux et al., 2001). The selection criteria was required to be 1σ, as extending this to 2σ, would seriously overlap with the field stars centred on 0,0. I did extend the selection criteria to 1.5σ, which yielded 14 additional objects, however, all were rejected due to their bright, but blue (I$\approx$17.0, I-Z<1.0) positions on the I, I-Z colour-magnitude diagram, which led me to believe that they were field objects. I also attempted to tighten the selection criteria to a circle with radius 10 mas yr^{-1}. This selection meant that candidate members PLZJ 78, 9, 77, 23 were lost (see table 4.5). PLZJ 78, 9 and 77 have all been identified and confirmed as proper motion members by Bihain et al. (2006), Moraux et al. (2003) and Bouvier et al. (1998).

Unfortunately, as two Gaussians cannot be fitted to the data, a probability of membership for these objects cannot be calculated by the standard method as defined by Sanders (1971). The proper motion measurements may be found in table 4.5, and the I, Z, J, H and K magnitudes for these candidate members to the cluster in table 4.6.

An attempt has been made to use control data to determine the level of contamination within the data, however, the numbers involved are very small, so any calculated probability will be uncertain. Control samples were used, two circles of radius 14 mas yr^{-1} (1σ), and an annulus of width 2$\times$14 mas yr^{-1}, at the same distance from 0,0 proper motion as the Pleiades. This control method involves regions that have an arbitrary proper motion that is not the same as

78

that for the cluster. The method is used to compare the number of objects that have been photometrically selected and have the desired proper motion that fall within the cluster and the controls. The σ value of 14 mas yr^{-1} does not quite encompass the very worst errors deduced from the method of adding artificial stars to the images. To these errors, one should also add (quadratically) the velocity dispersion of the low mass cluster members. For the 10 to 20 M$_{\rm Jup}$ members this is estimated to be 7 mas yr^{-1}, using figure 4 of Pinfield et al. (1998). Thus ideally the 14 mas yr^{-1} should be increased for the worst errors pus velocity dispersion to 18 mas yr^{-1} ($2 \times 12^2 + 7^2$). However, such a value would have led to unrealistically low membership probabilities. As stated above, the selection criteria of 14 mas yr^{-1} seems to be the pragmatic choice.

The data were separated into one magnitude bins, and the probability was calculated for each magnitude bin, using equation 4.6,

$$P_{\rm membership} = \frac{N_{\rm cluster} - N_{\rm control}}{N_{\rm cluster}}, \qquad (4.6)$$

where $P_{\rm membership}$ is the probability of membership for that magnitude bin, $N_{\rm cluster}$ is the number of stars belonging to the cluster in that magnitude bin. $N_{\rm control}$ is the number of dwarfs in the control circle of proper motion space, see figure 4.5. $N_{\rm cluster} - N_{\rm control}$ is the number of Pleiads plus contaminants. It can be seen that the probability depends on where the control circle is located. Thus rather than use a circle an annulus can be used, and the count scaled down to an area equal to that of a control circle. Note that figure 4.5 is for all of the magnitude bins together. Figure 4.6 is the same as figure 4.5, but for the ZJ selected objects only. The statistics are much poorer for the individual magnitude bins and the probabilities are correspondingly more uncertain. It can be seen in both figures 4.5 and 4.6 that there is not a symmetrical distribution of proper motions. In fact the distribution in the vector point diagram, is a classical "velocity ellipsoid" displaced from zero by reflex motion from the Sun's peculiar velocity, and happens to be in the direction of the Pleiades proper motion vector. The contamination has therefore probably been underestimated, as the annulus method of calculating probabilities assumes that the vector point diagram has a circularly symmetric distribution of objects. These probabilities are shown in table 4.3, and probabilities derived in the same way but for the ZJ only candidates can be found in table 4.4.
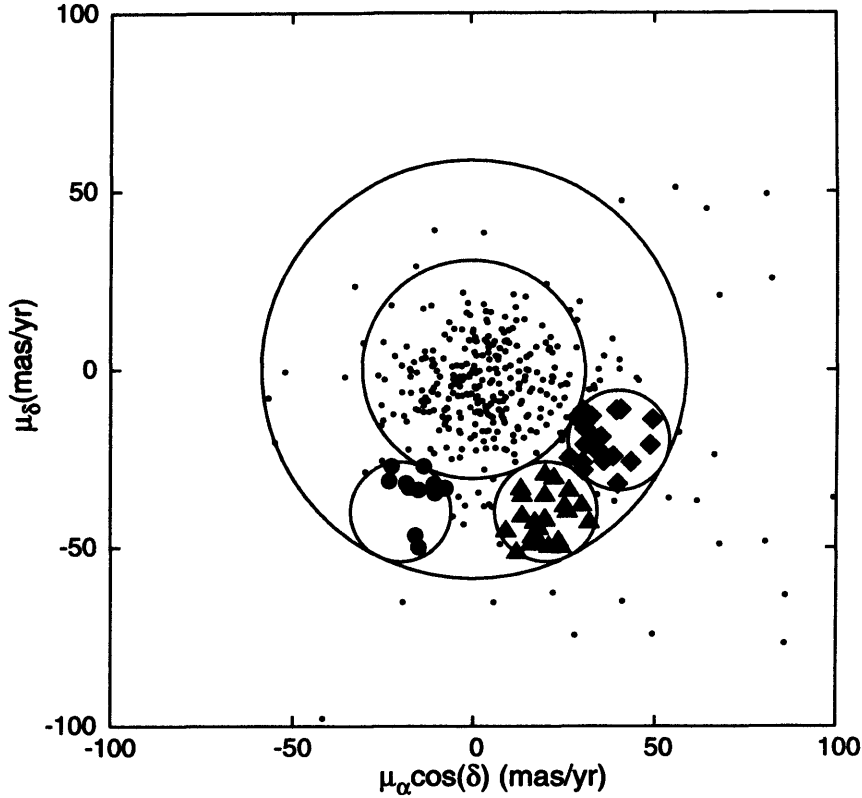
Figure 4.5: Proper motion vector point diagram of the photometrically selected candidate members. The filled triangles are candidate and known cluster members. The filled diamonds and filled circles are the two separate control clusters used. The annulus used for the radial method is also plotted.

An alternative approach to estimating the contamination is to use the field L and T dwarf luminosity functions. Chabrier (2005) gives the T dwarf luminosity function as being 10^{-3} dwarfs/pc^3/unit J mag interval. The 7 L and T dwarf candidates cover a total of 0.7 mag in the J band. Note PLZJ 323 and 23 may be late L dwarfs but they have been included in this analysis. The volume of space used is 836 pc^3, based on 2.5 square degrees and a distance to the Pleiades of 134±30 pc (Percival et al., 2005). This distance range corresponds to a distance modulus range of ±0.5 magnitudes, which is generous, given that the sequence shown in is clearly narrower than ±0.5 magnitudes (figures 4.7 and 4.8). Thus the expected number of contaminating field dwarfs is 0.6. The velocity dispersion of field T dwarfs is not known, so it is not possible to calculate by how much the 0.6 should be reduced for objects not moving with the cluster. It should be noted that the solar reflex motion can make field objects appear
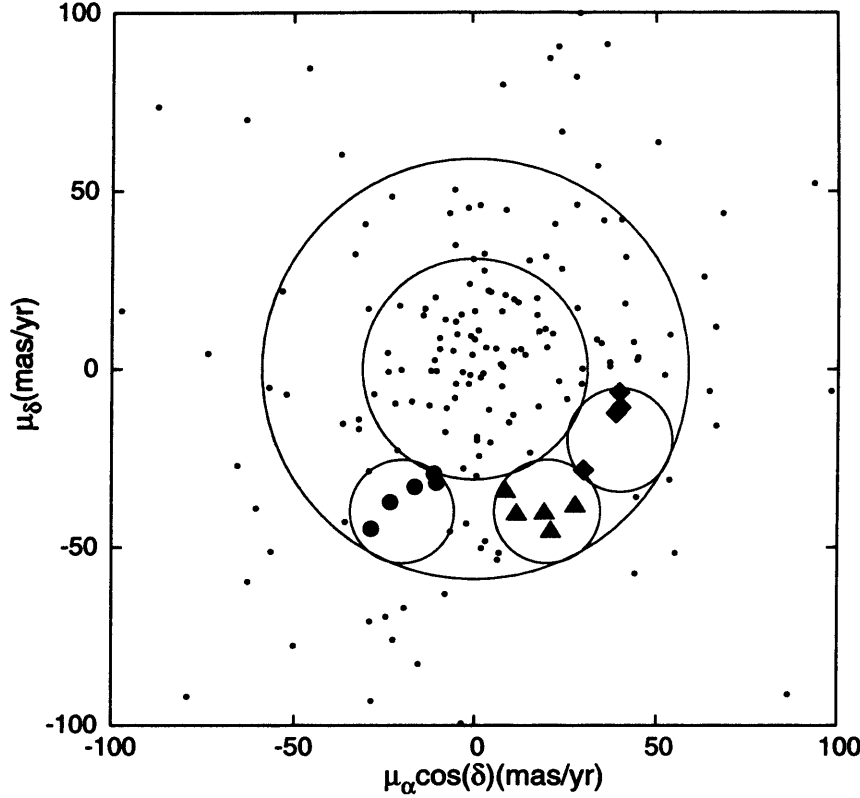
Figure 4.6: Proper motion vector point diagram of the photometrically selected candidate members. The filled triangles are candidate cluster members selected from the Z, Z-J colour-magnitude diagram only. The filled diamonds and filled circles are the two separate control clusters used. The annulus used for the radial method is also plotted.

to move with the proper motion of the Pleiades in this region of sky which will affect the contamination. However, it is clear that the luminosity function indicates that contamination by field T dwarfs should be trivial. For the field L dwarfs with $M_J \approx 13.0$ (i.e. $J \approx 18.5$ at the distance of the Pleiades) the luminosity function is 3×10^{-4} dwarfs/pc^3/unit J mag interval (Chabrier, 2005). A similar calculation then gives 0.25 contaminating L dwarfs which should be further reduced by considering proper motions. It is thus clear that the field luminosity function indicates that contamination by field L and T dwarfs should be negligible.

Table 4.3: Probability of membership, magnitude range for the radial method of calculating probabilities of membership as well as the two control areas.

Probability radial	Probability $\mu_\alpha cos\delta$=-20 mas yr^{-1} μ_δ=-40 mas yr^{-1}	Probability $\mu_\alpha cos\delta$=+40 mas yr^{-1} μ_δ=-20 mas yr^{-1}	Magnitude range (Z)
0.67	0.25	0.0	16 - 17
0.82	0.66	0.0	17 - 18
0.88	1.00	0.0	18 - 19
0.84	1.00	0.0	19 - 20
1.00	1.00	1.00	20 - 21
0.88	0.50	1.00	21 - 22
0.61	1.00	0.00	22 - 23

Table 4.4: Probability of membership, magnitude range for the radial method of calculating probabilities of membership as well as the two control areas for the candidates selected from the ZJ data only.

Probability radial	Probability $\mu_\alpha cos\delta$=-20 mas yr^{-1} μ_δ=-40 mas yr^{-1}	Probability $\mu_\alpha cos\delta$=+40 mas yr^{-1} μ_δ=-20 mas yr^{-1}	Magnitude range (Z)
0.61	1.00	1.00	21 - 22
0.35	0.67	0.33	22 - 23
-0.16	-2.00	0.00	23 - 24

4.5 Results

Most of these objects, except for two bright objects and the faintest seven, have been documented before in surveys - Moraux et al. (2003) and Bihain et al. (2006). It should be noted that the Bihain objects were discovered independently in this study before they were published. All of these objects within the overlapping area were recovered, and none were rejected by the IZ photometric selection. The objects we recovered were BRB 4, 8, 17, 13, 19, 21, 22, 27 and 28 and PLIZ 2, 3, 5, 6, 13, 14, 19, 20, 26, 28, 31, 34, 35 and 36. PLIZ 18, 27 and 39 were found to have no J counterpart in the WFCAM catalogues. Other information known about these objects indicates that PLIZ 18 has a previously recorded low log g (4.5) consistent with membership to the cluster , PLIZ 27 has a proper motion that is not consistent with cluster membership, and PLIZ 39 has a K magnitude of 17.8, which makes it too blue to be a member (Moraux, 2007b).

Of the recovered objects BRB 19 and PLIZ 14 and 26 met the selection criteria on the Z, Z-J colour-magnitude diagram, however, they were too blue in their Z-J colour for their place on the sequence. Out of the remaining objects agreement is found with the proper motion measurements as calculated by Bihain et al. (2006) for PLIZ 28, which is believed to be a member of the cluster. There is also agreement with Bihain et al. (2006) over their candidates BRB 13 and BRB 19 that they are not a proper motion members of the cluster, however, there is disagreement with their proper motion measurement for BRB 19. It is also found that PLIZ 5 is a non member of the cluster - i.e. its proper motion measurement is not within 14 mas yr^{-1} of the cluster proper motion value. PLIZ 14 and 26 also appear to not be proper motion members of the cluster, as well as not having met the prior selection criteria. PLIZ 19, 20, 34 and 36 are also not proper motion members of the cluster. However, this means there is disagreement with Moraux et al. (2003), over the object PLIZ 20. They find a proper motion of 25.6±7.3, -44.7±7.4 mas yr^{-1} for it. The newly calculated proper motion measurement is 0.88± 15.86, -0.92±8.42 mas yr^{-1}. It is possible that this object has been adversely affected by its position on the edge of one of the WFCAM chips, thus reducing the number of reference stars used to calculate its proper motion. An alternative method of measuring the proper motion using all

the objects on the same chip and taking into account radial distortion produced a measurement of 19.14±11.06, -28.989±11.94 mas yr^{-1}. This value does meet the proper motion selection criteria and it is suggested that PLIZ 20 is likely to be a member. PLIZ 26 was found to have a proper motion measurement of 35.73±9.00, -25.83±6.96 mas yr^{-1}, which did not fall within 14 mas yr^{-1} of the cluster, and also missed the selection made with the wider circle (21 mas yr^{-1}) as well. It is found that PLIZ 2, 3, 6, 31 and 35 are all proper motion members of the cluster. In addition to this, 2 brighter new candidate members to the cluster are identified. These objects are bright enough to have appeared in previous surveys, and in the UKIDSS GCS. This work has identified 2 fainter new members to the cluster, and 5 objects selected using the ZJ photometry only in addition to the two brighter objects. All of the objects identified as cluster members in this work are presented in tables 4.5 and 4.6. The most interesting result of this work is the seven faintest objects in the aforementioned tables. These objects are all on the L to T transition sequence.

Deep H band imaging was also undertaken for two WFCAM tiles, 1 and 4, (see figure 4.1). These tiles were observed at the same time as the J band imaging, and were observed under the same conditions, but with the exception that microstepping was not used - it was not necessary to obtain very accurate astrometry for these pointings as they were not to be used for proper motion measurements. These data were reduced using the same pipeline as the J band data, but the photometry and object detection software used a core radius of 2.5 pixels in this case, to take into account the fact that microstepping was not used. Fortunately these tiles also covered the faintest, previously undiscovered Pleiades candidates, PLZJ 23 and PLZJ 93, as well as two of the candidates selected from the ZJ data only, PLZJ 721 and 235.

The UKIDSS GCS has also covered the entire area at J, H and K. The UKIDSS data are reduced using the same pipeline as the WFCAM data (see Dye et al. 2006 for details of the pipeline).

K band photometry for the faintest object selected using all the photometry (PLZJ 93) was obtained, using UFTI on UKIRT in service time. The data were taken in photometric conditions with seeing of <1.1" on the night of 09/09/2006 . A five point dither pattern was used for the

Table 4.5: Name, coordinates and proper motion measurements for the new members of the cluster. Previously discovered members also also have their other known names listed.

Name	Alternate name	RA	dec	$\mu_\alpha \cos\delta$	μ_δ
		J2000.0		mas yr^{-1}	
PLZJ 29	BRB4	03 44 23.23	+25 38 45.11	23.40±8.24	-48.51±6.34
PLZJ 56		03 44 53.51	+25 36 19.46	19.68±7.34	-35.63±5.29
PLZJ 45	BRB8	03 52 58.2	+24 17 31.57	19.72±4.95	-42.37±7.44
PLZJ 50		03 43 55.98	+25 36 25.45	13.48±8.24	-35.65±5.38
PLZJ 60	CFHT-PL-10	03 44 32.32	+25 25 18.06	16.93±7.76	-43.15±5.72
PLZJ 78	PLIZ2	03 55 23.07	+24 49 05.18	19.72±10.06	-29.74±10.45
PLZJ 46	PLIZ3, BRB11	03 52 67.20	+24 16 01.00	19.55±5.15	-42.58±7.57
PLZJ 9	PLIZ6,BRB9	03 53 55.09	+23 23 36.38	24.13±13.83	-50.10±22.71
PLZJ 11	PLIZ20	03 54 05.33	+23 33 59.71	9.14±11.06	-28.98±11.94
PLZJ 77	PLIZ28,BRB18	03 54 10.04	+23 17 52.28	12.01±14.59	-51.60±15.84
PLZJ 21	PLIZ31	03 51 47.65	+24 39 59.18	17.84±9.41	-44.92±8.03
PLZJ 10	PLIZ35,BRB15	03 52 31.19	+24 46 29.61	15.84±8.88	-49.34±6.24
PLZJ 4	BRB21	03 54 10.25	+23 41 40.67	29.74±13.17	-38.46±8.88
PLZJ 61	BRB22	03 44 31.27	+25 35 14.97	25.82±7.89	-40.21±8.47
PLZJ 32	BRB27	03 44 27.27	+25 44 41.99	25.03±11.52	-38.65±23.46
PLZJ 37	BRB28	03 52 54.92	+24 37 18.85	18.13±11.53	-48.68±11.38
PLZJ 23		03 51 53.38	+24 38 12.11	20.75±10.51	-50.05±9.96
PLZJ 93		03 55 13.00	+24 36 15.8	13.11±14.36	-33.77±12.97
PLZJ 323		03 43 55.27	+25 43 26.2	29.87±12.05	-39.37±11.70
PLZJ 721		03 55 07.14	+24 57 22.34	19.18±22.23	-40.70±12.38
PLZJ 235		03 52 32.57	+24 44 36.64	20.92±12.16	-45.84±11.75
PLZJ 112		03 53 19.37	+24 53 31.85	8.56±14.08	-34.59±19.99
PLZJ 100		03 47 19.19	+25 20 53.3	20.23±14.27	-37.28±23.82

Table 4.6: Name, coordinates, I, Z, J, H and K magnitudes for the members to the cluster. All of the J, H and K photometry is on the MKO system.

Name	RA	dec	I	Z	J	H	K
		J2000.0					
PLZJ 29	03 44 23.23	+25 38 45.11	17.005 ± 0.001	16.163 ± 0.001	14.732 ± 0.001	14.132±0.004	13.744±0.004
PLZJ 56	03 44 53.51	+25 36 19.46	17.012 ± 0.001	16.351 ± 0.001	15.250 ± 0.001	14.650±0.005	14.342±0.006
PLZJ 45	03 52 58.2	+24 17 31.57	17.101 ± 0.001	16.417 ± 0.001	15.247 ± 0.001	14.614±0.005	14.251±0.006
PLZJ 50	03 43 55.98	+25 36 25.45	17.239 ± 0.001	16.496 ± 0.001	15.268 ± 0.001	14.693±0.006	14.319±0.006
PLZJ 60	03 44 32.32	+25 25 18.06	17.592 ± 0.001	16.810 ± 0.001	15.460 ± 0.001	14.884±0.007	14.465±0.006
PLZJ 78	03 55 23.07	+24 49 05.18	17.719 ± 0.001	16.948 ± 0.001	15.574 ± 0.001	14.963±0.007	14.552±0.007
PLZJ 46	03 52 67.20	+24 16 01.00	17.742 ± 0.001	16.945 ± 0.001	15.583 ± 0.001	14.966±0.007	14.503±0.008
PLZJ 9	03 53 55.09	+23 23 36.38	17.752 ± 0.001	16.804 ± 0.001	15.222 ± 0.001	14.548±0.005	14.054±0.005
PLZJ 11	03 54 05.33	+23 33 59.71	19.571±0.004	18.563±0.004	16.691±0.005	15.980±0.016	15.436±0.016
PLZJ 77	03 54 10.04	+23 17 52.28	20.760 ± 0.010	19.728 ± 0.010	17.647 ± 0.010	16.789±0.031	16.131±0.030
PLZJ 21	03 51 47.65	+24 39 59.18	20.944±0.014	19.762±0.013	17.575±0.012	16.774±0.026	16.089±0.028
PLZJ 10	03 52 31.19	+24 46 29.61	21.293±0.018	20.292±0.016	18.181±0.022	17.118±0.041	16.506±0.0416
PLZJ 4	03 54 10.25	+23 41 40.67	21.322 ± 0.010	20.215 ± 0.013	18.171 ± 0.010	17.141±0.045	16.377±0.039
PLZJ 61	03 44 31.27	+25 35 14.97	22.043 ± 0.030	20.782 ± 0.026	18.298 ± 0.020	17.393±0.059	16.657±0.04
PLZJ 32	03 44 27.27	+25 44 41.99	22.235 ± 0.040	20.962 ± 0.029	18.871 ± 0.030	17.793±0.094	16.950±0.070
PLZJ 37	03 52 54.92	+24 37 18.85	22.452 ± 0.05	21.216 ± 0.041	18.839 ± 0.030	17.742±0.071	16.921±0.058
PLZJ 23	03 51 53.38	+24 38 12.11	23.541 ± 0.140	22.187 ± 0.112	19.960 ± 0.100	19.362±0.100	18.510±0.030

				Table 4.6: Continued			
Name	RA	dec	I	Z	J	H	K
		J2000.0					
PLZJ 93	03 55 13.00	+24 36 15.8	24.488 ± 0.370	22.592 ± 0.164	19.968 ± 0.080	19.955±0.100	19.420 ±0.100
PLZJ 323	03 43 55.27	+25 43 26.2	-	21.597±0.054	19.613±0.076	-	-
PLZJ 721	03 55 07.14	+24 57 22.34	-	22.195±0.092	20.248±0.116	20.417±0.123	-
PLZJ 235	03 52 32.57	+24 44 36.64	-	22.339±0.115	20.039±0.112	20.245±0.127	-
PLZJ 112	03 53 19.37	+24 53 31.85	-	22.532±0.116	20.281±0.143	-	-
PLZJ 100	03 47 19.19	+25 20 53.3	-	23.563±0.373	20.254±0.114	-	-

images, and a standard star was also taken as a calibration frame. I reduced the data using the ORAC-DR pipeline, which dark subtracted, and flat fielded the images, using a sky-frame flat field created from the dithered frames. Aperture photometry was performed on the images using SExtractor and the standard star UKIRT FS115 (Casali & Hawarden, 1992) was used as the calibration. A K band magnitude of 19.42 ± 0.1 was calculated. This magnitude was checked using the 2MASS sources in the field, however, there were only 3 of them as the UFTI field of view is small, and they had to be transformed onto the MKO system from the 2MASS K_S filters using Carpenter (2001). Despite this, the magnitudes agreed to within the errors.

The K band photometry for PLZJ 23 was obtained on the night of 05/03/2007 using the LIRIS on the WHT in service time, using a nine point dither pattern in seeing of ≈ 0.9" with the K_S filter. The data were reduced using the IRAF package imcombine to median combine the individual images to create a sky flat field, before being stacked using xmosiac. The xmosaic routine removes bad pixels using a user defined bad pixel mask (one was created to remove a line of bad pixels using badpiximage), removed cosmic ray hits and also sky subtract the images as well as stacking them. The resultant stacked image was then astrometrically calibrated using ≈ 6 2MASS sources in the field and the STARLINK package ASTROM in fit to star positions mode running in Gaia. The object detection was done using SExtractor in Gaia, and a photometric zero point was calculated using the 15 common sources in the image and 2MASS. A zero point of 25.46734 was calculated for the image. This corresponds to a K_S magnitude of 18.417 ± 0.03. The colour transforms presented by Carpenter (2001) were used to calculate the K band magnitude from the K_S magnitude.

Thus I, Z, J, H and K band photometry for the majority of the Pleiades candidates is known. However, H or K band photometry is still needed for PLZJ 323, 721, 235, 112 and 100, (see table 4.6). Figures 4.7 and 4.8 show the K, J-K and H, J-H, colour magnitude diagrams, together with the NEXTGEN (Baraffe et al., 1998) and DUSTY (Chabrier et al., 2000) models for the Pleiades age of 120 Myr (Stauffer et al., 1998). The candidate members listed in table 4.6 are also plotted in figures 4.3 and 4.4 for clarity. In both of these diagrams the M dwarf tail, the redward L dwarf sequence and the L to T blueward transition sequence are clear. The

L-T transition sequence of course only has two objects plotted on it on figure 4.7 as there is no K band photometry for the ZJ candidates. The K, J-K diagram gives the best differentiation between the sequences. The redward L sequence in this diagram agrees with that found by Lodieu et al. (2007) derived from a much greater area of the Pleiades by the UKIDSS GCS. However, the GCS is not sensitive enough to see the L-T blueward transition sequence. The K, J-K diagram also shows the separation between single and binary dwarfs quite clearly. Note that the DUSTY theoretical track is too flat compared to the empirical sequence, in figures 4.7 and 4.8.

PLZJ 23, 93, 721 and 235 have J-H colours of 0.60, 0.00, -0.17 and -0.21 respectively. Comparing these colours with the spectral type colour relations of field dwarfs described in Leggett et al. (2002), yields estimated spectral types of T1.5, T4.5, T6 and T6 respectively. PLZJ 93 has J-K=0.60 which gives a spectral type of T3, which is consistent with the spectral type derived from the J-H colour (T4.5), within the errors. An H-K colour can be calculated for this dwarf of 0.6, although in this case the H-K colour is not a good choice for spectral typing, as H-K=0.6 covers a range of spectral types from L1 to T3 (Chiu et al., 2006). The Z-J colour is also not a good choice of colour for measuring spectral types until the later T dwarfs (>T2, Hawley et al. 2002) as it too remains constant. PLZJ 23 has J-K=1.45, which gives a spectral type of between L8 and T1. The H-K colour for this dwarf is 0.85. It may thus be assumed that PLZJ 23 has a spectral type between L8 and T1.5, and likewise that PLZJ 93 has a spectral type of between T3 and T5 to take into account the photometric errors. It should be noted that the Z band quoted in Hawley et al. (2002) is for the Sloan filter system, and so for this reason it was not chosen to spectral type these objects. The J-H and J-K colours give the best estimate available of spectral types. These spectral types have been estimated using the J-H colours. Two of the three candidate members without H band photometry PLZJ 112 and 100 have fainter J magnitudes than PLZJ 23 and 93, and so it is likely that they are also T dwarfs. PLZJ 323 is brighter and is therefore probably a late L dwarf. Indeed the faintest candidate at Z, PLZJ 100, may be a very late T dwarf, but this assumption is made using its Z-J colour, which is very red. Using J magnitudes and the COND models of Baraffe et al. (2003) for 120 Myr (the DUSTY models are no longer appropriate for calculating masses for

90
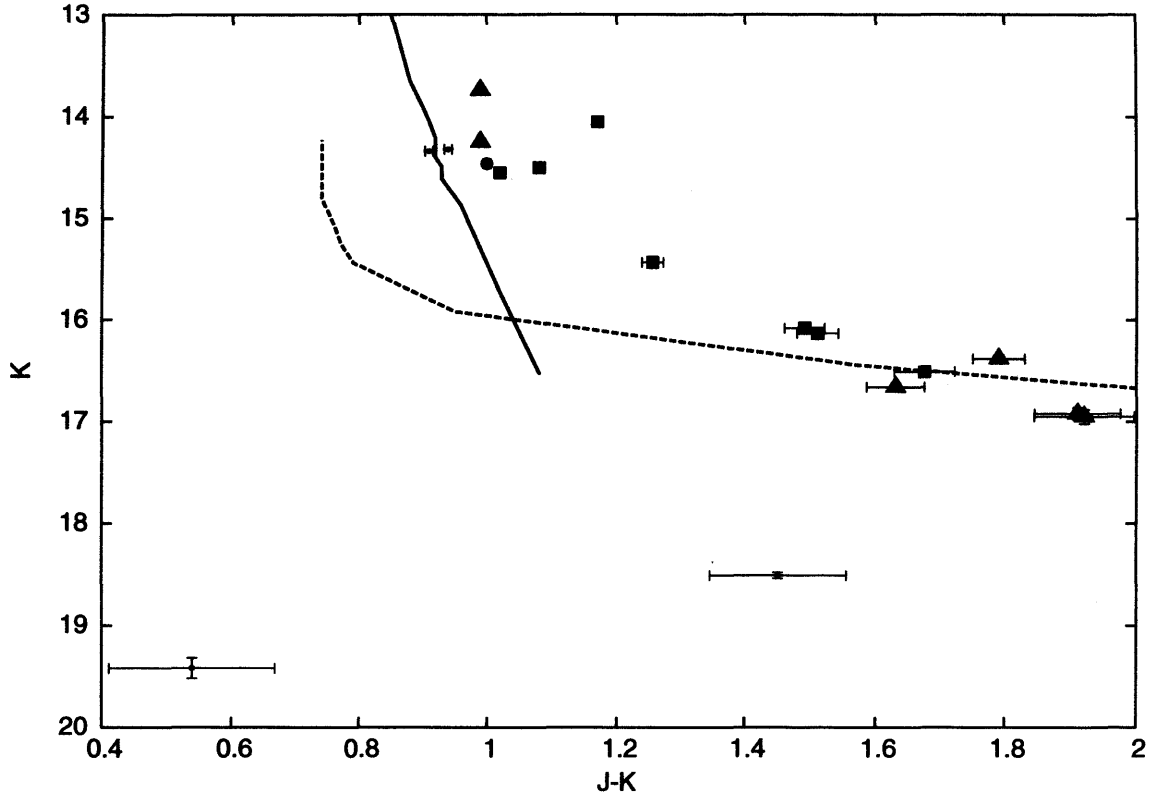
Figure 4.7: The K, J-K colour-magnitude diagram for the candidate cluster members. The solid line is the NEXTGEN model of Baraffe et al. (1998), and the dotted line is the DUSTY model of Chabrier et al. (2000). The filled squares are the candidates identified by Moraux et al. (2003), the filled triangles are the candidates identified by Bihain et al. (2006), the object enclosed by the open circle is CFHT-PL-10 identified by Bouvier et al. (1998). The objects marked by small points are the new candidate members. One of the T dwarf candidates, PLZJ 93, is found to the bottom of the plot, with a J-K of ≈ 0.6. PLZJ 23 is also present with a J-K of 1.45. It should be noted that these objects are on the L-T transition track and so have moved off the DUSTY model, but have not yet reached the region where the COND model is applied.
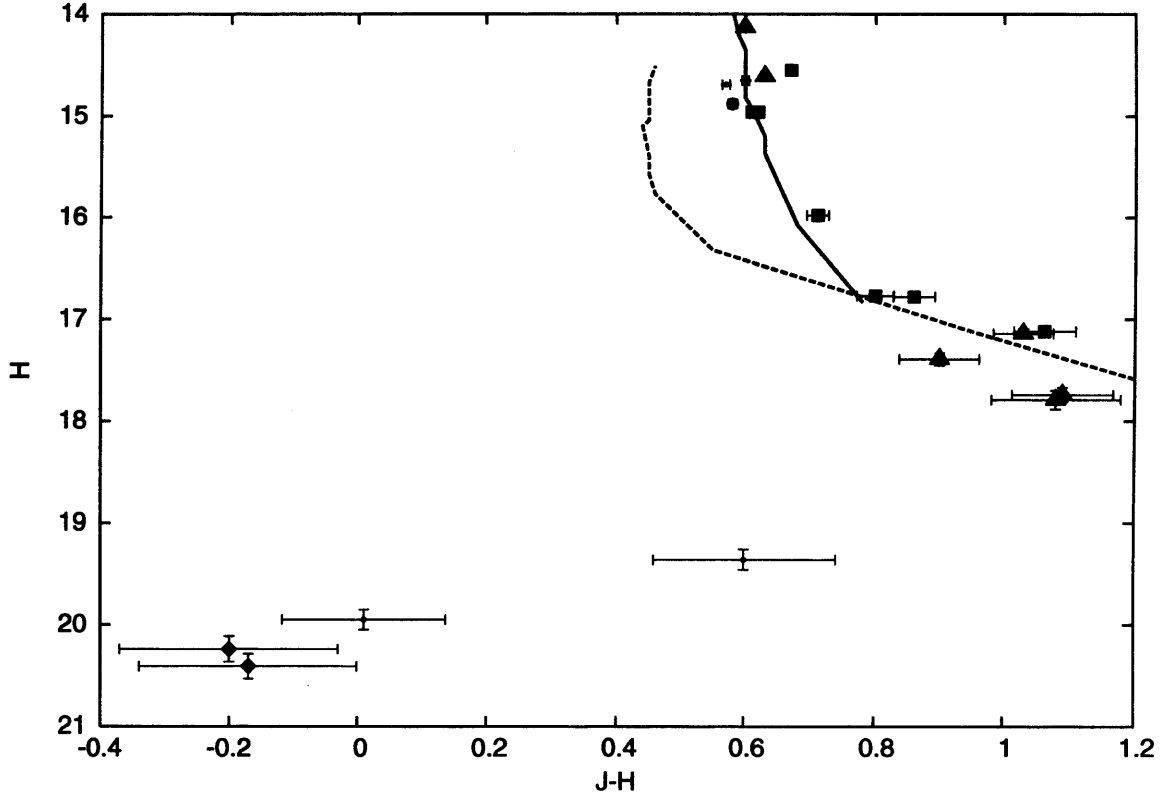
Figure 4.8: The H, J-H colour-magnitude diagram for the candidate cluster members. The filled squares are the candidates identified by Moraux et al. (2003), the filled triangles are the candidates identified by Bihain et al. (2006), the object enclosed by the open circle is CFHT-PL-10 identified by Bouvier et al. (1998). The objects marked by small points are the new candidate members.The filled diamonds are the two candidates with H magnitudes selected from the ZJ data only. The solid line is the NEXTGEN model of Baraffe et al. (1998), and the dotted line is the DUSTY model of Chabrier et al. (2000). It should be noted that these objects are on the L-T transition track and so have moved off the DUSTY model, but have not yet reached the region where the COND model is applied.

objects this faint in the Pleiades), and calculate masses of $\approx$ 11 M_{Jup} for PLZJ 23, 93, 323, 721, 235, 112 and 100. More photometry in the H and K bands is clearly needed to improve and extend these estimates of the spectral types.

Figures 4.8 and 4.7 are the first to show the L to T transition sequence for any cluster of known age. Until now this sequence has only been recognised for field dwarfs of unknown age. When completed with further H and K photometry this sequence will provide a good means to test the latest theoretical models. *Spitzer* time has been successfully applied for, to measure these objects in the mid-IR and I have been successful in obtaining Gemini time (using the Near InfraRed Imager) to image these objects in the methane filters. These data will hopefully prove or disprove cluster membership of these candidates.

4.6 Mass spectrum

To calculate the mass spectrum, the sample was divided into single dwarfs or single dwarfs with possible low mass companions and dwarfs that are close to 0.75 magnitudes above the single star sequence in the K, J-K colour magnitude diagram. The latter were assumed to be equal mass binaries and counted as dwarfs with masses the same as a dwarf on the single dwarf sequence below them. From figures 4.3, 4.4, 4.7, and 4.8 it can be seen that there are 2 such binaries all with J-K $\approx$ 1. Dwarfs with J-K <1.2 were assigned masses using their H magnitudes and the NEXTGEN models (Baraffe et al., 1998). For 1.2<J-K<2.0 the DUSTY models (Chabrier et al., 2000) and the J-H colour was used to assign a mass. Finally the T dwarf masses were calculated from their J magnitudes and the COND models (Baraffe et al., 2003). The masses were binned into three mass intervals, covering the low, medium and high mass ranges and the numbers per bin are weighted by the probabilities of membership calculated using the annulus, and the bin width has been taken into account. The candidate members with negative probabilities are obviously omitted from the mass spectrum. The resultant mass spectrum is shown in figure 4.9. The errors are Poissonian. Clearly the statistics are very poor, due to the small number of objects being dealt with. Using linear regression

the data have been fitted to the relationship $dN/dM \propto M^{-\alpha}$, and a value of $\alpha = 0.35 \pm 0.31$ is calculated. This is lower but still in agreement with values presented in the literature (within 1σ), but the error on this value is large, and the statistics are poor due to the small numbers involved. If it is taken into account the fact that the last mass bin is only 50% complete (using tables 4.2 and 4.6), then the lowest mass bin can be increased by 50% to compensate. If these compensated data are then fitted, a value for α of 0.62 ± 0.14 is derived, which is in agreement with the literature. Alternatively, if this final low mass bin is discounted as being incomplete it can be simply omitted from the fit. In this case a value for α of 0.86 is calculated, although the errors are by definition zero as two points are being with a straight line (ie using two parameters). Only the mass spectrum for the cluster in the area and magnitude surveyed is shown. This is to avoid trying to take into account biases caused by some areas being better studied than others, and also because there are only a maximum of 9 objects to be added to the mass function, 7 of which have low probabilities of membership and small masses, and so are not likely to have a considerable effect on previous results from larger samples. This mass spectrum appears to be rising towards the lowest masses, but this is not statistically significant due to the large error bars.

4.7 Conclusions

A number of L dwarf candidates in the Pleiades have been confirmed via this study. However, the main result is the discovery of one L and six T dwarf Pleiads of masses ≈ 10 M_{Jup}, all below the 13 M_{Jup} deuterium burning limit that is often used, somewhat artificially as the upper bound for planetary masses. Planetary mass brown dwarfs have, of course, been claimed in the Orion nebula (Lucas & Roche, 2000) and in the σ-Ori cluster (Zapatero Osorio et al., 2002). These clusters both have very young ages and may also have a spread of ages (Béjar et al., 2001), making mass determinations somewhat uncertain. Lodieu et al. (2006, 2007) have also found planetary mass brown dwarfs in the Upper Scoripus Association which has an age of 5 Myr (Preibisch & Zinnecker, 2002). At very young ages the theoretical models may have significant errors when used to assign masses Baraffe et al. (2002). This result is the
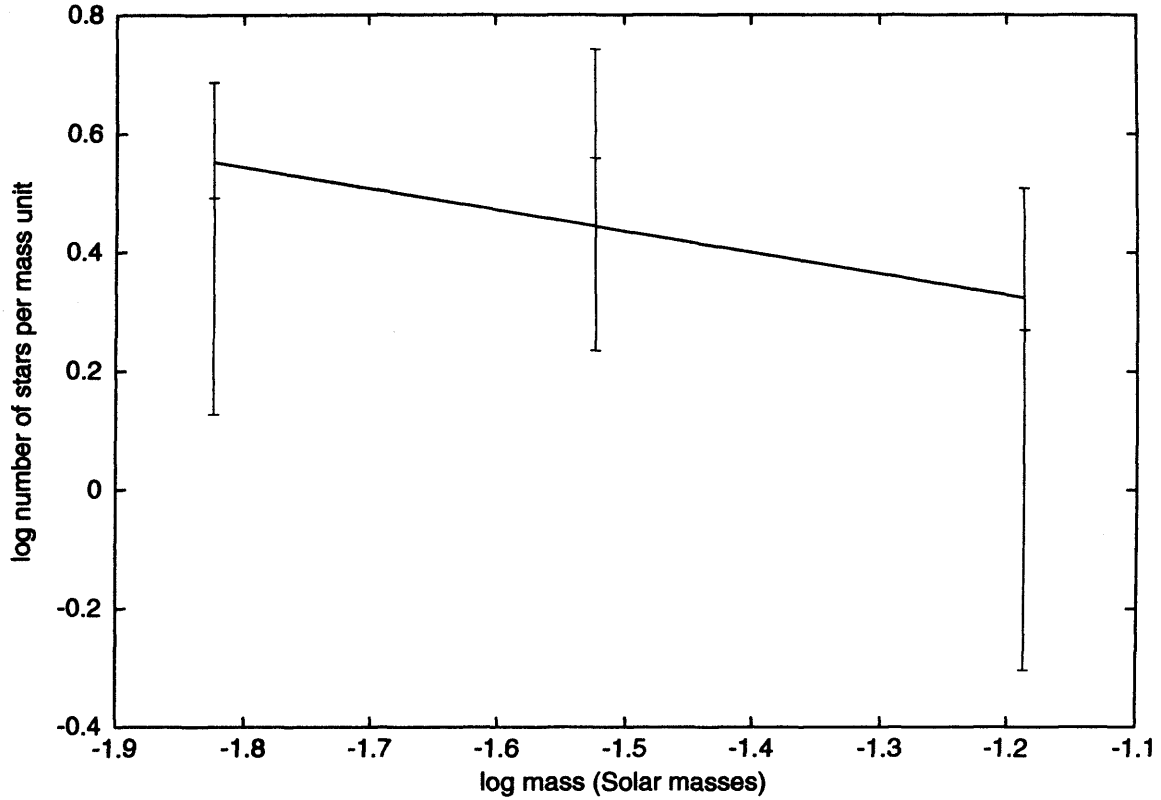
Figure 4.9: The mass spectrum for the Pleiades candidate members. The mass bin is in units of $M_\odot$. The solid line is the fit to the data, (α=0.35±0.31).

first detection of planetary mass objects in a mature cluster whose age is well established. It strengthens the case that the star formation process can produce very low mass objects. Also, if follow up photometry is successful, then the cluster will also be the first to show the first H, J-H and K, J-K L to T dwarf sequence.

4.8 Summary

This chapter has briefly discussed the Pleiades cluster and previous searches for brown dwarf members, before presenting the infrared survey on which this chapter is based. This survey was cross-correlated with a new reduction of an optical survey taken in 2000. The observing conditions have been discussed, as have the methods of data reduction and calibration. The

method used to estimate the completeness of the survey have also been discussed. This chapter has also included a discussion of how candidate members of the cluster have been selected using the I, I-Z and Z, Z-J colour magnitude diagrams, as well as a description of how the proper motion measurements were calculated. Using these methods, 9 new L and T dwarf proper motion and photometry selected members to the cluster have been discovered. 7 of these objects are of very low mass, ≈ 11 M_{Jup} as estimated using the COND models (Baraffe et al., 2003). Using follow up photometry from the UKIDSS GCS and UFTI and LIRIS K magnitudes taken in service time, estimations of spectral types have been made, and 5 of these 7 objects are likely to be T dwarfs, the first to be discovered in a mature star cluster. The mass spectrum was calculated for the cluster members found in the survey, and a value of α has been calculated which is in rough agreement with the literature, although the small number of objects used causes large Poissonian errors. The survey has been successful in discovering "planetary mass" Pleiads, which was its aim, although more photometry is required before more precise spectral types can be estimated. Due to the faint magnitudes of these objects, it is unlikely that spectra will be observed. *Spitzer* observations in the mid-IR and methane imaging would at least allow a confirmation of the T dwarf status of these objects.

Chapter 5

Melotte 111 open star cluster

5.1 Introduction

This chapter will focus on the open star cluster Melotte 111 (Coma Berenices) and a search for new candidate members to the cluster. These candidates come from two sources - firstly from the USNOB1.0, UCAC2 and 2MASS catalogues and were selected via their proper motion, and secondly from an iZ imaging survey of the centre of the cluster and subsequent follow up imaging and spectroscopy. The chapter will detail the methods used to reduce and analyse the data as well as containing a discussion of the findings.

5.1.1 Melotte 111

A survey of the Melotte 111 open star cluster (Coma Berenices, RA = $12^h23^m00^s$, Dec = +26°00'00", J2000.0) was performed to extend the knowledge of its luminosity function towards the hydrogen burning limit.

As has been previously discussed, many young open star clusters have been studied, and their mass functions defined, particularly at the lower mass end. Deep surveys of older open clusters

have been sorely neglected, due to their likely lack of low mass members, with the exception of the Hyades. Despite the interest in the Hyades, very few low mass and substellar members of the cluster have been found. This has meant that a stringent upper limit has been put on the Hyades mass function in the substellar regime, and the likely reasons for this deficit in substellar members explained (Gizis et al., 1999; Dobbie et al., 2002b). N-body simulations (e.g. de La Fuente Marcos & de La Fuente Marcos 2000) indicate that less than a fifth of the original substellar members should remain tidally bound to a cluster of this age. The lack of substellar members is put down to the ejection of these objects over time - in other words the dynamical evolution of the cluster has allowed them to escape the tidal radius. This scenario, while likely, does not rule out the possibility that the Hyades cluster formed in a way that did not favour the formation of substellar objects. As yet there is no answer to the question "where are the brown dwarfs in the Hyades?", however, in an endeavour to answer this question, other older clusters are beginning to be studied, such as Praesepe and Melotte 111.

Melotte 111 is the second closest open cluster to the Sun and Hipparcos measurements place it at d=89.9±2.1 pc (van Leeuwen, 1999), in agreement with older ground based estimates (e.g. d=85.4±4.9 pc, Nicolet 1981). Furthermore, foreground extinction along this line of sight is low, E(B-V)≈0.006±0.013 (Nicolet, 1981). The metallicity of the cluster is also relatively well constrained; spectroscopic examination of cluster members reveals it to be slightly metal poor with respect to the Sun. For example, Cayrel de Strobel (1990) determines [Fe/H] =-0.065±0.021 using a sample of eight F, G and K type associates, whereas Friel & Boesgaard (1992) determine [Fe/H]=-0.052±0.047 from fourteen F and G dwarf members. While estimates of the age of Melotte 111 vary considerably from 300 Myr to 1 Gyr, (e.g.Tsvetkov 1989), more recent determinations, based on fitting model isochrones to the observed cluster sequence, cluster around 400-500 Myr (e.g. Bounatiro & Arimoto 1992; Odenkirchen et al. 1998). Thus Melotte 111 is probably marginally younger than the 625 Myr old Hyades.

Despite being of similar age and distance to the Hyades, Melotte 111 has not been studied to the same extent. This is because Melotte 111 is projected over a large area of sky (~100 sq. deg.) and contains considerably fewer bright stellar members than the Hyades. For example, Odenkirchen et al. (1998) determines the cluster tidal radius to be ~5-6 pc but finds

only 34 kinematic members down to V=10.5 within a circular area of radius 5° centred on the cluster. They estimate the total mass of Melotte 111 to lie in the range 30-90 $M_\odot$, which can be compared to estimates of 300-460 $M_\odot$ for the mass of the Hyades (e.g.Oort 1979; Reid 1992). Unlike the Hyades, Melotte 111 is not known to contain any white dwarfs. Additionally, the small proper motion of its members (μ_α=-11.21 ±0.26 mas yr^{-1}, μ_δ=-9.16 ±0.15 mas yr^{-1}, van Leeuwen 1999) means that proper motion alone is not a suitable means by which to discriminate the members of Melotte 111 from the general field population. Fortunately, the convergent point for the cluster is sufficiently distant at $\alpha = 6^h40^m31.2^s$, $\delta = -41°33'00''$ (J2000) (Madsen et al., 2002), that it is expected that all the cluster members will have essentially the same proper motion.

5.2   Previous studies

Over the last 70 years there have only been a handful of in depth studies of Melotte 111 and its members. Brief descriptions of the most relevant are given below.

1. Trumpler (1938) used proper motion, spectrophotometric and radial velocity measurements to identify 37 probable members, m_p<10.5, in a circular region of 7° diameter centred on the cluster. This survey was limited to only the very brightest members of Melotte 111- stars with a photographic magnitude brighter than 10.5. This study was the first to determine that the stars in Melotte 111 actually formed a cluster and had a common motion.

2. A significant additional number of fainter candidate members were identified by Artyukhina (1955) from a deep (m_P<15) proper motion survey of ~7 sq. degrees of the cluster.

3. Argue & Kenworthy (1969) performed a photographic UBVI survey of a circular field, 3.3° in diameter, to a limiting depth of m_p=15.5. They rejected all but 2 of Artyukhina's

candidates with $m_p>11$ but identified a further 2 faint objects with photometry and proper motion which they deemed to be consistent with cluster membership.

4. Subsequently, Deluca & Weis (1981) obtained photoelectric photometry for 88 objects ($V>11$), drawn from these two previous studies. They concluded that only 4 stars, 3 of which were listed in Argue & Kenworthy (1969) as probable members, had photometry and astrometry consistent with association to Melotte 111.

5. More recently, Bounatiro (1993) searched an area of $6°\times6°$ centred on Melotte 111, using the AGK3 catalogue, and identified 17 new candidate members ($m_p<12$).

6. Following the study of Bounatiro (1993), Randich et al. (1996) identified 12 new potential low mass members ($V\approx11.5\text{-}16$) from a ROSAT PSPC survey of the cluster, however, a detailed follow-up study concluded that none of these are in fact associates of Melotte 111 (García López et al., 2000).

7. Odenkirchen et al. (1998) used the Hipparcos and ACT catalogues to perform a comprehensive kinematic and photometric study of 1200 sq. degrees around the cluster centre complete to a depth of $V\approx10.5$. They found a total of ~ 50 kinematic associates which appear to be distributed in a core-halo system. The core, which is elliptical in shape with a semi-major axis of $1.6°$, is dominated by the more massive members while the halo contains proportionately more low mass associates. They also found evidence of an extra-tidal 'moving group' located in front of the cluster in the context of its motion around the Galaxy. However, from a subsequent spectroscopic study, Ford et al. (2001), concluded that approximately half of the moving group were not associated with the cluster.

5.3 Method

Combining proper motion measurements and photometry is a widely accepted method of determining cluster membership for stars (e.g. Hambly et al. 1993; Reid 1992). Using the USNOB1.0 survey for robust (accurate to 2 mas yr^{-1}) proper motion measurements, and 2MASS for IR photometry, 50 sq. degs of the sky centred on Melotte 111 were surveyed. The UCAC2 catalogue was also used to illustrate the proper motion vector diagram for the cluster (figure 5.1), as the proper motion measurements are not quantised like those from the USNOB1.0 which results in many data points falling on top of one another (see Chapter 3 for the survey description and references). The photometry from the UCAC2 catalogue is, however, not sufficiently deep (≤16) to use the proper motion measurements for the selection of fainter candidate members. The method used is detailed below.

1. A circular area of radius 4 degrees centred on the cluster was extracted from the USNO B1.0 catalogue.

2. Stars were selected according to the criterion $(\mu_\alpha - X)^2 + (\mu_\delta - Y)^2 < 100$, where X = -11.21 and Y = -9.16, i.e. to lie within 10 mas yr^{-1} of the Hipparcos determined value for the proper motion of Melotte 111. This procedure was initially repeated for X = -11.21, Y = +9.16 and X = +11.21, Y = -9.16, to obtain two control samples (see figure 5.1). Two more control samples were later extracted from two further circular regions of USNO B1.0 data. These data had a similar galactic latitude to the cluster but were offset by 10° from the centre of Melotte 111. Stars were selected from these latter regions by applying the first proper motion criterion above. The known members have errors, or velocity dispersions amounting to about ± 2.0 km s^{-1}, (Odenkirchen et al., 1998). This corresponds to a proper motion of ± 4.8 mas yr $^{-1}$, and the USNO B1.0 catalogue astrometry errors are small - typically less than ± 5 mas yr $^{-1}$ for the studied stars. The USNO B1.0 proper motion errors in tables 5.1 and 5.2 are quantised in units of 1 mas yr^{-1} and a zero error thus indicates an error of less than 0.5 mas yr $^{-1}$. If a bounding circle of 10 mas yr was selected, and the total quadratically added error is 7 mas yr^{-1},
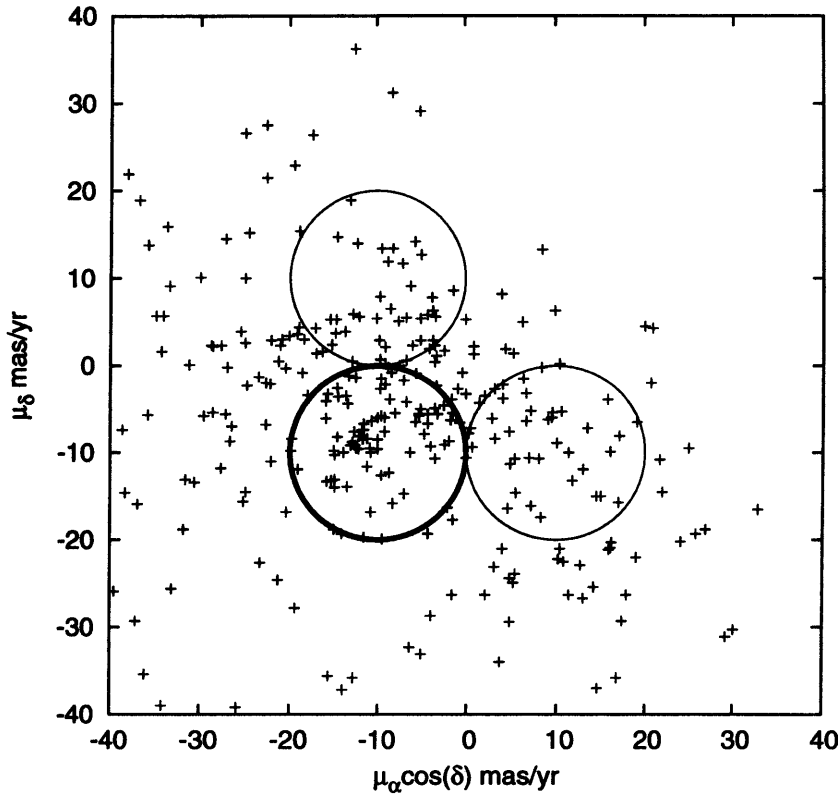
Figure 5.1: Plot of the UCAC2 (Zacharias et al., 2004) proper motions for 4 square degrees of the cluster centre. The thick line borders the cluster proper motion selection, and the thin lines, the controls. The shallower UCAC catalogue is used here for illustration as the USNO B1.0 catalogue only provides quantised values of 2 mas yr^{-1}.

all stars have been selected to a completeness level of 1.4 σ, which means the survey is complete to $\approx 90\%$.

3. Stars passing the above sets of criteria were cross-referenced against the 2MASS point source catalogue using a match radius of 2 arcseconds.

4. Subsequently the sample of candidate cluster members and the four control samples were plotted in the K_S, $J-K_S$ colour-magnitude diagram as illustrated in Figure 5.2.

A cursory glance at the colour-magnitude diagrams in figure 5.2 reveals that this control region method appears to be rather successful in finding new associates of Melotte 111. An obvious cluster sequence can be seen extending to $K_S \approx 12$ beyond which it is overwhelmed by field star contamination. This meant that to perform a quantitative selection of candidate members it was necessary to restrict the selection to objects with $K_S < 12$. As a guide to the location of the cluster sequence the previously known members and a 400 Myr NEXTGEN isochrone for solar metallicity (Baraffe et al., 1998), scaled to the Hipparcos distance determination for Melotte 111 were used. In the magnitude range where they overlap, the previously known cluster members of the single star sequence, congregate around the theoretical isochrone (all previously known cluster members are listed in table 5.1). Furthermore, the model isochrone appears to continue to follow closely the excess of objects in the top panel of figure 5.2, relative to the bottom panel, suggesting that it is relatively robust in this effective temperature regime.

The location of the theoretical isochrone at $J-K_S < 0.8$ is insensitive to the uncertainties in the age of the cluster. The cluster would have to be much younger to significantly shift the isochrone either to the blue or red. The bulk of the observed dispersion in the single star sequence here likely stems from the finite depth of the cluster (~ 0.15 mags). Nevertheless, in this colour range objects were selected which lie no more than 0.3 magnitudes below the theoretical isochrone as this ensures that all previously known cluster members are recovered (filled squares on figure 5.2). As binary members can lie up to 0.75 magnitudes above the single star sequence, only objects which also lie no more than 1.05 magnitudes above the theoretical sequence are deemed candidate members.

Redward of $J-K_S = 0.8$, the main sequence becomes very steep in this colour-magnitude diagram. Various combinations of 2MASS and USNOB1.0 photometry (e.g. colours such as R-K) were tried, in an attempt to circumvent this. However, as mentioned previously, the poorer quality of the photographic magnitudes provided by the USNOB1.0 catalogue results in a large amount of scatter in optical and IR colour-magnitude diagrams rendering them of little use for this study. Nonetheless, the finite depth of the cluster and a small error in cluster distance determination have a negligible effect in this part of the K_S, $J-K_S$, colour-magnitude
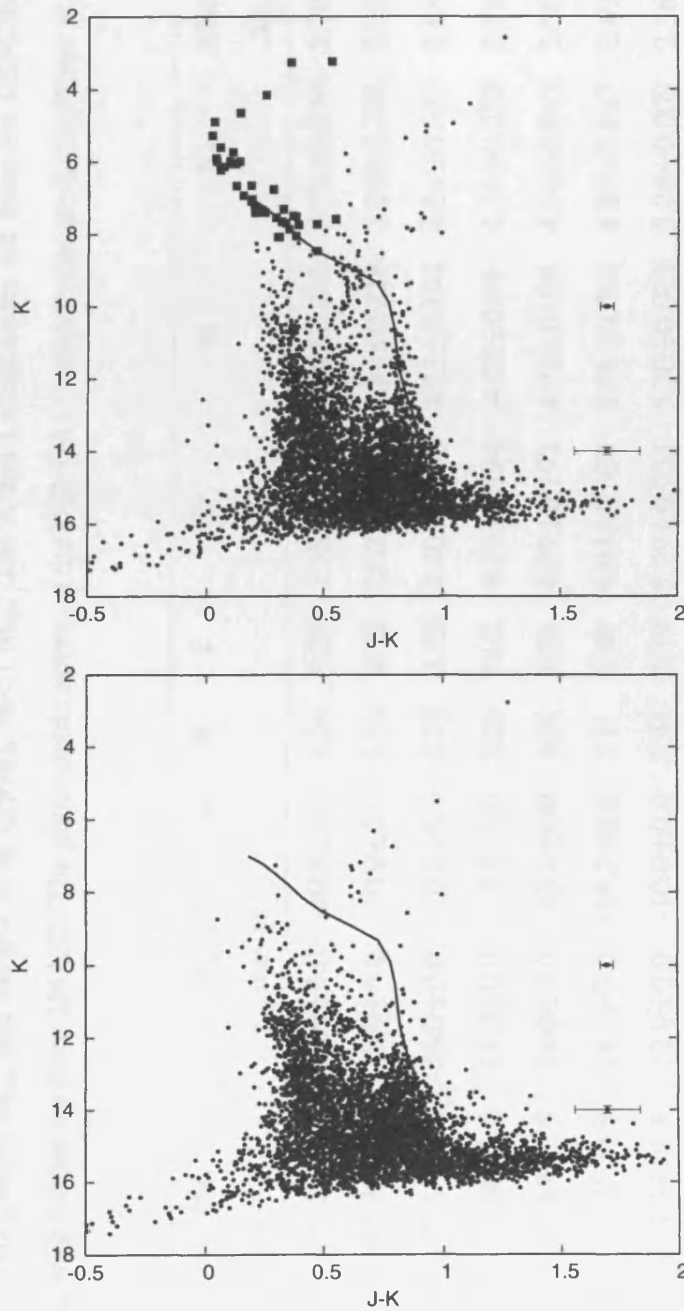
Figure 5.2: The colour-magnitude diagram for the cluster (top) and a control sample with μ_α=+11.21 μ_δ=-9.16 mas yr^{-1}(bottom). Previously known members of the cluster are high-lighted in the upper plot (solid squares). A 400 Myr NEXTGEN isochrone is overplotted from Baraffe et al. (1998); (solid line). This was converted into the 2MASS system using the transforms of Carpenter (2001).

Table 5.1: Name, coordinates, proper motion measurements, R, I, J, H and K magnitudes for the known cluster members as detailed in Bounatiro & Arimoto (1992) and Odenkirchen et al. (1998) for the area surveyed. The masses were calculated by linearly interpolating the models of Girardi et al. (2002), $M \geq 1$ $M_\odot$, and Baraffe et al. (1998), $M < 1$ $M_\odot$. The R and I magnitudes are from the USNOB1.0 catalogue and the J, H and K_S magnitudes are from 2MASS. The photometric errors on the USNOB1.0 magnitudes are 0.25 (Monet et al., 2003).

Name	RA	Dec.	μ_α	μ_δ	R	I	J	H	K_S	Mass
	J2000.0		mas yr^{-1}							$M_\odot$
BD+26 2337	12 22 30.31	+25 50 46.1	-12.0±0.0	-10.0±0.0	4.54	4.28	3.78±0.254	3.40±0.216	3.23±0.244	2.709
BD+28 2156	12 51 41.92	+27 32 26.5	-10.0±0.0	-10.0±0.0	4.55	4.20	3.62±0.296	3.36±0.218	3.26±0.286	2.709
BD+28 2115	12 26 24.06	+27 16 05.6	-14.0±0.0	-10.0±0.0	4.79	4.65	4.40±0.240	4.23±0.194	4.14±0.033	2.685
BD+24 2464	12 29 27.04	+24 06 32.1	-18.0±0.0	0.0±0.0	5.25	5.02	4.86±0.194	4.57±0.33	4.54±0.288	2.595
BD+27 2134	12 26 59.29	+26 49 32.5	-14.0±0.0	-10.0±0.0	4.91	4.88	4.79±0.192	4.72±0.013	4.64±0.019	2.568
BD+26 2344	12 24 18.53	+26 05 54.9	-14.0±0.0	-14.0±0.0	5.11	5.08	4.93±0.033	4.94±0.061	4.89±0.017	2.496
BD+25 2517	12 31 00.56	+24 34 01.8	-12.0±0.0	-10.0±0.0	5.41	5.39	5.29±0.033	5.30±0.023	5.26±0.009	2.363
BD+26 2354	12 28 54.70	+25 54 46.2	-24.0±0.0	-16.0±0.0	5.24	5.28	5.22±0.011	5.29±0.031	5.28±0.009	2.356
HD 105805	12 10 46.09	+27 16 53.4	-12.0±0.0	-12.0±0.0	5.92	5.86	5.65±0.023	5.66±0.027	5.60±0.029	2.216
BD+26 2345	12 24 26.79	+25 34 56.8	-14.0±0.0	-14.0±0.0	6.59	6.46	5.84±0.009	5.77±0.027	5.73±0.007	2.150
BD+23 2448	12 19 19.19	+23 02 04.8	-14.0±0.0	-10.0±0.0	6.14	6.04	5.94±0.013	5.96±0.015	5.90±0.013	2.057
BD+26 2326	12 19 02.02	+26 00 30.0	-14.0±0.0	-10.0±0.0	6.36	6.27	6.08±0.019	6.00±0.047	5.98±0.017	2.018
BD+25 2523	12 33 34.21	+24 16 58.7	-12.0±0.0	-10.0±0.0	6.19	6.13	6.03±0.025	5.98±0.027	5.98±0.021	2.014
BD+27 2138	12 28 38.15	+26 13 37.0	-16.0±0.0	-8.0±0.0	6.40	6.30	6.13±0.047	6.02±0.025	5.99±0.009	2.011

Name	RA	Dec.	μ_α	μ_δ	R	I	J	H	K_S	Mass
	J2000.0		mas yr^{-1}							$M_\odot$
BD+26 2343	12 24 03.46	+25 51 04.4	-14.0±0.0	-10.0±0.0	6.59	6.47	6.17±0.017	6.07±0.045	6.05±0.011	1.978
BD+26 2353	12 28 44.56	+25 53 57.5	-22.0±0.0	-18.0±0.0	6.52	6.40	6.16±0.019	6.10±0.019	6.05±0.017	1.977
BD+29 2280	12 19 50.62	+28 27 51.6	-12.0±0.0	-10.0±0.0	6.52	6.42	6.20±0.009	6.19±0.031	6.13±0.019	1.931
BD+26 2352	12 27 38.36	+25 54 43.5	-14.0±0.0	-12.0±0.0	6.57	6.48	6.28±0.015	6.22±0.023	6.22±0.009	1.879
BD+30 2287	12 31 50.55	+29 18 50.9	-12.0±0.0	-10.0±0.0	7.37	7.20	6.84±0.021	6.74±0.055	6.65±0.013	1.607
BD+25 2495	12 21 26.74	+24 59 49.2	-12.0±0.0	-10.0±0.0	7.23	7.08	6.79±0.011	6.74±0.021	6.66±0.009	1.600
BD+26 2347	12 25 02.25	+25 33 38.3	-14.0±0.0	-8.0±0.0	7.83	7.55	7.05±0.005	6.85±0.007	6.76±0.027	1.540
BD+26 2323	12 17 50.90	+25 34 16.8	-12.0±0.0	-12.0±0.0	7.66	7.47	7.08±0.007	6.98±0.019	6.92±0.009	1.451
BD+26 2321	12 16 08.37	+25 45 37.3	-12.0±0.0	-10.0±0.0	7.87	7.66	7.23±0.019	7.11±0.045	7.03±0.009	1.399
BD+28 2087	12 12 24.89	+27 22 48.3	-12.0±0.0	-12.0±0.0	7.85	7.64	7.27±0.017	7.13±0.015	7.08±0.015	1.380
BD+28 2095	12 16 02.50	+28 02 55.2	-24.0±0.0	-6.0±0.0	8.03	7.80	7.41±0.019	7.22±0.043	7.20±0.023	1.331
BD+27 2129	12 25 51.95	+26 46 36.0	-14.0±0.0	-10.0±0.0	8.09	7.86	7.41±0.017	7.30±0.057	7.20±0.021	1.331
BD+27 2122	12 23 41.00	+26 58 47.7	-14.0±0.0	-10.0±0.0	8.10	7.87	7.46±0.013	7.33±0.079	7.25±0.015	1.313
BD+23 2447	12 18 36.17	+23 07 12.2	-14.0±0.0	-10.0±0.0	8.39	8.13	7.63±0.009	7.38±0.017	7.30±0.013	1.294
BD+28 2109	12 21 56.16	+27 18 34.2	-10.0±0.0	-12.0±0.0	8.22	7.96	7.56±0.017	7.39±0.039	7.32±0.013	1.285
HD 107685	12 22 24.75	+22 27 50.9	-12.0±0.0	-10.0±0.0	8.23	8.00	7.60±0.009	7.39±0.011	7.38±0.013	1.263
BD+24 2457	12 25 22.49	+23 13 44.7	-14.0±0.0	-10.0±0.0	8.30	8.06	7.64±0.017	7.48±0.023	7.39±0.011	1.261
BD+28 2125	12 31 03.09	+27 43 49.2	-16.0±0.0	-8.0±0.0	8.27	8.01	7.61±0.009	7.46±0.053	7.40±0.011	1.256

Table 5.1: Continued

Name	RA	Dec.	μ_α	μ_δ	R	I	J	H	K_S	Mass
	J2000.0		mas yr^{-1}							$M_\odot$
BD+25 2488	12 19 28.35	+24 17 03.2	-12.0±0.0	-12.0±0.0	8.69	8.40	7.86±0.009	7.55±0.041	7.49±0.023	1.224
HD 109483	12 34 54.29	+27 27 20.2	-12.0±0.0	-10.0±0.0	8.67	8.40	7.89±0.023	7.58±0.037	7.51±0.013	1.217
BD+25 2486	12 19 01.47	+24 50 46.1	-12.0±0.0	-10.0±0.0	8.53	8.27	7.83±0.053	7.55±0.033	7.53±0.011	1.207
BD+27 2130	12 26 05.48	+26 44 38.3	-8.0±0.0	-14.0±0.0	9.44	9.04	8.13±0.019	7.68±0.029	7.58±0.019	1.193
HD 107399	12 20 45.56	+25 45 57.1	-12.0±0.0	-8.0±0.0	8.68	8.42	7.97±0.013	7.74±0.029	7.65±0.021	1.171
BD+26 2340	12 23 08.39	+25 51 04.9	-12.0±0.0	-10.0±0.0	8.80	8.52	8.02±0.011	7.76±0.015	7.68±0.017	1.160
BD+25 2511	12 29 40.92	+24 31 14.6	-10.0±0.0	-10.0±0.0	9.26	8.80	8.20±0.009	7.84±0.045	7.72±0.025	1.148
BD+27 2121	12 23 41.82	+26 36 05.3	-16.0±0.0	-12.0±0.0	8.85	8.49	8.13±0.015	7.79±0.029	7.73±0.013	1.143
BD+27 2117	12 21 49.02	+26 32 56.7	-12.0±0.0	-8.0±0.0	8.89	8.57	8.21±0.019	7.86±0.023	7.85±0.023	1.109
TYC1991-1087-1	12 27 48.29	+28 11 39.8	-12.0±0.0	-10.0±0.0	9.26	8.94	8.43±0.015	8.05±0.043	8.05±0.017	1.051
HD 105863	12 11 07.38	+25 59 24.6	-12.0±0.0	-10.0±0.0	9.14	8.84	8.38±0.015	8.11±0.009	8.07±0.029	1.043
BD+30 2281	12 29 30.02	+29 30 45.8	10.0±0.0	0.0±0.0	9.41	9.12	8.38±0.021	8.16±0.037	8.07±0.015	1.043
BD+28 2119	12 28 21.11	+28 02 25.9	-14.0±0.0	-12.0±0.0	9.92	9.54	8.94±0.017	8.47±0.041	8.46±0.023	0.915

diagram. Based on previous experience gained from investigations of the low mass members of the Pleiades and Praesepe open clusters, an uncertainty in the model J-K colour of ± 0.05 magnitudes was estimated. Hence for $J-K_S > 0.8$, all objects which overlap a region 0.1 magnitudes wide in J-K, centred on the theoretical isochrone were selected.

To assess levels of contamination in the list of candidate members, the same colour selection criteria were imposed on the control samples. The resulting sequences were divided into one magnitude bins (in K_S for $J-K_S > 0.8$, and in bins of 0.2 in $J-K_S$ for $J-K_S < 0.8$). The number of objects in each bin for both the cluster and control samples was then counted. Subsequently, the probability of membership for each candidate cluster member, $P_{membership}$, was estimated using equation 5.1,

$$P_{membership} = \frac{N_{cluster} - N_{control}}{N_{cluster}} \tag{5.1}$$

where $N_{cluster}$ is the number of stars in a magnitude bin from the cluster sample and $N_{control}$ is the mean number of stars in the same magnitude range but drawn from the control samples. The list of candidate associates of Melotte 111 is presented in table 5.2, along with these estimates of membership probability.

It should be noted that there is a slight increase in the level of contamination in the range $0.55 < J-K_S < 0.7$. A similar increase in the number of field stars was seen by Adams et al. (2002) when studying the Praesepe open cluster, which, like Melotte 111, has a relatively high galactic latitude (b=38° for Melotte 111). It is believed that this background contamination is due to K giants located in the thick disc of the galaxy.

5.4 Results

The catalogue survey of Melotte 111 has recovered 40 previously known members in total, 38 listed by Bounatiro & Arimoto (1992) and 7 unearthed by Odenkirchen et al. (1998). These are all but 5 of the previously known members in the area surveyed. These 5 objects are

Table 5.2: Coordinates, proper motion measurements, R, I, J, H and K magnitudes for the new members. Masses are calculated from linearly interpolating the NEXTGEN model for 400 Myr and the absolute K magnitude. The probability of membership for each of these 60 candidate members is in the final column. The R and I magnitudes are from the USNOB1.0 catalogue and the J, H and K_S magnitudes are from 2MASS.

RA J2000.0	Dec.	μ_α mas yr^{-1}	μ_δ	R	I	J	H	K_S	Mass $M_\odot$	Membership probability
12 24 17.15	+24 19 28.4	-18.0±0.0	-14.0±0.0	9.44	9.08	8.42±0.037	7.95±0.065	7.90±0.017	0.880	0.64
12 38 14.94	+26 21 28.1	-6.0±0.0	-2.0±0.0	9.57	9.13	8.56±0.027	8.07±0.027	8.00±0.027	0.836	0.64
12 23 28.69	+22 50 55.8	-14.0±0.0	-10.0±0.0	9.77	9.23	8.60±0.023	8.09±0.018	8.01±0.026	0.815	0.64
12 31 04.78	+24 15 45.4	-8.0±0.0	-4.0±0.0	9.76	9.19	8.81±0.025	8.28±0.034	8.20±0.026	0.798	0.79
12 27 06.26	+26 50 44.5	-12.0±0.0	-8.0±0.0	9.59	9.31	8.64±0.037	8.33±0.026	8.25±0.036	1.007	0.94
12 27 20.69	+23 19 47.5	-14.0±0.0	-10.0±0.0	9.83	9.46	8.91±0.021	8.54±0.021	8.45±0.017	0.936	0.64
12 23 11.99	+29 14 59.9	-2.0±0.0	-6.0±0.0	10.29	9.84	9.13±0.022	8.58±0.021	8.47±0.017	0.764	0.79
12 33 30.19	+26 10 00.1	-16.0±0.0	-10.0±0.0	10.59	10.14	9.24±0.029	8.72±0.030	8.59±0.022	0.766	0.79
12 39 52.43	+25 46 33.0	-20.0±0.0	-8.0±0.0	10.79	10.49	9.23±0.021	8.74±0.029	8.65±0.021	0.824	0.64
12 28 56.43	+26 32 57.4	-14.0±0.0	-8.0±0.0	10.53	10.25	9.21±0.026	8.77±0.031	8.66±0.023	0.852	0.64
12 24 53.60	+23 43 04.9	-4.0±0.0	-8.0±0.0	10.73	10.34	9.39±0.021	8.86±0.024	8.82±0.017	0.840	0.64
12 28 34.29	+23 32 30.6	-8.0±0.0	-14.0±0.0	10.40	9.97	9.47±0.024	8.93±0.045	8.86±0.023	0.798	0.79
12 33 00.62	+27 42 44.8	-14.0±0.0	-14.0±0.0	10.42	9.80	9.47±0.030	8.94±0.030	8.87±0.018	0.805	0.79
12 35 17.03	+26 03 21.8	-2.0±0.0	-10.0±0.0	10.69	10.35	9.51±0.025	9.01±0.028	8.93±0.021	0.818	0.64

RA	Dec.	μ_α	μ_δ	R	I	J	H	K_S	Mass	Membership
	J2000.0	mas yr^{-1}							$M_\odot$	probability
12 25 10.14	+27 39 44.8	-6.0±0.0	-12.0±0.0	10.69	10.10	9.57±0.018	9.07±0.022	8.93±0.018	0.777	0.79
12 18 57.27	+25 53 11.1	-12.0±3.0	-12.0±1.0	10.80	10.30	9.64±0.018	9.08±0.022	8.94±0.018	0.728	0.79
12 21 15.63	+26 09 14.1	-10.0±0.0	-8.0±0.0	10.87	10.41	9.62±0.019	9.09±0.024	8.97±0.020	0.773	0.79
12 32 08.09	+28 54 06.5	-10.0±0.0	-4.0±0.0	10.74	10.30	9.62±0.022	9.09±0.031	8.99±0.018	0.785	0.79
12 12 53.23	+26 15 01.3	-12.0±0.0	-12.0±0.0	10.54	9.72	9.58±0.019	9.11±0.016	8.99±0.018	0.819	0.64
12 23 47.23	+23 14 44.3	-12.0±0.0	-16.0±0.0	10.36	9.54	9.68±0.021	9.13±0.022	9.02±0.018	0.759	0.79
12 18 17.77	+23 38 32.8	-6.0±0.0	-14.0±0.0	10.77	10.28	9.76±0.022	9.20±0.020	9.10±0.017	0.759	0.79
12 22 52.37	+26 38 24.2	-8.0±0.0	-10.0±0.0	11.42	11.12	9.78±0.027	9.26±0.032	9.11±0.021	0.756	0.79
12 26 51.03	+26 16 01.9	-14.0±0.0	-2.0±0.0	11.07	10.56	9.85±0.022	9.27±0.026	9.16±0.020	0.725	0.79
12 09 12.44	+26 39 38.9	-16.0±0.0	-6.0±0.0	10.60	9.78	9.83±0.019	9.27±0.016	9.18±0.019	0.770	0.79
12 27 00.81	+29 36 37.9	-4.0±0.0	-6.0±0.0	11.07	10.70	9.80±0.022	9.33±0.028	9.20±0.023	0.806	0.79
12 23 28.21	+25 53 39.9	-10.0±1.0	-12.0±1.0	11.43	11.00	9.92±0.023	9.35±0.018	9.26±0.026	0.758	0.79
12 24 10.37	+29 29 19.6	-6.0±0.0	-2.0±0.0	10.77	10.27	10.06±0.026	9.50±0.057	9.33±0.017	0.683	0.79
12 34 46.93	+24 09 37.7	-12.0±2.0	-4.0±5.0	11.38	10.87	10.06±0.023	9.53±0.029	9.39±0.025	0.749	0.79
12 15 34.01	+26 15 42.9	-12.0±0.0	-6.0±0.0	11.08	10.26	10.13±0.018	9.57±0.016	9.47±0.016	0.757	0.79
12 26 00.26	+24 09 20.9	-10.0±2.0	-4.0±2.0	13.85	12.51	10.98±0.021	10.36±0.029	10.14±0.025	0.558	0.80
12 28 57.67	+27 46 48.4	-14.0±3.0	-2.0±2.0	13.04	11.37	10.99±0.022	10.35±0.028	10.19±0.022	0.552	0.80

Table 5.2: Continued

RA	Dec.	μ_α	μ_δ	R	I	J	H	K_S	Mass	Membership
	J2000.0	mas yr^{-1}							$M_\odot$	probability
12 16 00.86	+28 05 48.1	-12.0±2.0	-4.0±2.0	14.15	11.43	11.07±0.024	10.52±0.033	10.24±0.018	0.543	0.80
12 30 57.39	+22 46 15.2	-12.0±3.0	-4.0±1.0	14.37	12.13	11.24±0.021	10.65±0.029	10.42±0.021	0.514	0.80
12 31 57.42	+25 08 42.5	-10.0±0.0	-12.0±1.0	14.22	12.94	11.40±0.024	10.79±0.028	10.55±0.022	0.492	0.80
12 31 27.72	+25 23 39.9	-8.0±1.0	-6.0±2.0	14.07	12.96	11.44±0.022	10.84±0.029	10.63±0.02	0.478	0.80
12 25 55.76	+29 07 38.3	-8.0±2.0	-18.0±3.0	13.81	11.78	11.56±0.025	10.95±0.027	10.75±0.021	0.460	0.80
12 23 55.53	+23 24 52.3	-10.0±1.0	-4.0±0.0	14.37	12.64	11.59±0.020	10.99±0.023	10.77±0.017	0.455	0.80
12 25 02.64	+26 42 38.4	-8.0±0.0	-4.0±3.0	14.22	11.85	11.62±0.019	11.03±0.016	10.79±0.020	0.452	0.80
12 30 04.87	+24 02 33.9	-10.0±3.0	-8.0±0.0	14.76	13.27	11.77±0.022	11.18±0.022	10.94±0.020	0.428	0.80
12 18 12.77	+26 49 15.6	-8.0±1.0	0.0±1.0	15.61	12.78	12.02±0.022	11.46±0.021	11.15±0.020	0.392	0.60
12 15 16.93	+28 44 50.0	-12.0±4.0	-14.0±1.0	14.11	0.0	12.00±0.021	11.35±0.020	11.17±0.022	0.389	0.60
12 23 12.03	+23 56 15.1	-8.0±2.0	-6.0±1.0	15.40	13.31	12.20±0.022	11.61±0.022	11.38±0.017	0.352	0.60
12 31 00.28	+26 56 25.1	-16.0±3.0	-14.0±1.0	14.04	12.52	12.25±0.024	11.56±0.029	11.39±0.022	0.351	0.60
12 33 31.35	+24 12 09.1	-4.0±1.0	-16.0±2.0	14.76	13.45	12.29±0.030	11.59±0.033	11.40±0.020	0.348	0.60
12 16 37.30	+26 53 58.2	-10.0±2.0	-6.0±3.0	15.13	12.94	12.23±0.022	11.68±0.024	11.42±0.179	0.346	0.60
12 24 10.89	+23 59 36.4	-6.0±4.0	-4.0±1.0	15.60	13.67	12.27±0.021	11.66±0.020	11.45±0.017	0.340	0.60
12 28 38.70	+25 59 13.0	-6.0±1.0	-2.0±2.0	14.31	13.94	12.36±0.022	11.69±0.031	11.53±0.022	0.326	0.60
12 16 22.84	+24 19 01.1	-12.0±2.0	-2.0±4.0	14.78	13.96	12.39±0.022	11.73±0.023	11.55±0.021	0.323	0.60

Table 5.2: Continued

RA	Dec.	μ_α	μ_δ	R	I	J	H	K_S	Mass	Membership
J2000.0		mas yr^{-1}							$M_\odot$	probability
12 27 08.56	+27 01 22.9	-16.0±2.0	-2.0±3.0	14.14	12.52	12.38±0.022	11.73±0.026	11.57±0.023	0.319	0.60
12 28 04.54	+24 21 07.6	-12.0±1.0	-10±3.0.0	15.75	14.29	12.39±0.022	11.84±0.032	11.58±0.021	0.318	0.60
12 38 04.72	+25 51 18.5	-16.0±4.0	-6.0±0.0	14.96	13.43	12.46±0.024	11.84±0.028	11.64±0.022	0.308	0.60
12 14 19.78	+25 10 46.6	-6.0±3.0	-12.0±3.0	14.81	13.92	12.50±0.023	11.80±0.028	11.65±0.025	0.305	0.60
12 28 50.08	+27 17 41.7	-20.0±1.0	-12.0±2.0	14.46	12.84	12.55±0.027	11.84±0.032	11.70±0.019	0.297	0.60
12 36 34.30	+25 00 38.3	-14.0±4.0	-2.0±6.0	15.59	13.43	12.51±0.024	11.96±0.032	11.70±0.024	0.298	0.60
12 26 37.32	+22 34 53.4	-12.0±1.0	-8.0±1.0	15.19	13.34	12.60±0.021	11.97±0.023	11.77±0.017	0.288	0.60
12 33 30.31	+28 12 55.9	-12.0±2.0	-14.0±11.0	14.06	13.59	12.65±0.029	12.07±0.034	11.84±0.025	0.279	0.60
12 16 29.21	+23 32 32.9	-12.0±6.0	-8.0±1.0	15.08	14.55	12.77±0.020	12.13±0.023	11.91±0.020	0.270	0.60
12 30 46.17	+23 45 49.0	-10.0±1.0	-6.0±9.0	15.43	13.83	12.72±0.024	12.17±0.029	11.91±0.022	0.269	0.60
12 19 37.99	+26 34 44.7	-6.0±4.0	-8.0±2.0	16.46	14.03	12.78±0.029	12.24±0.033	11.92±0.023	0.269	0.60
12 14 23.97	+28 21 16.6	-4.0±2.0	-8.0±1.0	15.52	0.0	12.83±0.022	12.14±0.026	11.92±0.023	0.269	0.60

detailed in table 5.3.

The parallax and radial velocity measurements for these objects are all from Hipparcos (Perryman et al., 1997) and Hipparcos and USNOB1.0 proper motion measurements are listed. There are two exceptions, the radial velocity for BD+26 2354 is from Evans (1967), and there are no radial velocity or parallax measurements in the literature for BD+30 2281. Using the proper motion selection criteria for the survey on the Hipparcos measurements, only BD+26 2353 and BD+30 2281 appear to be members. This is supported by the distances derived from the parallax for these 5 objects. Using a cluster distance of $\approx$ 80 pc, BD+26 2353 and BD+26 2354 appear to be members, with distances of 78.9±6.4 and 82.9±5.4 pc respectively. The remaining two objects with parallax measurements have distances of 209.2±37 for BD+28 2095 and 66.2±3.5 for BD+24 2464 making it likely that they are non members. Their radial velocities also make them appear non members. The cluster has a radial velocity of -0.1 km s^{-1} as derived by Odenkirchen et al. (1998). Ford et al. (2001) used a 2σ value of 1 km s^{-1} when determining cluster members, and this leaves only BD+26 2353 as a likely member to the cluster. Both BD+26 2353 and BD+30 2281 are situated near bright stars in the USNO images, making this a possible reason for the discrepancies in the proper motions. These two objects are treated as members in the remainder of this work, whereas the other three are not.

This survey has been used to identify 60 new candidate cluster members with magnitudes down to K_S=12. Beyond this magnitude, no statistically significant difference between the cluster and the control samples was found, as the contamination by field stars is too great. It is believed that this survey is reasonably complete to this limit; proper motion search radii of 7 and 5 mas yr^{-1} were also used, but in both cases it was found that increasing numbers of likely members were excluded. Expanding the search radius to greater than 10 mas yr^{-1} unearthed no statistically significant increase in the number of candidate members, as the number of candidates and control stars increased proportionally, leading to many candidates, all with extremely small probabilities of being cluster members. It is believed that the survey is complete to 90% at the radius of 10 mas yr^{-1}, as explained earlier. As the stars get fainter, the errors in their proper motion do increase - which is to be expected. It is entirely possible that the completeness is less than 90% for the faint stars.

Table 5.3: Name, coordinates, USNO proper motion, Hipparcos proper motion, parallax and radial velocity for the 5 known members in the survey area, but not recovered by the proper motion selection criteria.

Name	RA	Dec.	USNO μ_α	USNO μ_δ	Hipparcos μ_α	Hipparcos μ_δ	parallax	radial velocity
	J2000.0		mas yr^{-1}		mas yr^{-1}		mas	km s^{-1}
BD+28 2095	12 16 02.50	+28 02 55.24	-24.0	-6.0	-24.91	-4.66	7.49±1.04	-8.6
BD+26 2353	12 28 44.56	+25 53 75.56	-22.0	-18.0	-18.50	-15.76	12.66±0.95	-1.7
BD+26 2354	12 28 54.70	25 54 46.26	-24.0	-16.0	-20.21	-15.0	12.06±0.95	-2.8
BD+24 2464	12 29 27.04	+24 06 32.13	-18.0	0.0	-18.09	1.84	15.10±0.82	25.1
BD+30 2281	12 29 29.98	+29 30 44.79	10.0	0.0	2.6	-14.0	-	-

The masses of the new candidates and the previously known cluster members were estimated using the evolutionary tracks of Girardi et al. (2002), for masses$\geq$ 1 M$_\odot$, and the NEXTGEN models of Baraffe et al. (1998) for M$<$1 M$_\odot$. The stars were binned according to K$_S$ magnitude or J-K$_S$ colour, for the vertical and diagonal portions of the main sequence. Linear interpolation was used between the model masses to estimate the masses of the cluster stars and the new candidates. These masses are shown in the final columns of tables 5.1 and 5.2. By multiplying the estimated masses of the stars by their membership probabilities (it was assumed $P_{membership}$=1.0 for previously known members) and summing, a total cluster mass of ~96 M$_\odot$ is determined. Equation 5.2 can be used to determine the tidal radius of the cluster,

$$r_t = R_g \left(\frac{M_c}{2M_g} \right)^{1/3}, \tag{5.2}$$

where r_t is the tidal radius, R_g is the orbital radius of the cluster, M_c is the mass of the cluster and M_g is the mass of the galaxy and $R_g >> r_t$ (Pinfield et al., 1998). Equation 5.2 can be simplified by using Oort's constants A and B. These constants originate from the equations describing radial velocity (v) and proper motion (μ) that result from circular motion around the Galactic Centre. The angular velocity for the solar neighbourhood (ω) is $A - B$ and is known to be 26.4$\pm$1.9 km s^{-1} kpc^{-1} (Kerr & Lynden-Bell, 1986) or 8.56 $\times$ 10^{-16} s^{-1}, which can be calculated using Newton's law of gravity and circular motion as in equation 5.3.

$$\omega^2 R_g = \frac{GM_g}{R_g^2} \tag{5.3}$$

Using equations 5.2 and 5.3,

$$r_t = \left[\frac{GM_c}{2(A-B)^2} \right]^{1/3} = 1.46 M_c^{1/3}, \tag{5.4}$$

where r_t and M_c have units of parsecs and solar masses respectively and G, the universal gravitational constant has a value of 4.517 $\times$10^{-30} pc^3 M$_\odot^{-1}$ s^{-2}. A tidal radius of $\approx$6.6 pc or 4.1° at 90 pc is derived. Thus within the adopted survey radius of 4°, 99 % of the gravitationally bound proper motion selected cluster members should be found. Indeed, increasing the search radius to 5°, led to a near equal increase in both candidate cluster members and stars in the control.

115
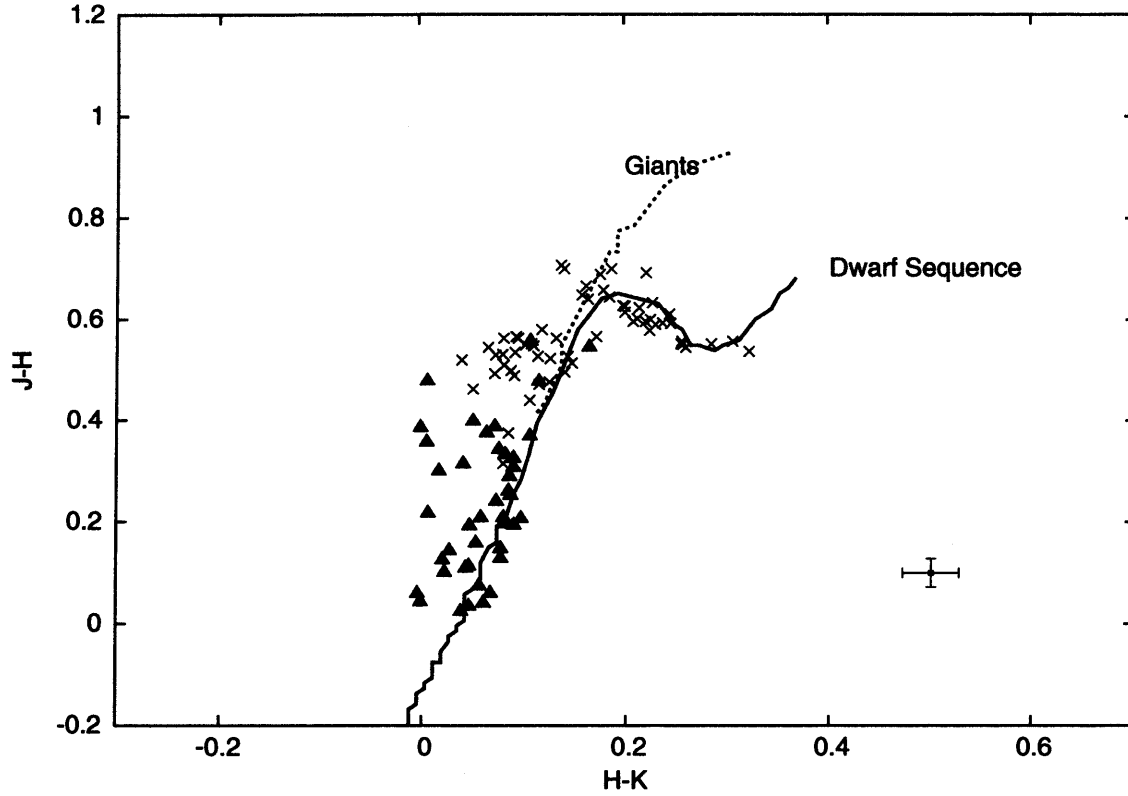
Figure 5.3: A JHK_S colour-colour diagram for candidate (crosses) and previously known (solid triangles) cluster members. Empirical dwarf (dotted line) and giant (dashed line) sequences of Koornneef (1983), are overplotted. The diagram has been plotted using the 2MASS system. The colour transformations of Carpenter (2001) were used to convert the model colours.

Figure 5.3 shows the J-H, H-K_S two colour diagram for all new candidate and previously known cluster members from the catalogue survey. The colours of the new candidates show a clear turnover at H-K ≈ 0.15, consistent with them being dwarfs and supporting the conclusion that these are low mass members of Melotte 111. Therefore, the K_S luminosity function has been constructed (figure 5.4). The luminosity function is seen to peak at K_S =7.5, M_{K_S}=2.7 (M$\approx$0.2 M$_\odot$) and to gradually decline towards fainter magnitudes. Superimposed on this decline is the Wielen dip (Wielen, 1971) at K_S=10.5. The Wielen dip is an effect seen on colour-magnitude diagrams, which is brought on by a change in gradient of the mass-magnitude relation, brought on by stars becoming completely convective. The mass spectrum has also been plotted for the cluster (figure 5.5). The mass spectrum appears to be flat, and does not

116
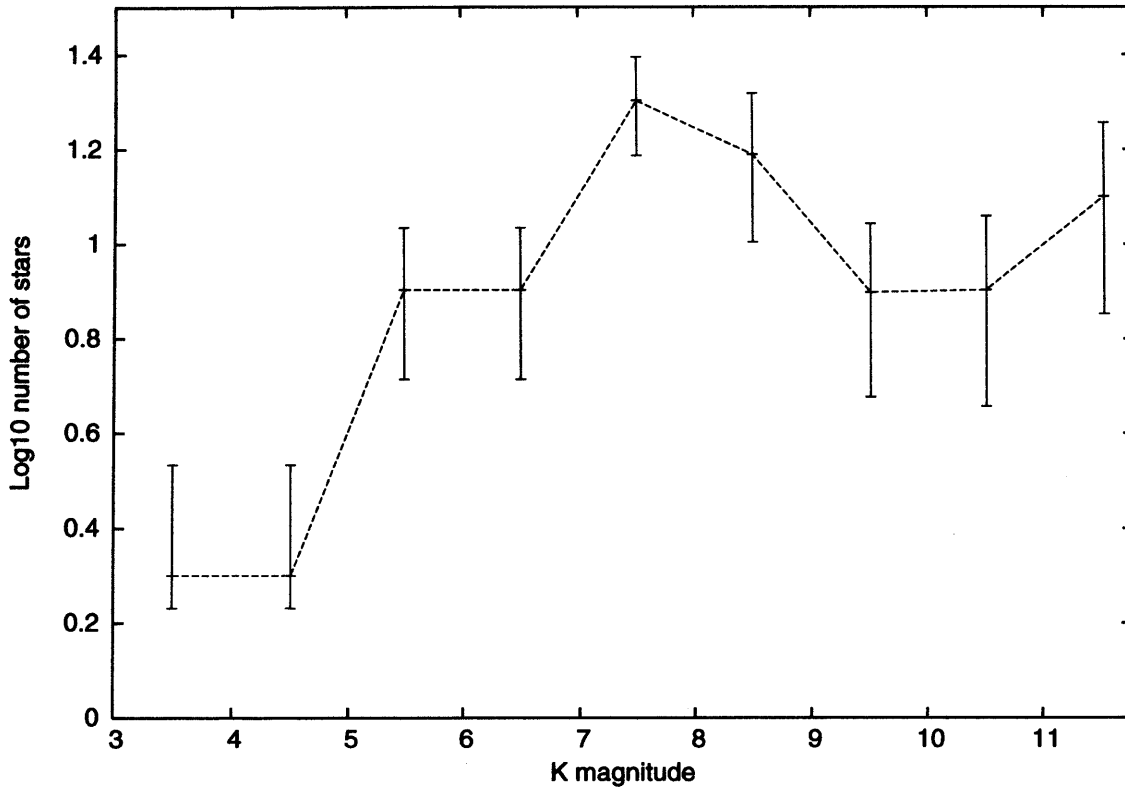
Figure 5.4: Luminosity function for the cluster calculated using the membership probabilities. The error bars indicate the Poisson error.

appear to be rising towards the lower masses, also supporting the conclusion that dynamical evolution may have removed some of the lower mass members of the cluster.

5.5 Substellar members

5.5.1 The i and Z band survey

In addition to the proper motion and photometric search for candidates as detailed above, a deeper survey of 15 sq. degs was undertaken using the WFC on the 2.5m INT at the Roque de la Muchachos on La Palma on the nights of 20 to 26 February 2002. The seeing varied from 1.5 to 1.0", which was within the acceptable limits, and the conditions were photometric. These
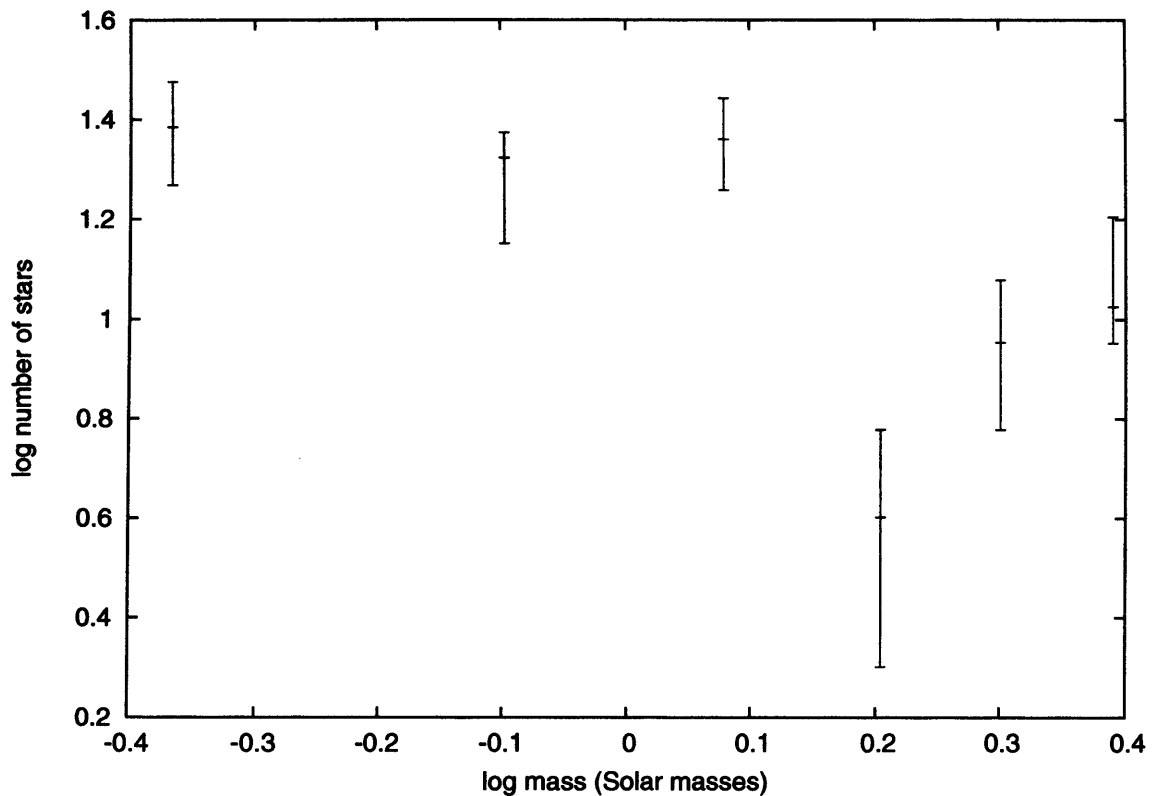
Figure 5.5: Mass spectrum for the cluster calculated using the membership probabilities. The error bars indicate the Poisson error.

observations were taken by Paul Dobbie and reduced by Simon Hodgkin using the CASU data reduction pipeline. The 15 square degrees were surveyed using exposure times of 600s and 900s with the Sloan i and RGO Z filters respectively. The i, i-Z colour-magnitude diagram is shown in figure 5.6. The field dwarf isochrone constructed using data from Dobbie et al. (2002c) has been over-plotted on the diagram. This isochrone is for the old field dwarfs (age $\approx$1 Gyr) that are expected to be found in the foreground of the cluster. These objects are older than any brown dwarf members of Melotte 111 and so are expected to be cooler, and hence redder, for the same mass.

From these data 105 low mass candidate members of the cluster were identified (filled circles on figure 5.6). A generous selection was made of any stars that sat on or near the isochrone, taking into account the photometric errors (figure 5.6). To estimate a level of completeness the method described in Dobbie et al. (2002b) was used. This makes use of a relationship
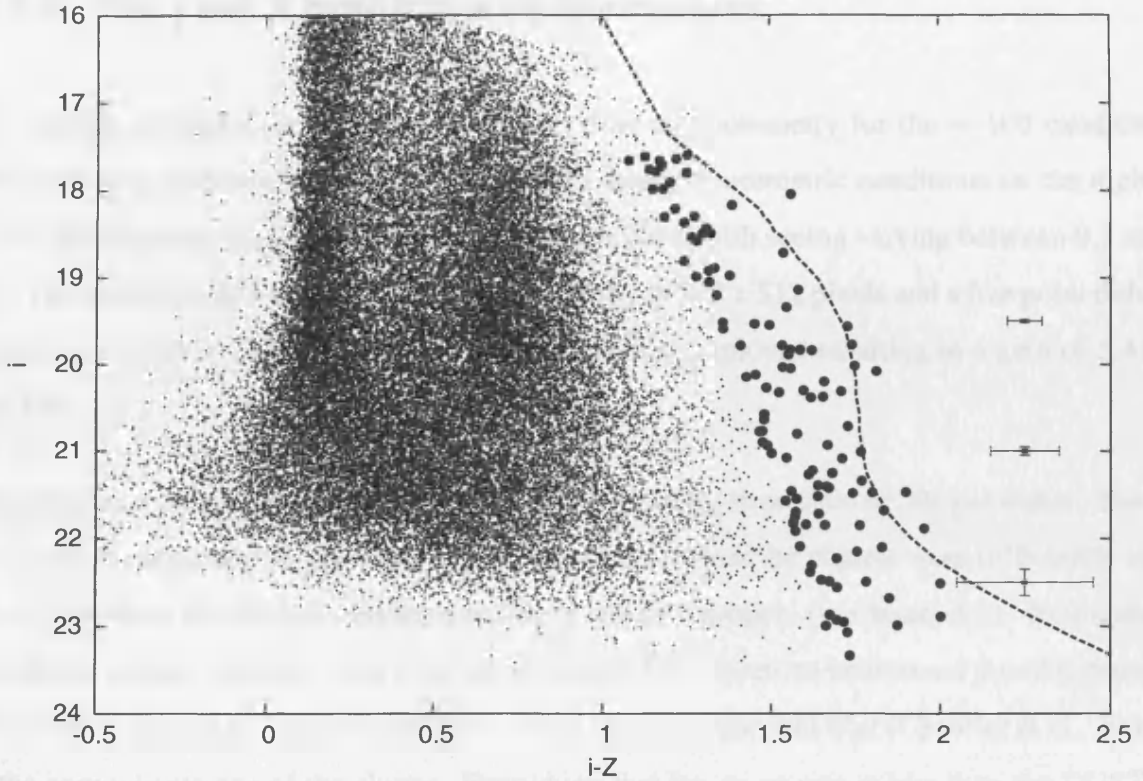
Figure 5.6: i, i-Z colour-magnitude diagram created using photometry from the INT survey. The dashed line is the field dwarf isochrone. The filled circles are the 105 objects that were selected for follow up photometry.

derived by Santiago et al. (1996), who showed that the relationship log N $\propto$I, where N is the number of sources and I is the magnitude, holds true for disk stars with galactic latitude |b| > 25 ° down to a limit of I $\approx$24, and so is applicable to Melotte 111. Using this relationship the sources were binned into one magnitude bins and a linear function was fitted to the region where the survey is believed to be complete (i=20, Z=19). The data were then divided by the linear function and multiplied by 100 to produce a percentage of completeness. Thus the statistics indicate that the survey is 90% complete to i and Z of 21.5.

5.5.2 The J and K band follow up observations

In addition to the i-Z survey, K and J band follow up photometry for the ≈ 100 candidate members was acquired using UKIRT and UFTI during photometric conditions on the nights of 18-20 February, 23-24 February and 3-5 March 2003, with seeing varying between 0.7 and 1". The observations were obtained using a subarray of 512 x 512 pixels and a five point dither pattern on the sky. The NDSTARE readout mode was employed resulting in a gain of 5.414 e/ADU.

The objects were all observed in the K band with an integration time of 30s per dither. The i, i-K colour-magnitude diagram was used to examine whether the objects were sufficiently red in i-K for them to still be considered as likely cluster members (see figure 5.7). Remaining candidate cluster members were then observed at J. For objects to be deemed possible brown dwarfs they should lie along the DUSTY model isochrone for 500 Myr (Chabrier et al., 2000) - the approximate age of the cluster. Everything that lay on or was redder than the DUSTY model isochrone on the colour-magnitude diagram was then observed at J with an integration time of 40s per dither. I reduced the data for these objects using the ORAC-DR package, which performed the following operations using the JITTER_SELF_FLAT_APHOT routine.

Firstly, the routine converts all of the frames from FITS format to NDF format to make the data compatible with the STARLINK software. A standard bad pixel mask is then applied to remove known bad pixels. This accounts for 0.7 percent of pixels in the array, which is actually only 95 percent of the bad pixels within the array. The remaining 5 percent are only occasionally problematic and are not accounted for by the mask. There is no bias frame subtraction as this is done within the instrument data system as it is being read out. The world co-ordinate system is then written to the FITS header in the terms of the CRPIX1, CRPIX2, CD1_1,CD1_2 CD2_1, CD2_2, CRVAL1 and CRVAL2 keywords. The frame is then displayed using the STARLINK package GAIA. The dark frames are reduced using the REDUCE_DARK routine, and then a dark is subtracted from the science frames to remove the dark current. Only one dark frame is subtracted - the previous dark frame to the science frame which has the same exposure time and read type. Flat fields are created within the recipe from
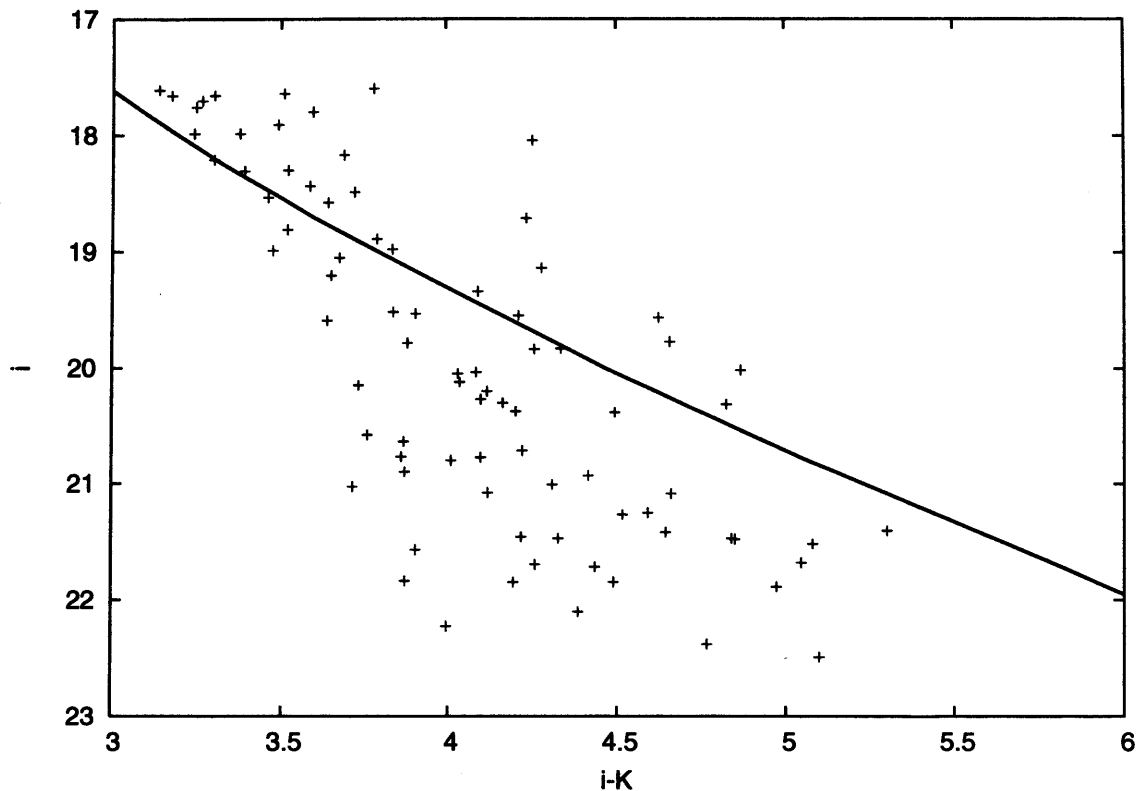
Figure 5.7: i, i-K colour-magnitude diagram created using photometry from our INT survey, and UKIRT. The solid line is the DUSTY model isochrone for 500 Myr (Chabrier et al., 2000).

the 5 point dither pattern and are are median stacked to produce a sky flat field. The science frames then undergo division by the flat field. The individual dithered images are then stacked to form a mosaic from which residual bad pixels are then removed by median filtering. The science frames are then ready to have aperture photometry performed on them.

Aperture photometry is performed using a circular aperture of size 5 arcseconds, which is standard to the APHOT recipes, with the size of the annulus used for measuring the sky counts ranging between values of 6.5 and 12.5". The sky level is estimated using 3 times the median minus twice the mean pixel value and also uses Chauvenet's rejection criterion. This criterion relies on the mean value and standard deviation of the data. Each data point is considered and depending on how much it differs from the mean, the normal distribution function is then used to determine the probability that a given data point will be at the value of the suspect data point. This probability is then multiplied by the number of data points taken. If the result

is less than 0.5, the suspicious data point may be discarded. Each image was observed as it passed through the pipeline, as the occurrence of binary objects or diffraction spikes close to the science object can affect the accuracy of the aperture photometry. Fortunately no such objects appeared in the data, mainly due to the fact that this region of sky is sparsely populated due to its high galactic latitude.

From the count rates calculated by the aperture photometry instrumental magnitudes are calculated as described in Chapter 3. The photometry was calibrated using standard stars, which were selected from the UKIRT Faint Standards list (Casali & Hawarden, 1992). These standard star images were reduced in exactly the same way as the science frames. ORAC-DR adds a routine to the standard star observations which calculates the zero point for the observation. The airmass corrections were then made for each image and the zero points corrected and subtracted accordingly.

The objects were then plotted on the K, J-K colour-magnitude diagram, and their positions compared to the main sequence NEXTGEN model for 400 Myr (Baraffe et al., 1998), and the 500 Myr DUSTY model (Chabrier et al., 2000). All objects were selected that fell on or within 0.75 magnitudes above the model to take into account a possible binary sequence.

This lead to 13 brown dwarf candidates as listed in table 5.4 (Casewell et al., 2005). These are shown as filled circles on figure 5.8.

5.5.3 Proper motion measurements

On 5 May 2005, eight of the substellar candidate members were observed using WFCAM on UKIRT. Four tiles were observed, which covered eight of the brown dwarf candidates in total. The images were taken in the K band and had exposure times of 5 seconds per pointing. The data were reduced using the CASU pipeline in Cambridge and the astrometry and photometry were calibrated to 2MASS as for the Pleiades images. The remaining five objects were observed in the K band as part of the UKIDSS GCS, and these images were
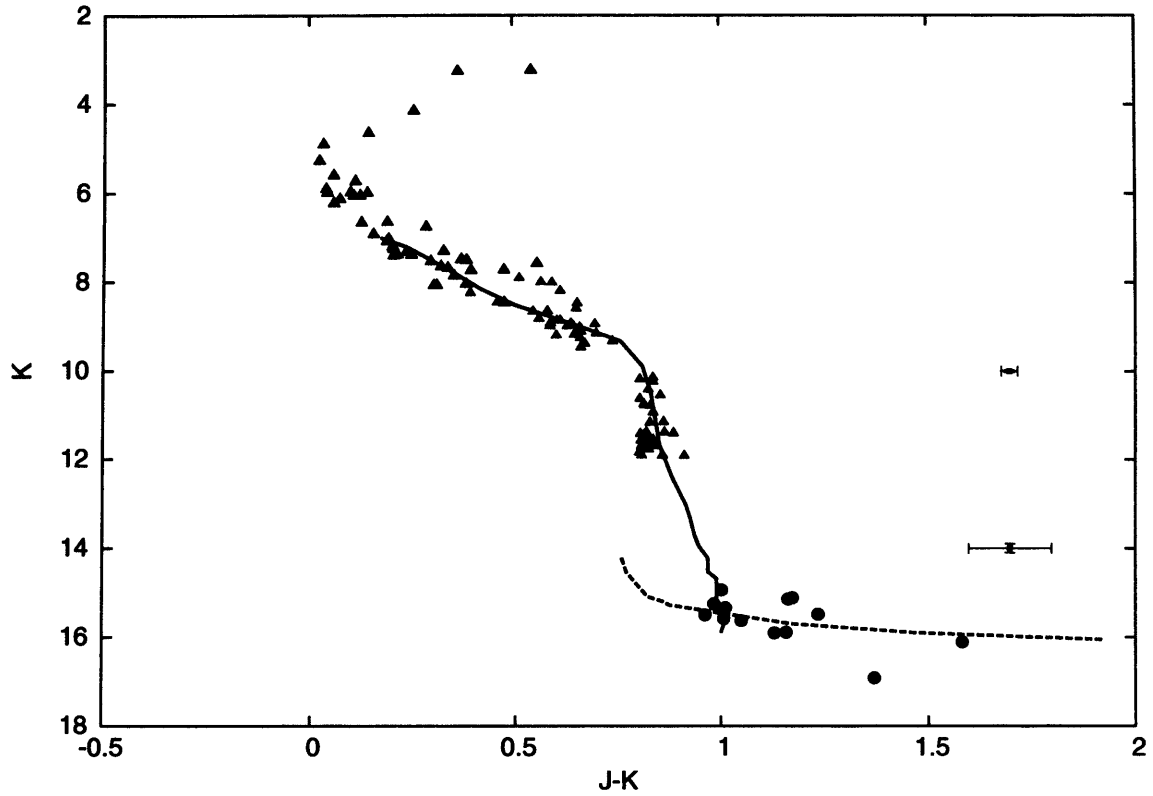
Figure 5.8: K, J-K colour-magnitude diagram for Melotte 111. The solid line is the NEXTGEN model for 400 Myr, the dashed line is the DUSTY model for 500 Myr, the triangles are the previously known cluster members from Bounatiro & Arimoto (1992); Odenkirchen et al. (1998) and Casewell et al. (2006) and the filled circles are the brown dwarf candidates (Casewell et al., 2005).

made public in DR2 which was released on 1 March 2007. The images of these objects were downloaded from the WFCAM science archive.

The perl CFITSIO module was utilised to extract the required data - x and y pixel positions and associated errors, flux, photometric zero points, exposure time and co-ordinate matrices from the tables and FITS headers. The pixel values and co-ordinate matrices were used to calculate accurate coordinates for the objects within the fields and photometry as detailed in Chapter 3. The proper motions were measured for each of these objects using the INT Z and WFCAM K images. Initially the proper motions were measured as described in Chapter 3. Each image was examined, and suitable objects selected with which to calculate the proper

Table 5.4: Table containing the name, co-ordinates and I, Z, J and K magnitudes for the 13 brown dwarf candidates

name	RA	Dec.	I	Z	J	K
		J2000.0				
CBD30	12 27 49.23	27 59 28.7	19.33	17.79	16.23	15.24
CBD32	12 19 33.41	24 32 49.1	19.53	18.07	16.67	15.62
CBD33	12 21 18.86	26 42 30.8	19.54	18.05	16.34	15.33
CBD34	12 23 57.37	24 53 29.0	19.56	17.83	15.94	14.93
CBD36	12 17 10.45	24 36 07.6	19.77	18.03	16.28	15.11
CBD37	12 32 11.91	27 06 57.1	19.78	18.37	17.03	15.90
CBD38	12 15 17.93	27 55 09.5	19.83	18.27	16.45	15.49
CBD39	12 13 43.89	27 18 41.6	19.83	18.21	16.58	15.58
CBD40	12 16 59.89	27 20 05.5	20.01	18.26	16.30	15.14
CBD48	12 21 02.46	26 22 04.2	20.31	18.60	16.71	15.48
CBD50	12 30 41.95	28 00 05.1	20.38	18.76	17.04	15.89
CBD67	12 18 32.71	27 37 31.3	21.40	19.74	17.68	16.10
CBD83	12 13 33.43	27 28 20.5	21.88	19.93	18.28	16.91

motions. The selection requirements for these objects were;

1. That they have positions within 10 arcseconds of the candidate in their field.

2. That they be classed as stellar, i.e. a point source (-1 in the flag column).

3. That they have an ellipticity of less than 0.2 (thus removing elongated objects such as diffraction spikes and elongated galaxies).

The proper motions for each object were then calculated using the STARLINK sla library

routines as described earlier. Having calculated these proper motion measurements it unfortunately became clear that they have large errors associated with them and were in general between 30 and 100 mas yr^{-1}. This is due to the rms of the linear fit typically being large (0.4 pixels), ideally it should be as small as possible ($\approx$0.1). The main reason for this large error is the sparse population of suitable (i.e. stationary) reference stars at the high galactic latitudes, at which the cluster is located, and that only small regions of the chips were used to select reference stars to avoid the radial distortion. An attempt was made to reduce the errors in the proper motion measurements by performing a more robust fit using circular (ellipticity < 0.2) galaxies. As galaxies are distant they are not expected to be moving and hence should provide good stationary reference points for the proper motion measurements. However, this did not result in a greater accuracy to the fit and hence made no improvement to the errors.

A second method for measuring the proper motions using the whole of the chips and a 12 parameter quadratic fit between the two epochs was developed by Paul Dobbie and Nigel Hambly. This method measures proper motions for everything present on the overlapping chips between the two epochs and fits the radial distortion, thus allowing $\approx$250 stars to be used as references as opposed to 20, or less, in the previous method. This method was much more successful at calculating proper motions with more realistic errors, as the rms fit was between 0.1 and 0.25 pixels in general. To estimate the error in the pixel measurements, the errors derived from the WFCAM chips in Chapter 4 were used. These were ≈ 0.15 pixels in both the x and y direction.

It was hoped that any fast moving objects that were present in these candidates could be eliminated - at this high galactic latitude there should be many, as all field objects will be moving faster than the cluster, thus leaving objects with no detectable proper motion as candidate cluster members. The calculated proper motions are detailed in table 5.5. Unfortunately due to the measurement errors being of the same magnitude as the measurements, no robust conclusions can be made about these objects in respect of the proper motion measurements. Another epoch difference in another 5 years will allow more measurements to be made, which hopefully will prove more conclusive. It is possible that data from UKIDSS will allow proper motions to be calculated between the second epoch UKIDSS K band and the INT Z band. It is currently

Table 5.5: Table containing the name, proper motion and errors in mas yr^{-1}

name	μ_α	μ_δ	μ_α error	μ_δ error
			mas yr^{-1}	
CBD30	16.141	-31.025	13.825	14.648
CBD32	16.841	-14.636	17.891	14.622
CBD33	-24.617	3.840	13.990	15.946
CBD34	-15.474	-3.260	19.025	15.061
CBD36	-12.052	-0.073	19.255	18.808
CBD37	-86.690	-17.476	17.302	15.121
CBD38	-124.544	12.392	13.053	16.250
CBD39	78.376	-68.824	11.168	13.494
CBD40	-51.818	-39.439	12.257	15.054
CBD48	-46.459	6.502	17.962	19.288
CBD50	-10.530	30.357	15.075	15.296
CBD67	-4.820	-65.143	18.138	16.639
CBD83	6.008	-41.250	15.995	9.331

unclear as to when these data will be made available. Another method would be to use radial velocity measurements from spectra to determine cluster membership. From the data in table 5.5 it appears that only CBD36 and CBD34 are likely to be members of the cluster.

5.5.4 Infrared spectra

Using their place on the DUSTY model isochrones for 500 Myr, their proper motions and also their places on the empirical isochrone for field dwarfs of age 500 Myr in the Ursa Major moving group (Bannister & Jameson, 2007) three objects were selected for infrared spectral follow up. These were CBD 36, 40 and 67, as shown on figure 5.9 with the empirical track and the DUSTY model for 500 Myr (Chabrier et al., 2000). It should be noted that the proper motions for CBD34, CBD37, CBD38, CBD39 and CBD83 had not been calculated at this point
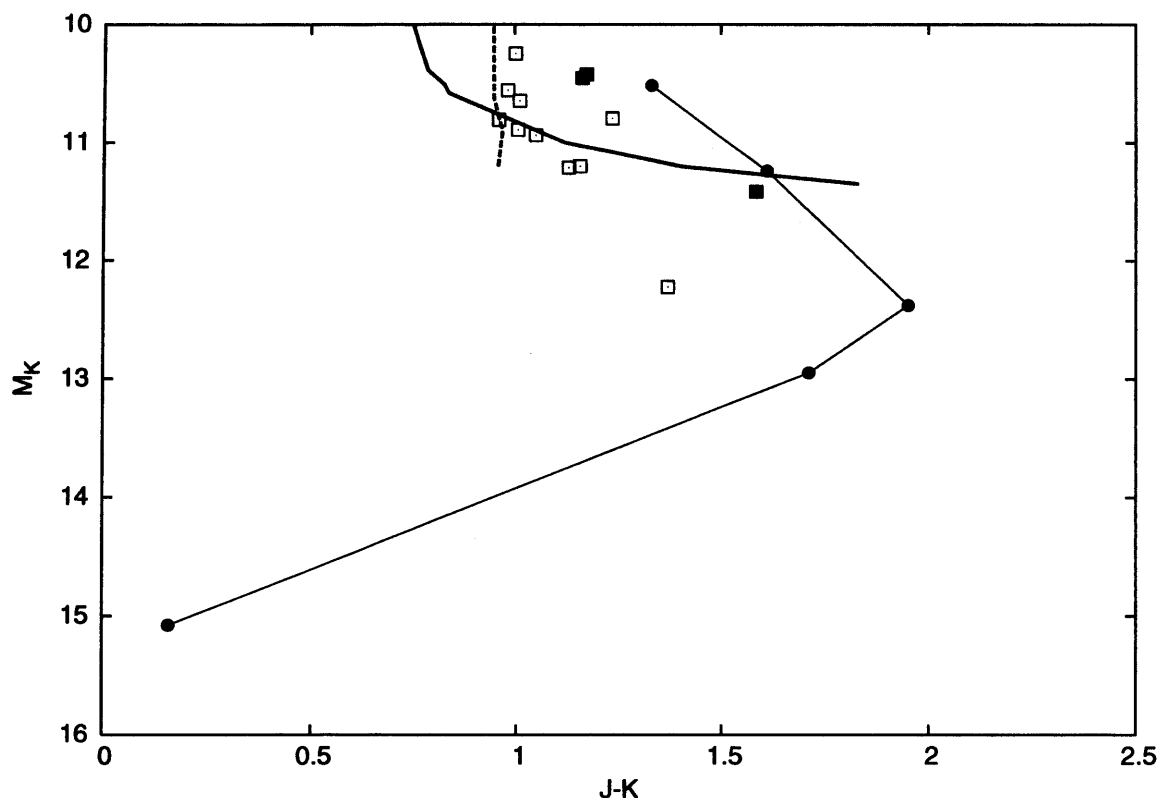
Figure 5.9: K, J-K colour-magnitude diagram for the Coma open star cluster brown dwarf candidates. The dashed line is the NEXTGEN model for 400 Myr, the bold solid line is the DUSTY model for 500 Myr and the thin solid line is the empirical isochrone as defined by the field dwarfs belonging to the 500 Myr old Ursa Major moving group. The squares (filled and hollow) are the brown dwarf candidates (Casewell et al., 2005). The filled squares are the three objects CBD36, CBD40 and CBD67 chosen for infrared spectral follow up. CBD67 has J-K=1.58 and the other two objects have J-K≈1.2.

as the GCS data had not been publicly released, and that the remaining proper motions had been calculated using small regions of the images, resulting in less accurate proper motions than those in table 5.5. The spectra were obtained on 18 March 2006 using LIRIS on the 4.2m WHT on La Palma.

The spectra were taken using a slit of 1" and the lrzj8 grism with resolution of 700 and in seeing of less than 1". Lamp flat fields and Xenon arc lamp calibration frames were also taken. Standard stars were observed within 0.1 airmass of the science objects, the standard star BS4738, an A4V star was used. This star was chosen due to the domination of hydrogen in the spectra and its lack of spectral peculiarities. The observations were taken as individual exposures of 300s at two dither points, A and B set 10" apart. The spectra were reduced as described in Chapter 3. The finished spectra are shown in figures 5.10, 5.11, 5.12. Table 5.6 details spectral features usually found in M dwarf spectra, including the location of the water bands.

All three of these objects were expected to show characteristics of late type objects - one, CBD40 indeed appears to possibly be a late M dwarf from its spectral features - particularly the FeH and KI lines as documented in table 5.6. However, the signal to noise is not high enough to make any firm conclusions about its nature, and other lines, particularly the sodium doublet which we would expect to see are not well resolved. The spectrum itself appears to be steadily rising as it progresses to longer wavelengths whereas M dwarfs tend to have a dome shaped spectrum. There is also some residual water in the spectrum which is believed to be atmospheric and not intrinsic to the object itself.

CBD67 has not been exposed for long enough and consequently the spectrum is very noisy and spectral features are indistinguishable from the noise (figure 5.12). CBD36 shows an unusual feature at 1.024 microns which may be from HeII, although this would be a very broad feature if this were so. This object shows some features that indicate it may be a late type star, although these features are not well resolved and HeII indicates a hot young object such as a white dwarf, or a galaxy. The lack of hydrogen lines in its spectrum indicates that it is unlikely to be a hot star or galaxy, or a white dwarf unless it is trapped in a binary system.
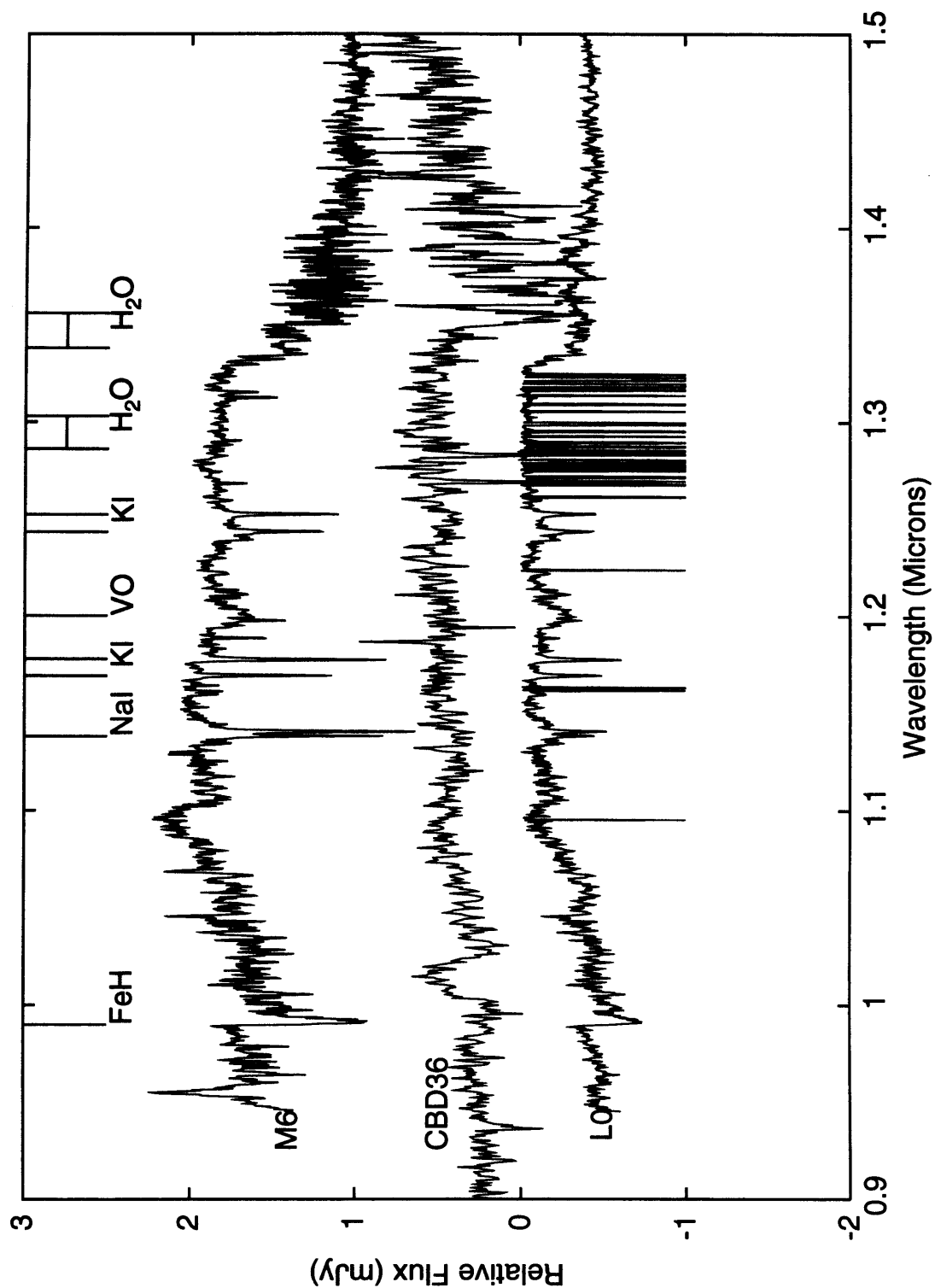
Figure 5.10: Infrared spectrum of CBD36. Note the unusual feature at 1.024 microns. Also plotted for comparison are NIRSPEC infrared spectra of the M6 dwarf Wolf 359 (top) and 2MASS345+25 an L0 dwarf (bottom) (McLean et al., 2003).
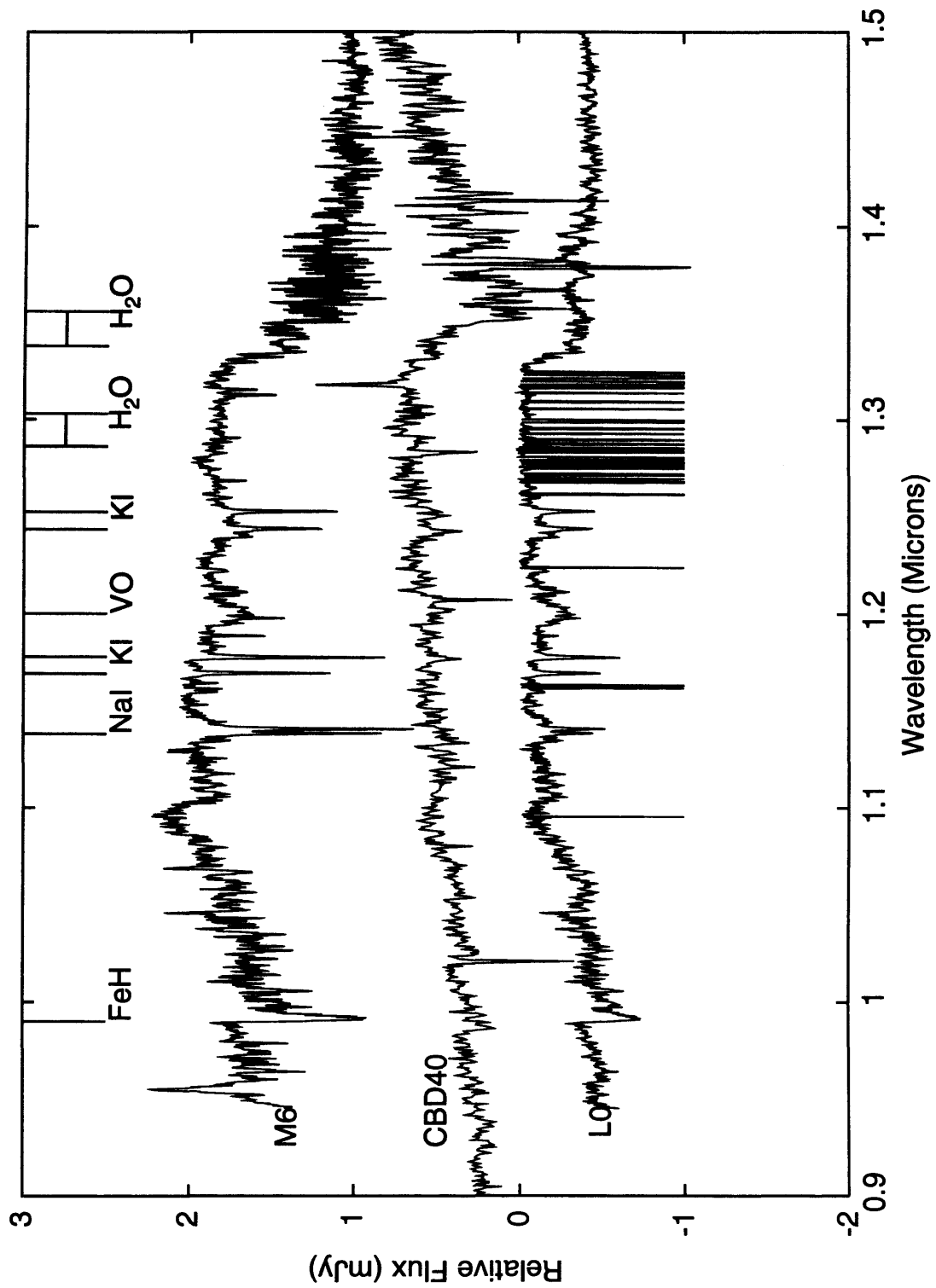
Figure 5.11: Infrared spectrum of CBD40. Believed to be a late M dwarf. Also plotted for comparison are NIRSPEC infrared spectra of the M6 dwarf Wolf 359 (top) and 2MASS345+25 an L0 dwarf (bottom) (McLean et al., 2003).
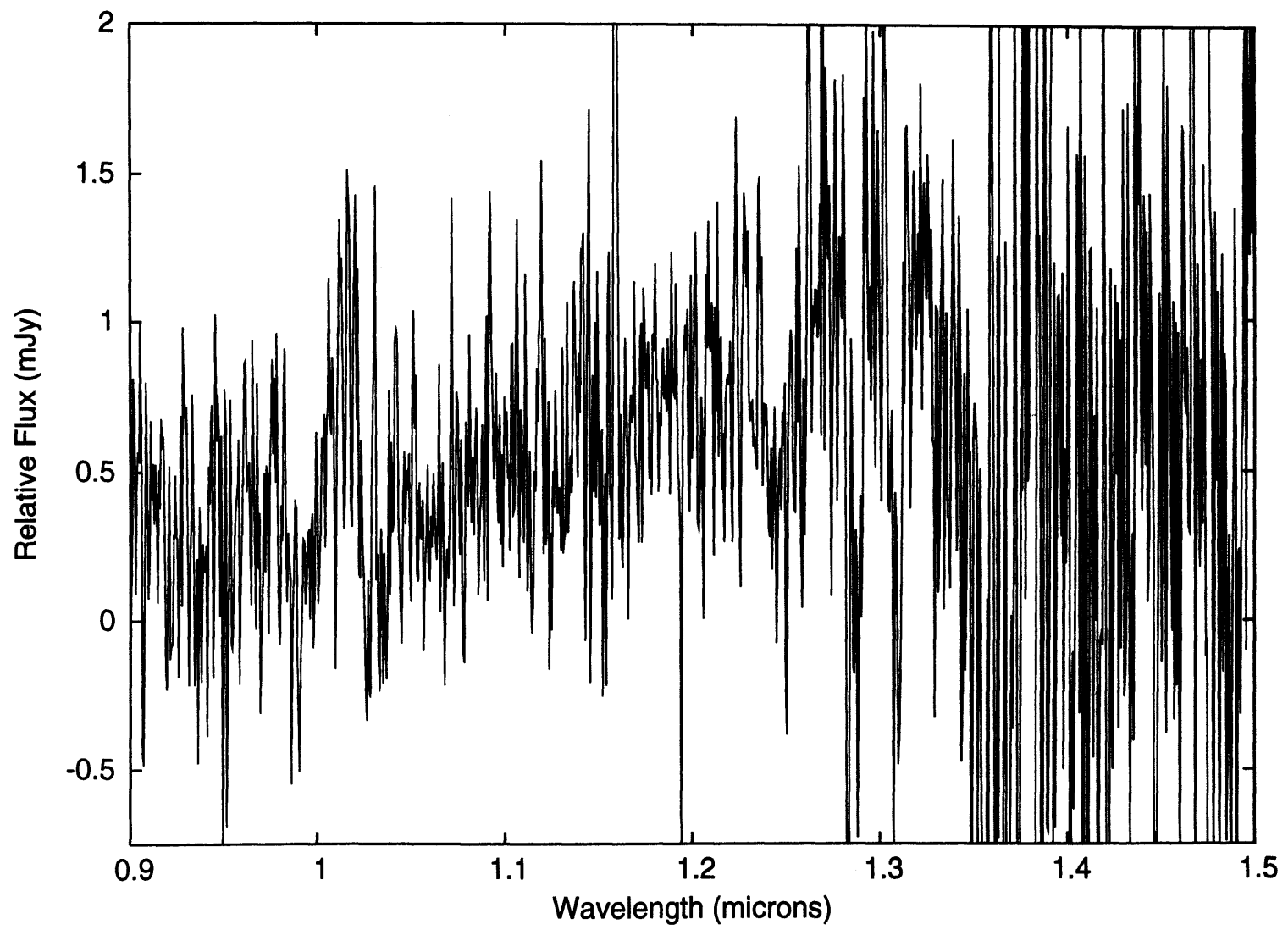
Figure 5.12: Infrared spectrum of CBD67.

131

Table 5.6: Table containing M dwarf infrared spectral features including the water and Carbon monoxide bands (Jones et al., 1994).

Line name	$\lambda(\mu m)$
FeH	0.99
NaI	1.1404, 1.1381
KI	1.1690
KI	1.1777, 1.1773
VO	1.20
KI	1.2432
KI	1.2522
CaI	1.3135
KI	1.5167, 1.5172
Al	1.6755, 1.6768
CaI	1.9272
CaI	1.95
CaI	1.987, 1.992
NaI	2.2062, 2.2090
H_2O	1.286-1.303
H_2O	1.338-1.356
CO	2.22-2.28
CO	2.30-2.36

There is always the possibility that this feature is not real, or that it is an artifact of processing. This spectrum also shows the same rising continuum as CBD40, and also shows evidence of atmospheric (not intrinsic) water which has not been removed during processing.

The two objects CBD36 and CBD67 were reobserved using LIRIS on the WHT in service time on the night of 28 April 2007. The instrument set up was as before and the seeing was 0.8" with no cloud and a 90% illuminated moon. CBD36 was reobserved for an hour, as before, but CBD67 was exposed for 2 hours as an attempt to improve the S/N of the observation. Unfortunately this attempt was unsuccessful, and one must conclude that the object is just too faint for a 4m telescope observation. The spectrum of CBD36 shows no sign of the unusual feature of the first observation, and appears to be a mid to late M dwarf as can be seen in figure 5.13. It is assumed that this was an artifact present in the data or created during the reduction. Unfortunately, the standard star was overexposed during this observation, and consequently is saturated. If CBD36 is reduced using this spectrum, the features in it are evident of a M dwarf, but the spectrum is lacking the characteristic "hump" of an M dwarf spectrum. If reduced using the standard from the previous set of observations in the previous year, the atmospheric water features are not successfully removed from the spectrum, as one would expect, however, the spectrum appears much more characteristic of an M dwarf, and so it is this spectrum that is presented in figure 5.13.

Unfortunately despite gaining infrared spectra for these three objects, the results are still inconclusive. It appears that CBD36 may be a cluster member, CBD40 is likely not to be a cluster member, from its spectrum and proper motion, and CBD67 is still unknown.

As far as the search for brown dwarfs in Melotte 111 is concerned, it must be concluded that while 13 candidate members have been identified, the follow up data so far has been inconclusive, and more data is required before any firm conclusions can be drawn as to whether these 13 objects are indeed cluster members, and if so, brown dwarfs.
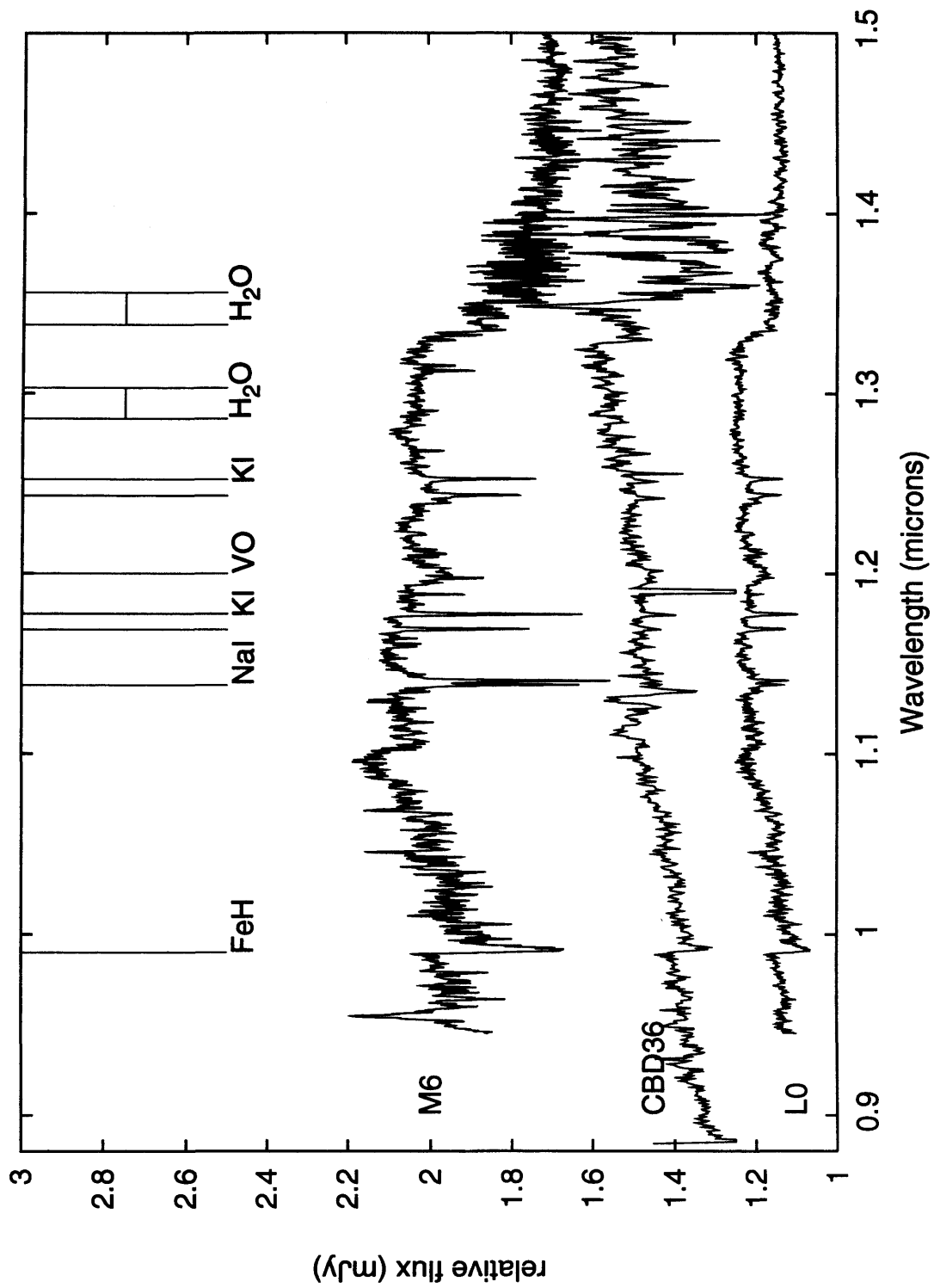
Figure 5.13: Infrared spectrum of CBD36. Also plotted for comparison are NIRSPEC infrared spectra of the M6 dwarf Wolf 359 (top) and 2MASS345+25 an L0 dwarf (bottom) (McLean et al., 2003).The unusual feature in the previous observation of this object is not present.

5.6 Summary

This chapter has briefly reviewed the previous studies of the Melotte 111 open star cluster, before describing a 50 square degree survey performed using proper motion measurements from the USNOB1.0 catalogue, and photometry from 2MASS. This survey recovered all 45 previously known members in the survey area, and identified 60 new candidate members of the cluster. The methods for calculating the probability of membership using control regions have been described, and using this information a luminosity and mass functions have been plotted for the cluster. An optical survey of the central 15 square degrees of the cluster has also been undertaken using WFC on the INT, and these data were used to identify over 100 possible low mass cluster members. These objects were then followed up in the J and K wavebands, leaving 13 brown dwarf candidate members of the cluster. Subsequent imaging in the K band with WFCAM allowed proper motions to be calculated, and 3 objects appeared to have the correct motion to be cluster members, and sat in the correct place on an empirical isochrone calculated using the Ursa Major moving group. These 3 objects were observed in March 2006 with LIRIS to gain infrared spectra of them. Unfortunately these spectra have too low S/N for any firm conclusions to be reached about their spectral types, although one object appears not to be a cluster member. More observations are needed, to calculate better proper motions, and to obtain better spectra for these objects. The results show that it is not entirely unreasonable to write off the idea that an older cluster may contain brown dwarfs, although obtaining conclusive evidence of this, may prove more difficult. It is hoped, however, that proper motion measurements calculated between the deeper Sloan and UKIDSS catalogues will allow a more in depth study of Coma to be performed in the future.

Chapter 6

Brown Dwarfs in moving groups

6.1 Introduction

This chapter describes a study that was undertaken to measure the proper motions of 143 known L and T field dwarfs. From this study, 8 high velocity L dwarfs have been identified as well as 5 wide common proper motion binary/multiple systems. Additionally, the moving group method is described, and how it has been used to identify members of the Hyades, Ursa Major and Pleiades moving groups.

6.2 Field brown dwarfs

Field brown dwarfs are relatively close and bright, making them easy to detect in a wide range of surveys via their photometry. Many brown dwarfs have been discovered using 2MASS infrared photometry, simply by analysing their location on a colour-magnitude diagram such as J, J-K and on colour-colour diagrams such as the J-H, H-K diagram. Although these objects are relatively easy to discover photometrically, there is no direct way of measuring their ages. However, their ages may be estimated by using their space motion, and possibly by surface

136

activity. Without their age, brown dwarfs cannot be fitted to isochrones to gain mass estimates, and without the distance to the object, we cannot calculate the absolute magnitude and hence use empirical isochrones. Taking a spectrum allows gravity and effective temperature to be calculated, and hence a mass (Burgasser et al., 2006c), as well as providing a spectral type for the brown dwarf. However, such measurements have quite large errors. Proper motion measurements also allow identification of the dwarf with moving groups such as the Hyades and Ursa Major moving groups, see for example, Bannister & Jameson (2007).

Bearing this in mind, a programme to measure proper motions of all of the currently known field brown dwarfs that do not have published proper motions has been undertaken. So far data for 143 have been obtained and I have calculated proper motion measurements for them all, and have used their proper motions along with convergent point theory to identify them with moving groups. Once identified with a moving group, the age and distance of the dwarf is known, allowing an empirical isochrone to be plotted for that moving group. Proper motion measurements can also identify "high velocity" dwarfs that probably belong to the thick disc or halo. They can also be used to find common proper motion wide (resolved) binaries.

6.3   Proper motion measurements

6.3.1   Data acquisition and reduction

Observations of 143 L and T dwarfs with declinations between -30° and 60° and J band magnitudes of less than 16.5 were taken, to use as a second epoch for proper motion measurements. These objects came from the M, L, and T dwarf compendium housed at DwarfArchives.org and maintained by Chris Gelino, Davy Kirkpatrick, and Adam Burgasser. The images were taken using WFCAM on UKIRT over the period of 2006a which ran from February 2006 to August 2006. This programme is continuing and further data is currently being taken (semester 2007a) in the north with WFCAM and in the south (declination<-30°) with Son OF Isaac (SOFI) on the 3.6m New Technology Telescope (NTT) at La Silla, Chile.

137

The tiling capacity of WFCAM (Casali et al., 2007) was not used as only an image of the brown dwarf in question was required. Array 3 is regarded as the least noisy array, and it was ensured that the brown dwarf was placed in the centre of the array to avoid any astrometric distortions. WFCAM is ideal for this work, as the large field of view per chip means there are many other stars in the image, which can be used as astrometric reference stars. The images were taken in the J band in non-photometric conditions using exposure times of ≈5-10 minutes and a nine point dither pattern. These exposure times gave S/N≈100 even in the poor conditions.

The images were reduced at CASU using procedures which have been custom written for the treatment of WFCAM data (Irwin et al., 2007). In brief, each frame was debiased, dark corrected and then flat fielded. The individual dithered images were stacked before having an object detection routine run on them. The frames were astrometrically calibrated using point sources from 2MASS to an accuracy of better than 0.1" (Dye et al., 2006). As for the images of the Pleiades and Melotte 111, the photometry was calibrated using 2MASS, although for these data it was more important that the astrometry was calibrated accurately than the photometry, which was not used.

6.3.2 Calculating proper motions

The astrometry for 2MASS is good to 80 mas over the whole survey, and to 50 mas over a small area (Skrutskie et al., 2006). Because the WFCAM astrometry is also calibrated to the 2MASS catalogue, accurate relative proper motion measurements could be calculated simply by taking the difference in 2MASS and WFCAM positions and dividing by the epoch difference. The epoch difference was calculated by taking the difference in the Julian date as given in the FITS header for each image, and is between 5 and 9 years, with an average epoch difference of 7.1 years. Lodieu et al. (2007) employ a similar method for calculating proper motions using the UKIDSS Galactic Cluster Survey, also using WFCAM and 2MASS. The proper motions they calculate are left as relative motions, and their errors are assumed to be ≈ 10 mas yr^{-1} although no formal error calculation was made.

138

The proper motion measurements for each object in every WFCAM image (i.e. array 3) was calculated by this method. This motion was then converted into mas yr^{-1}. The proper motion has been calculated directly from the RA and dec of the object in question, not from pixel motion on images. Hence $\mu_\alpha=(\Delta\alpha/\Delta T)\cos\delta$ arcseconds yr^{-1} if $\Delta\alpha$ is converted to arcseconds and ΔT is the epoch difference in years. These proper motions are relative proper motions, in the sense that they are relative to the bulk of the background stars in the field, which are generally moving slowly enough to be assumed to have zero motion. However, the motions of the reference stars were checked, so that the proper motion of the brown dwarf could be altered if there was a standard offset in the field. The proper motions for each field (for the dwarf and the reference stars) were separated in $\mu_\alpha\cos\delta$ and μ_δ from -500 to 500 mas yr^{-1} in each direction, in bins of size 20 mas yr^{-1}, and the number of objects falling into each bin were totalled. A two dimensional Gaussian was then fitted to the data for each field to determine the spread of the reference stars, and hence the error on the motion, as well as the true centre of the motion. The process was then repeated after the initial fit, rejecting any objects that lay outside 3σ of the fitted Gaussian, before fitting another Gaussian to this data. This fitting was important in some cases as the reference stars had quite a large spread, and in other cases the proper motion of the brown dwarf was of the same order of magnitude as the references. The centroiding errors, from the centre of the fit were subtracted from the calculated proper motion measurements.

The error on the proper motion measurements is simply the σ value of the Gaussian for each image. In general these were of the order of ~ 15 mas yr^{-1}. Strictly the astrometric errors from 2MASS and WFCAM should be added in quadrature to the σ, however, the centroiding errors are small compared to the σ value and so have been neglected.

Table 6.1 shows the name, RA, dec, proper motion and errors for the 143 objects and three examples of the data are shown in figures 6.1, 6.2 and 6.3.

Since the observations were obtained, a paper by Schmidt et al. (2007) has been published. This paper contains proper motions for 23 of these 143 objects. The proper motions as calculated here and as presented in Schmidt et al. (2007) are shown in table 6.2.
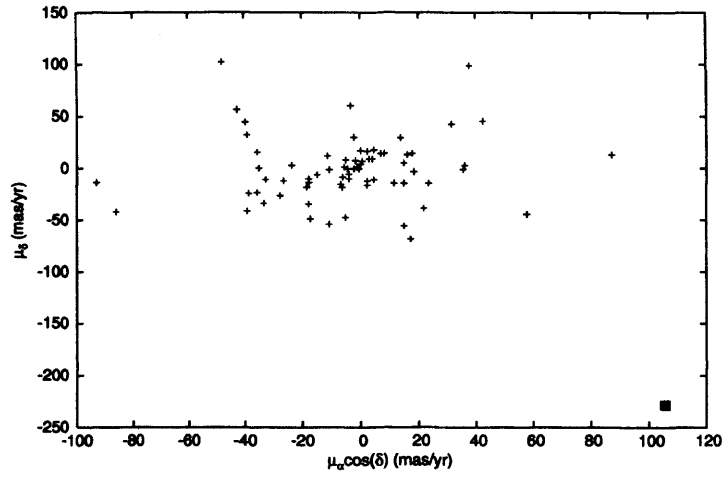
Figure 6.1: Proper motion vector diagram showing the case where there is a large spread in the reference stars compared to the motion of the dwarf i.e. they are not all concentrated around zero. The brown dwarf (J1338+04, L1, Reid et al. 2007) is marked by the filled square.
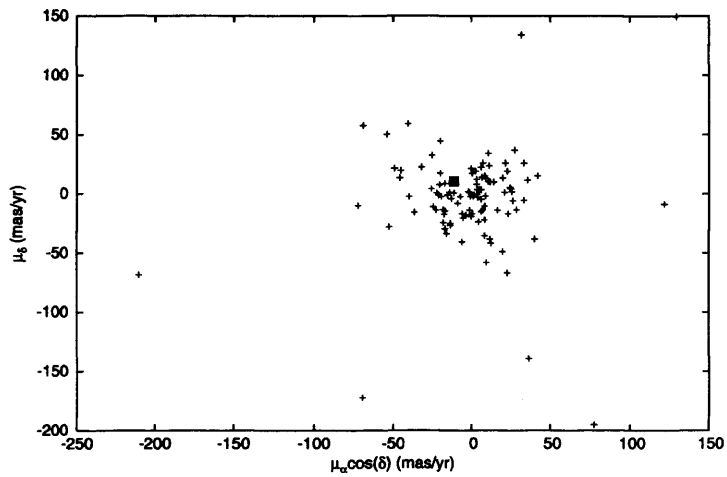
Figure 6.2: Proper motion vector diagram showing the case where the brown dwarf (J1439+03, L1, Hawley et al. 2002, filled square) has a proper motion very close to that of the reference stars in the field.

Table 6.1: Name, RA, Dec,$\mu_\alpha\cos\delta$ and μ_δ for all of the L and T dwarfs that proper motions were measured for. Hereafter these objects will be refereed to by shortened names of J followed by the first 4 digits, then the plus or minus sign and then the 2 digits after the sign. The discovery papers for these objects may be found in the DwarfArchive.

2MASS Name	RA	Dec	$\mu_\alpha\cos\delta$	μ_δ
2MASS	J2000		mas yr^{-1}	
J00001354+2554180	00 00 13.54	25 54 18.94	5.84 ± 19.47	130.03 ± 21.94
J00011217+1535355	00 01 12.23	15 35 34.45	149.65 ± 22.72	-169.14 ± 14.85
J00100009-2031122	00 10 00.15	-20 31 12.10	117.47 ± 19.59	30.74 ± 17.06
J0015447+351603	00 15 44.80	35 16 00.96	83.19 ± 17.57	-245.65 ± 13.80
J00191165+0030176	00 19 11.64	00 30 17.46	-28.79 ± 18.25	-25.01 ± 11.26
J0030438+313932	00 30 43.81	31 39 31.56	-49.44 ± 15.89	-56.86 ± 13.50
J00320509+0219017	00 32 05.26	02 18 59.82	417.19 ± 16.58	-311.77 ± 12.66
J0032431-223727	00 32 43.14	-22 37 27.14	115.06 ± 26.78	20.23 ± 14.88
J00384398+1343395	00 38 44.01	13 43 39.11	63.65 ± 16.16	-40.97 ± 8.33
J00412179+3547133	00 41 21.74	35 47 13.18	-101.90 ± 16.59	-16.66 ± 13.01
J00415453+1341351	00 41 54.46	13 41 34.35	-174.28 ± 23.61	-137.56 ± 36.03
J00452143+1634446	00 45 21.58	16 34 44.46	384.66 ± 17.12	-26.35 ± 12.27
J00464841+0715177	00 46 48.45	07 15 17.44	98.06 ± 21.53	-50.63 ± 10.04
J01033203+1935361	01 03 32.22	19 35 36.37	304.63 ± 16.54	35.18 ± 14.32
J02281101+2537380	02 28 11.15	25 37 37.84	256.53 ± 14.33	-13.98 ± 16.88
J02511490-0352459	02 51 15.48	-03 53 00.02	1128.19 ± 13.32	-1826.44 ± 19.76
J09083803+5032088	09 08 37.73	50 32 05.26	-394.92 ± 26.21	-477.67 ± 14.92
J09440279+3131328	09 44 02.81	31 31 32.46	42.96 ± 15.82	-32.53 ± 13.47
J10042066+5022596	10 04 20.55	50 22 58.18	-133.22 ± 39.63	-185.08 ± 15.42
J10101480-0406499	10 10 14.64	-04 06 49.81	-321.11 ± 15.90	20.12 ± 13.28
J10170754+1308398	10 17 07.57	13 08 39.05	60.54 ± 21.83	-93.74 ± 12.30
J10220489+0200477	10 22 04.81	02 00 45.11	-173.19 ± 18.24	-398.05 ± 15.76
J10292165+1626526	10 29 21.86	16 26 49.60	358.65 ± 14.91	-348.21 ± 17.05
J10352455+2507450	10 35 24.44	25 07 42.68	-181.48 ± 16.86	-271.82 ± 23.18

Table 6.1: continued

Name 2MASS	RA	Dec	$\mu_\alpha\cos\delta$	μ_δ
	J2000		mas yr^{-1}	
J10440942+0429376	10 44 09.41	04 29 38.20	-1.87 ± 12.11	94.47 ± 10.49
J10452400-0149576	10 45 23.76	-01 49 57.64	-494.98 ± 17.78	11.75 ± 12.05
J10473109-1815574	10 47 30.89	-18 15 57.10	-347.24 ± 17.09	54.03 ± 14.11
J10484281+0111580	10 48 42.62	01 11 56.71	-442.18 ± 13.09	-208.76 ± 12.19
J10511900+5613086	10 51 18.82	56 13 06.65	-231.49 ± 34.15	-288.05 ± 14.40
J10595138-2113082	10 59 51.45	-21 13 09.52	134.32 ± 17.06	-158.27 ± 13.58
J11040127+1959217	11 04 01.30	19 59 22.56	74.75 ± 14.65	138.77 ± 20.26
J11101001+0116130	11 10 09.91	01 16 11.50	-243.29 ± 20.82	-237.94 ± 17.78
J11131694-0002467	11 13 16.96	00 02 46.82	42.12 ± 21.73	5.91 ± 13.39
J11235564+4122286	11 23 55.56	41 22 28.09	-110.47 ± 25.23	-60.19 ± 13.22
J11455714+2317297	11 45 57.23	23 17 29.31	154.68 ± 16.47	-55.55 ± -6.46
J11480423+0254057	11 48 04.24	02 54 05.41	25.88 ± 24.78	-41.17 ± 10.28
J11480502+0203509	11 48 05.12	02 03 48.88	237.33 ± 25.57	-322.40 ± 13.25
J11533966+5032092	11 53 39.72	50 32 09.60	83.93 ± 22.95	60.19 ± 10.88
J11550087+2307058	11 55 00.89	23 07 05.96	25.80 ± 24.88	37.70 ± 20.68
J11593850+0057268	11 59 38.51	00 57 26.85	12.36 ± 22.82	6.65 ± 17.26
J12035812+0015500	12 03 57.61	00 15 48.33	-1209.29 ± 18.27	-260.69 ± 14.75
J12043036+3212595	12 04 30.40	32 12 59.37	91.42 ± 37.62	-17.54 ± 19.03
J12074717+0244249	12 07 46.96	02 44 25.72	-498.04 ± 17.54	137.51 ± 19.27
J12130336-0432437	12 13 03.18	-04 32 43.97	-353.58 ± 16.21	-12.40 ± 12.42
J12212770+0257198	12 21 27.65	02 57 19.71	-114.73 ± 30.13	-17.60 ± 27.17
J12321827-0951502	12 32 18.20	-09 51 50.97	-156.29 ± 13.04	-100.94 ± 16.93
J12392727+5515371	12 39 27.39	55 15 37.31	160.87 ± 29.34	38.06 ± 5.62
J12464678+4027150	12 46 46.85	40 27 14.45	145.05 ± 11.66	-78.75 ± 16.59
J12565688+0146163	12 56 56.80	01 46 16.14	-182.82 ± 13.21	-17.05 ± 17.81
J12573726-0113360	12 57 37.30	-1 13 36.18	81.10 ± 20.22	-2.79 ± 11.02
J13015465-1510223	13 01 54.61	-15 10 22.94	-69.22 ± 11.67	-74.28 ± 16.06

Table 6.1: continued

Name 2MASS	RA	Dec	$\mu_\alpha\cos\delta$	μ_δ
	J2000		mas yr^{-1}	
J13054106+2046394	13 05 41.05	20 46 39.95	-23.27 ± 17.49	73.37 ± 26.87
J13120707+3937445	13 12 07.00	39 37 44.61	-96.57 ± 23.23	13.43 ± 18.33
J13153094-2649513	13 15 30.53	-26 49 53.65	-677.53 ± 15.92	-280.48 ± 14.66
J13204427+0409045	13 20 44.06	04 09 05.90	-483.36 ± 19.44	210.86 ± 17.28
J13233597-1806379	13 23 35.92	-18 06 38.14	-86.89 ± 15.41	-22.18 ± 18.70
J13262009-2729370	13 26 19.90	-27 29 37.30	-363.71 ± 16.48	-15.80 ± 13.80
J13313310+3407583	13 31 32.92	34 07 57.20	-352.59 ± 18.85	-169.29 ± 18.43
J13314894-0116500	13 31 48.74	-01 16 57.65	-407.10 ± 18.61	-1029.84 ± 14.25
J13322863+2635079	13 32 28.53	26 35 08.22	-151.50 ± 12.41	40.80 ± 16.67
J13340623+1940351	13 34 06.19	19 40 36.01	-57.97 ± 12.32	98.09 ± 16.04
J13364062+3743230	13 36 40.49	37 43 22.52	-200.46 ± 8.54	-60.43 ± 13.81
J13382615+4140342	13 38 26.04	41 40 31.66	-153.13 ± 24.17	-310.98 ± 24.70
J13384944+0437315	13 38 49.49	04 37 30.13	111.65 ± 13.88	-224.27 ± 12.50
J13422362+1751558	13 42 23.57	17 51 55.59	-70.09 ± 11.13	-1.92 ± 8.31
J13431670+3945087	13 43 16.46	39 45 09.59	-343.16 ± 31.26	115.99 ± 24.80
J13484591+0353545	13 48 46.00	03 53 52.28	206.90 ± 22.82	-355.69 ± 11.19
J14023175+0148301	14 02 31.66	01 48 30.19	-232.37 ± 13.59	7.60 ± 11.06
J14044167+0235501	14 04 41.70	02 35 48.51	53.77 ± 17.37	-248.28 ± 13.22
J14044495+4634297	14 04 44.79	46 34 30.74	-231.37 ± 30.27	142.97 ± 26.38
J14075361+1241099	14 07 53.47	12 41 10.41	-312.48 ± 19.16	81.69 ± 18.75
J14111735+3936363	14 11 16.87	39 36 37.06	-910.82 ± 15.25	136.59 ± 16.18
J14122449+1633115	14 12 24.50	16 33 10.93	28.97 ± 15.90	-80.04 ± 29.96
J14304358+2915405	14 30 43.49	29 15 41.51	-184.81 ± 20.15	142.49 ± 16.41
J14305589+0013523	14 30 55.91	00 13 52.03	57.81 ± 24.21	-35.69 ± 11.98
J14321073-0058483	14 32 10.72	00 58 48.71	-9.00 ± 20.30	-31.78 ± 17.14
J14385498-1309103	14 38 55.08	-13 09 10.57	161.23 ± 21.79	-17.37 ± 15.99
J14393343+0317591	14 39 33.43	03 17 59.25	-5.58 ± 20.66	19.25 ± 16.03

Table 6.1: continued

Name 2MASS	RA	Dec	$\mu_\alpha\cos\delta$	μ_δ
	J2000		mas yr^{-1}	
J14394092+1826369	14 39 40.91	18 26 36.95	-13.43 ± 17.75	1.26 ± 25.30
J14400180+0021457	14 40 01.77	00 21 45.90	-73.61 ± 17.97	37.23 ± 17.96
J14413716-0945590	14 41 37.07	-09 45 59.20	-203.39 ± 10.97	-11.16 ± 13.96
J14482563+1031590	14 48 25.74	10 31 58.34	248.93 ± 15.43	-99.49 ± 15.58
J14493784+2355378	14 49 37.86	23 55 37.98	50.32 ± 13.25	26.69 ± 23.62
J15031961+2525196	15 03 19.66	25 25 23.56	8.98 ± 17.07	20.72 ± 17.60
J15065441+1321060	15 06 53.87	13 21 06.07	-1086.93 ± 12.67	13.63 ± 11.38
J15150083+4848416	15 15 00.24	48 47 50.74	-949.93 ± 21.33	1471.48 ± 21.40
J15210327+0131426	15 21 03.18	01 31 43.12	-211.76 ± 19.36	83.55 ± 16.58
J15394189-0520428	15 39 42.18	-05 20 42.02	599.49 ± 13.83	117.47 ± 15.23
J15472723+0336361	15 47 27.21	03 36 36.34	-62.57 ± 12.75	52.34 ± 16.99
J15474719-2423493	15 47 47.12	-24 23 50.32	-133.02 ± 14.53	-121.93 ± 16.23
J15500845+1455180	15 50 08.50	14 55 17.04	105.15 ± 18.60	-127.21 ± 12.86
J15525906+2948485	15 52 58.99	29 48 48.20	-157.35 ± 20.31	-50.89 ± 19.89
J15530228+1532369	15 53 02.05	15 32 38.22	-402.29 ± 17.20	170.52 ± 16.47
J15551573-0956055	15 55 16.18	-09 56 22.83	928.70 ± 13.98	-2375.90 ± 16.67
J15552614+0017204	15 55 26.04	00 17 20.15	-234.00 ± 17.60	-40.91 ± 18.14
J16000548+1708328	16 00 05.47	17 08 32.89	-8.80 ± 15.38	15.37 ± 21.45
J16142048+0046434	16 14 20.46	00 46 43.19	-56.83 ± 21.23	-31.32 ± 21.14
J16154416+3559005	16 15 44.15	35 58 56.29	-17.40 ± 11.94	-512.44 ± 15.48
J16184503-1321297	16 18 44.98	-13 21 30.28	-101.25 ± 14.75	-62.28 ± 14.63
J16192830+0050118	16 19 28.33	00 50 11.25	74.16 ± 16.12	-88.01 ± 16.96
J16304139+0938446	16 30 41.36	09 38 44.19	-63.77 ± 15.27	-55.79 ± 13.53
J16304999+0051010	16 30 49.96	00 51 00.15	-80.28 ± 14.87	-138.74 ± 17.95
J16452211-1319516	16 45 21.93	-13 19 57.49	-364.32 ± 17.68	-804.06 ± 15.75
J16573454+1054233	16 57 34.51	10 54 22.94	-83.53 ± 17.38	-61.18 ± 21.24

Name	RA	Dec	$\mu_\alpha\cos\delta$	μ_δ
2MASS		J2000		mas yr^{-1}
J17054834-0516462	17 05 48.40	-05 16 47.06	129.32 $\pm$ 14.10	-102.57 $\pm$ 14.92
J17073334+4301304	17 07 33.21	43 01 30.20	-200.33 $\pm$22.02	-21.50$\pm$ 13.67
J17111353+2326333	17 11 13.49	23 26 32.96	-53.24 $\pm$ 11.33	-35.65 $\pm$ 16.02
J17210390+3344160	17 21 02.69	33 44 20.85	-1853.63 $\pm$ 17.27	601.67 $\pm$ 16.84
J17260007+1538190	17 26 00.05	15 38 18.49	-31.20 $\pm$ 12.73	-47.96 $\pm$ 14.38
J17282217+5845095	17 28 22.19	58 45 10.12	23.65 $\pm$ 13.39	101.69 $\pm$ 12.00
J17312974+2721233	17 31 29.71	27 21 21.79	-81.88 $\pm$ 15.32	-239.88 $\pm$ 17.02
J17502385+4222373	17 50 23.82	42 22 38.02	-43.75 $\pm$ 15.94	94.51 $\pm$ 14.29
J17580545+4633099	17 58 05.47	46 33 14.57	25.51 $\pm$ 15.45	593.64 $\pm$ 15.77
J18071593+5015316	18 07 15.94	50 15 30.86	34.61 $\pm$ 18.53	-125.71 $\pm$ 14.26
J20025073-0521524	20 02 50.69	-05 21 53.29	-97.78 $\pm$ 13.02	-104.97 $\pm$ 13.65
J20251584-2943124	20 26 15.87	-29 43 15.25	42.87 $\pm$ 19.44	-347.63 $\pm$ 14.97
J20282035+0052265	20 28 20.39	00 52 26.53	114.08 $\pm$ 14.20	6.95 $\pm$ 15.27
J20343769+0827009	20 34 37.66	08 26 58.05	-76.65 $\pm$ 15.34	-467.88 $\pm$ 14.90
J20360316+1051295	20 36 03.11	10 51 28.42	-115.22 $\pm$ 13.57	-167.99 $\pm$ 14.07
J20543585+1519043	20 54 35.83	15 19 03.79	-44.56 $\pm$ 17.50	-82.44 $\pm$ 17.60
J20571538+1715154	20 57 15.42	17 15 15.70	90.42 $\pm$ 16.27	66.20 $\pm$ 14.74
J21041491-1037369	21 04 15.23	-10 37 39.22	614.32 $\pm$ 15.90	-280.70 $\pm$ 14.53
J21073169-0307337	21 07 31.76	-03 07 33.83	169.62 $\pm$ 17.75	-9.94 $\pm$ 13.29
J21241387+0059599	21 24 13.95	01 00 01.49	201.78 $\pm$ 14.07	287.22 $\pm$ 14.24
J21304464-0845205	21 30 44.80	-08 45 20.84	360.41 $\pm$ 12.75	-31.18 $\pm$ 14.18
J21373742+0808463	21 37 10.38	14 50 46.82	-138.19 $\pm$ 13.82	-122.41 $\pm$ 17.00
J21371044+1450475	21 37 37.70	08 08 46.91	704.52 $\pm$ 21.14	102.28 $\pm$ 18.58
J21404656+0112594	21 40 46.51	01 12 58.38	-78.42 $\pm$ 20.34	-164.35 $\pm$ 22.03
J21522609+0937575	21 52 26.20	09 37 58.42	293.64 $\pm$ 18.65	170.15 $\pm$ 17.32
J21580457-1550098	21 58 04.60	-15 50 10.14	69.64 $\pm$ 11.27	-33.12 $\pm$ 14.92
J22081363+2921215	22 08 13.70	29 21 21.33	111.25 $\pm$ 14.37	-11.47 $\pm$ 14.05
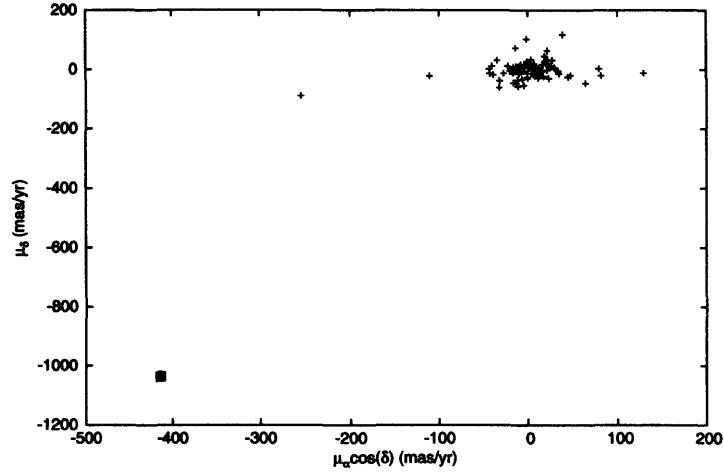
Figure 6.3: Proper motion vector diagram showing the ideal case. The reference stars are concentrated on zero, and the brown dwarf marked by the filled square (J1331-01, L6, Hawley et al. 2002) has a large proper motion.

Table 6.1: continued

Name	RA	Dec	$\mu_\alpha \cos\delta$	μ_δ
2MASS	J2000		mas yr^{-1}	
J22134491-2136079	22 13 44.94	-21 36 08.56	59.56 ± 10.65	-62.73 ± 16.88
J22425317+2542573	22 42 53.40	25 42 56.94	408.77 ± 15.46	-45.19 ± 16.17
J22443167+2043433	22 44 31.81	20 43 41.34	251.74 ± 13.97	-213.74 ± 10.81
J22521073-1730134	22 52 10.92	-17 30 12.48	404.85 ± 20.23	153.57 ± 20.33
J22541892+3123948	22 54 18.96	31 23 51.33	67.94 ± 15.11	200.74 ± 11.26
J22545194-2840253	22 54 51.94	-28 40 25.20	8.20 ± 18.69	51.81 ± 30.09
J22591388-0051581	22 59 13.91	00 51 57.87	83.81 ± 16.71	67.87 ± 16.80
J233302258-0347189	23 30 22.71	-03 47 18.84	231.86 ± 17.43	31.93 ± 13.63
J23440624-0733282	23 44 06.25	-07 33 28.72	21.34 ± 16.63	-51.27 ± 7.71
J23453909+0055137	23 45 39.07	00 55 13.45	100.97 ± 18.74	-34.01 ± 14.45
J23515044-2537367	23 51 50.65	-25 37 35.27	377.56 ± 20.85	210.93 ± 22.14

Table 6.2: Name, proper motion (from Schmidt et al. 2007), position angle(from Schmidt et al. 2007), proper motion (from this study) and position angle (from this study) for the 23 dwarfs which appear in Schmidt et al. (2007).

Name 2MASS	μ (Schmidt) $"\,yr^{-1}$	PA (Schmidt) $^\circ$	μ $"\,yr^{-1}$	PA $^\circ$
J0045+16	0.36±0.04	102±7	0.38±0.02	93±2
J0251-03	2.17±0.11	148±2	2.14±0.02	148±0.6
J0908+50	0.52±0.25	202±21	0.61±0.02	220±1
J1045-01	0.46±0.12	266±8	0.49±0.02	272±1.5
J1048+01	0.52±0.1	241±9	0.48±0.01	240±0.6
J1051+56	0.32±0.09	197±23	0.36±0.0	219±3
J1104+19	0.14±0.08	24±31	0.15±0.02	28±1
J1203+00	1.00±0.15	257±6	1.23±0.02	258±0.5
J1213-04	0.15±0.09	260±38	0.35±0.02	268±2
J1221+02	0.09±0.16	258±76	0.11±0.02	262±11.5
J1448+10	0.71±0.15	98±13	0.26±0.02	111±4
J1506+13	1.11±0.08	274±3	1.08±0.01	271±0.6
J1515+48	1.71±0.05	327±1	1.75±0.02	328±1
J1539-05	0.6±0.04	85±7	0.61±0.01	78±1
J1721+33	1.92±0.11	287±3	1.94±0.02	288±0.6
J1731+27	0.28±0.05	200±5	0.25±0.02	199±2
J1807+50	0.16±0.05	167±15	0.13±0.01	164±9
J2028+00	0.14±0.09	105±28	0.11±0.01	86±7
J2036+10	0.26±0.09	216±21	0.20±0.01	215±1
J2057-02	0.08±0.02	171±17	0.07±0.01	170±12
J2104-10	0.66±0.05	115±3	0.68±0.02	114±1.6
J2251-17	0.45±0.12	71±10	0.43±0.02	69±1.6
J2351-25	0.42±0.11	62±15	0.43±0.02	60±01

There are two objects for which there is not a good agreement between this data and the results of Schmidt et al. (2007). These objects are J1213-04 and J1448+10. Both J1213-04 and J1448+10 have position angles that agree, but the proper motion measurements do not. The discrepancy involving J1213-04 can almost be explained by the errors on the Schmidt et al. (2007) measurement (μ_α=144±80, μ_δ=-25±98, Cruz 2007a). My μ_δ agrees with that of Schmidt et al. (2007), although the large disagreement with μ_α (my measurement=248±15, Schmidt et al. measurement=708±142) may be explained by the object being faint and a small epoch difference (<4 years) for the Schmidt et al. (2007) measurement.

There are two notes that should be made regarding these 143 objects. The first is that J1048+01 has a somewhat unclear spectral type. Using an optical spectrum, Hawley et al. (2002) identify it as an L1 dwarf. Using infrared spectra, Kendall et al. (2004) identify it as an L4 dwarf, and Wilson et al. (2003) identify it as an M7 dwarf also using infrared spectra. It is unknown as to why this discrepancy has occurred.

The second note is that J2213-21 has been identified as a possible low gravity object by Cruz et al. (2007b) from the VO bands, K I doublet and Na I doublet in the optical spectrum of this object. These features are gravity sensitive, and low gravity features indicate youth and low mass, although Hα was not detected in the spectrum.

6.4 Common proper motion objects

Brown dwarfs in binary or multiple star systems are of great interest as their properties such as masses and separations can allow constraints to be put on star formation models. This is especially important as no one mechanism has been found that can account for the formation of all known brown dwarf binaries. Many searches have been undertaken for close binary systems using imaging, however, wider systems are found more infrequently. Only one brown dwarf-brown dwarf system has been discovered to date with a separation of greater than 15 AU (Billères et al., 2005), in contrast to several known systems with a high mass primary and

brown dwarf companion. Allen et al. (2007) estimate the wide binary fraction for these objects to be 2.3% for companions with masses greater than 0.03-0.05 $M_\odot$.

A "standard" σ value of 15 mas yr^{-1} was selected within which to search for common proper motion companions to the L and T dwarfs. This value was chosen as an average value of the errors, and therefore this search is by no means conclusive. However, as some objects have very little proper motion compared to the background stars, searching for common proper motion objects yields many candidates. No more can be said about these objects, other than they are candidates and more information is required. For the objects that have proper motions that are much higher than the background stars (129 out of the 143 objects), as one would expect for nearby L and T dwarfs, searching for proper motion companions (i.e. objects with proper motions that fall within a radius of 15 mas yr^{-1} of the motion of the dwarf) is more robust and yields a few results.

Six new potential common proper motion wide binary or multiple systems are found, although it is concluded that one of these is probably not a genuine multiple. Two previously discovered common proper motion wide binaries are also confirmed

Previously confirmed binaries in the data

J1004+50 is an L2 dwarf identified from its optical spectrum by Kirkpatrick et al. (2001). J1004+50 is also known as G 196-3B and was discovered by direct imaging (Rebolo et al., 1998). It is estimated to have a mass of $\approx$25 M_{Jup} by Rebolo et al. (1998), although Kirkpatrick et al. (2001) calculates a mass of $\approx$35 M_{Jup}. G 196-3 itself is a high proper motion M3 dwarf which has proper motion of -138, -199 mas yr^{-1} (Salim & Gould, 2003). I calculate proper motion of -133.21$\pm$39.61, -185.08$\pm$15.41 for the L dwarf. This difference in motion is within the 15 mas yr^{-1} required for an object to be selected as a binary, although the M dwarf is saturated in the WFCAM image, thus resulting in an incorrect proper motion being calculated for it due to bad centroiding. The separation of the two is estimated to be 16.2 arcseconds which corresponds to 350 AU at an estimated distance of 21 pc.

J1441-09 belongs to a triple system consisting of a primary dM4.5e. J1440-09 is in fact the secondary, which has been proved to also be a binary star system, consisting of two L1 dwarfs (Seifahrt et al., 2005). I have calculated a proper motion for J1441-09 to be $\mu_\alpha\cos\delta$=-203.38±10.96, μ_δ=-11.16±13.96 yielding a magnitude of 203.68±20 mas yr^{-1} which is consistent with the 206±13 mas yr^{-1} calculated by Seifahrt et al. (2005). I find the proper motion of the primary to be -213.62±10.96, -7.20±13.96. Seifahrt et al. (2005) also calculate a parallax for this objects of 34±7 mas, and using this value along with the convergent point method have shown that this system is likely to be a member of the Hyades Supercluster.

There are 6 objects that were selected as possibly having binary companions, although on closer inspection one object appears unlikely. These objects all appear to have proper motion companions. The proper motions, distance from the dwarf, J, H and K_S magnitudes of these objects and the L dwarf "primary" are given in table 6.3.

New binary candidates

J0041+13 has a spectral type of L0 (Hawley et al., 2002) and has very similar proper motion to a brighter field object 2MASSJ00415543+1341162 which is also known as NLTT 2274. This object and is labelled as a high proper motion star by SIMBAD, which lists a proper motion of -191, -167 mas yr^{-1} (Salim & Gould, 2003), consistent with the proper motions presented here.

J1017+13, a brown dwarf of spectral type L2 (Cruz et al., 2003) was reported as a candidate binary system by Bouy et al. (2003). Their HST imaging program using WFPC2 determined a separation of 104±2.8 mas and a position angle of 92°.6±1°.2. The two components are found to have differences in magnitudes, suggesting they are of different mass. The photometric distance for this object was calculated to be ≈21.4 pc. I calculate a proper motion

Table 6.3: Name (2MASS), proper motion for each component, J, H and K$_S$ magnitudes and distance from L dwarf for the 6 new possible binaries.

Name	$\mu_\alpha\cos\delta$	μ_δ	J	H	K$_S$	Separation
	mas yr^{-1}					"
J0041+13	-174.28±23.60	-137.55±36.02	14.454±0.031	13.673±0.036	13.236±0.024	-
J00415543+1341162	-182.28±23.60	-141.99±36.02	10.164±0.029	9.574±0.033	9.347±0.018	32.02
J1017+13	60.53±21.83	-93.74±12.29	14.096±0.021	13.284±0.026	12.710±0.021	-
J10171515+1307419	58.08±21.83	-105.12±12.29	16.827±0.157	16.497±0.296	17.365	125.32
J1153+50	83.92 ±22.95	60.19±10.88	14.189±0.026	13.305±0.024	12.851±0.025	-
J11535018+5035593	87.50±22.95	70.37±10.88	17.145±0.173	16.349±0.233	15.832±0.203	251.12
J1449+23	40.31±13.25	26.69±23.61	15.818±0.074	15.004±0.086	14.311±0.084	-
J14493550+2357118	48.3±13.25	30.71±23.61	16.663±0.154	17.709	14.311	99.36
J1547+03	-62.56±12.74	52.33±16.98	16.077±0.071	15.070±0.062	14.270±0.072	-
J15470234+0338260	-51.91±12.74	57.67±16.98	16.275±0.094	15.843±0.124	15.691±0.233	388.44
J2259-00	83.81±16.70	67.87±16.79	16.357±0.097	15.315±0.087	14.651±0.087	-
J22590929-0051556	69.93±16.70	72.91±16.79	11.264±0.026	10.993±0.026	10.872±0.021	68.80
J22590491-0052407	87.59±16.70	60.30±16.79	17.123±0.214	16.300±0.231	15.692±0.229	141.11

of $\mu_\alpha \cos\delta$=60.53±21.83, μ_δ= -93.74 ±12.29 for the brown dwarf, and $\mu_\alpha \cos\delta$=58.08±21.83, μ_δ=-93.74±12.29 for another object in the field, 2MASSJ10171515+1307419. This would make the system a triple system. The objects are separated by 125".35.

2MASSJ10171515+1307419 has J=16.827±0.157, H=16.497±0.296 and K_S=17.365 (2MASS gives no error for this measurement), compared to J=14.096±0.021 H=13.284±0.026 and K_S=12.710±0.021 for the brown dwarf. This wide companion appears to be a T dwarf at the distance of 22.8 pc (as calculated from spectral type of the L dwarf, Cruz et al. 2003) from its colours (using the empirical data in Leggett et al. 2002) and absolute magnitude. This object does form a sequence with the L2 primary, which may also be a binary. It should be noted that this object is faint so the 2MASS measurement and the WFCAM measurements of it are of low signal to noise. More information is needed before conclusions can be drawn.

J1153+50 has a spectral type of L1 (Reid et al., 2007) and appears to have a much fainter field object associated with it. Assuming a distance of 27.4 pc for this dwarf (calculated from its spectral type using equation 6.1) and the companion, the colours of the companion indicate a spectral type of between L5 and L8 (Leggett et al., 2002) and the absolute magnitude of the companion fits the L-T dwarf sequence, strengthening the case that these dwarfs are companions.

J1449+23 is reported as being a binary by Gizis et al. (2003). This is currently one of the widest L dwarf doubles known, at a separation of 13 AU. J1449+23 has a spectral type of L0 (Kirkpatrick et al., 2000) and it is not known if the components are very low mass stars or brown dwarfs. I calculate a proper motion for J1449+23 of $\mu_\alpha \cos\delta$=50.31±13.25, μ_δ=26.69±23.61. This study has also found an object situated 1'39".35 away from J1449+23 which has proper motion of $\mu_\alpha \cos\delta$=48.3±13.25, μ_δ=30.71±23.61, making this a prospective triple system. The object, J14493550+2357118 has J=16.663±0.154, H=17.709, K_S=16.860 (2MASS does not give errors for the latter two measurements). J1449+23 itself has magnitudes of J=15.818±0.074, H=15.004±0.086 and K_S=14.311±0.084. J14493550+2357118 has impossibly blue colours (J-K=-0.197, J-H=-1.046), although this may simply mean the

2MASS magnitudes are very unreliable and an upper limit. It is, however, possible that this object is a white dwarf. When SDSS colours are compared to the Holberg & Bergeron (2006) synthetic hydrogen white dwarf photometry, it falls along the hydrogen track, with a mass of 0.2 $M_\odot$, $T_{eff} \approx 4000$ K and log g ≈ 1.75. If this object is a white dwarf it will be one of only a few white dwarf-brown dwarf known binaries (GD165, Becklin & Zuckerman 1988, GD1400, Farihi & Christopher 2004, Dobbie et al. 2005, WD0137-349, Maxted et al. 2006; Burleigh et al. 2006, SDSS1212, Burleigh et al. 2006) although more are suspected. See Steele et al. (2007) for a list of low mass companions to white dwarfs.

It seems unlikely that a white dwarf with a mass of 0.2 $M_\odot$ could have a log g of 1.75, which is very low and is not consistent with the mass-radius relation for white dwarfs. It seems more probable that this object is a background high proper motion, metal poor K dwarf, which would also exhibit these colours. Many common proper motion objects are in fact high velocity background dwarfs, particularly at large separations (Farihi et al., 2005). A spectrum of this object is needed before any conclusions can be drawn.

J1547+03 has a spectral type of L2 (Hawley et al., 2002) and appears to be associated with a field object, that appears to be only slightly fainter. This object has blue J-K and J-H colours that are not consistent with a T dwarf of the same distance as J1547+03 as it would be too bright. The Sloan photometry and JHK photometry is consistent with a white dwarf at the same distance (58.8 pc) as the brown dwarf according to the Helium track of the Holberg & Bergeron (2006) models. This white dwarf would have a log g of 7.4, a T_{eff}=5500, a mass of 0.3$M_\odot$ and an age of $\approx$ 1.7 Gyr. As for J1449+23. As with J1449+23, the mass for this white dwarf would be incredibly low, making it more likely that this object is a high velocity K dwarf. An optical spectrum of this object taken using ISIS on the WHT, has confirmed that this object is a K dwarf.

J2259-00 has a spectral type of L2 (Hawley et al., 2002) and has similar proper motion to two field objects, one which is much brighter and one, which is much fainter. This fainter object has a possible spectral type of L3 (using the colours and Leggett et al. 2002) at a distance of

64.6 pc (derived from spectral type). However, when plotted on the M_K, J-K colour magnitude diagram, these three objects do not form a sequence. The brighter object has colours that are approximately those of a G8 dwarf main sequence star, but at this distance, the object in question is too faint. It is not believed that this brighter object is a companion to the dwarf. The fainter companion also does not lie on a sequence with the L2 dwarf. It is believed that these three objects have similar proper motions, but are not related.

Out of the 129 dwarfs with isolated enough motion to study, 5 appear to have companions. Of these 5, only 2 appear to be possible brown dwarf-brown dwarf binaries. From this study the wide brown dwarf-brown dwarf binary fraction is 1.55%, which is in agreement with the 2.3% upper limit calculated by Allen et al. (2007). This binary fraction is obviously not derived from a statistically sound sample and should not be treated as a robust statistic. The binary fraction for white dwarf-brown dwarf systems is estimated to be less than 0.5% (Farihi et al., 2005). Many more such binaries will ultimately be discovered by the UKIDSS large area survey when its second epoch for proper motions is complete.

6.5 High velocity dwarfs

From the proper motions calculated using the WFCAM and 2MASS data, nine objects were selected as having an extremely high proper motion (>0.85" yr^{-1}, figure 6.4). Five of these nine objects appear in Schmidt et al. (2007) and two are mentioned in the text as having large proper motions. These proper motion and position angle measurements agree with those that appear in table 1 of Schmidt et al. (2007) to within the errors as shown in table 6.4. Tables 6.4 and 6.5 show the data for the 9 L dwarfs selected as high velocity L dwarfs. Distances are calculated using the M_J spectral type relation given by Cruz et al. (2003) and shown in equation 6.1,

$$M_J = -4.410 + 5.043(ST) - 0.6193(ST)^2 + 0.03453(ST)^3 - 0.0006892(ST)^4, \quad (6.1)$$
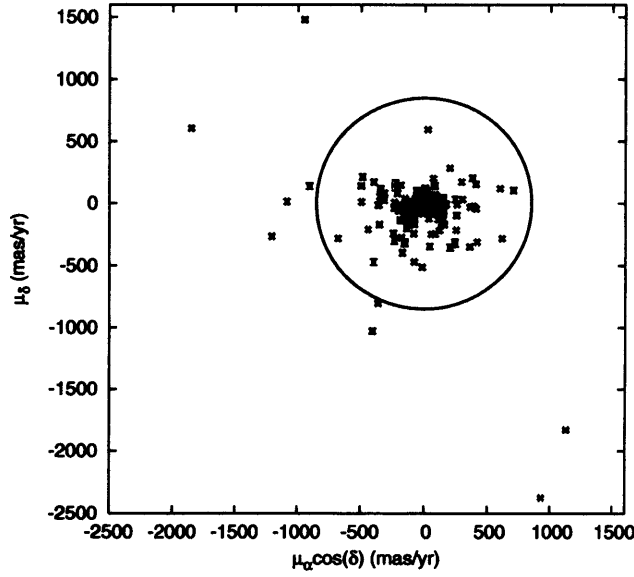
Figure 6.4: Proper motions of the 143 brown dwarfs. The circle has a radius of 0.85". The objects outside this circle, are the nine fast moving objects.

where $ST = 0$, 10 and 18 for spectral types M0, L0 and L8 respectively. Cruz et al. (2003) state that the error on this relationship comes from the uncertainties in spectral types. An approximate error of 13% on the distance based on the scatter in the Cruz relation and an assumed uncertainty of ± half a spectral class has been calculated. This relationship has less scatter than relationships using J-K$_S$ colours to derive M$_J$. The tangential velocities can then be derived from the proper motions and distances. All nine dwarfs have tangential velocities exceeding 70 kms^{-1}. The error on the velocities has been taken to be 13%, dominated by the distance error. Schmidt et al. (2007) find the mean tangential velocity for a sample of M and L dwarfs to be 31.5 kms^{-1}, with a velocity dispersion of 20 kms^{-1}. It should be noted that although J1645-31 has a high proper motion, at a distance of ≈ 12 pc, it is not actually moving that fast, compared to the other fast moving objects, all of which have much higher velocities. The remaining 8 L dwarfs clearly have extreme velocities and the natural interpretation is that they belong to the old disc, thick disc or possibly galactic halo population. Schmidt et al. (2007) also identified two of these dwarfs, J1721+33 and J2051-03 as high velocity dwarfs.

To better understand the motion of these fast moving objects, the proper motion measurements in right ascension and declination (μ_α, μ_δ) were transformed into proper motion on the galactic

155

Table 6.4: Name, spectral type (from optical spectra), distance (as calculated from spectral type), proper motion (from Schmidt et al. (2007)), position angle(from Schmidt et al. (2007)), proper motion (from this study), position angle (from this study) for the 9 high velocity dwarfs, 5 of which appear in Schmidt et al. (2007).

Name 2MASS	Spt	d pc	μ (Schmidt) " yr^{-1}	PA (Schmidt) °	μ " yr^{-1}	PA °
J0251-03	L3	11.98	2.17±0.11	148±2	2.14±0.02	148±0.6
J1203+00	L3	18.53	1.00±0.15	257±6	1.23±0.02	258±0.5
J1331-01	L6	19.53	-	-	1.07±0.01	202±0.6
J1411+39	L1.5	31.56	-	-	0.92±0.02	279±1.1
J1506+13	L3	13.80	1.11±0.08	274±3	1.08±0.01	271±0.6
J1515+48	L6	10.50	1.71±0.05	327±1	1.75±0.02	328±1.0
J1555-09	L1	12.94	-	-	2.55±0.02	158±0.5
J1645+13	L1.5	11.52	-	-	0.88±0.01	205±1.0
J1721+33	L3	15.56	1.92±0.11	287±3	1.94±0.02	288±0.5

co-ordinate (μ_l, μ_b) system using equations 6.2 where ϕ is the angle between the direction towards the north celestial pole and the north galactic pole (Reid & Hawley, 2005).

$$\mu_l = \mu_\alpha \cos(\phi) + \mu_\delta \sin(\phi),$$

$$\mu_b = -\mu_\alpha \sin(\phi) + \mu_\delta \cos(\phi). \tag{6.2}$$

Using spherical trigonometry it can be shown that

$$\cot(\phi) = \frac{\cos(\delta) \tan(\delta_0) - \sin(\delta) \cos(\alpha - \alpha_0)}{\sin(\alpha - \alpha_0)}, \tag{6.3}$$

where α and δ are the right ascension and declination of the star in question and α_0 and δ_0 are the co-ordinates of the north galactic pole.

The Cruz relationship (a fourth order polynomial fit) between M_J and spectral type applies for

spectral types between M6 and L8 and was previously shown in equation 6.1. This relationship was used to calculate distances for these dwarfs (using optical spectral types which are more reliable for this range of spectral types), and this distance was then used to transform the proper motions into velocities (V_l, V_b) in galactic coordinates,

$$V_l = 4.74\mu_l d,$$

$$V_b = 4.74\mu_b d,$$

$$V_r = \frac{c\Delta\lambda}{\lambda},$$

$$(6.4)$$

where d is the distance and proper motions are in arcseconds per year, λ is the wavelength of the observation, and $\Delta\lambda$ is the wavelength shift due to the dwarf's motion. The value 4.74 comes from the unit conversion factor, and is the ratio between the number of kilometres in a parsec, and the number of seconds in a year multiplied by the number of arcseconds in a radian.

To be able to study these velocities in relation to the galaxy, these velocities were transformed onto a right handed co-ordinate system, with orthogonal axes directed towards the galactic centre, the U velocity, in the direction of galactic rotation (l=90°, b=0°), V velocity and perpendicular to the galactic plane, W velocity,

$$U = V_r \cos(l)\cos(b) - V_b \cos(l)\sin(b) - V_l \sin(l),$$

$$V = V_r \sin(l)\cos(b) - V_b \sin(l)\sin(b) + V_l \cos(l),$$

$$W = V_r \sin(b) + V_b \cos(b). \qquad (6.5)$$

The radial velocity is unknown for these dwarfs. If l≈0 or 180° it is possible to find V, since $V_r \sin l \approx 0$ (see equation 6.5). Likewise if l≈90 or 270° it is possible to find U.

Table 6.5 gives approximate U and V velocities for those dwarfs close to such special locations. J0251-03 and J1555-09 have V=-120.20 kms^{-1} and V=-73.18 kms^{-1} respectively and J1203+00 and J1515-09 have U=-81.61 and U=-86.81 kms^{-1} respectively.

Table 6.5: Name, l, b, V_{Total} (total velocity), U (velocity in the direction of the galactic centre), V (velocity in the direction of galactic rotation), K_S, J-K_S and $L/L_\odot$ for the eight fast moving dwarfs. The values in bold are the reliable values of V and U.

Name 2MASS	l °	b	V_{Total}	U kms^{-1}	V	K_S	J-K_S	$L/L_\odot$ $\times 10^{-4}$
J0251-03	179.10	-53.15	121.97	15.86	**-120.20**	11.662	1.39	1.18
J1203+00	277.98	60.81	108.71	**-81.61**	-65.33	12.476	1.53	1.33
J1331-01	323.42	59.97	102.55	15.78	-93.32	14.073	1.38	0.34
J1411+39	74.98	69.25	137.81	-110.37	-73.41	13.239	1.40	1.91
J1506+13	16.21	55.52	71.10	-40.29	-46.60	11.741	1.62	1.45
J1515+48	80.75	54.88	87.18	**-86.81**	4.12	12.500	1.61	0.41
J1555-09	359.58	32.05	156.52	73.05	**-73.18**	11.443	1.14	1.68
J1721+33	57.35	32.52	143.70	-52.09	120.70	12.489	1.36	0.92

These eight dwarfs have velocities that are typical of a thick disc population (Burgasser et al., 2007c). All eight L dwarfs have spectral types derived from optical spectra (Cruz et al., 2003; Fan et al., 2000; Hawley et al., 2002; Kirkpatrick et al., 2001; Gizis et al., 2000; Wilson et al., 2003; Gizis, 2002) and none of the authors comment on any of the spectra being abnormal. The spectrum is shown for J1411+39 which appears quite usual (figure 6.5).

J1203+00 possibly shows a stronger FeH band than some of the other spectra (Fan et al., 2000). Schmidt et al. (2007) comment that J1721+33 has unusually blue J, H, K_S colours and a similar point was discussed in Gizis et al. (2000) for J13004255+1912354, which, while not one of the dwarfs studied here, has a high velocity. Figure 6.6 shows a plot of J-K_S vs spectral type for all of the L dwarfs in the Dwarf Archive. The 8 high velocity dwarfs are also shown and it can be seen that they tend to have bluer values of J-K_S. The fastest moving objects J1721+33, J1331-01 and J1555-09 are also the bluest. From the spectral type vs J-H and H-K_S diagrams (figures 6.7 and 6.8) it appears that the blueness is more prominent in J-H for early spectral types, while for the L6 dwarfs the H-K_S colour is very blue. It should be
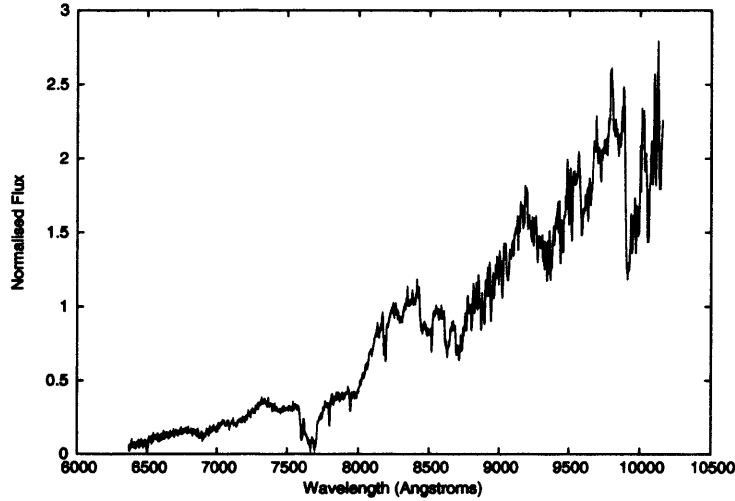
Figure 6.5: Near infrared spectrum of J1411+39 from Kirkpatrick et al. (2000).

noted that J1506+13 and J1203+00 are only marginally blue for their spectral type.

The blue J, H and K_S colours are expected for metal poor stars since the collisionally induced molecular hydrogen opacity is relatively more important and this increases rapidly from J to K depressing the longer wavelengths (Burgasser, 2007b). Burgasser et al. (2007c) discuss 16 spectroscopically confirmed subdwarfs. The L4 subdwarf 2MASS J1626+3925 shows a broad dip from 6700 - 7300 Å when compared to a "standard" L4 dwarf. This dip is much less pronounced in the L7 subdwarf 2MASS J0532+8246 when compared to a "standard" L7 dwarf. Indeed, it is difficult to distinguish the L7 subdwarf from an ordinary L7 dwarf by its 6500 - 9000 Å spectrum. The L7 spectra are shown in figure 6.9.

The 6700 - 7300 Å dip is not obvious in the published spectrum of the L3 dwarf J1721+33 and is not expected in the L6 spectra of J1331-01 and J1555-09. Thus the only supporting evidence that these high velocity dwarfs are metal poor is the blue J-K_S colour. These objects are not blue enough to be considered subdwarfs as defined by Burgasser et al. (2007c).

If it is assumed that all 8 of these dwarfs are likely to belong to the thick disc population (they are not blue enough to belong to the population II halo) then it is expected that they will be old, with an age of ~10 Gyr. This is most likely for the three having the most obviously blue J-K_S colour, J1721+33, J1331-01 and J1555-09. With an age of ~10 Gyr they cannot be
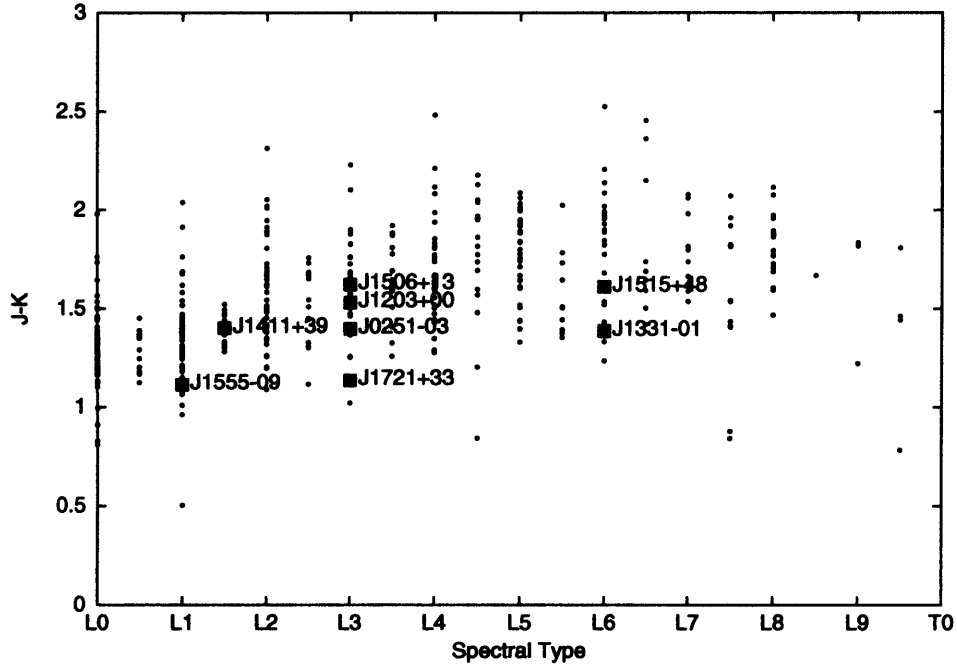
Figure 6.6: J-K_S vs spectral type for all L dwarfs in the Dwarf Archive. The marked objects are the 8 fast moving dwarfs which tend to have bluer J-K_S than other dwarfs of the same spectral type.

brown dwarfs, which would have cooled to much lower effective temperatures (Burrows et al., 2001). It is therefore expected that they would be extremely low luminosity stars. Leggett et al. (2002) find the K_S band bolometric correction to be 3.3 for L dwarfs. Using this number and the absolute K magnitude then gives L/$L_\odot$ as shown in table 6.5. It should be noted that using BC_K=3.3 may be unsuitable for L dwarfs with unusually blue J-K_S colours. These L/$L_\odot$ $\approx$ 10^{-4} are in agreement with theoretical models for very low mass old stars (Burrows et al., 2001). Indeed, J1331-01 and J1515+48 may be the lowest luminosity stars found to date.

6.6 Moving groups

Moving groups are loosely bound groups of stars that all appear to be moving towards the same point in space. This point is the convergent point. These stars all formed from the same protostellar cloud, and hence should all have the same age and metallicity. It should be noted

160
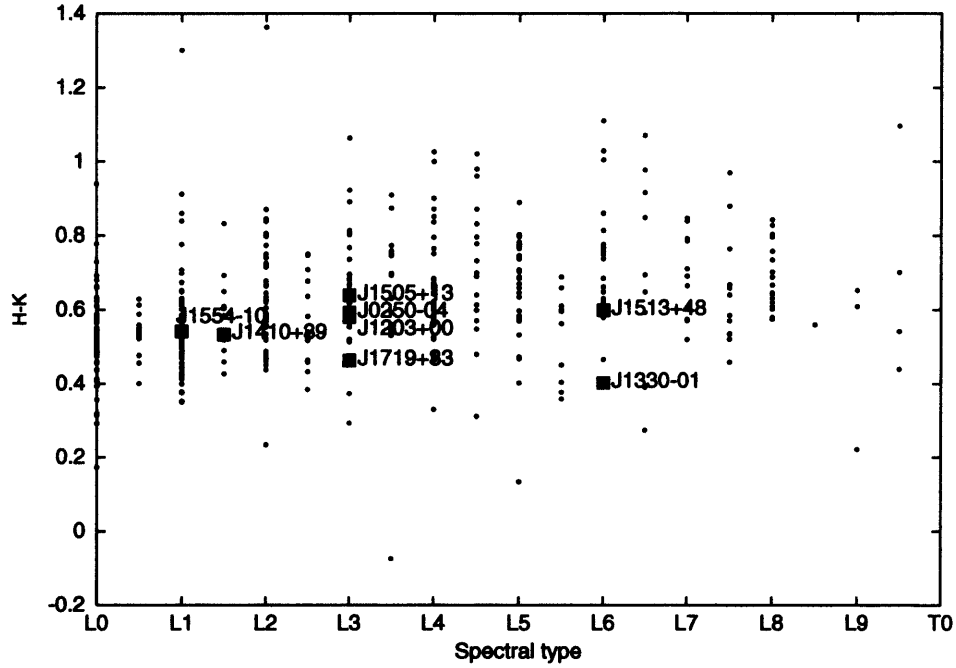
Figure 6.7: H-K$_S$ vs spectral type for all L dwarfs in the Dwarf Archive. The marked objects are the 8 fast moving dwarfs which tend to have bluer H-K$_S$ than other dwarfs of the same spectral type, particularly for dwarfs with spectral types greater than L6.

that galactic resonances can also produce common velocities similar to those of a moving group (Dehnen, 1998). Thus members of a moving group may have the same age, but the coevality is not always guaranteed. A good example of a moving group is the Ursa Major moving group, which the Sun is not a member of, but is located in the middle of. Another example is the 625 Myr old Hyades moving group, which not only encompasses the Hyades cluster itself, but also the Praesepe cluster (Eggen, 1960). By examining a star's motion it can be determined whether it is moving towards the convergent point of a moving group, and then a distance for it can be calculated. This distance is critical, as it allows empirical isochrones to be created for the age of the moving group, using the absolute magnitudes of its members (Bannister & Jameson, 2007). Contamination wise, any object that appears to be a member from its proper motion analysis and distance measurement will easily show up in the wrong place on a colour magnitude diagram and then can be eliminated as a candidate member. The moving groups the brown dwarfs were considered to be possible members of were, Ursa Major, Hyades-Praesepe, Coma Berenices, Pleiades, Upper Scorpius, Alpha
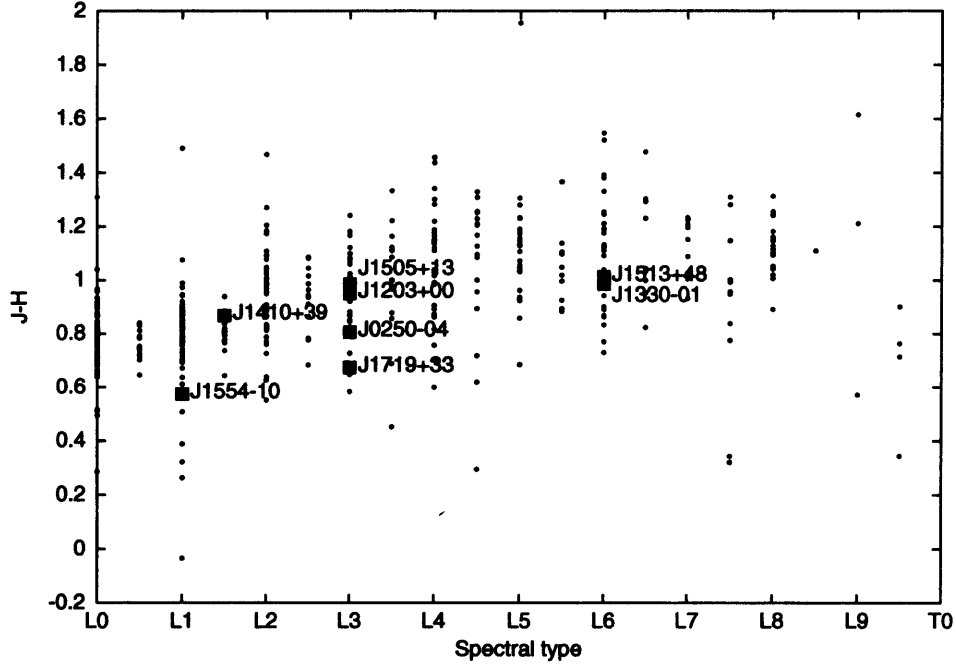
Figure 6.8: J-H vs spectral type for all L dwarfs in the Dwarf Archive. The marked objects are the 8 fast moving dwarfs which tend to have bluer J-H than other dwarfs of the same spectral type, particularly for dwarfs with early L spectral types.

Persei, Upper Centaurus, Lower Centaurus, Scorpius OB2, and HIP98321. The data for these moving groups are shown in table 6.6, and illustrated in figures 6.10 and 6.11, which show the positions of the clusters the moving groups are associated with, and their motion across the sky.

To implement this method, first the angle between the star in question, $S(*)$, from the convergent point, CP, must be calculated as shown in equation 6.6,

$$\cos D = \cos(90 - \delta_S)\cos(90 - \delta_{CP}) + \sin(90 - \delta_S)\sin(90 - \delta_{CP})\cos DA, \quad (6.6)$$

where

$$DA = \alpha_{CP} - \alpha_S, \quad (6.7)$$

and α_{CP} and α_S are the right ascensions of the convergent point and star respectively, δ_S is the declination of the star, and δ_{CP} the declination of the convergent point. The spherical geometry
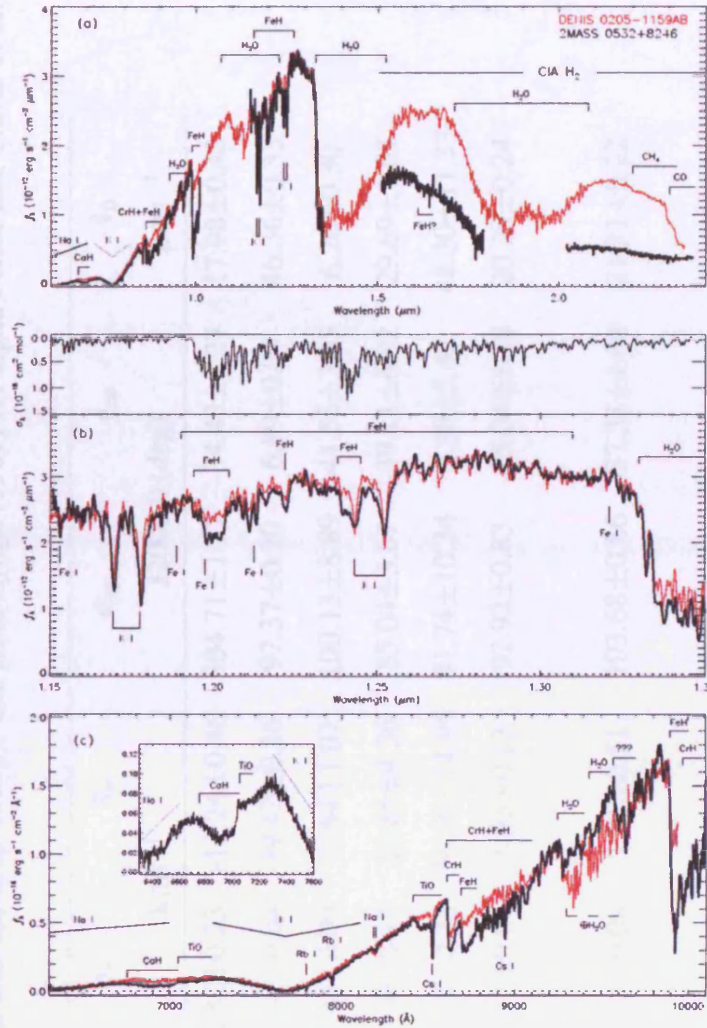
Figure 6.9: Spectrum of 2MASS 0532+8246 (thick black line) as compared with the L7 DE-NIS 0205-1159AB (thin grey line: data from Kirkpatrick et al. (1999); McLean et al. (2003) (a) Observed 0.63-2.35 μm spectrum, with NIRSPEC bands scaled to 2MASS photometry. Key atomic and molecular features are indicated; note that the 2.2 μm CH_4 and 2.3 μm CO bands present in the spectrum of DENIS 0205-1159AB (McLean et al., 2001) are not present in that of 2MASS 0532+8246. (b) Top: FeH absorption coefficient vs. wavelength, from Dulick et al. (2003). Bottom: J-band spectrum of 2MASS 0532+8246, with line identifications for K I, Fe I, FeH, and H_2O. (c) Red optical spectrum, with key features indicated. Uncorrected telluric H_2O absorption in the DENIS 0205-1159AB data is indicated by the dashed bracket. Inset window shows a close-up of the 6350-7600 Å spectral region, highlighting strong CaH and weak TiO bands; no Li I or Hα lines are seen. Figure and caption taken from Burgasser et al. (2003).

163

Table 6.6: The ages and coordinates of the centres of the used moving groups. Also shown is the estimated internal velocity dispersion among individual stars, $\hat{\sigma}_v$, the space velocity component directed towards the centre of the cluster - i.e. the cluster radial velocity, $\hat{v}_r$, the co-ordinates of the convergent point of the moving group and the total velocity of the cluster, $\hat{v}_0$. All values are taken from Madsen et al. (2002), with the exception of the ages which are from Dravins et al. (1999), and from Lyngå (1987) for alpha Persei and Claver et al. (2001) for Praesepe.

Cluster name	age	α_0	δ_0	$\hat{\sigma}_v$	$\hat{v}_r$	α_{cp}	δ_{cp}	$\hat{v}_0$
	Myr	J2000.0 (deg)		kms^{-1}		J2000.0 (deg)		kms^{-1}
Ursa Major	300	187.3	+56.4	2.82±0.23	-12.24±0.46	304.71±1.31	-34.43±1.27	17.98±0.42
Hyades	625	66.5	+16.9	0.49±0.04	39.42±0.36	97.37±0.20	6.89±0.09	46.36±0.33
Coma Berenices	460	187.5	+26.4	0.47±0.09	-1.64±1.07	100.13±8.89	-41.55±3.65	6.20±0.30
Pleiades	130	56.4	+24.0	0.50±0.13	10.85±4.36	85.04±3.67	-39.11±6.92	29.69±1.67
Praesepe	625	130.2	+19.6	0.67±0.23	36.20±14.95	91.74±10.34	2.38±5.42	48.20±11.33
Lower Centaurus Crux	10	189.6	-56.2	1.13±0.07	5.95±0.53	92.92±0.83	-25.04±1.18	20.29±0.24
Upper Centaurus Lupus	13	230.3	-41.6	1.23±0.08	1.01±0.51	103.68±0.86	-37.31±1.08	21.31±0.22
Upper Scorpius	5	243.4	-24.1	1.33±0.12	-0.17±1.33	111.70±2.96	-55.33±3.12	17.71±0.26
Scorpius OB2	5	225.1	-43.9	1.52±0.06	-1.17±0.26	95.41±0.42	-29.73±0.59	21.04±0.13
alpha Persei	50	52.9	+47.8	0.71±0.13	+47.8±4.53	96.78±1.96	-23.27±3.67	29.76±0.64
'HIP 98321'	60	297.5	+39.4	2.56±0.26	-19.68±1.74	102.51±1.30	-37.60±1.01	20.11±1.72

164
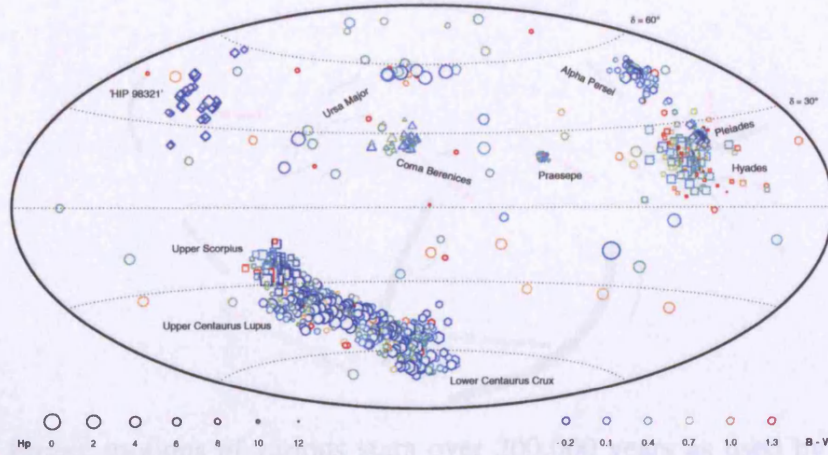
Figure 6.10: Map of the full sky, showing the stars in clusters and associations, whose radial velocities have been astrometrically determined from Hipparcos data by Madsen et al. (2002). These are the moving groups used in this study. Symbol shape identifies different clusters; symbol size denotes apparent magnitude as determined by Hipparchos, while symbol shading denotes B-V (note how some clusters are dominated by very blue stars). The Aitoff projection in equatorial coordinates is used. Figure taken from Madsen et al. (2002)

of this method is shown in figure 6.12.

Equation 6.6 may be simplified to equation 6.8,

$$\cos D = \sin \delta_S \sin \delta_{CP} + \cos \delta_S \cos \delta_{CP} \cos DA. \tag{6.8}$$

Then the angle T must be found, which is the direction of the proper motion measured east from north. Once more by using the cosine rule again yields equation 6.9,

$$\cos(90 - \delta_{CP}) = \cos(90 - \delta_S) \cos D + \sin(90 - \delta_S) \sin D \cos T, \tag{6.9}$$

where T is the required angle, and D and δ are as previously defined. Equation 6.9 can be rearranged into equation 6.10,

$$\cos T = \frac{\sin \delta_{CP} - \sin \delta_S \cos D}{\cos \delta_S \sin D}. \tag{6.10}$$

165
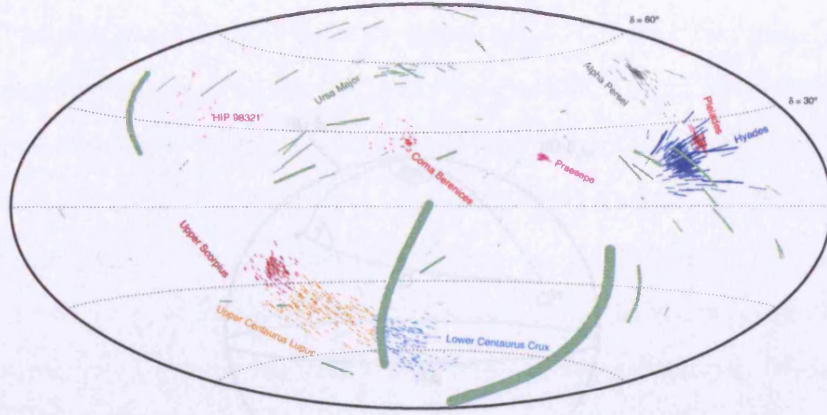
Figure 6.11: Proper motions of various stars over 200,000 years as used by Madsen et al. (2002) to plot their motion over time using radial velocities. The best radial-velocity accuracy has been obtained in rich nearby clusters with large angular extent, and large proper motions. However, the accuracy in the largest associations (Ursa Major, Scorpius-Centaurus) is limited by the partly unknown expansion of these systems. Stellar paths in the Ursa Major group (green) cover large areas of the sky. The thickness of the proper-motion vectors is inversely proportional to stellar distance: the closest star is Sirius and the two next ones are faint red dwarfs. Proper motions vary greatly among different clusters. Figure taken from Madsen et al. (2002).

This angle T can now be compared with the observed angle of the direction of the proper motion, θ, which is defined in equation 6.11.

$$\tan \theta = \frac{\mu_\alpha}{\mu_\delta}.$$ (6.11)

Clearly T will not exactly match θ due principally to the velocity dispersion of the moving group. Allowing a generous and therefore very safe $\sigma/V_o = 0.25$ gives $\Delta \theta$ as defined in equation 6.12, less than 14° plus or minus the errors. If a star meets this criteria it is regarded as a potential member of the moving group. This angular difference corresponds to $1.5\sigma_v$, or 87% completeness for the Bannister & Jameson (2007) sample.
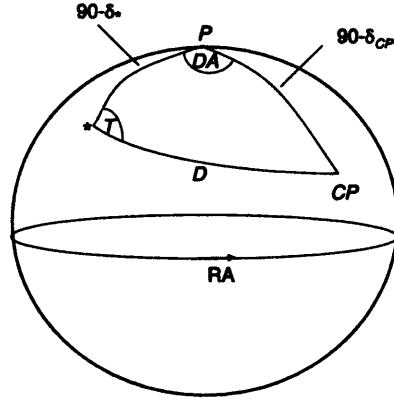
Figure 6.12: Spherical geometry of the moving group method. The asterisk (*) refers to the star's position, CP is the convergent point and P is the pole. DA, D and T are defined in equations 6.6 to 6.10.

$$\Delta\theta = T - \theta \qquad (6.12)$$

The distance to the star in parsecs, d, was then calculated, assuming it was a moving group member, using equation 6.13 (Carroll & Ostlie, 1996),

$$d = \frac{V \sin D}{4.74\mu}, \qquad (6.13)$$

where V is the cluster velocity in kms^{-1}, μ is the proper motion vector in arcseconds, and D is as before. As in equations 6.4, 4.74 comes from the unit conversion factor, and is the ratio between the number of kilometres in a parsec, and the number of seconds in a year multiplied by the number of arcseconds in a radian.

Once the distance to the star, assuming it is a moving group member has been calculated, the distance formula can be used to calculate the absolute magnitude of the object in question, and plot it on a colour-magnitude diagram. The objects that have been selected - i.e. have the

167

correct proper motion angle, which must be less than 14° for the difference between the observed and calculated angles as in Bannister & Jameson (2007), and have the correct distance to fit on a colour-magnitude diagram, were then subject to another check. Using equation 6.1, a distance was calculated for these objects using their spectral types. If the ratio between the moving cluster distance and the spectral type distance was greater than 0.72 and less than 1.28, as calculated in Bannister & Jameson (2007) then the objects were considered to be members. Parallax measurements for these members could confirm these distances. While some objects may have the correct direction and magnitude of motion, few will have the correct distances and appear to sit in the correct position on the colour magnitude diagram. In their study Bannister & Jameson (2007) estimated 0.5% probablility of an object passing all three tests (distance, direction and colour magnitude diagram). They suggest that it is likely that 99.5 % of selected objects therefore are members of the moving groups. They also estimate that there is ≈ 3% chance of passing the distance and direction test, and that these objects that then do not belong to the moving group are not selected once they have been placed on the colour magnitude diagram.

6.6.1   The Hyades

The Hyades cluster has a distance of 46 pc and covers ≈ 20° of the sky. The Hyades has almost no known low mass members (Gizis et al., 1999; Dobbie et al., 2002b) as due to its age (625 Myr Perryman et al. 1998) they have evaporated from the cluster. In fact for a cluster of this age ∼ 70% of stars and ∼ 85% of brown dwarfs are expected to have escaped the cluster (Adams et al., 2002). The Hyades moving group is made up of objects that may have escaped from the Hyades. Chereul et al. (1998) first identified escaped Hyads, and more recently Bannister & Jameson (2007) have identified 7 L and T field dwarfs that belong to the Hyades moving group. Zapatero Osorio et al. (2007) have confirmed membership for one of these objects (2MASS J1217110-031113), and have disproved membership for two (2MASS J0205293-115930 and 2MASS J16241436+0029158) using radial velocity measurements. To illustrate the method shown in figure 6.13 are all the remaining proper motion dwarfs with
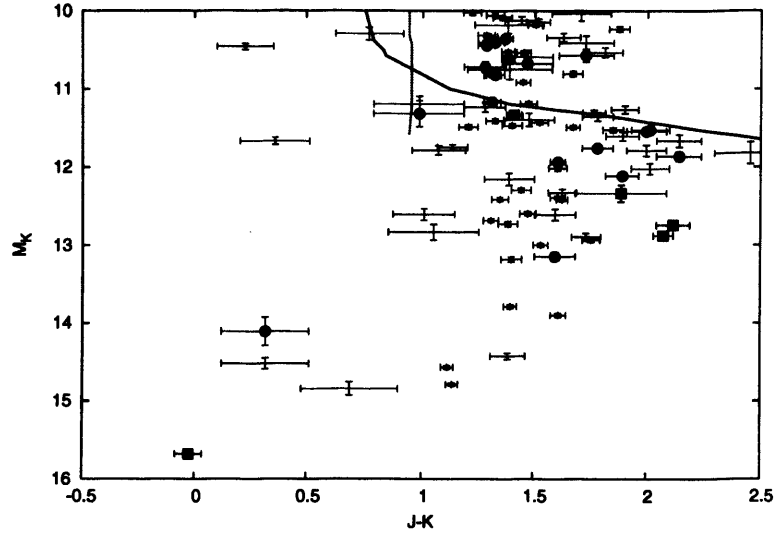
Figure 6.13: M_K, J-K colour magnitude diagram for the Hyades moving group. The members identified by Bannister & Jameson (2007) are plotted as filled squares. The dotted line is the NEXTGEN model (Baraffe et al., 1998) and the solid line is the DUSTY model (Chabrier et al., 2000) both for an age of 500 Myr. All of the 143 objects are plotted, with M_K calculated from the moving group distance. The objects selected from the moving group method (correct angle of proper motion and distance ratio) are marked as filled circles. The errors are Poissonian and from the photometry only.

their M_K calculated from their moving group distances. Since they are not members, they form a scattered distribution. Fifteen of the 143 proper motion objects had the correct proper motion, direction (distance between the observed angle of proper motion and moving group angle must be less than 14°) and distance (ratio between the moving cluster distance and the Cruz spectral type distance greater than 0.72 and less than 1.28) to belong to the Hyades moving group. Of these, 8 are possible binaries as they lie up to 0.75 magnitudes above the main sequence as shown on figure 6.14. J1047-18 and J1750+42 had the correct motion, direction and distance to belong to the moving group, however, they lie in the wrong place on the main sequence in the M_K, J-K colour magnitude diagram (figure 6.14). Four objects, J0103+19, J0908+50, J1326-27 and J1343+29 are marked as being uncertain members to the moving group. They lie above the binary sequence in the colour magnitude diagram when the spectroscopic distance is used making them narrowly non members, however, when the

169

moving cluster distance is used, J1326-27 and J1343+29 become more likely to be members and the remaining two objects as well as J1206+02 become less likely to be members.

As was mentioned earlier, J1441-09 is believed to be a member of the Hyades moving group. It was not selected as a member here as the ratio of moving group distance to spectral type distance was 1.47. If the parallax distance is used, this ratio decreases to 1.35 which is still too high to be selected. However, $\Delta\theta$ is only small, indicating possible membership ($\approx 3°$). For the purposes of this study, it is not treated as a member. For clarity figure 6.14 repeats figure 6.13 without the obvious non members. The Bannister & Jameson (2007) sequence is shown by a dashed line. Table 6.7 contains more information about the suggested moving group members.

The following four objects are possible members and are marked by boxes around filled circles on figure 6.14.

J0103+19 is an L6 dwarf as identified by optical spectra (Kirkpatrick et al., 2000).

J0908+50 is an L5 dwarf as identified by optical spectra by Cruz et al. (2003). However, Knapp et al. (2004) identify it as an L9±1 dwarf using infrared spectra.

J1326-27 is an L5 dwarf (from optical spectrum) (Gizis, 2002). This is another object that was found not to be a member of the TW Hydrae association by Gizis (2002).

J1343+39 is an L5 dwarf, identified by optical spectrum from Kirkpatrick et al. (2000).

The remaining objects were selected as being more probable members of the moving group and are plotted as encircled filled circles on figure 6.14.

J0228+25 is an L0 dwarf as identified by Wilson et al. (2003) using an infrared spectrum and by Cruz et al. (2003) using an optical spectrum.

J1010-04 is an L6 which was discovered in 2003 by Cruz et al. (2003) and identified using an optical spectrum.

J1045-01 is an L1 dwarf (from optical spectrum). Gizis (2002) took a spectrum of this object to search for gravity features in the spectrum that would indicate youth and hence membership of the TW Hydrae association. However, it was not found to be a member.
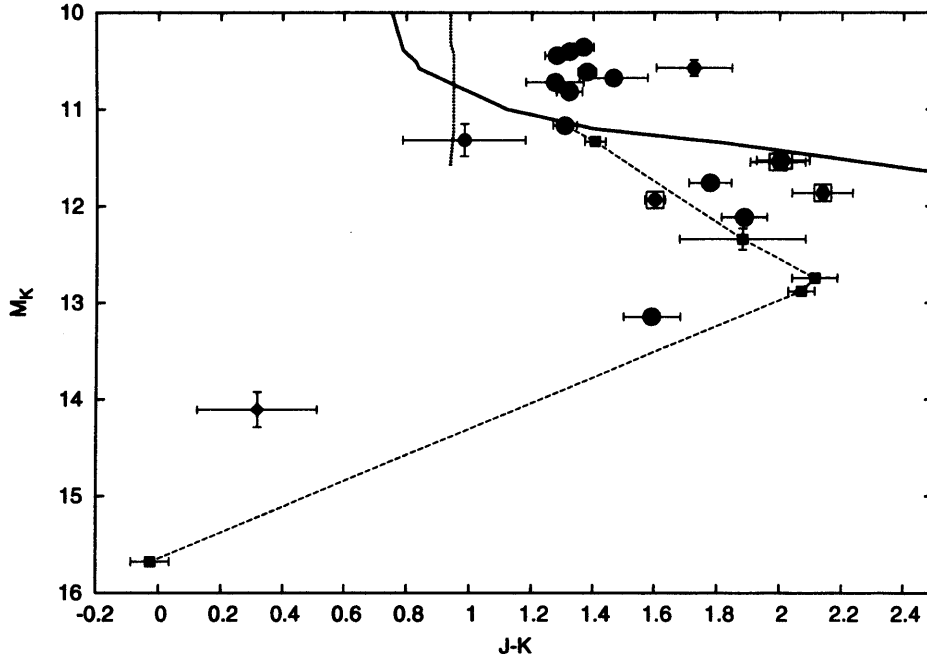
Figure 6.14: M_K, J-K colour magnitude diagram for the Hyades moving group. The members identified by Bannister & Jameson (2007) are plotted as filled squares. The dotted line is the NEXTGEN model (Baraffe et al., 1998) and the solid line is the DUSTY model (Chabrier et al., 2000) both for an age of 500 Myr. All of the objects that were selected as possible members are marked as filled circles and the selected members are marked by a ring around the filled circle. The diamond is the object J1553+15.The 4 objects that are uncertain members are marked with boxes around the filled circles. The errors are Poissonian and from the photometry only. The dashed line indicates the possible single star sequence.

J1047-18 is an L2.5 dwarf (from optical spectrum) (Martín et al., 1999) and was originally discovered using the DENIS catalogue (The Denis Consortium, 2005).

J1207+02 is an L8 dwarf as measured from optical spectra by Hawley et al. (2002) and a T0 dwarf as measured from infrared spectra by Burgasser et al. (2006a).

J1402+01 is an L1 dwarf discovered from the SDSS by Hawley et al. (2002).

J1404+46 is identified as an L0 dwarf from its optical spectrum (Cruz et al., 2007b).

J1407+12 is identified as an L5 dwarf by (Reid et al., 2007).

J2057+17 is identified as a L1 dwarf from its optical spectrum by Kirkpatrick et al. (2000).

J2107-03 is an L0 dwarf (from optical spectrum) (Cruz et al., 2003).

171

J2130-08 is identified as an L1.5 dwarf by Kirkpatrick et al. (2007).

J1553+15 is identified as a T7 dwarf, and is also a binary separated by 0.349" (Burgasser et al., 2006a). As the spectroscopic distance used here is only valid for dwarfs with spectral types from M6 to L8, the distance is incorrect and it is likely that this object is not actually a member. Burgasser et al. (2006b) calculate a distance for this object of 12±2 pc using the relationships of Tinney et al. (2003). If this distance is used, a the ratio of moving cluster distance to spectral type distance is 1.31, which while close, is outside the limits of the selection criteria used here. The M_K of this object then becomes too faint to sit on the L-T transition sequence for this moving group. It is thus believed that J1553+15 is not a member of the moving group. It is plotted as a filled diamond on figure 6.14.

This result indicates that many brown dwarfs may have escaped the Hyades cluster over time, as has been suggested, however, they may have remained members of the Hyades moving group. If so, these objects may allow a study of the initial mass function of the Hyades to be made down to substellar masses.

6.6.2   Ursa Major

The Ursa Major moving group has been estimated to have an age of between 300 Myr (Soderblom & Mayor, 1993) and 500±100 Myr (King et al., 2003). Castellani et al. (2002) found the age of the group to be 400 Myr. The age of 400±100 Myr is adopted in this work. Out of the 143 brown dwarfs examined, 5 appear to have the correct motion, distance and the correct direction of motion to be members of the Ursa Major moving group and are shown on figure 6.15.

These objects are J0030+31, J1204+32, J1239+55, J1246+40 and J1550+14. Three other objects had the correct motion, distance and direction, however, when placed on the colour magnitude diagram didn't fit the sequence. These objects are the binary J1017+13, J1147+02 and J1619+00, all of which lie too low on the main sequence to belong to the cluster. J1017+13

172

Table 6.7: Name J, H, K_S magnitudes, $\Delta\theta$, ratio of moving group distance to spectral type distance (d_{mg}/d_{sp}) and spectral type distance d_{sp} for the potential Hyades moving group members discussed.

| Name	J	H	K_S	$\Delta\theta$ °	d_{mg}/d_{sp} pc	d_{sp}
J0103+19	16.28 ± 0.07	14.89 ± 0.05	14.14 ± 0.05	2.87 ± 2.68	1.09	28.62
J0228+25	13.83 ± 0.02	12.99 ± 0.02	12.47 ± 0.02	3.78 ± 3.76	1.25	26.44
J0908+50	14.54 ± 0.02	13.47 ± 0.02	12.94 ± 0.02	11.51 ± 2.06	0.80	15.91
J1010-04	15.50 ± 0.05	14.38 ± 0.03	13.61 ± 0.04	7.54 ± 2.36	1.26	19.98
J1045-01	13.15 ± 0.02	12.35 ± 0.02	11.77 ± 0.02	7.17 ± 1.39	1.04	17.09
J1047-18	14.19 ± 0.02	13.42 ± 0.02	12.89 ± 0.02	6.61 ± 2.31	1.17	22.10
J1207+02	15.57 ± 0.07	14.56 ± 0.06	13.98 ± 0.05	-8.77 ± 2.12	1.27	14.72
J1326-27	15.84 ± 0.07	14.74 ± 0.05	13.85 ± 0.05	2.12 ± 2.17	0.89	28.93
J1343+39	16.16 ± 0.07	14.85 ± 0.05	14.14 ± 0.04	-1.38 ± 4.04	0.79	33.44
J1402+01	15.45 ± 0.06	14.65 ± 0.06	14.17 ± 0.07	6.37 ± 2.72	0.78	49.08
J1404+46	14.33 ± 0.02	13.53 ± 0.02	13.05 ± 0.02	-9.35 ± 5.79	1.06	33.27
J1407+12	15.37 ± 0.05	14.34 ± 0.05	13.59 ± 0.04	-1.68 ± 3.33	1.20	23.31
J2057+17	15.96 ± 0.08	15.19 ± 0.08	14.49 ± 0.07	5.82 ± 7.81	1.03	58.11
J2107-03	14.19 ± 0.02	13.44 ± 0.03	12.87 ± 0.02	-10.39 ± 4.4	1.17	31.22
J2130-08	14.13 ± 0.02	13.33 ± 0.03	12.81 ± 0.03	-5.94 ± 2.24	0.76	25.04
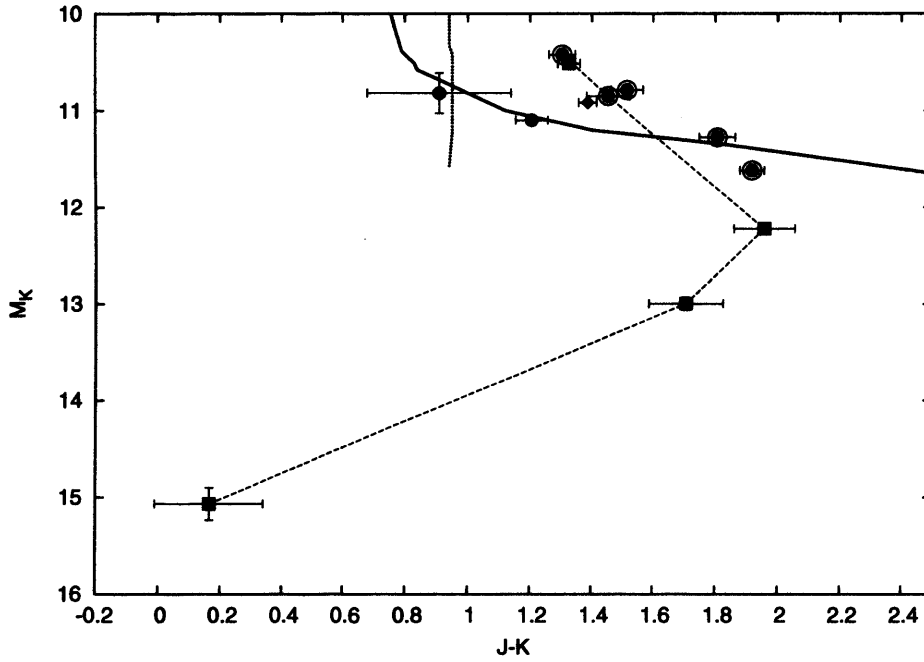
Figure 6.15: M_K, J-K colour magnitude diagram for the Ursa Major moving group. The members identified by Bannister & Jameson (2007) are plotted as filled squares. The dotted line is the NEXTGEN model (Baraffe et al., 1998) and the solid line is the DUSTY model (Chabrier et al., 2000), both for an age of 500 Myr. All of the objects that were selected as possible members are marked as filled circles and the selected members are marked by a ring around the filled circle. The diamond is the object J1017+13. The errors are Poissonian and from the photometry only. The dashed line indicates the possible single star sequence.

appears to be a possible member of the moving group although, it should be moved downwards to compensate for the fact that it is a binary, hence making it appear more likely to be a non member. It is shown as a filled diamond on figure 6.15. The spectral types of these objects agree with their placement on the main sequence.

These objects were selected as being probable members of the moving group and are plotted as encircled filled circles on figure 6.15.

J0030+31 is an L2 (spectral type from optical spectrum) dwarf identified from 2MASS by Kirkpatrick et al. (1999).

J1204+32 is an L0 dwarf (spectral type from optical spectrum), with an estimated distance of 26.9 pc (from spectral type) (Cruz et al., 2003). Wilson et al. (2003) find a spectral type for

174

Table 6.8: Name J, H, K_S magnitudes, $\Delta\theta$, d_{mg}/d_{sp} and d_{sp} for the potential Ursa Major moving group members discussed.

Name	J	H	K_S	$\Delta\theta$	d_{mg}/d_{sp}	d_{sp}
				°	pc	pc
J0030+31	15.47 ± 0.05	14.61±0.05	14.02±0.047	6.29±11.33	1.16	43.18
J1204+32	13.81±0.03	13.09±0.03	12.51±0.027	8.02±12.30	1.13	26.18
J1239+55	14.71±0.02	13.56±0.03	12.79±0.027	16.17±3.01	1.00	17.14
J1246+40	15.08±0.04	13.94±0.03	13.28±0.038	12.26±5.41	0.72	25.17
J1550+14	14.77±0.04	13.79±0.03	13.26±0.034	10.83±5.73	0.72	31.23

this object of M9 from an infrared spectrum.

J1239+55 is an L5 dwarf identified by its optical spectrum by Kirkpatrick et al. (2000). It is also part of a resolved binary system.

J1246+40 is an L4 dwarf (spectral type from optical spectrum) (Kirkpatrick et al., 2000). It has an estimated distance of 25 pc calculated from spectral type.

1550+14 is an L2 dwarf (spectral type from optical spectrum) (Cruz et al., 2007b).

Figure 6.15 is the colour magnitude diagram of the Ursa Major moving group and the data for the likely members is in table 6.8.

6.6.3 Pleiades

The Pleiades cluster is 125 Myr old and is situated at a distance of ≈130 pc (Stauffer et al., 1998). As a cluster it has been studied in depth and has been found to contain many brown dwarfs (Lodieu et al., 2007; Casewell et al., 2007; Bihain et al., 2006; Moraux et al., 2003). The Pleiades moving group has a convergent point of 85.04°±3.67, −39.11°±6.92 (Madsen et al., 2002). This convergent point is very close to that of many other moving groups such as AB Doradus, Alpha Persei and Tucana/Horologium, and it has been theorised that many of

these moving groups have a common origin (Ortega et al., 2007). Three objects were selected to be potential members of the Pleiades moving group, and in addition to these three, two objects with previously measured proper motion, and parallax measurements also appear to fit the sequence. These 5 objects were compared to the L-T dwarf sequence for the objects identified as being potential members of the Pleiades cluster by Casewell et al. (2007), Lodieu et al. (2007), Bihain et al. (2006) and Moraux et al. (2003), assuming all of the cluster members have the cluster distance of 130 pc. The spectral types of all of these objects are consistent with their places on the colour magnitude diagram as shown in figure 6.16 and their data is in table 6.9.

These objects were selected as members of the Pleiades moving group and are plotted as encircled filled points on figure 6.16.

J0001+15 is an L4±1 dwarf as identified by Knapp et al. (2004) who used an optical spectrum.

J1123+41 is an L2.5 dwarf discovered by Kirkpatrick et al. (2000).

J1552+29 has been identified as an L1 dwarf by Wilson et al. (2003).

These two objects with known parallaxes were selected as members of the moving group and are plotted as filled, encircled diamonds on figure 6.16:

Gl 417B is a L4.5 dwarf discovered by Kirkpatrick et al. (2000). It has a proper motion of 0.291±0.00072" yr^{-1} and a position angle of 238.67±0.14° (Perryman et al., 1997). This object has a parallax of 46.04±0.9 mas which corresponds to a distance of ≈21.72 pc (Perryman et al., 1997). This L dwarf was identified as a binary by Kirkpatrick et al. (2001) who had noted in Kirkpatrick et al. (2000) that it was in close proximity to Gl 417, a G type dwarf star. These two objects were found to have a common proper motion. It is noted in Kirkpatrick et al. (2001) that the age of this system is not inconsistent with that of the Pleiades (the age was calculated using the ratio of X-ray to bolometric luminosity vs B-V). Comparing Gl 417A to the evolutionary models of Girardi et al. (2000), using the measured parallax as above,of shows that it lies to the left of the main sequence at this point, indicating that it is not a member of the moving group, however, it is recorded as a variable star of the BY Dra type which may account for this difference. Further study would be needed of this object to prove a membership of the moving group.
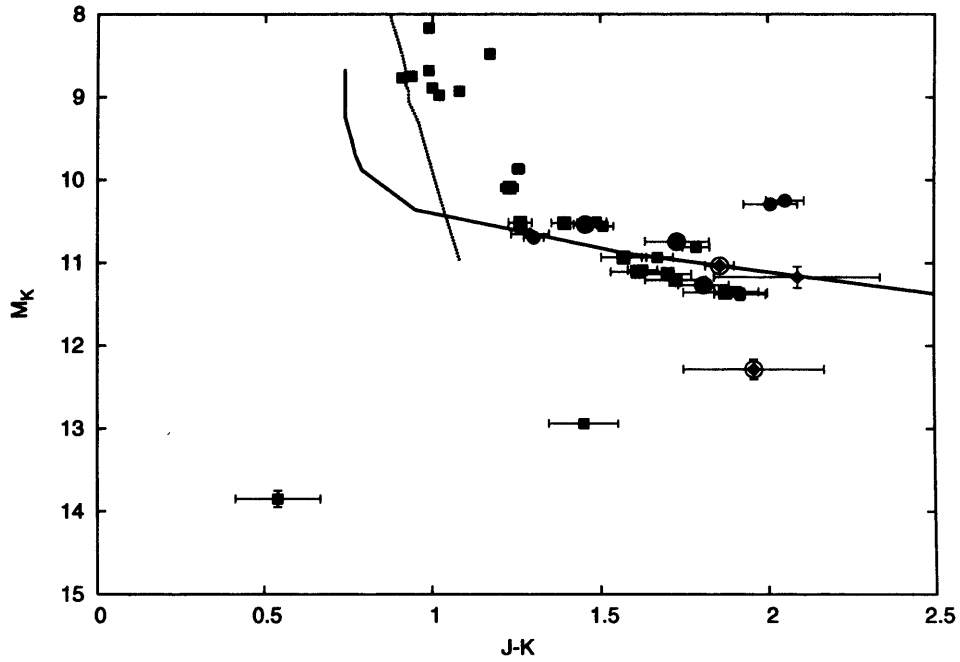
Figure 6.16: M_K, J-K colour magnitude diagram for the Pleiades moving group. The cluster members members identified by Casewell et al. (2007), Lodieu et al. (2007), Bihain et al. (2006) and Moraux et al. (2003) are plotted as filled squares. The dashed line is the NEXTGEN model (Baraffe et al., 1998) and the solid line is the DUSTY model (Chabrier et al., 2000) both for an age of 120 Myr. All of the objects that were selected as possible members are marked as filled circles and the selected members are marked by a ring around the filled circle. The filled diamonds are objects that were selected as possible members that had measured parallax, and are outlined by a ring if considered a selected member. The errors are Poissonian and from the photometry only.

2MASSWJ2101154+175658 is an L7.5 dwarf also identified by Kirkpatrick et al. (2000). Vrba et al. (2004) measure a proper motion of 0.2085 ± 0.00037 " yr^{-1} and a position angle of $136.33 \pm 0.51°$ for it. It has a measured parallax of 30.14 ± 3.42 mas which corresponds to a distance of ≈ 33.17 pc. Gizis et al. (2003) identified this L dwarf as a binary using the HST and suggest that both components must be brown dwarfs and the secondary must have a spectral type of later than L8. The separation is estimated to be 0.232".

6.6.4 Other moving groups

The remaining moving groups contain very few objects that are considered to be members. For instance no potential members of the Coma Berenices moving group were found. The Praesepe moving group, although it has a separate convergent point is suggested by Eggen (1960) to in fact be the same as the Hyades moving group, and so is not discussed further. Unfortunately the remaining moving groups all have very similar convergent points and, with the exception of Alpha Persei, similar ages (5-10 Myr). The age of Alpha Persei is itself in question, with Lyngå (1987) deriving a main sequence turn off age of ≈ 50 Myr. Basri & Martín (1999) calculate a lithium age for the cluster of 65-75 Myr and Stauffer et al. (1999) a lithium age of 90 Myr. Assuming that Alpha Persei is younger than the Pleiades, as all of these estimates seem to suggest, it should have a main sequence that sits higher than that of the Pleiades on the colour magnitude diagram. 2 such objects are found from this study, however, it is impossible to claim a sequence has been found using solely 2 objects. Upper Scorpius appears to have a convergent point that is different enough for members to be selected, however, only two possible members were found. These moving groups may be more easily studied when a larger sample of brown dwarfs is available. There are also many additional moving groups that have been recently discovered such as those detailed in Zuckerman & Song (2004), however, these moving groups all have similar motion to that of the Pleiades, making the identification of members difficult. There are also no accurately constrained convergent points for these recently discovered groups. More accurate ages of these groups and distances of the

Table 6.9: Name J, H, K_S magnitudes, $\Delta\theta$, d_{mg}/d_{sp} for the potential Pleiades moving group members discussed. The last two objects have parallax measurements and hence this column is the ratio of moving group distance to parallax distance, not the spectral type distance. The final column is the distance in pc derived from spectral types.

Name	J	H	K_S	$\Delta\theta$	d_{mg}/d_{sp}	d_{sp}
				°	pc	pc
J0001+15	15.52 ± 0.06	14.50 ± 0.05	13.71 ± 0.04	9.45 ± 4.98	0.89	30.74
J1123+41	16.07 ± 0.07	15.08 ± 0.08	14.34 ± 0.05	4.77 ± 7.62	0.88	52.41
J1552+29	13.47 ± 0.02	12.60 ± 0.02	12.02 ± 0.02	12.20 ± 6.90	0.77	19.78
Gl 417B	14.58 ± 0.03	13.50 ± 0.03	12.72 ± 0.03	5.00 ± 0.14	0.94	21.72
2MASSWJ2101154+175658	16.85 ± 0.17	15.86 ± 0.18	14.89 ± 0.12	9.48 ± 0.51	0.67	33.18

dwarfs would be required before it can be determined if any of the brown dwarfs studied here belong to them.

6.7 Summary

This chapter has described a search for members of moving groups in the galaxy, and has described the methods used. 143 brown dwarfs with previously unknown proper motions were studied, and proper motion measurements made for all of them using 2MASS and images taken using WFCAM on UKIRT. Of these 143 brown dwarfs, nine are known binaries, two of which are confirmed in this work. An additional 5 objects appear to have common proper motion companions in the data. Eight fast moving brown dwarfs were selected from the study for their high proper motion and by examining their blue colours, it appears likely that they are members of a thick disc population of stars, making them stellar and not brown dwarfs, but possibly some of the least luminous stars known. The main result of the chapter is how the moving group method has been used to select members of moving groups, namely the Hyades, Ursa Major and Pleiades moving groups. The moving group method has been described in detail, and results for the three aforementioned clusters presented. Of the 143 brown dwarfs studied, three (and an additional two with known proper motions) were found to be possible members of the Pleiades moving group, five were found to be candidate members of the Ursa Major moving group, and 15 are found to be likely members or possible members of the Hyades moving group.

Chapter 7

White Dwarfs in the Praesepe open star cluster

7.1 Introduction

This chapter will focus on another class of electron degenerate object found in open star clusters - white dwarfs. Eleven white dwarf candidate members of Praesepe (M44) have been identified to date and this work present the results of a spectroscopic study of nine of these objects. The reduction and the analysis of high resolution optical spectroscopy of these stars will be described including the modelling of the H-balmer line profiles and the measurement of radial velocities. The results of this work are then discussed in the context of cluster membership status and the initial mass-final mass relation.

7.2 Praesepe

Praesepe is a modestly rich open star cluster at a distance of $177^{+10.3}_{-9.2}$ pc (as determined from Hipparcos measurements Mermilliod et al. 1997). The cluster is slightly metal rich with re-

spect to the Sun ([Fe/H] = 0.038, [C/H] = 0.01). There is, however, some measure of uncertainty in the age of the cluster, with estimates ranging from 0.4 to 2 Gyr. The age determinations based on isochrone fitting generally support an age between 0.7 and 1.1 Gyr, although Claver et al. (2001) favour a value nearer to that of the Hyades (625 Myr) from a method using cluster main sequence fitting and also based on the grounds that the two clusters have very similar metallicities and belong to the Hyades moving group (Eggen, 1960). To date eleven white dwarfs have been identified as members of Praesepe (Luyten, 1962; Eggen & Greenstein, 1965; Anthony-Twarog, 1982, 1984; Claver et al., 2001; Dobbie et al., 2004, 2006a), all of which have been identified through proper motion surveys of the region. Open star clusters are ideal regions in which to study white dwarfs due to the common age, metallicity and distance of their members. Also, cluster white dwarfs provide the only means by which the shape on the initial mass-final mass relation (IFMR) can be determined because the age of the cluster allows the lifetime of the progenitor star to be reliably calculated.

7.3 Initial mass-final mass relation

The IFMR describes the amount of material primordial stars ($M < 10$ $M_{\odot}$) lose during post main sequence evolution as they become white dwarfs. This material forms the majority of carbon, oxygen and nitrogen in the interstellar medium, and thus this relation is important for studies of the chemical evolution of the galaxy. The processes of mass loss from high mass stars are also relevant to Supernova studies, as theory is sensitive to the minimum mass possible for core collapse. The IFMR can be used to predict this mass, using observational data.

All stars with $M \lesssim 10$ $M_{\odot}$ end their lives as white dwarfs, which totals about 95% of all stars. These white dwarfs come from stars that have either evolved from the asymptotic giant branch, with carbon-oxygen degenerate cores, or from low mass stars which never underwent helium burning. However, none of these latter objects will have become white dwarfs in the Hubble time.

When the star runs out of hydrogen fuel, in intermediate mass stars ($2 \leq M_\odot \leq 8$) the helium in the core has already started to burn and the core is never degenerate. In lower mass stars ($\sim 0.8 \leq M_\odot \leq 2$), the core may be partially degenerate before helium burning begins. The degeneracy pressure in the core supports it against gravity, and so as the ignition occurs, the core does not expand, due to the pressure only having a weak dependence on temperature. Instead the ignition of the helium causes an effect known as the "helium flash" which is an expansion caused by the fact that nuclear burning in degenerate material is very unstable. Once the core has expanded, the star is no longer degenerate and the helium flash ends. As the core expands, the envelope of the star contracts and heats up. The luminosity then drops. These stars may pulse, and eventually when the helium has been all used up, a carbon and oxygen core is left surrounded by a helium layer and a hydrogen envelope. The core of this star then contracts due to gravity and heats due to a lack of energy source. As a result of this, the envelope of helium and hydrogen then expands and cools, and becomes convective. A process known as dredge up occurs when the helium convective layer overlaps with the hydrogen layer and the remnants of the hydrogen burning, mainly helium and nitrogen is dredged up and mixed into the envelope. The expanding star becomes cooler and redder and joins the asymptotic giant branch. This asymptotic giant branch (AGB) phase is where the majority of the star's mass is lost. Stars in the AGB stage cool, as they expand which briefly extinguishes the core burning. The core becomes degenerate as it contracts. AGB stars have three main characteristics:

1. Nuclear burning takes place in two shells which is a thermally unstable configuration, causing thermal pulses.

2. The luminosity is determined by the core mass, independent of the stellar mass.

3. A strong stellar wind develops due to the radiation pressure in the envelope.

The third characteristic causes large mass loss from the star, however, the processes involved

are very complicated and not fully understood, making it difficult to model. It is thought that radiation pressure drives accelerating material away from the star and into the interstellar medium. The difficulty arises in the interaction of particles with gravity which depends on their mass, and their interaction with the radiation field which depends on the particle composition, structure, size density and the wavelength of the radiation (Prialnik, 2000). There may also be a superwind phase of evolution, causing more mass loss, before the core burning is finally extinguished and the star forms a white dwarf. The internal pressure in white dwarfs is supplied by degenerate electrons, which counteracts gravity, thus supporting the white dwarf. The white dwarf gradually cools over time, with the thermal energy stored by the internal ions being radiated away. Current theory predicts that more massive stars leave more massive white dwarf remnants, which in turn have smaller radii than hotter, less massive white dwarfs.

The IFMR is extremely difficult to model, due to many unknowns involved in the complex process of mass loss from white dwarfs. This means that the IFMR must be constrained empirically, although, this is also problematic. The main problem being that calculating the lifetime of the progenitor star, and hence its mass, is difficult if the age of the white dwarf is unknown. Open star clusters are arguably the best place to try and constrain the IFMR (Weidemann, 1977, 2000; Dobbie et al., 2006a), as the ages of the white dwarfs are known, usually from the main sequence turn off mass (King & Schuler, 2005), as well as the metallicity of the progenitor, which can help to make calculations more accurate. The white dwarf cooling age can be calculated using evolutionary models such as those of Fontaine et al. (2001), and when subtracted from the cluster age, yields the lifetime of the progenitor star. This lifetime can then be used with stellar evolutionary models such as those of Girardi et al. (2000), for the metallicity of the cluster to calculate the mass of the progenitor star. The final mass of the white dwarf can be calculated using T_{eff} and log g as well as photometry. The IFMR can then be plotted, and a linear relation fitted.

However, until recently, very few white dwarfs were known in open star clusters (≈ 30 in 14 clusters, Dobbie et al. 2006a). This meant that uncertainties in the ages/metallicities and the difficulties in determining distances of these faint objects contributed to the large scatter in the IFMR (Claver et al., 2001). There are only a few white dwarfs that have accurate

radial velocity measurements (to 2-3 kms^{-1}) and accurate distance measurements ($\leq 10\%$), and these measurements have introduced uncertainties into studies comparing spectroscopic and gravitational redshift mass estimates (Bergeron et al., 1995). It is thus vitally important that these cluster white dwarfs are studied in some detail to ascertain whether they are really cluster members. Proper motions and comparing photometry to models can help to select cluster white dwarfs, but radial velocities, T_{eff} and log g measurements are needed to be sure.

There have been many attempts to constrain the IFMR (Weidemann, 1977, 2000; Dobbie et al., 2006a), and the success of the relation depends on the scatter of the data points, which is related to the uncertainties in age etc as discussed earlier. Figure 7.1 taken from Weidemann (2000) compares many of these relationships from Girardi et al. (2000), Dominguez et al. (1999), Herwig (1995), Marigo (1998), Weidemann (1987) and Weidemann (2000). The Girardi and Dominguez relations use synthetic AGB calculations, whereas Marigo investigated core mass reductions from a third dredge up phase in that relation. The Herwig relation is from observational data, as are both Weidemann relations. Weidemann (2000) came to the conclusion that both empirically and theoretically the IFMR should be represented by a single valued relation.

There have been many searches for white dwarfs in Praesepe (Claver et al., 2001; Dobbie et al., 2004, 2006a) and these have generally used photometry and proper motions from surveys (e.g. USNOB1.0, SuperCOSMOS), to identify candidates, and follow up spectra to identify white dwarfs and to measure T_{eff} and log g. There have always been at least 5 white dwarf members of Praesepe known (Eggen & Greenstein, 1965; Anthony-Twarog, 1982, 1984). Reid (1996) measured T_{eff} and log g for three of them. Claver et al. (2001) obtained UVBRI photometry of ≈ 2.1 square degrees of Praesepe, selected candidates using theoretical isochrones and followed up 10 candidates with spectroscopy. Five of the 10 candidates were determined to be white dwarfs belonging to Praesepe, three of which were the Reid objects. The Claver study identified no new white dwarf cluster members. In 2004, Dobbie et al. (2004) discovered 6 new candidate members of the cluster, again by using a photometric and proper motion study, taking the total to 11 (one of the previously known 5 was discounted due to bad photometry). Spectra for two of these 6 were obtained, and they were confirmed as white dwarfs. Follow-
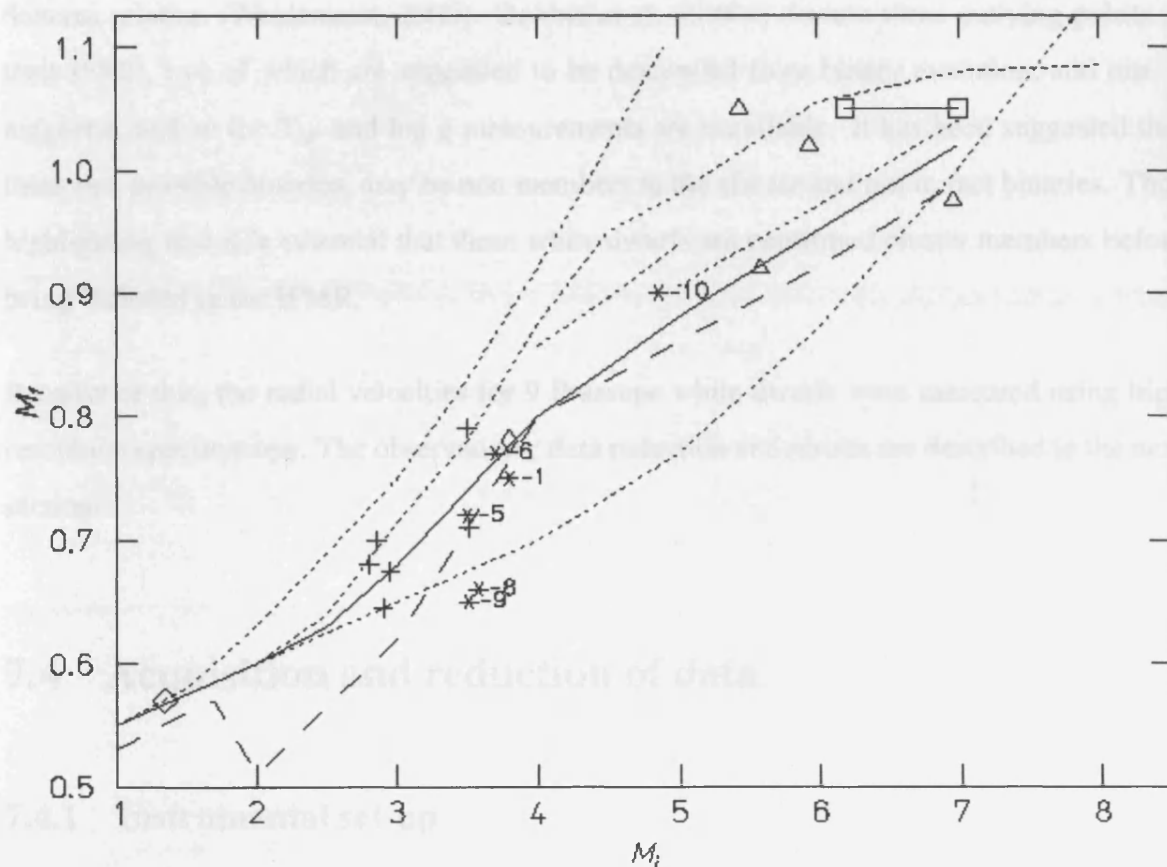
Figure 7.1: Initial-to-final mass relations (from top to bottom): relations from Girardi et al. (2000), Herwig (1995), Marigo (1998), Dominguez et al. (1999) and Weidemann (1987). Long dashed line: Thermally Pulsing relation from Herwig & Blöcker (priv. comm). Full line: Weidemann (2000) relation. Figure and caption from Weidemann (2000). The x axis is progenitor mass and the y axis the final mass.

ing up this work Dobbie et al. (2006a) gained spectra of the remaining 4 candidate members which were found to be members and indeed, white dwarfs, and an IFMR was plotted. The IFMR is shown in figure 7.2. The fit to the relationship has a gradient of 0.133 ± 0.015 and a constant of 0.289 ± 0.051 which was found by linear regression and is compared to the Weidemann relation (Weidemann, 2000). Dobbie et al. (2006a) discuss three outlying points in their IFMR, two of which are suggested to be descended from binary evolution, and one is magnetic, and so the T_{eff} and log g measurements are unreliable. It has been suggested that these two possible binaries, may be non members to the cluster and not in fact binaries. Thus highlighting that it is essential that these white dwarfs are confirmed cluster members before being included in the IFMR.

Because of this, the radial velocities for 9 Praesepe white dwarfs were measured using high resolution spectroscopy. The observations, data reduction and results are described in the next sections.

7.4 Acquisition and reduction of data

7.4.1 Instrumental set-up

High resolution spectroscopy of nine of the eleven DA white dwarf members of Praesepe was taken using UVES, the high resolution optical spectrograph on UT2 at the VLT in Paranal, Chile. The data were taken in service mode between 16/11/2005 and 19/01/2006 in seeing of better than 1.4" with thin cirrus. The instrument was set up to use 1.5" slit in dichroic mode. The observations are detailled in table 7.1.

The instrument contains three CCDs, one in the blue arm and two in the red arm, referred to as the red upper (longer wavelength) and lower (shorter wavelengths) CCDs, terminology which will be used in this chapter. UVES was set up to observe in the parallel mode, using dichroic1 (390+580), with central wavelengths of 390 and 564 nm in the blue and red arms respectively.
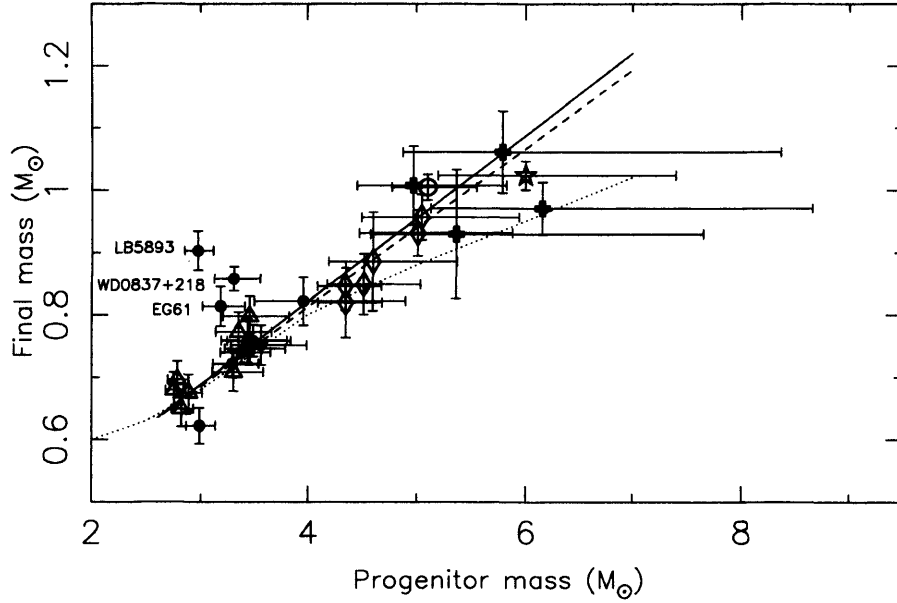
Figure 7.2: The initial mass final mass relation for members of the Hyades(open triangles), Praesepe (black circles), M35 (open diamonds), NGC2516 (open +s) and the Pleiades (open star). Sirius B is an open circle. A linear fit to the data based in CO(solid line)/C(dashed line) cores and the relation of Weidemann (2000), dotted line are overplotted. Figure and caption from Dobbie et al. (2006a).

Table 7.1: Names and observation dates for the nine observed white dwarfs.

Name	Obs 1	Obs 2	Obs 3	Obs 4
WD0833+194	26/12/2005	26/12/2005	26/12/2005	26/12/2005
WD0836+199	25/12/2005	25/12/2005	30/12/2005	30/12/2005
WD0836+201	08/01/2006	08/01/2006	08/01/2006	08/01/2006
WD0837+185	16/11/2005	24/12/2005	24/12/2005	-
WD0837+199	08/01/2006	08/01/2006	19/01/2006	19/01/2006
WD0837+218	25/12/2005	25/12/2005	25/12/2005	-
WD0840+190	24/12/2005	19/01/2006	19/01/2006	-
WD0840+200	08/01/2006	08/01/2006	08/01/2006	08/01/2006
WD0843+184	05/01/2006	05/01/2006	19/01/2006	19/01/2006

The cross dispersion settings were CD2 and CD3 both gratings of 600 g mm^{-1} and allowing a wavelength range of 370 to 500 nm in the blue and 420 to 680 in the red to be observed. Filters HER5 (5mm clear filter allowing a wavelength range of 310 to 500 nm to pass through) and SHP700 (420-700 nm wavelength range, which also rejects stray red light) were used in the red and blue arms. The data were reduced using the UVES pipeline, which is based on the MIDAS software supplied by ESO (Ballester & Hensberge, 1995). Calibration frames were taken every night with the data including format-check frames, bias frames, flat fields, an order definition template, and a ThAr arc lamp spectrum. In addition to these calibrations, the spectrum of a DC white dwarf (WD0000-345) which was observed on 03/07/2006 and reduced in exactly the same way as the science data, was used to remove the signature of the UVES spectral response from the data. This is possible as DC spectra are essentially featureless.

7.4.2 Data reduction

The UVES pipeline requires some non standard calibration frames before the data can be reduced, namely the format-check frame, and the order definition template. The format-check frame is a frame taken with the ThAr lamp and a narrow slit. This frame is used in combination with a physical model of UVES, the information in the FITS header of the file being reduced, and a ThAr line list to find a "guessed" solution of the spectral format - i.e. the wavelength calibration. This is done by using the physical model to predict the positions of a few hundred ThAr lines (contained in the line list), and projecting them onto the format check frame. This initial dispersion relation is then refined with successive iterations until the most lines, and hence the best solution is found.

The order definition frame is a calibrated exposure with a narrow slit (0.5") illuminated by a continuum lamp. This frame provides an accurate position of the spectrum along the cross-dispersion direction and it has a very high signal to noise ratio, describing the precise locations of the orders. The physical model of UVES is then used in conjunction with this frame to find the location of the orders in an image (usually a flat field frame).

The pipeline begins the data reduction by using the format-check frame and the order definition frame to predict the geometry of the spectral format (order position and wavelength calibration). There are three separate solutions, one per CCD. Once this has been completed, the pipeline proceeds to reduce the data following the standard method with each CCD being treated separately. Master bias and flat field frames are created and applied to the science frames. The bias frame is subtracted to remove the bias level. The inter-order background is then calculated from the flat field and subtracted, and cosmic rays are rejected from the image before the spectrum is extracted from the science frames. The pipeline was used in its OPTI-MAL extraction mode. This mode of extraction assumes a Gaussian shape for the object to be extracted, and uses the full slit width as the extraction slit. To remove ripples that can affect the data, particularly in the red CCDs a black magic routine written by Ralf Napiwotzki was used. This routine shifts the flat field by a few pixels in the spectral direction. The flat field is then extracted and the science frame divided by it. This resultant spectrum is then measured for ripples. This process runs on a loop between a shift of 30 and -30 pixels. The result that produces the least ripples in the final spectrum is the one that is then used. The OPTIMAL extraction mode extracts and divides by the flat field during the extraction process, so the reduction routine is run many times to determine the best value of the pixel shift to reduce the ripples.

The resulting spectrum is then more precisely wavelength calibrated using the arc and the orders are merged together to provide a single spectrum per CCD. The DC standard star was reduced in the same way as the science data, median filtered using 5 pixels and smoothed with a smoothing radius of 20 pixels before being re-sampled onto the wavelength grid of each science object. The science frames were then divided by this DC spectrum. These science frames were then converted into the format (.spek) required by the data analysis software (FITSB2, see next section for details).

7.5 Data analysis

The first step in analysing the echelle data was to remove the signature of telluric water absorption from around H-alpha using a water absorption template constructed from numerous UVES spectra of white dwarfs obtained at Paranal Observatory as part of the SpY programme (Napiwotzki et al., 2001a).

Next, the data were compared to the predictions of white dwarf model atmospheres using the spectral fitting programme FITS2B (v2.04).

These model atmospheres were calculated using the plane-parallel, hydrostatic, non-local thermodynamic equilibrium (non-LTE) atmosphere code TLUSTY, v200 (Hubeny, 1988; Hubeny & Lanz, 1995) and the spectral synthesis code SYNSPEC v47 (Hubeny & Lanz, 2001). TLUSTY assumes plane-parallel geometry and hydrostatic equilibrium. These models include a treatment for convective energy transport according to the ML2 prescription of Bergeron et al. (1992), adopting a mixing length parameter, $\alpha=0.6$. In these calculations a model H-atom was utilised which incorporates explicitly the eight lowest energy levels and represents levels n=9 to 80 by a single superlevel. The dissolution of the high lying levels is treated by means of the occupation probability formalism of Hummer & Mihalas (1988) generalised to the non-LTE atmosphere situation by Hubeny et al. (1994). All calculations include the bound-free and free-free opacities of the H^- ion and incorporate a full treatment for the blanketing effects of HI lines and the Lyman $-\alpha$, $-\beta$ and $-\gamma$ satellite opacities as computed by N. Allard (Allard et al., 2004). During the calculation of the model structure the lines of the Lyman and Balmer series were treated by means of an approximate Stark profile but in the spectral synthesis step detailed profiles for the Balmer lines were calculated from the Stark broadening tables of Lemke (1997). The grid of spectra were calculated to have pure hydrogen atmospheres and covered the T_{eff} range of 10000-34000 K and log g between 7.0 and 9.0 as in Dobbie et al. (2006a).

FITSB2 was developed by Ralf Napiwotzki (Napiwotzki et al., 2004). The code compares the grid of models to the data by means of the χ^2 statistic. It searches for the best model repre-

sentation of the data by attempting to minimise χ^2 using a downhill simplex algorithm (based on the AMOEBA routine from Press et al. 1992). This allows a high degree of flexibility, and almost always produces a fit solution, however, there is no guarantee that this is the global best fit. Because of this, once it has found a fit solution, FITSB2 then restarts the fitting with a simplex constructed around the best fit solution, but with the size of the simplex taken from the initial values. In the case where the new best fit has a lower χ^2 than the first solution, then this solution is replaced by the new one, and the process repeated. The computation of the χ^2 for the model fit uses an estimate of S/N and σ by fitting a parabola through the neighbouring pixels of the point in question and σ is calculated from the scatter around this fit. This method used ± 20 pixels for the estimate of σ, which was then smoothed over ± 50 pixels. The errors on the fits were calculated using both the traditional method and the bootstrapping method. The traditional method involves varying the individual parameters until the difference in χ^2 exceeds a common threshold corresponding to 1σ error limits. This corresponds to the traditional formal error limits quoted in the literature and these errors were used for the T_{eff} and log g calculations. The bootstrapping method involves constructing new spectra from the old ones by randomly selecting points from the observed spectra. Repeats are allowed, which has the effect that on average only $1-\frac{1}{e}$ points of the original spectrum are represented in the new spectrum. FITSB2 then carries out fits of the simulated spectra and computed error limits from the variance of these fitted spectra. These more robust errors were used for the radial velocity measurements.

7.5.1 Determination of effective temperature and gravity

The sets of spectra were combined for each object to illustrate the spectra (figure 7.3). There are either 3 or 4 observations per object, and all were fitted separately using the software.

FITSB2 was used to fit 8 absorption lines in the white dwarf spectra - Hα, Hβ, Hγ, Hδ, Hϵ, H8, H9 and H10. Using a grid of model spectra with effective temperatures from 13000 to 20000 K in steps of 1000 K and log g from 7.50 to 8.50 in steps of 0.01 dex, with sampling of 0.25 Å, the spectra were fitted by the program using a 3σ clipping of deviant points, with a

192
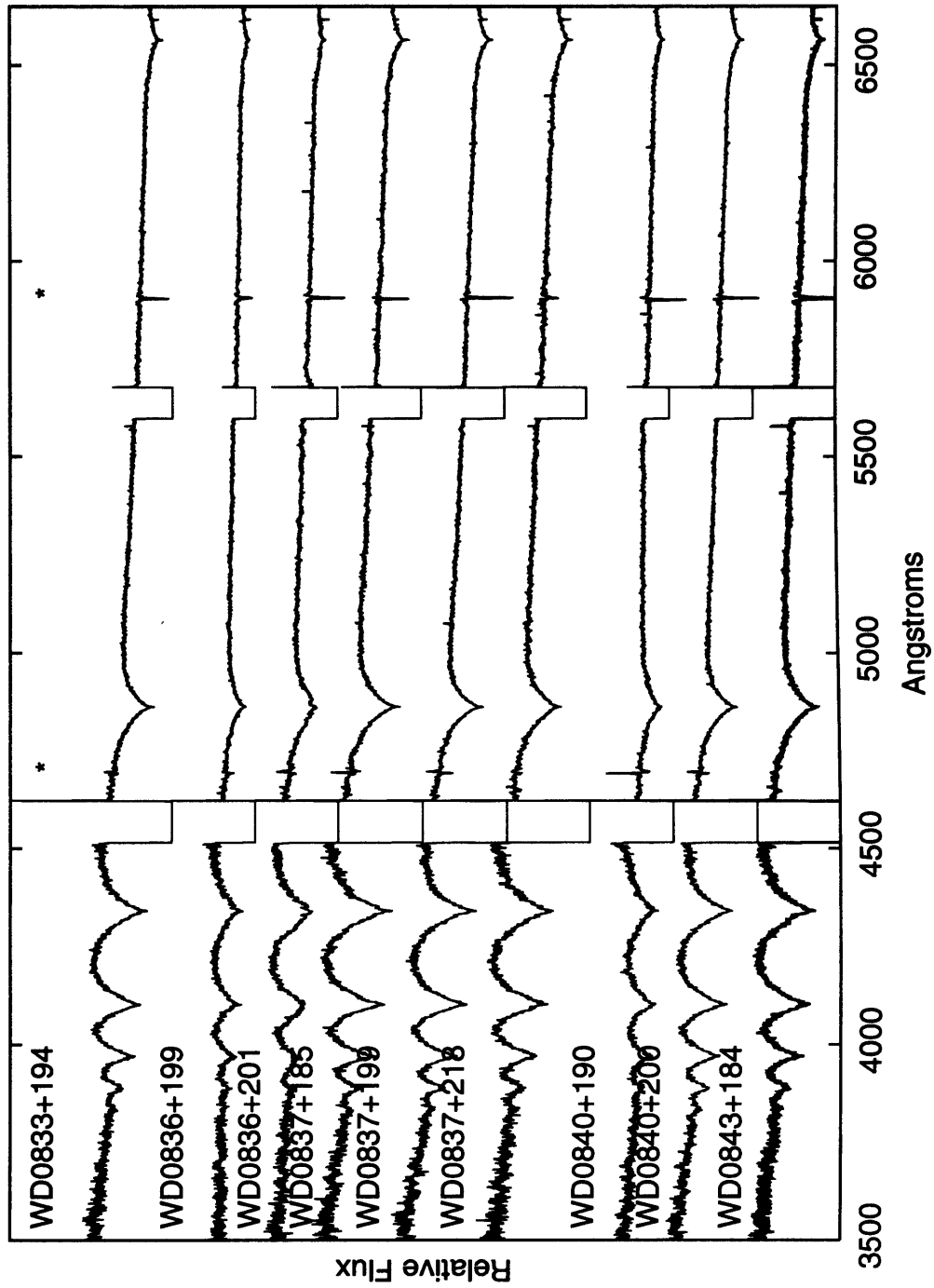
Figure 7.3: The full UVES spectra for all nine white dwarfs observed (median filtered, smoothed and stacked). There are two gaps in the data of width $\approx$80 Å at 4580 and 5640 Å which are caused by the edges of the three CCDs. There are also two artifacts in the data caused by dead pixels in the CCD which are marked by asterisks.

Gaussian convolution FWHM of 0.2 Å for the models. The initial values of T_{eff} and log g for each white dwarf are given in table 7.2, along with these newly calculated values. The newly calculated estimates for T_{eff} and log g are in general consistent with the previously published values, with one exception. It is believed that WD0837+199 and WD0836+201 have been confused somewhere in the past, most noticeably in Reid (1996), Claver et al. (2001), Dobbie et al. (2004) and Dobbie et al. (2006a). In Claver et al. (2001) WD0836+201 is quoted as having a T_{eff} of 16,629 and log g of 8.01, and WD0837+199 has T_{eff} of 17,098 and log g 8.32. WD0836+201 is also believed to be a magnetic white dwarf, as shown by Reid (1996), where he states that WD0836+201 (LB390) has a badly fitted line core to Hα. LB390, however, is in fact WD0837+199 and not WD0836+201. Hence he quotes the T_{eff} of WD0837+199 to be 16000 K. Despite this mix up in the tables, the spectrum presented as WD0836+201 is correct. In Claver et al. (2001), there is a plot of the fitted spectra of EG61, which in table 3 is labelled as also being WD0836+201. However, in the text of the paper it states correctly that EG61 is WD0837+199, and goes on to incorrectly discuss its magnetic properties. WD0836+201 is in fact the magnetic white dwarf, and the spectrum presented in Claver et al. (2001) has been mislabelled, the spectrum of EG59 is in fact that of EG61 and vice versa. This error is also propagated by Dobbie et al. (2006a) who state that EG61 is the magnetic object. This assumption is borne out by the UVES spectrum WD0836+201, which clearly appears to be magnetic. Using the SIMBAD database confirmed that the co-ordinates of this object match those recorded as belonging to WD0836+201. The full spectrum of WD0836+201 is shown in figure 7.4.

Because of the magnetic nature of WD0836+201, it was not possible to fit the absorption lines to get a meaningful result. The new calculated values of 16819 ± 336 and 9.451 ± 0.005 for the T_{eff} and log g differ wildly from the previously calculated values - most noticeably, the log g value is completely different from previously fitted values and also from log g values calculated from its position on evolutionary tracks. This is because the synthetic spectra used do not take into account Zeeman splitting. To gain a more meaningful log g and T_{eff} for this object, a set of models that take into account magnetism should be used. Because of this, no radial velocity analysis was done for this object and the values stated in Claver et al. (2001) as
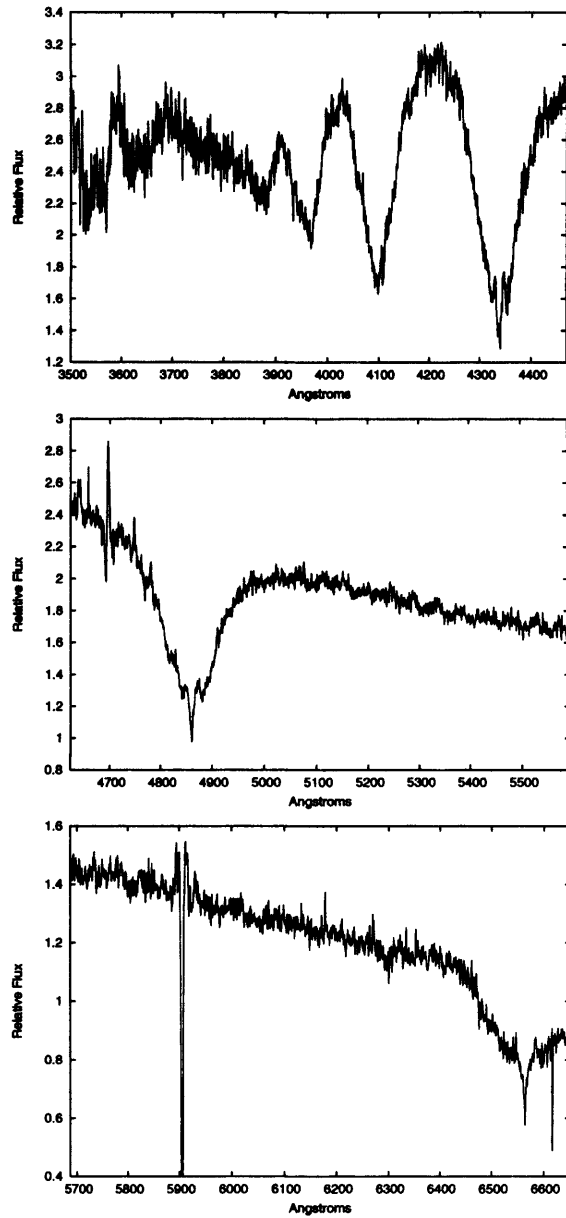
Figure 7.4: The full median filtered, smoothed and stacked UVES spectrum for WD0836+201.
Notice the Zeeman splitting in the hydrogen lines

Table 7.2: Name, effective temperature and log g for the 9 studied Praesepe White dwarfs. The previous values are from Dobbie et al. (2006a) for the first 5 objects and Claver et al. (2001) for the remaining 4. These values are as displayed in the literature.

Name	T_{eff}(K)	log g	FITSB2 T_{eff}	FITSB2 log g
WD0833+194	14999.0^{+208}_{-258}	$8.1800^{+0.04}_{-0.03}$	14852.0±41	8.182±0.005
WD0836+199	14060.0 ±630	8.3400±0.06	14571±60	8.233±0.01
WD0836+201	16629.0 ±350	8.0100±0.05	16819±5	9.451±0.005
WD0837+185	14748.0^{+396}_{-404}	$8.2400^{+0.06}_{-0.05}$	15076.0±60	8.306±0.01
WD0837+199	17098.0±350	8.3200±0.05	17240±38	8.195±0.006
WD0837+218	16833.0^{+236}_{-272}	$8.3900^{+0.04}_{-0.02}$	16875±44	8.473±0.008
WD0840+190	14765.0^{+264}_{-277}	$8.2100^{+0.03}_{-0.03}$	14935±68	8.381±0.010
WD0840+200	14178.0 ±350	8.2300±0.05	14983±42	8.176±0.005
WD0843+184	14498.0^{+199}_{-206}	$8.2200^{+0.04}_{-0.04}$	15018±50	8.340±0.008

the T_{eff} and log g for this object have been used in the subsequent IFMR analysis. The errors given in table 7.2 for T_{eff} have been calculated using the standard method. These errors are unrealistically small and so in the following calculations an error of 2%, which is larger than those given by FITSB2 ($\approx$ 40) using both the standard and bootstrapping method, is used as it is more realistic (Napiwotzki et al., 1999).

7.5.2 Determination of Doppler shifts

Using the newly calculated values of T_{eff} and log g (with the exception of WD0836+201) as input parameters, FITSB2 was used with a model grid which was more finely sampled in wavelength space than the first, to calculate radial velocity measurements for each of the observations. This finer grid was necessary to fit to the Hα and Hβ absorption lines to calculate radial velocities. The synthetic spectra were again generated using SYNSPEC. The grid, again covered the effective temperatures from 13000 to 20000 K in steps of 1000 K and log g from

Table 7.3: Name and radial velocity measurements for the 8 studied Praesepe White dwarfs.

Name	RV_1	RV_2	RV_3	RV_4
WD0833+194	77.13± 1.97	79.60± 2.03	83.54± 2.77	75.69±2.68
WD0836+199	75.11± 4.83	85.86±3.66	84.66±2.39	94.57±3.42
WD0837+185	70.39± 4.02	83.44± 1.85	90.89± 2.41	-
WD0837+199	75.47± 1.81	76.71± 2.41	71.25±2.67	70.09±2.00
WD0837+218	80.18± 1.65	81.95± 2.34	83.66± 1.75	-
WD0840+190	91.32± 7.61	84.66± 3.02	82.77± 3.47	-
WD0840+200	73.76±3.20	75.42± 1.69	74.82±2.07	74.64±2.13
WD0843+184	93.40 ±3.00	86.10± 1.86	87.66± 3.02	87.80±1.94

7.50 to 8.50 in steps of 0.01 dex, but with a sampling of 0.05 Å. Initial values for radial velocities were calculated, then the line fitting was redone using the calculated radial velocities as the initial values for the fit, thus reducing the errors and ensuring that the fit was robust. The bootstrapping error method was used for the radial velocity calculations, as the errors are more robust, and as variability in the radial velocities may be seen, it is important that the errors be as robust as possible.

The radial velocity measurements for each observation may be seen in table 7.3. An independent check of these results was performed using a different set of model atmospheres (the LTE atmospheres used by Koester et al. 2001). The differences were well within the errors of the measurements and no systematic discrepancies were found.

To determine whether these radial velocities were in fact varying, a χ^2 was calculated for each object using equations 7.1 and 7.2.

$$\bar{x} = \frac{\sum x_i/\sigma_i^2}{\sum 1/\sigma_i^2},$$
(7.1)

$$\chi^2 = \sum \left(\frac{x - \bar{x}}{\sigma}\right)^2,$$
(7.2)

197

Table 7.4: Name, χ^2, number of measurements (N) and $\log_{10}$ probability for the eight white dwarfs.

Name	χ^2	N	$\log_{10}$ prob
WD0833+194	5.145308	4	-0.792
WD0836+199	11.67742	4	-2.067
WD0837+185	19.66526	3	-4.270
WD0837+199	6.575641	4	-1.062
WD0837+218	2.320046	3	-0.504
WD0840+190	1.054191	3	-0.229
WD0840+200	0.236846	4	-0.013
WD0843+184	4.304755	4	-0.638

where $\bar{x}$ is the weighted mean of the measurement, x, and the error of that measurement, σ. The χ^2 for each set of measurements was calculated, and the log of the probability that the χ^2 corresponds to. These data are shown in table 7.4.

From table 7.4, it can be seen that WD0837+185 appears to have a very small probability of the statistical fluctuation in its radial velocities occurring naturally. The probability for this difference in radial velocity occurring in WD0837+185 corresponds to $10^{-4.2}$. The SPY project have produced radial velocity measurements for a sample of 1000 white dwarfs. If a probability of 10^{-3} is used as the significance limit, on average one "detection" is expected to be due to chance statistical fluctuations. Using 10^{-4} as the significance limit, only 0.1 detection is expected to be due to chance, which probably means none in the total sample. When dealing with a smaller sample, such as here, a probability of 10^{-3} could be used as a reasonable limit as it corresponds to a $\approx 3\sigma$ limit. These statistics mean that WD0837+185 is statistically likely to be a radial velocity variable white dwarf.
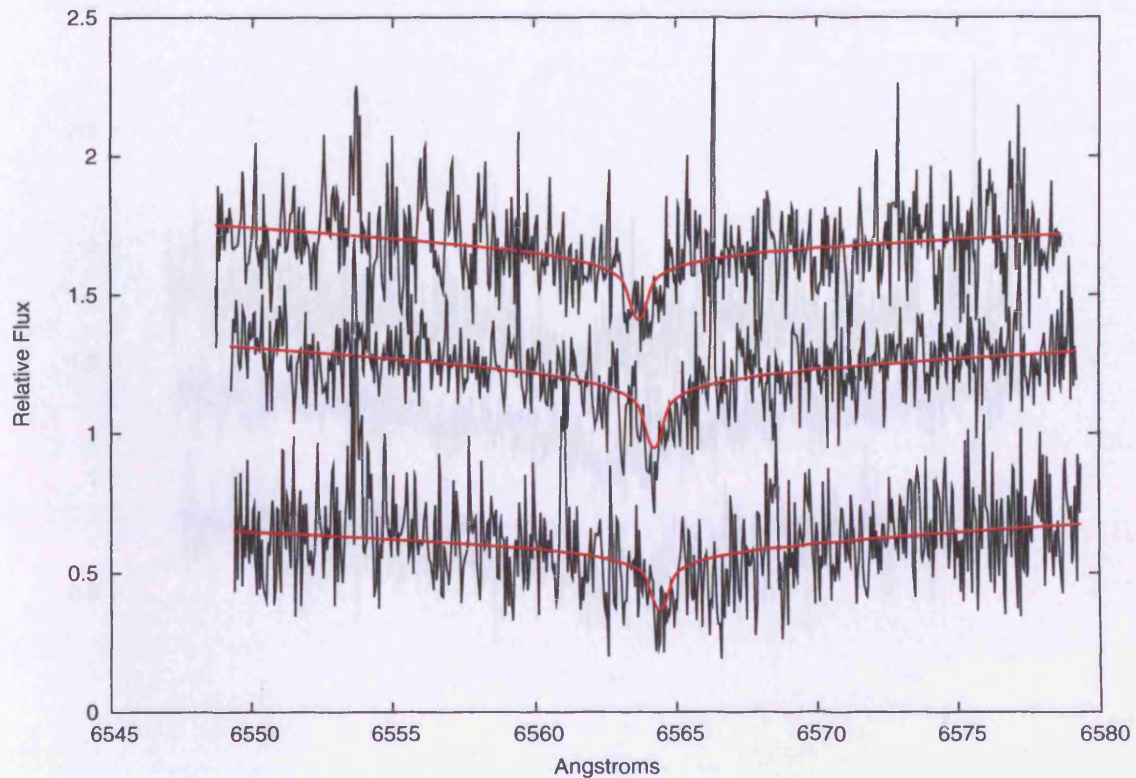
Figure 7.5: The three Hα lines from the three sets of spectra observed for WD0837+185. The red lines are the FITSB2 fit to the data. The core of the lines can be seen moving. The observations were taken on 16/11/2005 and two on the 14/12/2005. The observations are plotted in chronological order with the earliest observation at the top of the plot.

7.6 Results

7.6.1 Double degenerate

As described above, it is statistically likely that WD0837+185 is a double degenerate system. It can be seen in figures 7.5 and 7.6 that the cores of the H_α and H_β lines are moving.

No trace of a companion is detectable within the spectrum of this object, and it has no 2MASS detection, making the companion likely to be another white dwarf. The SDSS spectrum of this object also shows no sign of a companion. As white dwarfs with large masses have small
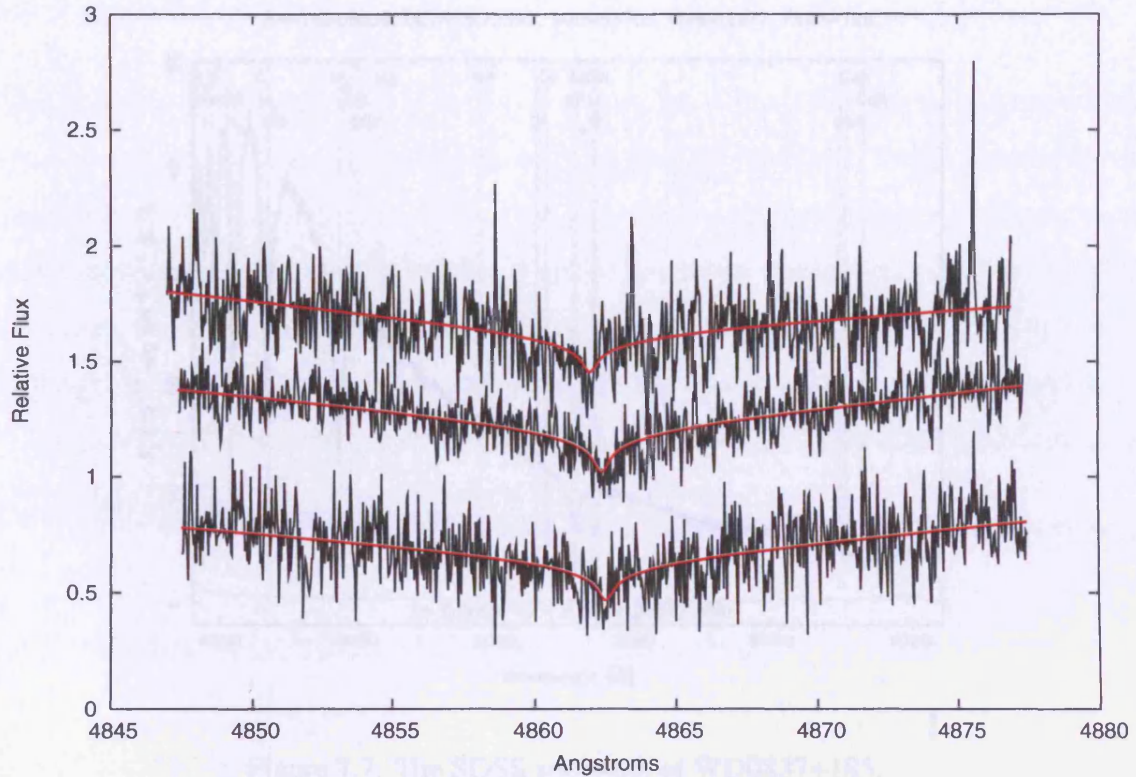
Figure 7.6: The three Hβ lines from the three sets of spectra observed for WD0837+185. The red lines are the FITSB2 fit to the data.The core of the lines can be seen moving.The observations were taken on 16/11/2005 and two on the 14/12/2005. The observations are plotted in chronological order with the earliest observation at the top of the plot.

radii, the unseen companion must have a larger mass than WD0837+185. The total mass of this system is therefore larger than the Chandrasekhar limit ($\approx$ 1.4 M$_\odot$), therefore if this binary were to merge, it is likely that a supernova would occur. The predicted temperature and gravity from the evolutionary models of Bergeron et al. (1995) agree with the measured values, indicating that it is likely that the fainter secondary is not contributing much flux to the system. WD0837+185 is the first close white dwarf-white dwarf binary known within an open star cluster. Close white dwarf-white dwarf binaries (double degenerates, DDs) are one possible outcome of the binary evolution of stars. DDs have been theorised to be supernova type Ia progenitors (Iben & Tutukov, 1984; Livio, 2000; Napiwotzki et al., 2001a, 2003). They are also important sources of gravitational waves, which are yet to be detected, although there are upcoming experiments designed to do this (Laser Interferometer Space Antenna, Stroeer et al.
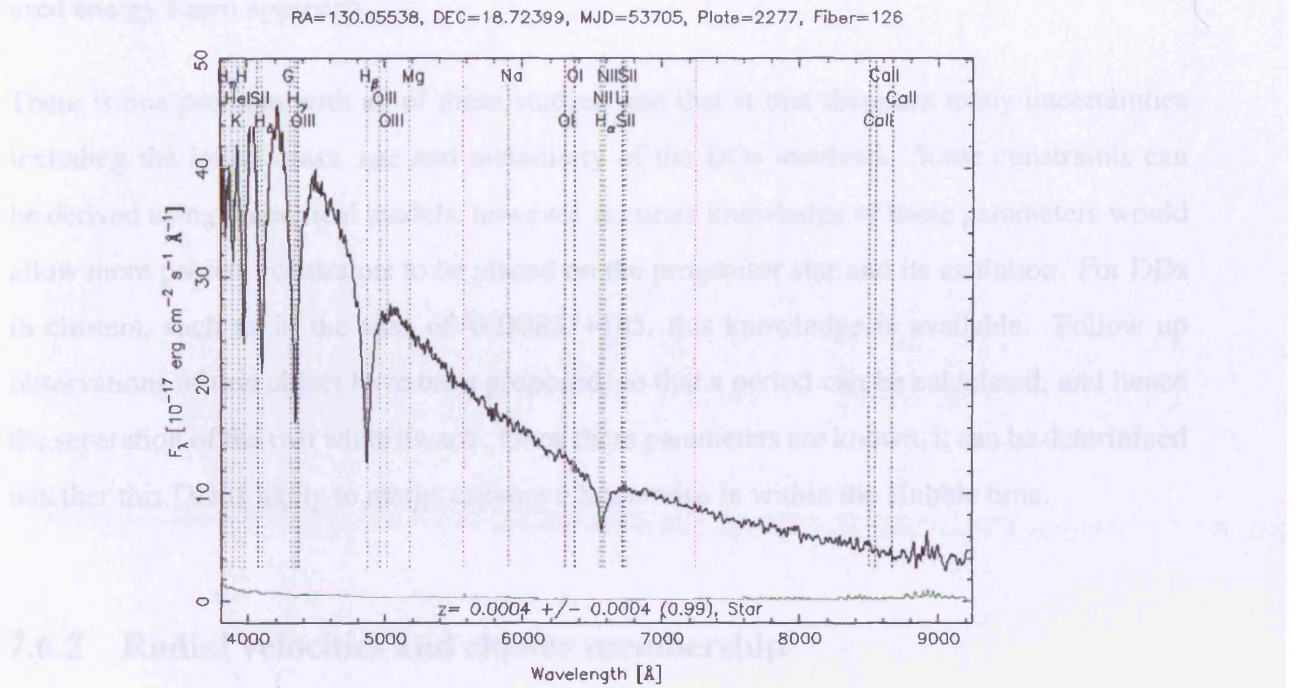
Figure 7.7: The SDSS spectrum of WD0837+185.

2005). Very little is known about the evolution of close binaries up to the point where they become DDs, particularly the common envelope phase. This lack of knowledge affects predictions of the numbers of Supernova Ia produced by the different methods. Common envelope evolution is described by the parameter α_{CE} which is defined as the fraction of orbital energy released by the orbital contraction, which is then used to eject the envelope. This parameter is only weakly constrained by theoretical calculations and so it is necessary to define α_{CE} using empirical data. DDs are therefore important for this task (Saffer et al., 1998; Nelemans et al., 2000, 2001). To understand the results of common envelope evolution, we must be able to constrain this parameter, as the results not only affect DDs but also cataclysmic binaries, very low mass and very high mass white dwarfs, close binary stars in planetary nebulae and double neutron stars etc. Recently a study by Nelemans & Tout (2005) reconstructed the evolution of known DDs and concluded that the common envelope evolution using the parameter α_{CE} does not provide a good description of the first phase of the mass transfer involved. They suggest that an angular momentum based approach is more appropriate than the commonly

used energy based approach.

There is one problem with all of these studies, and that is that there are many uncertainties including the initial mass, age and metallicity of the DDs involved. Some constraints can be derived using theoretical models, however, accurate knowledge of these parameters would allow more precise constraints to be placed on the progenitor star and its evolution. For DDs in clusters, such as in the case of WD0837+185, this knowledge is available. Follow up observations of this object have been proposed, so that a period can be calculated, and hence the separation of the two white dwarfs. Once these parameters are known, it can be determined whether this DD is likely to merge causing a Supernova Ia within the Hubble time.

7.6.2   Radial velocities and cluster membership

As has been discussed, white dwarfs in clusters are very important for calculating the IFMR, however, one must be sure that the white dwarfs used to calculate the relationship are bona fide members of the cluster. To determine the membership status of these white dwarfs, radial velocities must also be used. The gravitational redshift can be calculated from the Fontaine et al. (2001) models using the measured T_{eff} and log g and is then subtracted from the Doppler shift measurements, leaving the radial velocity of the white dwarf, which can be compared to the radial velocity of the cluster. From table 7.5 it can be seen that it is likely that WD0837+218 is not a member of the cluster as the difference between the expected and measured radial velocities divided by the standard deviation of the measured radial velocity for this dwarf is 2.17. Only 3 objects in 100 should have a radial velocity that varies this much from the prediction, and as only 9 objects were observed, it seems likely that it is not a member. WD0837+218 is also an outlier in the IFMR as shown by Dobbie et al. (2006a) who noted that Claver et al. (2001) and Dobbie et al. (2004) have commented that this white dwarf was too hot for its relatively high mass. It is also pointed out in Dobbie et al. (2004), that WD0837+218 lies $\approx 2°$ away from the cluster centre, making it the white dwarf furthest away from the cluster, which may also indicate that it is a non member.

202

Table 7.5: The expected line-of-sight velocity assuming cluster membership. The spectral velocity shift as determined from simultaneously fitting the H-α and H-β lines. The gravitational redshift estimated from $T_{\rm eff}$ and log g using the thick H layer CO evolutionary models of Fontaine et al. (2001). The "observed" line-of-sight velocity. The ratio of the radial velocity difference to the measured error, where RV_O is the observed radial velocity and RV_C is the cluster radial velocity.

WD	Name	RA	Dec	RV_C	H-α,H-β shift	GR.	$RV_O \pm \Delta RV_O$	$(RV_O-RV_C)/\Delta RV_O$
WD0833+194	–	08:36:10.01	+19:38:19.1	35.0	78.8±1.2	40.1±4.4	38.7±4.6	0.80
WD0836+199	LB1847,EG60	08:39:47.20	+19:46:12.1	34.5	85.8±1.6	48.4±5.1	37.4±5.3	0.55
WD0837+185	LB5959	08:40:13.30	+18:43:26.4	34.8	84.3±1.4	47.6±5.1	36.7±5.3	0.36
WD0837+199	LB393, EG61	08:40:28.09	+19:43:34.8	34.5	75.7±1.1	40.8±4.4	34.9±4.5	0.09
WD0837+218		08:40:31.47	+21:40:43.1	33.9	82.5±0.9	62.9±6.5	19.6±6.6	2.17
WD0840+190		08:42:58.03	+18:54:35.5	34.4	84.7±2.2	53.9±5.7	30.8±6.1	0.59
WD0840+200	LB1876	08:42:52.32	+19:51:11.3	34.2	74.9±1.6	40.7±4.4	34.2±4.7	0.00
WD0843+184	LB8648	08:46:01.91	+18:30:48.5	34.2	88.5±1.4	48.4±5.1	40.1±5.3	1.11

7.6.3 Proper motion survey

I performed my own proper motion survey using the SDSS and SuperCOSMOS databases to check the membership of the known white dwarfs. Firstly a 10 × 10 degree square centred around Praesepe (08 40 24 +19 41 00 J2000, Kharchenko et al. 2005) was selected from the SDSS data release 5 (York et al., 2000). This region was then cross correlated with the SuperCOSMOS catalogue (Hambly et al., 2001a). This meant that each white dwarf had proper motions and optical photometry (u, g, r, i, z). SuperCOSMOS was used as the proper motions are more robust, and not calculated in integer values as in the USNOB1.0 catalogue. All sources were selected that had $24 \geq g \geq 17$, which eliminated saturated and extremely faint sources. These selected objects were then culled and those that lay more than 1 magnitude below the NEXTGEN model of 500 Myr (Baraffe et al., 1998), scaled to the distance of the cluster were rejected. This conservative selection of allowing points to fall as much as 1 magnitude below the model was to take into account any errors in photometry, and because the NEXTGEN model being used is younger than the assumed age of the cluster (500 Myr whereas the age of Praesepe is 625 Myr). Two 2D Gaussian were then fitted to all of the points selected, one centred around 0, 0 and one at -35.7, -12.7 mas yr^{-1}. The Gaussian fitted to the cluster had a width of 9.0 mas yr^{-1}. Using this σ as the selection radius, all objects that fell within a circle of radius 9.0 mas yr^{-1} around -35.7, -12.7 mas yr^{-1} were selected to be potential proper motion members of Praesepe. A further selection was then imposed, which was that only objects with g-i<0 were selected, thus selecting all potential white dwarfs. These criteria resulted in ≈100 objects being selected. Of these objects, the majority had 0>g-i>-3. The g, g-i colour magnitude diagram was plotted, and on it was over-plotted the modern evolutionary models of Holberg & Bergeron (2006) (based on those of Bergeron et al. 1995) with masses of 0.7, 0.8 and 0.9 $M_{\odot}$. Nine of the selected objects fall onto these tracks as can be seen in figure 7.8. The tenth object is WD0836+199 which was not found in the SDSS, but as spectra were observed for it, these SDSS colours have been estimated for it.

All of these objects have g magnitudes between 17.7 and 18.2 which are reasonable for white dwarfs belonging to the cluster. There are eleven known white dwarfs in Praesepe and only
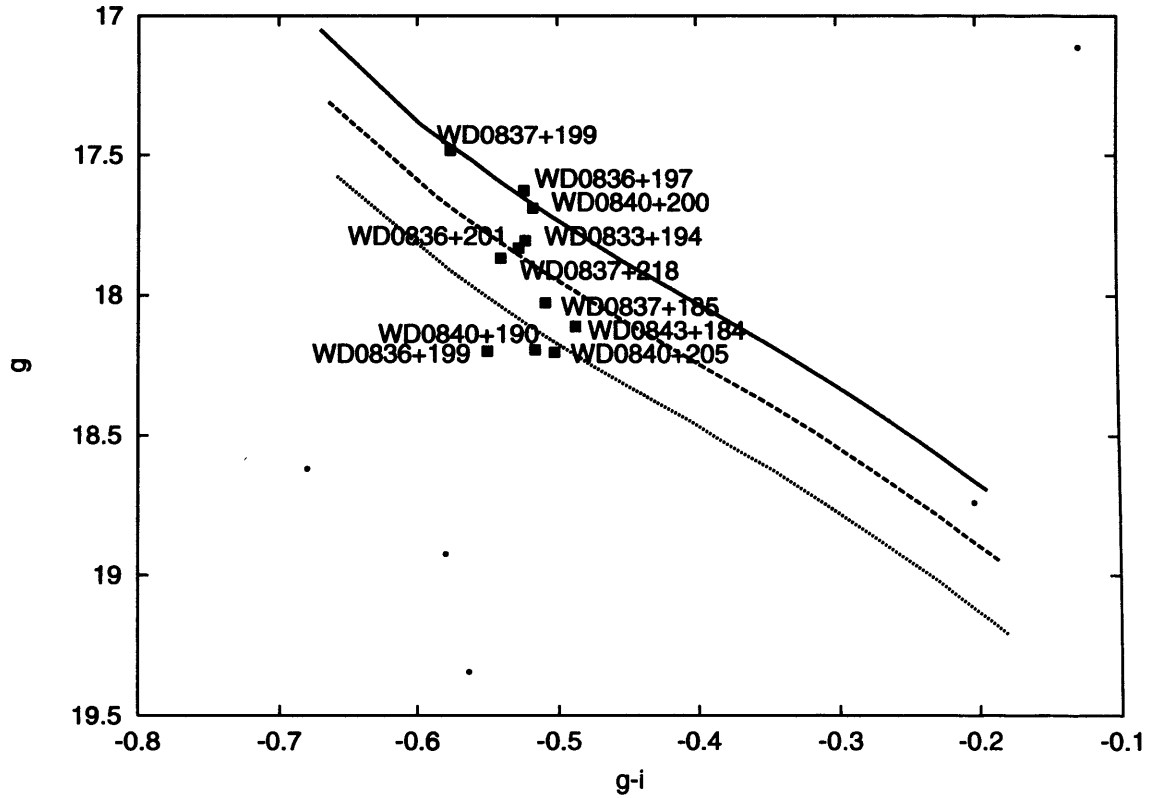
Figure 7.8: g, g-i colour magnitude diagram. The ten white dwarfs selected from their photometry and proper motions, including the two objects known to be missing are labelled on the plot. The small points are other objects that were selected from their photometry and proper motions. The models are from Bergeron et al. (1995) and the solid line is mass=0.7 $M_\odot$, dashed line, mass=0.8 $M_\odot$, dotted line, mass=0.9 $M_\odot$. It should be noted that due to incorrect proper motion WD0836+197 was not selected from the original sample. The photometry for WD0836+199 is estimated as it is not present in the SDSS.

eight were recovered. The white dwarfs not recovered by this survey are WD0836+199, WD0836+197 and WD0837+199. WD0836+199 was not found in the SDSS. The reason for this object not being recovered is unknown. The area containing the white dwarf has been surveyed by the SDSS, however, no objects with the correct characteristics, e.g. g-i<0, show up within 1' of its recorded coordinates. It is present in the USNOB1.0 survey and has a recorded proper motion of -38, -10 mas yr^{-1} which is consistent with cluster membership. The g, r and i magnitudes have been estimated for this object using the T_{eff} and log g that have been previously calculated for it and the USNOB1.0 magnitudes. WD0836+197 is present in the SDSS and SuperCOSMOS surveys, however, it falls within a "drill hole" in the Super-COSMOS data as does WD0837+199. This means that they are located in areas of the survey around bright stars, and so their photometry and proper motion measurements may have been affected. The proper motion of WD0837+199 appears to be a member of the cluster if we assume that the proper motion is unaffected by the drill hole, however, the same cannot be said for WD0836+197. It has been previously discussed in Claver et al. (2001) and Dobbie et al. (2004, 2006a) that in the POSS-1 (USNOB1.0) plate image of WD0836+197, its astrometry is likely to have been affected by the proximity the star KW195. The SuperCOSMOS proper motion measurement for this object is recorded as -342, 0 with errors of 66.75, 66.25 mas yr^{-1}, which confirms the hypothesis that it has been affected by the brighter star. Dobbie et al. (2006a) calculate a proper motion of $\mu_{\alpha}cos\delta$=-34±9, μ_{δ}=-18±12 mas yr^{-1} using the POSS-II F band and an V band image taken using CFHT with an epoch difference of 12 years, which supports the hypothesis that despite the USNOB1.0 proper motion, that it is a member of the cluster. Table 7.6 presents the photometry for each of these white dwarfs.

WD0840+205 is not present in the radial velocity data, however, there is an SDSS Data Release 6 spectrum of it as shown in figure 7.9. It appears that all 10 recovered objects are members of the cluster from their proper motions and photometry alone. The radial velocity measurements indicate that WD0837+218 is likely to be a non member.
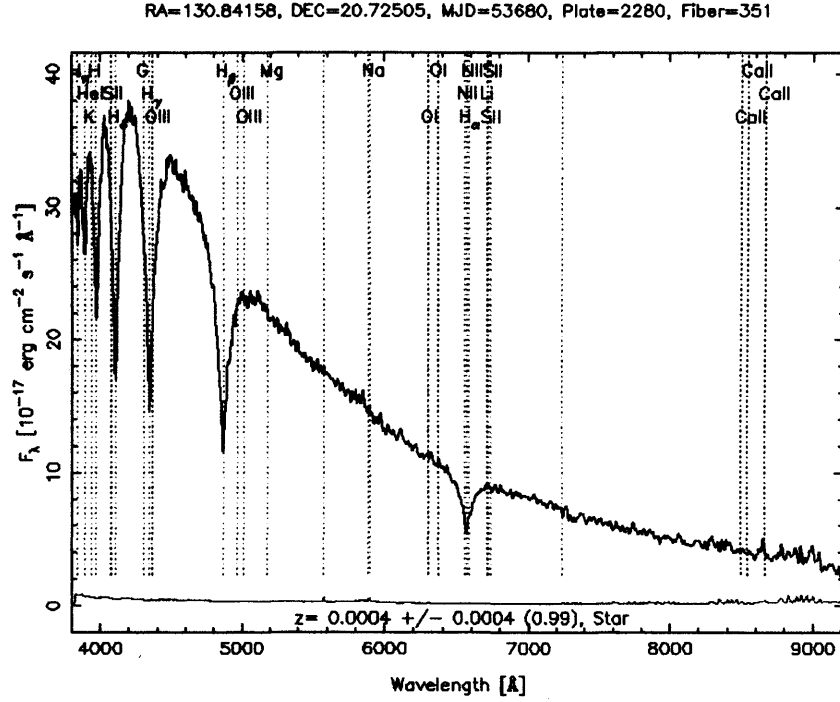
Figure 7.9: SDSS spectrum of WD0840+205.

Table 7.6: Name and photometry (g, r, i, z) from the SDSS, for the Praesepe white dwarfs with radial velocity measurements. WD0836+201 has been omitted due to its magnetic nature. The magnitudes for WD0836+199 are not present in the SDSS.

name	g	r	i	z
WD0833+194	17.806±0.006	18.081± 0.007	18.329± 0.010	18.657±0.036
WD0837+185	18.027± 0.006	18.308 ± 0.008	18.535± 0.011	18.771±0.043
WD0837+199	17.484 ± 0.005	17.797 ± 0.007	18.060± 0.009	18.301±0.026
WD0837+218	17.869 ± 0.006	18.134± 0.008	18.410± 0.011	18.703±0.042
WD0840+190	18.204± 0.006	18.445± 0.008	18.707 ± 0.012	19.002±0.049
WD0840+200	17.690± 0.005	17.988 ± 0.007	18.208 ± 0.008	18.552±0.034
WD0843+184	18.111± 0.006	18.334 ± 0.008	18.599 ± 0.011	18.843±0.039

7.6.4 Radius and mass calculations

The radii and masses for the white dwarfs were calculated by Paul Dobbie by fitting a bi-cubic spline to the pure H models of Holberg & Bergeron (2006) between $5000\ K < T_{eff} < 110000$ K and $7.0 < \log g < 9.5$, using surface fluxes calculated for the white dwarfs using the r, i and z Sloan magnitudes. Ignoring the small radius change ($\sim 3\%$ between 20000 K and 12000 K) it can be seen that r, i and z are parallel to a first order approximation when plotted against temperature for a constant log g, thus minimising errors in estimating T_{eff} from surface flux (see figure 7.10). The accuracy of these values depend on the z, r and i magnitudes of the white dwarf, and also on the accuracy of the distance to the cluster.

More specifically, the radius of each white dwarf was first determined by scaling the distance (D) to each by the ratio $(f/F)^{0.5}$ (from the relation between luminosity and radius), where F and f are the surface flux and the observed flux respectively.

The surface flux (F) in the Sloan filters (r, i and z) for each star was obtained from the pure-H model grid of Pierre Bergeron (Holberg & Bergeron, 2006). These model fluxes are believed to be good to $<1\%$. The uncertainty in the surface flux due to the error in the surface gravity determination was assumed negligible. However, the error in the effective temperature determination was found to introduce an uncertainty of only 3.5% in the surface flux (r, i and z) in the temperature range of interest. These uncertainties are larger if the u or g magnitudes are used (see figure 7.10).

As has been discussed, white dwarfs in clusters are very important for calculating the IFMR, however, one must be sure that the white dwarfs used to calculate the relationship are bona fide members of the cluster. The distance to each white dwarf was assumed to be the distance to the centre of the Praesepe open cluster. This distance (184.5 ± 6 pc) was based on a weighted mean of the Hipparcos measurement ($177^{+10.3}_{-9.2}$ pc, Mermilliod et al. 1997), a ground based parallax measurement (Gatewood & de Jonge, 1994) and a recent photometric determination which takes into account a new spectroscopic determination of the cluster metallicity (An et al., 2007). However, as a given white dwarf will not lie exactly at the cluster centre, there is
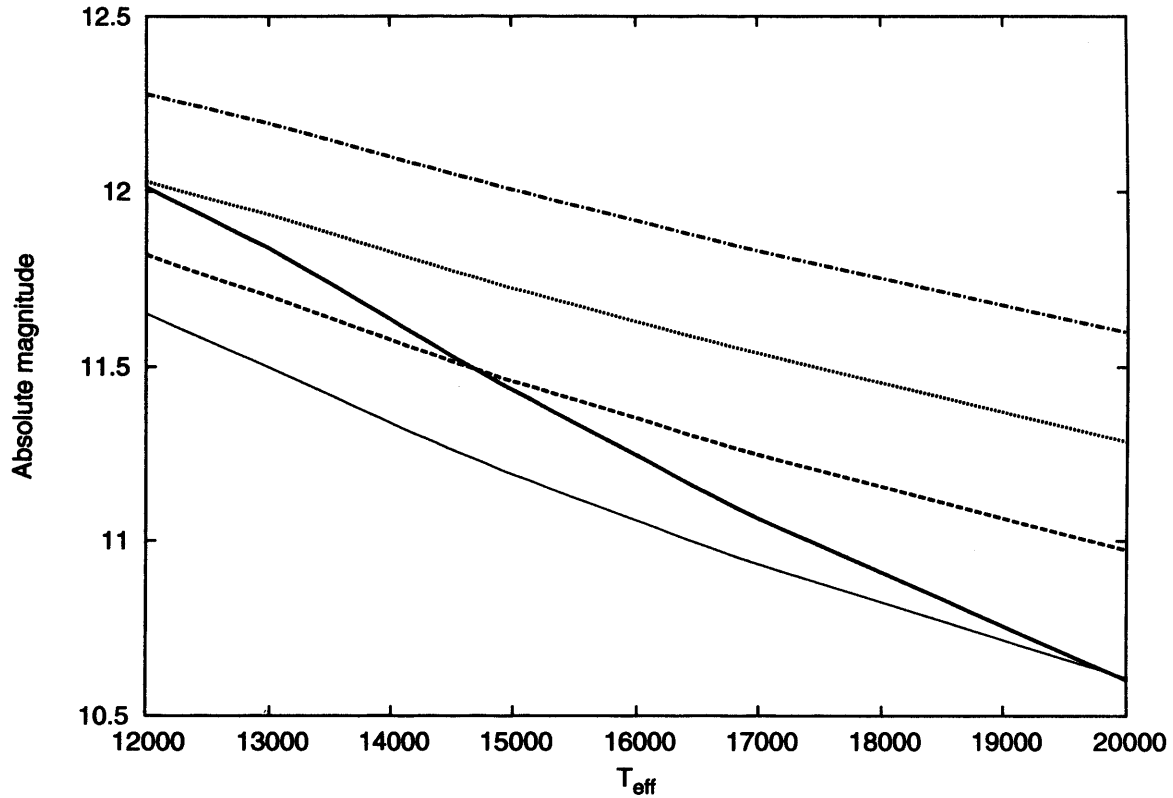
Figure 7.10: A plot of SDSS u (bold, solid line), g (thin, solid line), r (dashed line), i (dotted line) and z (dot-dashed line) absolute magnitudes against T_{eff} for constant log g of 8.

a further uncertainty in the distance to each dwarf. This can be estimated from the projected spatial distribution of the white dwarfs. Despite the initial survey extending out to 2.5-3.0 degrees from the cluster centre, all probable white dwarf members are found to lie within 2 degrees of central Praesepe, which at a distance of 184.5 pc corresponds to 6.5 pc. Assuming the distribution of the white dwarfs is spherically symmetric about the cluster centre, all should thus lie within the distance range 184.5±8.5pc (4.6%).

There are systematic uncertainties in the observed SDSS fluxes at the level of 2% (see Fukugita et al. 1996 for more details). Thus the total combined uncertainty in the radius determinations from the white dwarf distances, the observed fluxes and the predicted fluxes is estimated to be $\sim5\%$ (i.e. $\sqrt{4.6^2 + 1.75^2 + 1^2}$).

The masses for each star were calculated using equation 7.3,

$$M = \frac{RG}{0.635},$$ (7.3)

where M is the mass of the star in solar masses, R the radius of the star in solar radii and G, the gravitational redshift in kms^{-1}.

The gravitational redshift has been determined by measuring the shift of the non-LTE cores of the Hα and Hβ lines in the spectra of each white dwarf and then subtracting from this the line-of-sight velocity, assuming each white dwarf is a cluster member. The radial velocity of the cluster has been measured to be 34.53 kms^{-1} using Coravel, with a 1D dispersion of only 0.4 kms^{-1} (Mermilliod & Mayor, 1999). It is extremely unlikely that the cluster white dwarfs will have velocities which differ by a large amount from the mean velocity due to evolutionary effects (e.g. asymmetric mass loss) since they remain within the cluster despite having formed 200-300 Myr ago as calculated from their cooling times.

It should be noted that in section 7.6.2 a model gravitational redshift was used to determine the measured radial velocity. Here, the cluster radial velocity has been assumed and been used to determine the gravitational redshift, G, and hence the mass.

A detailed study of the wavelengths of prominent water absorption lines in a large number of UVES spectra obtained as part of the SpY project, which uses an identical instrumental set-up to this study, indicates that the external calibration of the wavelength scale of UVES is stable at the 0.7 kms^{-1} level.

Thus the total uncertainty in the mass determinations is estimated to be $\sim$6%. The masses and radii are shown in table 7.7 and also in figure 7.11 for the objects believed to be members of the cluster. The radial velocity variable object WD0837+185, and WD0836+199 which has no SDSS photometry have been omitted in addition to the magnetic white dwarf.

The masses for these objects are all higher than the field distribution, which peaks at a mass of 0.565 $M_\odot$ (Bergeron et al., 1995; Marsh et al., 1997; Liebert et al., 2005). The high masses indicate that they are likely to be members of Praesepe.
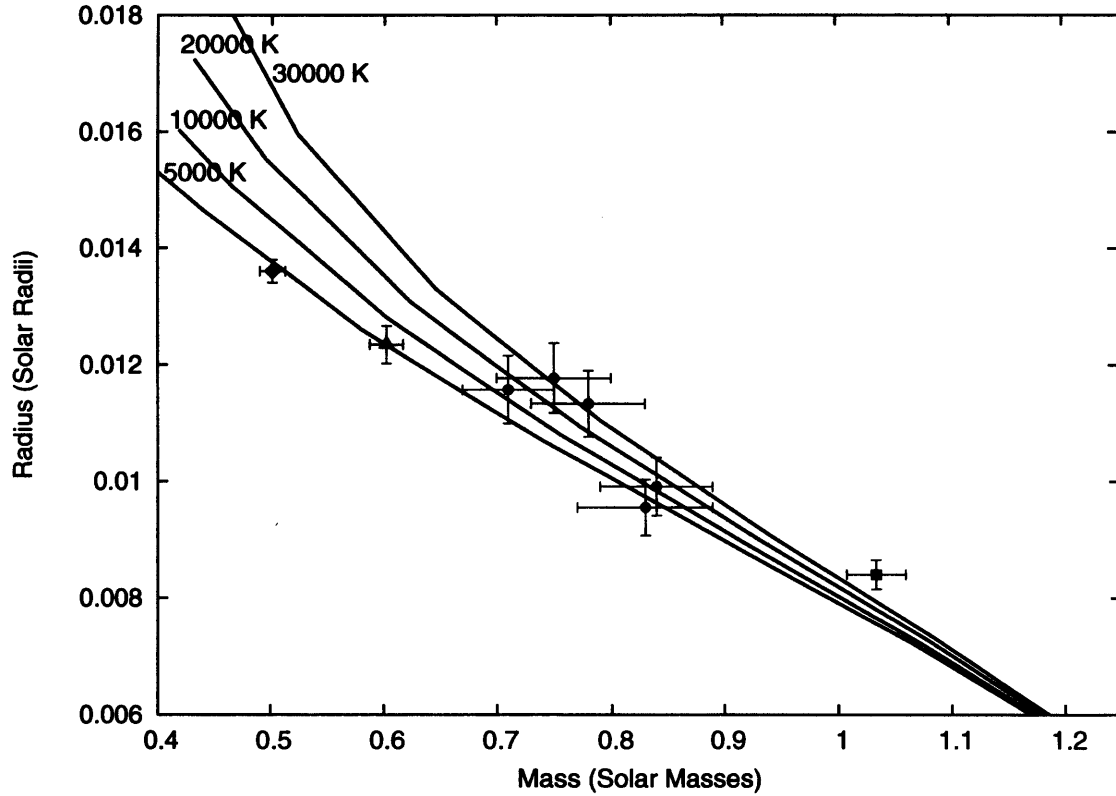
Figure 7.11: Mass radius plot for the studied white dwarfs. Procyon B (filled triangle), 40 Eri B (filled diamond) and Sirius B (filled square) which are shown for comparison (Provencal et al., 2002). The 5 objects plotted with filled circles are the objects WD0833+194, WD0837+199, WD0840+190, WD0840+200 and WD0843+184. The objects that have been omitted are WD0837+218 as it is likely to be a non member, WD0836+199 has no SDSS photometry and WD0837+185 is likely to be a radial velocity variable. The lines on the plot are the theoretical mass radius relations from the models of Fontaine et al. (2001) using a thick H layer (1.0^{-4} M$_\odot$) and CO cores. These relations are for temperatures of 5000, 10000, 20000 and 30000 Kelvin.

Table 7.7: Masses and radii for the white dwarfs believed to be Praesepe members calculated using the Fontaine et al. (2001) models and the SDSS photometry. The objects that have been omitted are WD0837+218 as it is likely to be a non member, WD0836+199 has no SDSS photometry and WD0837+185 is likely to be a radial velocity variable.

Name	M	R
	$M_\odot$	$\times 10^{-2} R_\odot$
WD0833+194	0.78 ± 0.05	1.133 ± 0.057
WD0837+199	0.71 ± 0.04	1.157 ± 0.058
WD0840+190	0.83 ± 0.06	0.955 ± 0.048
WD0840+200	0.75 ± 0.05	1.177 ± 0.060
WD0843+184	0.84 ± 0.05	0.991 ± 0.050

7.6.5 Revised Initial Mass-Final Mass Relation

The cooling time of each white dwarf was calculated using cubic splines to interpolate between the models of Fontaine et al. (2001). These calculations include a mixed CO core and thick surface H surface layer as in Dobbie et al. (2006a). Dobbie et al. (2006a) found that if thin H layer models had been used, the final masses systematically decrease by 0.02 $M_\odot$. The progenitor lifetime was then calculated for each object by subtracting this lifetime from the age of the cluster (625 Myr). To calculate the mass of the progenitor star, the models of Girardi et al. (2000) for solar metallicity were used, and again cubic splines were used to interpolate between the points. The cooling time and final mass of these white dwarfs are shown in table 7.8. The initial and final masses were then plotted. The cooling times and initial masses for WD0836+197, WD0840+205 and WD0836+201 have been calculated using T_{eff} and log g from the literature (Claver et al., 2001; Dobbie et al., 2006a). To make this work consistent with that of Dobbie et al. (2006a), the white dwarfs belonging to the Hyades, M35, NGC2516 and the Pleiades are also plotted as well as Sirius B. The white dwarfs from M37 are not included due to uncertainties in the age of the cluster. It should be noted that the Pleiades, NGC2516 and M35 (age <200 Myr) are much younger than Praesepe, whereas the Hyades is

Table 7.8: Cooling time and initial mass for the white dwarfs in Praesepe.

Name	T_{cool}	$M_{initial}$
	Myr	$M_{\odot}$
WD0833+194	269±4	3.320±0.183
WD0837+185	313±5	3.483±0.228
WD0837+218	304±5	3.734±0.307
WD0840+190	367±6	3.491±0.297
WD0843+184	338±6	3.591±0.261
WD0836+199	308±5	3.461±0.221
WD0837+199	175±3	3.062±0.124
WD0840+200	385±22	3.375±0.269

the same age. The temperatures and surface gravities used to calculate the masses for these other cluster white dwarfs are as for Dobbie et al. (2006a).

The white dwarfs that deviated from this relation as shown in Dobbie et al. (2006a) are WD0836+197, WD0837+218 and WD0836+201. WD0836+201 is magnetic, thus making any T_{eff} and log g calculation unreliable. WD0837+218 is believed to be a non member as it has a radial velocity that greatly varies from that of the cluster, and WD0836+197 was not observed for this work as a bright nearby star KW195 was observed by mistake. The location of WD0836+197 near KW195 makes proper motion measurements difficult. It may be that this object is a member of the cluster, however, accurate observations of it are difficult to make, causing it to be an outlier in the IFMR. Dobbie et al. (2006a) observed this object to measure T_{eff} and log g for it, but as yet, no radial velocity measurements have been taken of it.

The initial mass-final mass data in figure 7.12 is reasonably approximated by a linear function. The two outlying objects and the known magnetic white dwarf have been omitted from this fit, as it is possible that they have been formed via binary evolution or are non members of the cluster. Curiously, WD0837+185, the radial velocity variable is not an outlier to the fit to the data, although if the common envelope phase of the system evolution occurred late during
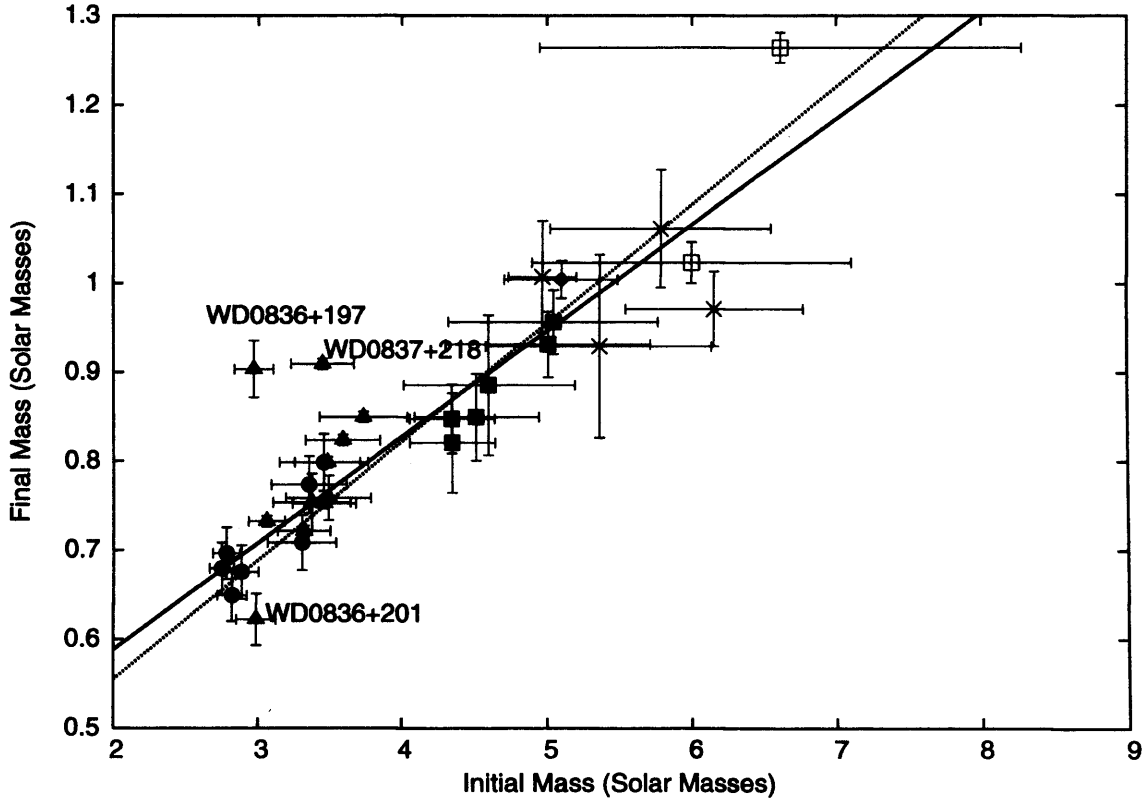
Figure 7.12: The initial mass final mass relation for cluster white dwarfs. The Praesepe white dwarfs are plotted with filled triangles, the Hyades white dwarfs with filled circles, Sirius B with a filled diamond, the Pleiades with open boxes, M35, filled squares and NGC2516 with stars. The solid line is the linear fit to the data from this work, and the dotted line is the relation of Dobbie et al. (2006a). GD50 is the highest mass white dwarf used for this IFMR.

the AGB phase, then the evolution of this white dwarf binary can be approximated to that of a single white dwarf. After performing a linear least squares fit to the 27 remaining white dwarfs, the gradient of the fit is found to be 0.119 ± 0.008 and the constant, 0.349 ± 0.034. This is consistent with the gradient of 0.133 ± 0.015 and constant of 0.289 ± 0.051 as calculated by Dobbie et al. (2006a). It is stated in Dobbie et al. (2006a) that if pure-C core white dwarf evolutionary models had been used instead of CO core models, then the cooling times would have been systematically larger by 5-30 Myr, resulting in a flatter IFMR. Both of these relations are steeper than the Weidemann (2000) relation. It should be noted that since the relationship was presented in Dobbie et al. (2006a), Dobbie et al. (2006b) have found GD50 to be a member of the Pleiades, and therefore it is included in this work and fit.

214

7.7 Summary

This chapter has described a study of the white dwarfs in the Praesepe open star cluster. High resolution spectra were obtained for 9 white dwarfs and the data reduction and subsequent analysis has been described here, including a discussion of the models and fitting routines used to measure radial velocity, T_{eff} and log g. A search for proper motion white dwarf members of the cluster has also been described. One possible double degenerate white dwarf has been discovered due to its varying radial velocity, and another white dwarf, WD0837+218 has been shown to be a probable non member due to its radial velocity differing from that of the cluster. The IFMR has been plotted using these objects and white dwarfs from other open star clusters, and a resultant linear fit very similar to that of Dobbie et al. (2006a) has been calculated. This IFMR indicates that WD0837+218 is an outlier, strengthening the case that it is a non member. One other object WD0836+197 is also a possible non member, but was not observed for this study. It is suggested that more observations are needed of this object before it can be determined to be a member or not. WD0836+201 was also not included in the IFMR due to its magnetic nature. The rejection of WD0837+218, WD0836+197 and WD0836+201 considerably improves the overall IFMR.

Chapter 8

Conclusions and Future Work

This chapter will review the work presented in this thesis. Chapter 2 described brown dwarfs, their theory and formation and discussed methods of finding brown dwarfs and their success in finding brown dwarfs in the field, open clusters and binaries. Chapter 3 introduced the basic astronomy and tools used in this work. Photometry, astrometry, proper motion, data reduction in the infrared and optical wavelengths, and various sky surveys were discussed. The remaining four chapters discuss the work that has been done during the course of this PhD. Each chapter will be reviewed, as well as providing the main conclusions and suggesting possibilities for future work.

8.1 Chapter 4 - The Pleiades

This chapter described a study on the Pleiades which was undertaken using four WFCAM tiles observed in 2005 in the J band (Casewell et al., 2007). This J band data was cross correlated with the I and Z band images taken in 2000 from CFH12k at CFHT. Candidates were selected using the I, I-Z colour magnitude diagram, and the Z, Z-J colour magnitude diagrams. Proper motions were measured for all of the selected objects using the WFCAM J and CFH12k Z band images. Control regions were used to estimate probability of membership

216

for these objects. 23 objects were found to meet the selection criteria to be cluster members. Nine of these appear to be new cluster members, 3 L dwarfs and 6 T dwarfs. H and K band photometry from UKIDSS, WFCAM and additional service time photometry from UFTI and LIRIS, strengthen the case that these objects are members of the cluster. Five of the T dwarf candidates were selected from the Z and J band data only, and still require H and/or K band measurements.

8.1.1 Conclusions

The 6 new T dwarfs and one late L dwarf are currently the latest type objects found to date in an open star cluster. A mass function was derived for these data, however, very small number statistics make the lower mass end unreliable, although the value of α derived from the data is consistent with previous studies. The colour magnitude diagrams, particularly the K, J-K and H, J-H diagrams strengthen the case that these objects are members, as a clear L-T dwarf transition sequence is seen in these figures. The H-K colour appears to be redder for the T dwarfs discovered in the Pleiades, compared to the H-K colour recorded for field dwarfs (Leggett et al., 2002). Zapatero Osorio et al. (2002) also have discovered what they believe to be a T dwarf in σ Ori. However, it is known that at these very young ages the brown dwarf models are uncertain (Baraffe et al., 2002), and mass estimates are therefore unreliable. This dwarf, σ Ori70 also has a redder colour than field dwarfs, and it may be that brown dwarfs, in particular T dwarfs, exhibit this difference, although more work is needed before this hypothesis can be proved. This work has discovered the first T dwarfs in the Pleiades, and in fact in any mature open star cluster.

8.1.2 Future Work

It is likely that with the advent of surveys such as VISTA and UKIDSS, and the ability to cross correlate them with surveys such as 2MASS, DENIS and the SDSS that more T dwarfs will be found in open star clusters. Bannister & Jameson (2007) have already associated field

dwarfs with moving groups associated with Ursa Major and the Hyades, and it is likely that many more low mass dwarfs in clusters will be found, aiding the research into the initial mass function.

Spitzer space telescope time has been obtained to observe the six T dwarf candidates in the 3.6 and 4.5 micron wavebands. Due to the nature of *Spitzer*, observations at 5.8 and 8.0 microns will also be taken, but at low signal to noise. These observations will allow more precise spectral types to be derived for these objects as well as allowing a comparison between field and cluster brown dwarfs in the mid infrared. The longer wavelengths will also allow a study of the brown dwarfs to be made, and any excesses due to a protoplanetary or accretion disk should be seen. As these objects are so faint, obtaining spectra for them is yet unrealistic. However, to confirm that they are T dwarfs, I have successfully applied for observing time using Gemini North and the Near InfraRed Imager (NIRI) to methane image the 6 T dwarf candidates. Using methane long and short filters, methane rich objects (T dwarfs) will blink on and off between the two filters. The relationships of Tinney et al. (2005) will be used to determine spectral types for these objects based on their methane index. These objects have been observed, but the data have not yet been analysed.

Observations using WFCAM and array 3 have also been successfully applied for, to obtain the missing H and K photometry for the newly discovered brown dwarfs in the Pleiades. These observations will take place after October 2007. This photometry will again allow more precise spectral types to be calculated, and also will allow a comparison between the H-K colour for these dwarfs and field objects.

8.2   Chapter 5 - Melotte 111

This chapter presented work on the Melotte 111 open star cluster, describing a 50 square degree survey performed using proper motion measurements from the USNOB1.0 catalogue, and J, H, K_S photometry from 2MASS. The candidate members were selected using proper

motion measurements, and the K_S, J-K_S colour magnitude diagram. Control regions were used to estimate probabilities of membership for the new candidate members, all of which were stellar, and had magnitudes of less than 12 in the K_S band, after which there was too much contamination, highlighting the need for more photometry. Another survey was also described, using i and Z band images taken using the WFC on the INT. Fifteen square degrees were imaged in total, and candidate members selected from the i, i-Z colour magnitude diagram. These objects were then followed up using UFTI on UKIRT, and photometry obtained in the K, and then the J band if they still appeared to be members on the i, i-K colour magnitude diagram. Thirteen of these objects appeared to be members of the cluster, and follow up K band images were used to measure proper motions for them, although the epoch difference was not adequate to accurately measure the motion, faster moving objects were eliminated as members, and spectra for three objects was obtained in the infrared using LIRIS on the WHT.

8.2.1   Conclusions

The USNOB1.0-2MASS survey recovered all 45 previously known members in the survey area, and identified 60 new candidate members of the cluster, more than doubling the known members to this large, but sparsely populated cluster. The deeper i, Z survey, yielded 13 possible M and L dwarfs belonging to the cluster after the J and K photometry had been examined, and 3 of these objects appeared to have the correct motion to be cluster members. These objects were also compared to the Ursa Major moving group isochrone from Bannister & Jameson (2007) and appeared to be cluster members. The spectra of these objects were of low S/N, although the highest S/N spectrum indicated that one of the objects is not a member. After the objects were reobserved, one appears to be a mid to late M dwarf, making it a possible member, although a saturated standard star has made the examination of this spectrum difficult. The remaining object's spectrum was still of too low a S/N for any features to be determined. It is possible that there are brown dwarfs in Melotte 111, but more detailed work is needed to prove this. It should be noted that Melotte 111 is a sparse, low mass cluster so it is likely that it has lost its low mass members over time, making future work not very profitable.

8.2.2 Future Work

The UKIDSS GCS has covered the majority of Melotte 111 in the K band. Future work in searching for new members to the cluster, stellar and substellar, will concentrate on using UKIDSS either with the SDSS or 2MASS to calculate more accurate proper motions for the objects presented in Casewell et al. (2006) and Casewell et al. (2005). The SDSS may not have a large enough epoch difference to measure the proper motions using UKIDSS, but could be used with 2MASS, or the Z band survey presented in Chapter 5 to calculate proper motions, and to verify the new cluster members. The SDSS also provides more accurate photometry in more wavebands with which to study the cluster, which should be done. More spectroscopy should be taken of the possible brown dwarf members of Melotte 111, although from the spectra presented it is clear that a 4m telescope is not an adequate tool for this task. Optical spectra of these objects would reveal whether they contain lithium, although at this age, the lithium test may be inconclusive. Radial velocity measurements may provide a more accurate way of determining cluster membership, than the very small proper motion that must be measured.

8.3 Chapter 6 - Moving Groups

Chapter 6 presented work on field brown dwarfs. Observations of 143 of these field objects, situated between declinations of 60 and -30° were taken in the J band using array 3 of WFCAM on UKIRT. These observations were second epoch images which were used with 2MASS images to calculate proper motions for these brown dwarfs. Possible binary objects were also discussed, as well as brown dwarfs that appeared to have the same proper motion as other field objects in their vicinity. Eight fast moving dwarfs (>0.85" yr^{-1}) were also found during this work, and using a relation between M_J and spectral type, distances for these objects were calculated and approximate velocities and luminosities. The moving group method was used to determine the direction of the proper motions of the brown dwarfs, and to see if they were moving in the direction of the convergent point of any well known moving groups.

8.3.1 Conclusions

Of the 143 brown dwarfs observed, 5 may have common proper motion companions with other objects in the field. The nine fast moving brown dwarfs were noted to have blue colours, making it likely that they are members of a thick disc population of stars. Calculated luminosities make them in fact stellar, and not brown dwarfs, and making them some of the least luminous stars known. These interesting objects should be a subject for future work, and their motion should be studied in more detail. The moving group method was used to select members of moving groups, namely the Hyades, Ursa Major and Pleiades moving groups. The other moving groups tested yielded no new members. Three (and an additional two with known proper motions) were found to be members of the Pleiades moving group, five were found to belong to the Ursa Major moving group, and 15 are found to be members or candidate members of the Hyades moving group. It is likely that these objects were once low mass members of the Hyades and Pleiades, and over time were ejected from the cluster. These objects may help to explain why in the case of older clusters such as the Hyades, no brown dwarfs are found within the cluster.

8.3.2 Future Work

I am currently part of two programmes to image more of the known field brown dwarfs. In the southern hemisphere, (more particularly dec $\leq 30°$) SOFI on the NTT is being used to image the 40 southern brown dwarfs that currently have no proper motion measurements and will continue to do so until October 2007. SOFI is a wide field imager, and provides a large field of view, making proper motion measurements easy due to the large amount of reference stars in the image.

In the rest of the sky (between 60 and -30°), WFCAM is continuing to image the remaining brown dwarfs.

Once both of these programmes have been completed, not only will there be a much larger

sample of brown dwarfs with proper motions, but they can be compared to moving groups, which may strengthen the case that they are ejected from clusters. Parallax measurements should be made of the fast moving brown dwarfs, to determine their position in the galaxy, and possibly radial velocity measurements taken for them to determine their precise motion. Parallax measurements would also be valuable for the potential moving group members as accurate distances strengthen the case for group membership.

Service time using ISIS on the WHT has been applied for to obtain optical spectra of two of the objects making up these proper motion companions to the brown dwarfs. Both appear superficially to be white dwarfs, however, they may be fast moving, metal poor background K dwarfs, and spectra will determine this.

8.4   Chapter 7 - Praesepe White Dwarfs

This chapter presents the results of a study of nine of the eleven Praesepe white dwarfs. A review of the formation of white dwarfs and of the Praesepe cluster was presented at the start of the chapter. High resolution optical spectra were obtained of these white dwarfs, and the hydrogen absorption lines were used to measure their T_{eff}, log g and radial velocity. These measurements were then used to confirm cluster membership for the dwarfs along with SDSS magnitudes and proper motions from the SuperCOSMOS survey. State of the art models were used to calculate their mass, radius, cooling time and progenitor mass. These white dwarfs were then used to further constrain the initial mass-final mass relation, which can only be constrained empirically, due to difficulties in modelling the mass loss of a star as it progresses through the asymptotic giant branch phase of its evolution.

8.4.1 Conclusions

Using proper motions and the radial velocities, one previously believed cluster member has been shown to be a non member, and one of the previously known members has been shown to be a double degenerate binary. Using the models of Holberg & Bergeron (2006), the masses and radii of these white dwarfs were calculated. Using the Fontaine et al. (2001) models their cooling times, progenitor lifetimes and progenitor masses were also calculated. The initial mass-final mass relation as derived from this work is very similar to that presented in Dobbie et al. (2006a), thus strengthening the case for a single valued, linear relation. There is still some scatter in the white dwarfs used for this relation, and future work should concentrate on minimising the errors in masses etc for these white dwarfs, to tighten the relationship. Consequently, as the relationship is so similar to the Dobbie relation, the questions that are described in Dobbie et al. (2006a) still remain. It is still not understood as to why the initial mass-final mass relation yields an initial mass of ≈ 6.2 $M_{\odot}$ for a white dwarf of final mass 1.1 $M_{\odot}$, whereas recent models (Garcia-Berro et al., 1997) indicate that more massive, stable NeO degenerate core can form via single star evolution. Weidemann (2000) suggested the upper limit for a white dwarf mass is ≈ 1.3 $M_{\odot}$, but the initial mass-final mass relation yields a progenitor mass of ≈ 7.9 $M_{\odot}$ for this white dwarf, not the 10-11 $M_{\odot}$ that is suggested by the models. It may be possible that the initial mass-final mass relation cannot be represented by a linear extrapolation of the linear function. There is no observational evidence, due to no massive white dwarfs being found in clusters to date, although Dobbie et al. (2006b) have associated GD50 with the Pleiades.

8.4.2 Future Work

As was discussed in Chapter 7, white dwarfs in open star clusters are the best objects to use to constrain the initial mass-final mass relation. However, the distances to these clusters, and the fact that white dwarfs are intrinsically faint, means that there are often large errors on the initial mass calculations, particularly if the age of the cluster is not well known. Thus to constrain the

initial mass-final mass relation, the white dwarfs involved, must be definite cluster members, and high resolution spectra must be taken of them, to obtain the best results. There are two Praesepe white dwarfs that were not included in the study, and so high resolution spectra are still needed for them, particularly as one is an outlier to the initial mass-final mass relation calculated, and there are some questions as to its membership status, due to its proximity to a bright star, making proper motion measurements, and possibly photometry, unreliable.

A similar programme using UVES and the VLT is underway to obtain high resolution spectra of the white dwarfs in the Hyades, so that radial velocities and T_{eff} and log g can be accurately measured for them, thus reducing their errors on the initial mass-final mass relation.

Follow up time on the VLT, again using UVES has been successfully applied for, to obtain more observations of the suspected double degenerate white dwarf, WD0837+185. Using the same set up for UVES as was used for this study, observations have been proposed using three exposures in each of the first and second nights of observations, which reduces to two observations in the third night. Subsequent observations of one exposure in a few following nights has also been proposed. These observations should allow the period of the double degenerate to be calculated, which will then enable the mass and separation of both constituents to be calculated. A similar observing strategy was used by Napiwotzki et al. (2001b) to observe a double degenerate discovered as part of the SpY programme. These observations will commence in October 2007. This new information about WD0837+185 will allow astronomers to determine whether it is a supernova progenitor, and to determine how its binary evolution has affected its place on the initial mass-final mass diagram.

In an attempt to constrain the high mass end of the initial mass-final mass relation, there is a programme underway at the VLT, again using UVES to measure radial velocities for massive white dwarfs. The results of this programme may be used to associate these white dwarfs with moving groups or clusters that could allow an accurate progenitor lifetime to be calculated for them, thus allowing them to be used to constrain the upper part of the initial mass-final mass relation.

8.5 Summary

This thesis has presented work on degenerate objects (both brown and white dwarfs) in open star clusters (Melotte 111, Pleiades and Praesepe) and has also investigated field brown dwarfs and the likelihood of their belonging to moving groups (Ursa Major, Hyades, Pleiades). Overall, the idea that the age of the dwarf (brown, or white), has been a common theme to this thesis. If the age of the dwarf is known, much more information can be calculated about them, and if the dwarf can be connected to a moving group or cluster a metallicity can be assumed. The fundamental physics involved in astronomy is extremely sensitive to age, irrelevant of whether star formation or supernovae are being studied. In finding brown dwarfs that belong to mature clusters such as Melotte 111 or the Hyades, the dynamical evolution of the cluster is effectively being studied along with the initial mass function of that cluster. In younger clusters such as the Pleiades, few brown dwarfs are expected to have escaped, and so the initial mass function is being studied, along with the differences between cluster and field brown dwarfs, that may be due to evolution or position in the galaxy. Finding brown dwarfs that belong to moving groups allows the study of the dynamical evolution of the cluster. Proper motions have also discovered some of the least luminous stars known. Finally, white dwarfs in clusters yield information about the relationship between a star's mass and the mass of the white dwarf it will become. This information, not only aids models into mass loss from the star as it nears the end of its life, but also informs about the maximum mass of a white dwarf, and in the case of the double degenerate system, supernovae rates. The main conclusion of this work is that age is crucial to all studies concerning brown and white dwarfs.

Bibliography

Adams F. C., Fatuzzo M., 1996, *ApJ*, 464, 256

Adams J. D., Stauffer J. R., Skrutskie M. F., Monet D. G., Portegies Zwart S. F., Janes K. A., Beichman C. A., 2002, *AJ*, 124, 1570

Allard F., Hauschildt P. H., Alexander D. R., Starrfield S., 1997, *ARA&A*, 35, 137

Allard N. F., Hébrard G., Dupuis J., Chayer P., Kruk J. W., Kielkopf J., Hubeny I., 2004, *ApJL*, 601, L183

Allen P. R., Koerner D. W., McElwain M. W., Cruz K. L., Reid I. N., 2007, *AJ*, 133, 971

An D., Terndrup D. M., Pinsonneault M. H., Paulson D. B., Hanson R. B., Stauffer J. R., 2007, *ApJ*, 655, 233

Anthony-Twarog B. J., 1982, *ApJ*, 255, 245

Anthony-Twarog B. J., 1984, *AJ*, 89, 267

Ardila D., Martín E., Basri G., 2000, *AJ*, 120, 479

Argue A. N., Kenworthy C. M., 1969, *MNRAS*, 146, 479

Artyukhina N. M., 1955, Trudy Gosudarstvennogo Astron. Inst., 26, 3

Ballester P., Hensberge H., 1995, in Benvenuti P., ed., Calibrating and Understanding HST and ESO Instruments Data reduction for the UVES echelle spectrograph. p. 139

Bannister N. P., Jameson R. F., 2007, *MNRAS*, 378, L24

Baraffe I., Chabrier G., Allard F., Hauschildt P. H., 1998, *A&A*, 337, 403

Baraffe I., Chabrier G., Allard F., Hauschildt P. H., 2002, *A&A*, 382, 563

Baraffe I., Chabrier G., Barman T. S., Allard F., Hauschildt P. H., 2003, *A&A*, 402, 701

Barrado y Navascués D., Stauffer J. R., Briceño C., Patten B., Hambly N. C., Adams J. D., 2001, *ApJS*, 134, 103

Barry D. C., Cromwell R. H., Hege K., Schoolman S. A., 1981, *ApJ*, 247, 210

Barsony M., Kenyon S. J., Lada E. A., Teuben P. J., 1997, *ApJS*, 112, 109

Basri G., Marcy G. W., Graham J. R., 1996, *ApJ*, 458, 600

Basri G., Martín E. L., 1999, *ApJ*, 510, 266

Bate M. R., Bonnell I. A., Bromm V., 2003, *MNRAS*, 339, 577

Becklin E. E., Zuckerman B., 1988, *Nature*, 336, 656

Béjar V. J. S., Martín E. L., Zapatero Osorio M. R., Rebolo R., Barrado y Navascués D., Bailer-Jones C. A. L., Mundt R., Baraffe I., Chabrier C., Allard F., 2001, *ApJ*, 556, 830

Béjar V. J. S., Zapatero Osorio M. R., Rebolo R., 1999, *ApJ*, 521, 671

Bergeron P., Liebert J., Fulbright M. S., 1995, *ApJ*, 444, 810

Bergeron P., Saumon D., Wesemael F., 1995, *ApJ*, 443, 764

Bergeron P., Wesemael F., Fontaine G., 1992, *ApJ*, 387, 288

Bihain G., Rebolo R., Béjar V. J. S., Caballero J. A., Bailer-Jones C. A. L., Mundt R., Acosta-Pulido J. A., Manchado Torres A., 2006, *A&A*, 458, 805

Billères M., Delfosse X., Beuzit J.-L., Forveille T., Marchal L., Martín E. L., 2005, *A&A*, 440, L55

Blaauw A., 1964, in Kerr F. J., ed., The Galaxy and the Magellanic Clouds Vol. 20 of IAU Symposium, The Scorpio-Centaurus association. p. 50

227

Boesgaard A. M., 1989, *ApJ*, 336, 798

Bonnell I. A., Bate M. R., Clarke C. J., Pringle J. E., 1997, *MNRAS*, 285, 201

Bonnell I. A., Clarke C. J., Bate M. R., Pringle J. E., 2001, *MNRAS*, 324, 573

Bontemps S., et al., 2001, *A&A*, 372, 173

Boss A. P., 2001, *ApJL*, 551, L167

Boss A. P., Fisher R. T., Klein R. I., McKee C. F., 2000, *ApJ*, 528, 325

Bounatiro L., 1993, *A&AS*, 100, 531

Bounatiro L., Arimoto N., 1992, *A&A*, 260, 112

Bouvier J., Stauffer J. R., Martin E. L., Barrado y Navascues D., Wallace B., Bejar V. J. S., 1998, *A&A*, 336, 490

Bouy H., Brandner W., Martín E. L., Delfosse X., Allard F., Basri G., 2003, *AJ*, 126, 1526

Briceño C., Calvet N., Hernández J., Vivas A. K., Hartmann L., Downes J. J., Berlind P., 2005, *AJ*, 129, 907

Briceño C., Hartmann L., Stauffer J., Martín E., 1998, *AJ*, 115, 2074

Briceño C., Luhman K. L., Hartmann L., Stauffer J. R., Kirkpatrick J. D., 2002, *ApJ*, 580, 317

Brown A. G. A., de Geus E. J., de Zeeuw P. T., 1994, *A&A*, 289, 101

Brown A. G. A., Walter F. M., Blaauw A., 1998, ArXiv Astrophysics e-prints, astro-ph/9802054

Burgasser A. J., 2007b, ArXiv Astrophysics e-prints, astro-ph/0701793

Burgasser A. J., Burrows A., Kirkpatrick J. D., 2006c, *ApJ*, 639, 1095

Burgasser A. J., Cruz K. L., Kirkpatrick J. D., 2007c, *ApJ*, 657, 494

Burgasser A. J., Geballe T. R., Leggett S. K., Kirkpatrick J. D., Golimowski D. A., 2006a, *ApJ*, 637, 1067

Burgasser A. J., Kirkpatrick J. D., Burrows A., Liebert J., Reid I. N., Gizis J. E., McGovern M. R., Prato L., McLean I. S., 2003, *ApJ*, 592, 1186

Burgasser A. J., Kirkpatrick J. D., Cruz K. L., Reid I. N., Leggett S. K., Liebert J., Burrows A., Brown M. E., 2006b, *ApJS*, 166, 585

Burgasser A. J., Kirkpatrick J. D., McGovern M. R., McLean I. S., Prato L., Reid I. N., 2004, *ApJ*, 604, 827

Burgasser A. J., Reid I. N., Siegler N., Close L., Allen P., Lowrance P., Gizis J., 2007a, in Reipurth B., Jewitt D., Keil K., eds, Protostars and Planets V Not Alone: Tracing the Origins of Very-Low-Mass Stars and Brown Dwarfs Through Multiplicity Studies. pp 427–441

Burleigh M. R., et al., 2006, *MNRAS*, 373, 1416

Burleigh M. R., Hogan E., Dobbie P. D., Napiwotzki R., Maxted P. F. L., 2006, *MNRAS*, 373, L55

Burrows A., Hubbard W. B., Lunine J. I., Liebert J., 2001, Reviews of Modern Physics, 73, 719

Burrows A., Liebert J., 1993, Reviews of Modern Physics, 65, 301

Burrows A., Sudarsky D., Hubeny I., 2006, *ApJ*, 640, 1063

Calabretta M., Greisen E. W., 2000, in Manset N., Veillet C., Crabtree D., eds, ASP Conf. Ser. 216: Astronomical Data Analysis Software and Systems IX Representations of World Coordinates in FITS. p. 571

Carpenter J. M., 2001, *AJ*, 121, 2851

Carroll B. W., Ostlie D. A., 1996, An Introduction to Modern Astrophysics. An Introduction to Modern Astrophysics, by B.W. Carroll and D.A. Ostlie. Benjamin Cummings, 1996. ISBN 0-201-54730-9.

Casali M., et al., 2007, *A&A* , 467, 777

Casali M. M., Hawarden T. G., 1992, UKIRT Newsletter, 4, 33

Casanova S., Montmerle T., Feigelson E. D., Andre P., 1995, *ApJ* , 439, 752

Casewell S. L., Dobbie P. D., Hodgkin S. T., Moraux E., Jameson R. F., Hambly N. C., Irwin J., Lodieu N., 2007, *MNRAS* , 378, 1131

Casewell S. L., Jameson R. F., Dobbie P. D., 2005, Astronomische Nachrichten, 326, 991

Casewell S. L., Jameson R. F., Dobbie P. D., 2006, *MNRAS* , 365, 447

Castellani V., Degl'Innocenti S., Prada Moroni P. G., Tordiglione V., 2002, *MNRAS* , 334, 193

Cayrel de Strobel G., 1990, Memorie della Societa Astronomica Italiana, 61, 613

Chabrier G., 2005, in Corbelli E., Palla F., Zinnecker H., eds, ASSL Vol. 327: The Initial Mass Function 50 Years Later The Initial Mass Function: from Salpeter 1955 to 2005. p. 41

Chabrier G., Baraffe I., 1997, *A&A* , 327, 1039

Chabrier G., Baraffe I., Allard F., Hauschildt P., 2000, *ApJ* , 542, 464

Chereul E., Creze M., Bienayme O., 1998, *A&A* , 340, 384

Chini R., 1981, *A&A* , 99, 346

Chiu K., Fan X., Leggett S. K., Golimowski D. A., Zheng W., Geballe T. R., Schneider D. P., Brinkmann J., 2006, *AJ* , 131, 2722

Claver C. F., Liebert J., Bergeron P., Koester D., 2001, *ApJ* , 563, 987

Close L. M., Lenzen R., Guirado J. C., Nielsen E. L., Mamajek E. E., Brandner W., Hartung M., Lidman C., Biller B., 2005, *Nature* , 433, 286

Comeron F., Rieke G. H., Burrows A., Rieke M. J., 1993, *ApJ* , 416, 185

Cossburn M. R., Hodgkin S. T., Jameson R. F., Pinfield D. J., 1997, *MNRAS* , 288, L23

230

Crawford D. L., Perry C. L., 1976, *AJ* , 81, 419

Cruz K. L., , 2007a, Private communication

Cruz K. L., Reid I. N., Kirkpatrick J. D., Burgasser A. J., Liebert J., Solomon A. R., Schmidt
S. J., Allen P. R., Hawley S. L., Covey K. R., 2007b, *AJ* , 133, 439

Cruz K. L., Reid I. N., Liebert J., Kirkpatrick J. D., Lowrance P. J., 2003, *AJ* , 126, 2421

de Bruijne J. H. J., Hoogerwerf R., Brown A. G. A., Aguilar L. A., de Zeeuw P. T., 1997, in
ESA SP-402: Hipparcos - Venice '97 Improved Methods for Identifying Moving Groups.
pp 575–578

de Geus E. J., 1992, *A&A* , 262, 258

de La Fuente Marcos R., de La Fuente Marcos C., 2000, *Astrophys. Space. Sci.* , 271, 127

de Zeeuw P. T., Hoogerwerf R., de Bruijne J. H. J., Brown A. G. A., Blaauw A., 1999, *AJ* ,
117, 354

Dehnen W., 1998, *AJ* , 115, 2384

Dekker H., D'Odorico S., Kaufer A., Delabre B., Kotzlowski H., 2000, in Iye M., Moorwood
A. F., eds, Proc. SPIE Vol. 4008, p. 534-545, Optical and IR Telescope Instrumentation and
Detectors, Masanori Iye; Alan F. Moorwood; Eds. Design, construction, and performance
of UVES, the echelle spectrograph for the UT2 Kueyen Telescope at the ESO Paranal Ob-
servatory. pp 534–545

Delfosse X., Tinney C. G., Forveille T., Epchtein N., Borsenberger J., Fouqué P., Kimeswenger
S., Tiphène D., 1999, *A&AS* , 135, 41

Deluca E. E., Weis E. W., 1981, *PASP* , 93, 32

Dobbie P. D., Burleigh M. R., Levan A. J., Barstow M. A., Napiwotzki R., Holberg J. B.,
Hubeny I., Howell S. B., 2005, *MNRAS* , 357, 1049

Dobbie P. D., Kenyon F., Jameson R. F., Hodgkin S. T., 2002c, *MNRAS* , 331, 445

Dobbie P. D., Kenyon F., Jameson R. F., Hodgkin S. T., Hambly N. C., Hawkins M. R. S., 2002b, *MNRAS*, 329, 543

Dobbie P. D., Kenyon F., Jameson R. F., Hodgkin S. T., Pinfield D. J., Osborne S. L., 2002a, *MNRAS*, 335, 687

Dobbie P. D., Napiwotzki R., Burleigh M. R., Barstow M. A., Boyce D. D., Casewell S. L., Jameson R. F., Hubeny I., Fontaine G., 2006a, *MNRAS*, 369, 383

Dobbie P. D., Napiwotzki R., Lodieu N., Burleigh M. R., Barstow M. A., Jameson R. F., 2006b, *MNRAS*, 373, L45

Dobbie P. D., Pinfield D. J., Napiwotzki R., Hambly N. C., Burleigh M. R., Barstow M. A., Jameson R. F., Hubeny I., 2004, *MNRAS*, 355, L39

Dominguez I., Chieffi A., Limongi M., Straniero O., 1999, *ApJ*, 524, 226

Dravins D., Lindegren L., Madsen S., 1999, *A&A*, 348, 1040

Dulick M., Bauschlicher Jr. C. W., Burrows A., Sharp C. M., Ram R. S., Bernath P., 2003, *ApJ*, 594, 651

Dye S., et al., 2006, *MNRAS*, 372, 1227

Eggen O. J., 1960, *MNRAS*, 120, 540

Eggen O. J., Greenstein J. L., 1965, *ApJ*, 141, 83

Evans D. S., 1967, in Batten A. H., Heard J. F., eds, IAU Symp. 30: Determination of Radial Velocities and their Applications The Revision of the General Catalogue of Radial Velocities. p. 57

Fan X., et al., 2000, *AJ*, 119, 928

Farihi J., Becklin E. E., Zuckerman B., 2005, *ApJS*, 161, 394

Farihi J., Christopher M., 2004, *AJ*, 128, 1868

Festin L., 1997, *A&A*, 322, 455

Festin L., 1998, *A&A* , 333, 497

Fontaine G., Brassard P., Bergeron P., 2001, *PASP* , 113, 409

Ford A., Jeffries R. D., James D. J., Barnes J. R., 2001, *A&A* , 369, 871

Franciosini E., Pallavicini R., Sanz-Forcada J., 2006, *A&A* , 446, 501

Friel E. D., Boesgaard A. M., 1992, *ApJ* , 387, 170

Fukugita M., Ichikawa T., Gunn J. E., Doi M., Shimasaku K., Schneider D. P., 1996, *AJ* , 111, 1748

Garcia-Berro E., Ritossa C., Iben I. J., 1997, *ApJ* , 485, 765

García López R. J., Randich S., Zapatero Osorio M. R., Pallavicini R., 2000, *A&A* , 363, 958

Gatewood G., Castelaz M., de Jonge J. K., Persinger T., Stein J., Stephenson B., 1992, *ApJ* , 392, 710

Gatewood G., de Jonge J. K., 1994, *ApJ* , 428, 166

Gatti T., Testi L., Natta A., Randich S., Muzerolle J., 2006, *A&A* , 460, 547

Girardi L., Bertelli G., Bressan A., Chiosi C., Groenewegen M. A. T., Marigo P., Salasnich B., Weiss A., 2002, *A&A* , 391, 195

Girardi L., Bressan A., Bertelli G., Chiosi C., 2000, *A&AS* , 141, 371

Gizis J. E., 2002, *ApJ* , 575, 484

Gizis J. E., Kirkpatrick J. D., Burgasser A., Reid I. N., Monet D. G., Liebert J., Wilson J. C., 2001, *ApJL* , 551, L163

Gizis J. E., Monet D. G., Reid I. N., Kirkpatrick J. D., Liebert J., Williams R. J., 2000, *AJ* , 120, 1085

Gizis J. E., Reid I. N., Knapp G. R., Liebert J., Kirkpatrick J. D., Koerner D. W., Burgasser A. J., 2003, *AJ* , 125, 3302

Gizis J. E., Reid I. N., Monet D. G., 1999, *AJ*, 118, 997

Goodwin S. P., Ward-Thompson D., Whitworth A. P., 2002, *MNRAS*, 330, 769

Goodwin S. P., Whitworth A. P., Ward-Thompson D., 2004a, *A&A*, 414, 633

Goodwin S. P., Whitworth A. P., Ward-Thompson D., 2004b, *A&A*, 423, 169

Gould A., 2003, *AJ*, 126, 472

Greene T. P., Young E. T., 1992, *ApJ*, 395, 516

Grosbol P., 1989, in Klare G., ed., Reviews in Modern Astronomy MIDAS.. pp 242–247

Guinan E. F., Ribas I., 2001, *ApJL*, 546, L43

Hambly N. C., Davenhall A. C., Irwin M. J., MacGillivray H. T., 2001c, *MNRAS*, 326, 1315

Hambly N. C., Hawkins M. R. S., Jameson R. F., 1993, *A&AS*, 100, 607

Hambly N. C., Hodgkin S. T., Cossburn M. R., Jameson R. F., 1999, *MNRAS*, 303, 835

Hambly N. C., Irwin M. J., MacGillivray H. T., 2001b, *MNRAS*, 326, 1295

Hambly N. C., Jameson R. F., Hawkins M. R. S., 1991, *MNRAS*, 253, 1

Hambly N. C., MacGillivray H. T., Read M. A., Tritton S. B., Thomson E. B., Kelly B. D.,
    Morgan D. H., Smith R. E., Driver S. P., Williamson J., Parker Q. A., Hawkins M. R. S.,
    Williams P. M., Lawrence A., 2001a, *MNRAS*, 326, 1279

Hawley S. L., et al., 2002, *AJ*, 123, 3409

Hayashi C., Nakano T., 1963, Progress of Theoretical Physics, 30, 460

Hennebelle P., Whitworth A. P., Cha S.-H., Goodwin S. P., 2004, *MNRAS*, 348, 687

Hernández J., Hartmann L., Megeath T., Gutermuth R., Muzerolle J., Calvet N., Vivas A. K.,
    Briceño C., Allen L., Stauffer J., Young E., Fazio G., 2007, *ApJ*, 662, 1067

234

Herwig F., 1995, in Noels A., Fraipont-Caro D., Gabriel M., Grevesse N., Demarque P., eds, Liege International Astrophysical Colloquia Vol. 32 of Liege International Astrophysical Colloquia, The Impact of Improved Theoretical and Observational Data on the Initial-Final Mass Relation. p. 441

Hester J. J., et al., 1996, *AJ*, 111, 2349

Hillenbrand L. A., 1997, *AJ*, 113, 1733

Hillenbrand L. A., Carpenter J. M., 2000, *ApJ*, 540, 236

Hillenbrand L. A., White R. J., 2004, *ApJ*, 604, 741

Hodgkin S. T., et al.,, 2007, In preparation

Holberg J. B., Bergeron P., 2006, *AJ*, 132, 1221

Hubeny I., 1988, Computer Physics Communications, 52, 103

Hubeny I., Hummer D. G., Lanz T., 1994, *A&A*, 282, 151

Hubeny I., Lanz T., 1995, *ApJ*, 439, 875

Hubeny I., Lanz T., , 2001, http://nova.astro.umd.edu/

Hummer D. G., Mihalas D., 1988, *ApJ*, 331, 794

Iben Jr. I., Tutukov A. V., 1984, *ApJS*, 54, 335

Irwin M., Lewis J., 2001, New Astronomy Review, 45, 105

Irwin M. J., 1985, *MNRAS*, 214, 575

Irwin M. J., et al.,, 2007, In preparation

Jameson R. F., Dobbie P. D., Hodgkin S. T., Pinfield D. J., 2002, *MNRAS*, 335, 853

Jameson R. F., Skillen I., 1989, *MNRAS*, 239, 247

235

Janson M., Brandner W., Lenzen R., Close L., Nielsen E., Hartung M., Henning T., Bouy H., 2007, *A&A*, 462, 615

Jeffries R. D., 2000, in Pallavicini R., Micela G., Sciortino S., eds, Stellar Clusters and Associations: Convection, Rotation, and Dynamos Vol. 198 of Astronomical Society of the Pacific Conference Series, Lithium depletion in open clusters. p. 245

Johnson H. L., Morgan W. W., 1953, *ApJ*, 117, 313

Jones B. F., 1981, *AJ*, 86, 290

Jones H. R. A., Longmore A. J., Jameson R. F., Mountain C. M., 1994, *MNRAS*, 267, 413

Kendall T. R., Delfosse X., Martín E. L., Forveille T., 2004, *A&A*, 416, L17

Kendall T. R. o., 2007, *A&A*, 466, 1059

Kerr F. J., Lynden-Bell D., 1986, *MNRAS*, 221, 1023

Kharchenko N. V., Piskunov A. E., Röser S., Schilbach E., Scholz R.-D., 2005, *A&A*, 438, 1163

King J. R., Schuler S. C., 2005, *PASP*, 117, 911

King J. R., Villarreal A. R., Soderblom D. R., Gulliver A. F., Adelman S. J., 2003, *AJ*, 125, 1980

Kirkpatrick J. D., Dahn C. C., Monet D. G., Reid I. N., Gizis J. E., Liebert J., Burgasser A. J., 2001, *AJ*, 121, 3235

Kirkpatrick J. D., et al.,, 2007, In preparation

Kirkpatrick J. D., Reid I. N., Liebert J., Cutri R. M., Nelson B., Beichman C. A., Dahn C. C., Monet D. G., Gizis J. E., Skrutskie M. F., 1999, *ApJ*, 519, 802

Kirkpatrick J. D., Reid I. N., Liebert J., Gizis J. E., Burgasser A. J., Monet D. G., Dahn C. C., Nelson B., Williams R. J., 2000, *AJ*, 120, 447

Kitchin C. R., 1997, Astrophysical Techniques. Adam Hilger

Knapp G. R., et al., 2004, *AJ*, 127, 3553

Koester D., Napiwotzki R., Christlieb N., Drechsel H., Hagen H.-J., Heber U., Homeier D., Karl C., Leibundgut B., Moehler S., Nelemans G., Pauli E.-M., Reimers D., Renzini A., Yungelson L., 2001, *A&A*, 378, 556

Koornneef J., 1983, *A&A*, 128, 84

Kroupa P., 1995, *MNRAS*, 277, 1522

Kumar S. S., 1963, *ApJ*, 137, 1121

Lada C. J., Muench A. A., Lada E. A., Alves J. F., 2004, *AJ*, 128, 1254

Landolt A. U., 1992, *AJ*, 104, 340

Lawrence A., et al., 2007, *MNRAS*, p. 615

Leggett S. K., et al., 2000, *ApJL*, 536, L35

Leggett S. K., Golimowski D. A., Fan X., Geballe T. R., Knapp G. R., Brinkmann J., Csabai I., Gunn J. E., Hawley S. L., Henry T. J., Hindsley R., Ivezić Ž., Lupton R. H., Pier J. R., Schneider D. P., Smith J. A., Strauss M. A., Uomoto A., York D. G., 2002, *ApJ*, 564, 452

Lemke M., 1997, *A&AS*, 122, 285

Levine S. E., 2005, *AJ*, 130, 319

Liebert J., Bergeron P., Holberg J. B., 2005, *ApJS*, 156, 47

Lin C. C., Mestel L., Shu F. H., 1965, *ApJ*, 142, 1431

Livio M., 2000, in Niemeyer J. C., Truran J. W., eds, Type Ia Supernovae, Theory and Cosmology. Edited by J. C. Niemeyer and J. W. Truran. Published by Cambridge University Press, 2000., p.33 The Progenitors of Type Ia Supernovae. p. 33

Lodders K., Fegley Jr. B., 2006, Chemistry of Low Mass Substellar Objects. Astrophysics Update 2, p. 1

Lodieu N., Dobbie P. D., Deacon N. R., Hodgkin S. T., Hambly N. C., Jameson R. F., 2007, *MNRAS*, 380, 712

Lodieu N., Hambly N. C., Jameson R. F., 2006, *MNRAS*, 373, 95

Lodieu N., Hambly N. C., Jameson R. F., Hodgkin S. T., Carraro G., Kendall T. R., 2007, *MNRAS*, 374, 372

Low C., Lynden-Bell D., 1976, *MNRAS*, 176, 367

Lucas P. W., Roche P. F., 2000, *MNRAS*, 314, 858

Lucas P. W., Roche P. F., Tamura M., 2005, *MNRAS*, 361, 211

Lucas P. W., Weights D. J., Roche P. F., Riddick F. C., 2006, *MNRAS*, 373, L60

Luhman K. L., 2000a, *ApJ*, 544, 1044

Luhman K. L., 2004, *ApJ*, 617, 1216

Luhman K. L., Briceño C., Stauffer J. R., Hartmann L., Barrado y Navascués D., Caldwell N., 2003a, *ApJ*, 590, 348

Luhman K. L., Rieke G. H., 1998, *ApJ*, 497, 354

Luhman K. L., Rieke G. H., 1999, *ApJ*, 525, 440

Luhman K. L., Rieke G. H., Young E. T., Cotera A. S., Chen H., Rieke M. J., Schneider G., Thompson R. I., 2000b, *ApJ*, 540, 1016

Luhman K. L., Stauffer J. R., Mamajek E. E., 2005, *ApJL*, 628, L69

Luhman K. L., Stauffer J. R., Muench A. A., Rieke G. H., Lada E. A., Bouvier J., Lada C. J., 2003b, *ApJ*, 593, 1093

Luhman K. L., Wilson J. C., Brandner W., Skrutskie M. F., Nelson M. J., Smith J. D., Peterson D. E., Cushing M. C., Young E., 2006, *ApJ*, 649, 894

238

Luyten W. J., 1962, in The Observatory, Univ. Minnesota, Minneapolis,1953, 31, 1 (1962) A search for faint blue stars. XXXI. One thousand blue stars in the region of Praesepe.. p. 1

Lyngå G., , 1987, Catalogue of open cluster data.

Madsen S., Dravins D., Lindegren L., 2002, *A&A* , 381, 446

Marcy G. W., Butler R. P., 2000, *PASP* , 112, 137

Marigo P., 1998, *A&A* , 340, 463

Marsh M. C., Barstow M. A., Buckley D. A., Burleigh M. R., Holberg J. B., Koester D., O'Donoghue D., Penny A. J., Sansom A. E., 1997, *MNRAS* , 286, 369

Martín E. L., Basri G., Zapatero-Osorio M. R., Rebolo R., López R. J. G., 1998, *ApJL* , 507, L41

Martín E. L., Delfosse X., Basri G., Goldman B., Forveille T., Zapatero Osorio M. R., 1999, *AJ* , 118, 2466

Martín E. L., Delfosse X., Guieu S., 2004, *AJ* , 127, 449

Martín E. L., Dougados C., Magnier E., Ménard F., Magazzù A., Cuillandre J.-C., Delfosse X., 2001, *ApJL* , 561, L195

Martín E. L., Osorio M. R. Z., 2003, *ApJL* , 593, L113

Maxted P. F. L., Jeffries R. D., 2005, *MNRAS* , 362, L45

Maxted P. F. L., Napiwotzki R., Dobbie P. D., Burleigh M. R., 2006, *Nature* , 442, 543

Mazzei P., Pigatto L., 1989, *A&A* , 213, L1

McCaughrean M. J., Andersen M., 2002, *A&A* , 389, 513

McLean I. S., McGovern M. R., Burgasser A. J., Kirkpatrick J. D., Prato L., Kim S. S., 2003, *ApJ* , 596, 561

McLean I. S., Prato L., Kim S. S., Wilcox M. K., Kirkpatrick J. D., Burgasser A., 2001, *ApJL*, 561, L115

Meeus G., McCaughrean M. J., 2005, Astronomische Nachrichten, 326, 977

Mermilliod J. C., 1981, *A&A*, 97, 235

Mermilliod J.-C., Mayor M., 1999, *A&A*, 352, 479

Mermilliod J.-C., Turon C., Robichon N., Arenou F., Lebreton Y., 1997, in ESA Special Publication Vol. 402 of ESA Special Publication, The Distance of the Pleiades and Nearby Clusters. pp 643–650

Monet D. G., , 2005, Private communication

Monet D. G., et al., 2003, *AJ*, 125, 984

Moraux E., , 2007b, Private communication

Moraux E., Bouvier J., Stauffer J. R., 2001, *A&A*, 367, 211

Moraux E., Bouvier J., Stauffer J. R., Cuillandre J.-C., 2003, *A&A*, 400, 891

Moraux E., Bouvier J., Stauffer J. R., Navascués D. B. Y., Cuillandre J.-C., 2007, *A&A*, 471, 499

Muench A. A., Lada E. A., Lada C. J., Alves J., 2002, *ApJ*, 573, 366

Muench A. A., Lada E. A., Lada C. J., Elston R. J., Alves J. F., Horrobin M., Huard T. H., Levine J. L., Raines S. N., Román-Zúñiga C., 2003, *AJ*, 125, 2029

Nakajima T., Oppenheimer B. R., Kulkarni S. R., Golimowski D. A., Matthews K., Durrance S. T., 1995, *Nature*, 378, 463

Napiwotzki R., Christlieb N., Drechsel H., Hagen H.-J., Heber U., Homeier D., Karl C., Koester D., Leibundgut B., Marsh T. R., Moehler S., Nelemans G., Pauli E.-M., Reimers D., Renzini A., Yungelson L., 2003, The Messenger, 112, 25

Napiwotzki R., Edelmann H., Heber U., Karl C., Drechsel H., Pauli E.-M., Christlieb N., 2001b, *A&A* , 378, L17

Napiwotzki R., et al., 2001a, Astronomische Nachrichten, 322, 411

Napiwotzki R., Green P. J., Saffer R. A., 1999, *ApJ* , 517, 399

Napiwotzki R., Yungelson L., Nelemans G., Marsh T. R., Leibundgut B., Renzini R., Homeier D., Koester D., Moehler S., Christlieb N., Reimers D., Drechsel H., Heber U., Karl C., Pauli E.-M., 2004, in Hilditch R. W., Hensberge H., Pavlovski K., eds, Spectroscopically and Spatially Resolving the Components of the Close Binary Stars Vol. 318 of Astronomical Society of the Pacific Conference Series, Double degenerates and progenitors of supernovae type Ia. pp 402–410

Nelemans G., Tout C. A., 2005, *MNRAS* , 356, 753

Nelemans G., Verbunt F., Yungelson L. R., Portegies Zwart S. F., 2000, *A&A* , 360, 1011

Nelemans G., Yungelson L. R., Portegies Zwart S. F., Verbunt F., 2001, *A&A* , 365, 491

Nelson L. A., Rappaport S., Chiang E., 1993, *ApJ* , 413, 364

Nicolet B., 1981, *A&A* , 104, 185

Odenkirchen M., Soubiran C., Colin J., 1998, New Astronomy, 3, 583

Oke J. B., 1974, *ApJS* , 27, 21

Oliveira J. M., Jeffries R. D., Kenyon M. J., Thompson S. A., Naylor T., 2002, *A&A* , 382, L22

Oort J. H., 1979, *A&A* , 78, 312

Oppenheimer B. R., Kulkarni S. R., Matthews K., Nakajima T., 1995, Science, 270, 1478

Ortega V. G., Jilinski E., de La Reza R., Bazzanella B., 2007, *MNRAS* , 377, 441

Ozawa H., Grosso N., Montmerle T., 2005, *A&A* , 429, 963

Padoan P., Nordlund Å., 2002, *ApJ* , 576, 870

Pan X., Shao M., Kulkarni S. R., 2004, *Nature* , 427, 326

Percival S. M., Salaris M., Groenewegen M. A. T., 2005, *A&A* , 429, 887

Perryman M. A. C., Brown A. G. A., Lebreton Y., Gomez A., Turon C., de Strobel G. C., Mermilliod J. C., Robichon N., Kovalevsky J., Crifo F., 1998, *A&A* , 331, 81

Perryman M. A. C., et al., 1997, *A&A* , 323, L49

Pinfield D. J., Dobbie P. D., Jameson R. F., Steele I. A., Jones H. R. A., Katsiyannis A. C., 2003, *MNRAS* , 342, 1241

Pinfield D. J., Hodgkin S. T., Jameson R. F., Cossburn M. R., Hambly N. C., Devereux N., 2000, *MNRAS* , 313, 347

Pinfield D. J., Jameson R. F., Hodgkin S. T., 1998, *MNRAS* , 299, 955

Pinsonneault M. H., Stauffer J., Soderblom D. R., King J. R., Hanson R. B., 1998, *ApJ* , 504, 170

Pogson N., 1856, *MNRAS* , 17, 12

Preibisch T., Guenther E., Zinnecker H., Sterzik M., Frink S., Roeser S., 1998, *A&A* , 333, 619

Preibisch T., Zinnecker H., 2002, *AJ* , 123, 1613

Press W. H., Teukolsky S. A., Vetterling W. T., Flannery B. P., 1992, Numerical recipes in FORTRAN. The art of scientific computing. Cambridge: University Press, —c1992, 2nd ed.

Prialnik D., 2000, An Introduction to the Theory of Stellar Structure and Evolution. An Introduction to the Theory of Stellar Structure and Evolution, by D. Prialnik. ISBN 052165937X. http://www.cambridge.org/us/catalogue/catalogue.asp?isbn=052165937X. Cambridge, UK: Cambridge University Press, 2000.

Prosser C. F., Stauffer J. R., Hartmann L., Soderblom D. R., Jones B. F., Werner M. W., McCaughrean M. J., 1994, *ApJ* , 421, 517

Provencal J. L., Shipman H. L., Koester D., Wesemael F., Bergeron P., 2002, *ApJ* , 568, 324

Randich S., Schmitt J. H. M. M., Prosser C., 1996, *A&A* , 313, 815

Rebolo R., Beckman J. E., Crivellari L., Castelli F., Foing B., 1986, *A&A* , 166, 195

Rebolo R., Zapatero Osorio M. R., Madruga S., Bejar V. J. S., Arribas S., Licandro J., 1998, Science, 282, 1309

Rebolo R., Zapatero-Osorio M. R., Martin E. L., 1995, *Nature* , 377, 129

Rees M. J., 1976, *MNRAS* , 176, 483

Reid I. N., 1996, *AJ* , 111, 2000

Reid I. N., 1999, in Nakamoto T., ed., Star Formation 1999, Proceedings of Star Formation 1999, held in Nagoya, Japan, June 21 - 25, 1999, Editor: T. Nakamoto, Nobeyama Radio Observatory, p. 327-332 M Dwarfs, L Dwarfs, T Dwarfs and Subdwarfs: Ψ(M) at and below the Hydrogen-Burning Limit. pp 327–332

Reid I. N., et al.,, 2007, In preparation

Reid I. N., Hawley S. L., 1999, *AJ* , 117, 343

Reid I. N., Hawley S. L., 2005, New light on dark stars : red dwarfs, low-mass stars, brown dwarfs. Springer-Praxis books in astrophysics and astronomy. Praxis Publishing Ltd, 2005. ISBN 3-540-25124-3

Reid I. N., Mahoney S., 2000, *MNRAS* , 316, 827

Reid N., 1992, *MNRAS* , 257, 257

Reid N., 1993, *MNRAS* , 265, 785

Ruiz M. T., Leggett S. K., Allard F., 1997, *ApJL* , 491, L107+

Saffer R. A., Livio M., Yungelson L. R., 1998, *ApJ* , 502, 394

Salim S., Gould A., 2003, *ApJ* , 582, 1011

Sanders W. L., 1971, *A&A* , 14, 226

Santiago B. X., Gilmore G., Elson R. A. W., 1996, *MNRAS* , 281, 871

Schmidt S. J., Cruz K. L., Bongiorno B. J., Liebert J., Reid I. N., 2007, *AJ* , 133, 2258

Seifahrt A., Guenther E., Neuhäuser R., 2005, *A&A* , 440, 967

Sherry W. H., Walter F. M., Wolk S. J., 2004, *AJ* , 128, 2316

Skrutskie M. F., et al., 2006, *AJ* , 131, 1163

Slesnick C. L., Carpenter J. M., Hillenbrand L. A., 2006, *AJ* , 131, 3016

Soderblom D. R., Mayor M., 1993, *AJ* , 105, 226

Soderblom D. R., Nelan E., Benedict G. F., McArthur B., Ramirez I., Spiesman W., Jones
    B. F., 2005, *AJ* , 129, 1616

Stassun K. G., Mathieu R. D., Valenti J. A., 2006, *Nature* , 440, 311

Stauffer J., Hamilton D., Probst R., Rieke G., Mateo M., 1989, *ApJL* , 344, L21

Stauffer J. R., Barrado y Navascués D., Bouvier J., Morrison H. L., Harding P., Luhman K. L.,
    Stanke T., McCaughrean M., Terndrup D. M., Allen L., Assouad P., 1999, *ApJ* , 527, 219

Stauffer J. R., Hamilton D., Probst R. G., 1994, *AJ* , 108, 155

Stauffer J. R., Schultz G., Kirkpatrick J. D., 1998, *ApJL* , 499, L199+

Steele I. A., Jameson R. F., Hambly N. C., 1993, *MNRAS* , 263, 647

Steele I. A., Jameson R. F., Hodgkin S. T., Hambly N. C., 1995, *MNRAS* , 275, 841

Steele P. R., Burleigh M. R., Dobbie P. D., Barstow M. A., 2007, ArXiv e-prints, 709

Stroeer A., Vecchio A., Nelemans G., 2005, *ApJL* , 633, L33

244

Strom K. M., Kepner J., Strom S. E., 1995, *ApJ*, 438, 813

Strom K. M., Strom S. E., 1994, *ApJ*, 424, 237

The Denis Consortium 2005, VizieR Online Data Catalog, 1, 2002

Tinney C. G., Burgasser A. J., Kirkpatrick J. D., 2003, *AJ*, 126, 975

Tinney C. G., Burgasser A. J., Kirkpatrick J. D., McElwain M. W., 2005, *AJ*, 130, 2326

Trumpler R. J., 1938, Lick Observatory Bulletin, 18, 167

Tsvetkov T. G., 1989, *Astrophys. Space. Sci.*, 151, 47

Udry S., Mayor M., Queloz D., 2003, in Deming D., Seager S., eds, Scientific Frontiers in Research on Extrasolar Planets Vol. 294 of Astronomical Society of the Pacific Conference Series, Extrasolar Planets: from Individual Detections to Statistical Properties. pp 17–26

van Altena W. F., et al., 1997, *ApJL*, 486, L123+

van Leeuwen F., 1999, *A&A*, 341, L71

Vrba F. J., et al., 2004, *AJ*, 127, 2948

Walter F. M., Vrba F. J., Mathieu R. D., Brown A., Myers P. C., 1994, *AJ*, 107, 692

Walter F. M., Wolk S. J., Freyberg M., Schmitt J. H. M. M., 1997, Memorie della Societa Astronomica Italiana, 68, 1081

Warren S. J., et al., 2007, ArXiv e-prints, 708

Warren S. J., et al., 2007b, *MNRAS*, 375, 213

Warren Jr. W. H., Hesser J. E., 1978, *ApJS*, 36, 497

Weidemann V., 1977, *A&A*, 59, 411

Weidemann V., 1987, *A&A*, 188, 74

Weidemann V., 2000, *A&A*, 363, 647

Whitehouse S. C., Bate M. R., 2006, *MNRAS*, 367, 32

Whitworth A., Bate M. R., Nordlund Å., Reipurth B., Zinnecker H., 2007, Protostars and Planets V, pp 459–476

Wielen R., 1971, *A&A*, 13, 309

Wilson J. C., Miller N. A., Gizis J. E., Skrutskie M. F., Houck J. R., Kirkpatrick J. D., Burgasser A. J., Monet D. G., 2003, in Martín E., ed., Brown Dwarfs Vol. 211 of IAU Symposium, New M and L Dwarfs Confirmed with CorMASS. p. 197

York D. G., et al., 2000, *AJ*, 120, 1579

Zacharias N., Urban S. E., Zacharias M. I., Wycoff G. L., Hall D. M., Monet D. G., Rafferty T. J., 2004, *AJ*, 127, 3043

Zapatero Osorio M. R., Béjar V. J. S., Martín E. L., Rebolo R., Barrado y Navascués D., Bailer-Jones C. A. L., Mundt R., 2000, Science, 290, 103

Zapatero Osorio M. R., Béjar V. J. S., Martín E. L., Rebolo R., Barrado y Navascués D., Mundt R., Eislöffel J., Caballero J. A., 2002, *ApJ*, 578, 536

Zapatero Osorio M. R., Lane B. F., Pavlenko Y., Martín E. L., Britton M., Kulkarni S. R., 2004, *ApJ*, 615, 958

Zapatero Osorio M. R., Martin E. L., Bejar V. J. S., Bouy H., Deshpande R., Wainscoat R. J., 2007, ArXiv e-prints, 0706.0784

Zapatero Osorio M. R., Rebolo R., Martin E. L., Basri G., Magazzu A., Hodgkin S. T., Cossburn M. R., Jameson R. F., 1998, in Donahue R. A., Bookbinder J. A., eds, ASP Conf. Ser. 154: Cool Stars, Stellar Systems, and the Sun Brown Dwarfs in the Pleiades Cluster. p. 1912

Zinnecker H., 1984, *MNRAS*, 210, 43

Zuckerman B., Song I., 2004, *ARA&A*, 42, 685